8-1-2019

Integrated Control in Tokamaks using Nonlinear Robust Techniques and Actuator Sharing Strategies

Andres Pajares
Lehigh University

Integrated Control in Tokamaks using Nonlinear Robust Techniques and Actuator Sharing Strategies

by

Andres Pajares

Presented to the Graduate and Research Committee
of Lehigh University
in Candidacy for the Degree of
Doctor of Philosophy
in
Mechanical Engineering

Lehigh University
August 2019

Final Dissertation Signature Sheet

Approved and recommended for acceptance as a dissertation in partial fulfillment of the requirements for the degree of Doctor of Philosophy.

Date

Professor Eugenio Schuster, Dissertation Advisor

Accepted Date

Committee Members:

Professor Donald Rockwell

Professor Gary Harlow

Professor Nader Motee

Doctor David Humphreys

Acknowledgements

I want to express my deepest gratitude to all those who helped me during the course of this dissertation work.

First, I want to profoundly thank my advisor, Prof. Eugenio Schuster, for offering me the opportunity to come to the United States of America and work in the nuclear-fusion control field, and for his supportive guidance and all the trust deposited on me during my studies and future post-doctoral research. It has been a life-changing experience for me both personally and professionally.

Special thanks to Prof. Rafael Vazquez for putting me in contact with my advisor, and for always offering his useful advice.

I would like to thank my colleagues at the Lehigh University Plasma Control Group, specially Dr. William P. Wehner, Dr. Hexiang Wang, Dr. Menno Lauret, and Dr. Zeki Ilhan, for their help and support during the completion of this work.

Furthermore, I want to thank all the scientists working at the DIII-D National Fusion Facility, specially Dr. David Humphreys for his supportive guidance during my integration into the DIII-D team, and for serving in my dissertation committee. Special thanks to Dr. Michael Walker, Dr. Anders Welander, Dr. John Ferron, Dr. Robert La Haye, Dr. Nicholas Eidietis, Dr. Jayson Barr, Dr. Al Hyatt, Benjamin Penaflor and Robert Johnson for their great help and support during the planning and execution of experiments in DIII-D.

I would also like to thank my dissertation committee members from Lehigh University, Prof. Donald Rockwell, Prof. Gary Harlow, and Prof. Nader Motee. Thanks to Prof. Arnold Kritz, who helped me with my general and PhD proposal examinations. It would have been a pleasure to have him in my dissertation committee for my defense as well.

Finally, thanks to my family, and specially to my parents, Andres and Adela, and my sisters, Olga, Eva and Isa, for their unconditional support and for teaching me the basics that cannot be learnt in any school or university. This work would have not been possible without them.

Contents

List of Tables

List of Figures

Abstract

Tokamaks are devices whose final purpose is obtaining energy by means of nuclear fusion reactions. To achieve such purpose, a gas is injected into the tokamak's torus-shaped chamber and heated up to extremely high temperatures, giving birth to a plasma. When the necessary conditions of temperature, density, and confinement time are achieved, virtually inexhaustible energy can be produced in a tokamak.

The main contribution of this dissertation is the development of integrated control strategies for tokamak plasmas. The development of integrated control architectures is necessary for tokamaks to become efficient and commercially competitive power plants. Because a tokamak plasma is a highly nonlinear, coupled dynamical system, the great diversity of complex control problems that coexist in a tokamak are indeed closely interrelated. However, this variety of control problems must be tackled by means of a limited number of actuators. A functional design for integrated tokamak-control architectures should employ multi-input multi-output controllers to simultaneously regulate as many plasma variables as possible with the available actuators. Supervisory and exception handling systems that monitor the plasma state arise as a necessity to ensure a safe tokamak-operation. Finally, actuator sharing and management capabilities should also exist in order to utilize the available actuators in an optimal way. Various control problems are tackled in this dissertation, including kinetic, magnetic, and instability control problems. Control-oriented, physics-based models that characterize some specific aspects of the plasma dynamics have been employed to develop new control-oriented simulation codes and integrated-control solutions that employ nonlinear, robust control techniques and optimization-based actuator-management strategies. Some of those control solutions have been experimentally tested in the DIII-D tokamak.

Chapter 1

Introduction to Nuclear Fusion and Tokamak-Plasma Control

The objective of this Chapter is to briefly introduce the most basic concepts related to nuclear fusion, tokamaks, and tokamak-plasma control problems, particularly for those who are not familiar with such topics. The experienced reader is advised to go directly to Chapter 2 or to the dissertation outline in this Chapter, Section 1.4.

1.1 Nuclear Fusion: Basics

1.1.1 A Brief History of Nuclear Fusion Research

Nuclear fusion was a total mystery until the XX century. In the 1920's, Sir Arthur Eddington was the first scientist to correctly suggest that the energy created in the stars was due to the fusion of hydrogen and helium [1]. Fusion reactions, which release relatively high amounts of energy from small amounts of mass, are possible in the stars due to the huge masses and the gravitational forces that these cosmic giants generate, which produce the necessary conditions for particles to fuse. This mechanism is known as gravitational confinement. Such a powerful (and, for some, almost "magical") source of stellar energy soon aroused interest within the scientific community. However, for evident reasons, reproducing nuclear fusion on Earth

by means of gravitational confinement is not feasible, and significant research was initiated to find new confinement methods and understand the physics involved in the nuclear fusion processes. Until the 1950's, most research was classified due to its link with the development of thermonuclear weapons. Since then, nuclear fusion research has been characterized by a high degree of international collaboration. Two alternative confinement methods are the main focus of the ongoing fusion-science research program: *inertial confinement*, whose goal is to attain fusion conditions by compressing a fuel target by means of high-energy lasers, and *magnetic confinement*, whose goal is to attain fusion conditions by confining the fuel particles by means of magnetic fields. The latter is the one that has experienced the biggest progress throughout the years and, nowadays, is the main focus of the fusion-science research program, exploring the path towards a clean, safe, and virtually inexhaustible source of energy that could solve most of the problems associated with the current means of producing energy.

1.1.2 Nuclear Reaction Physics

A nuclear reaction is the process in which two or more nuclei (and possibly subatomic particles, such as protons or neutrons) get combined and form at least one different nuclei (and possibly other subatomic particles as well). A nuclear reaction can be represented as follows,

$$r_1 + r_2 + ... + r_i + ... + r_M \rightarrow p_1 + p_2 + ... + p_j + ... + p_N, \tag{1.1}$$

where r_i is the i-th reactant for a total of M reactants, and p_j is the j-th product for a total of N products. When the reactant nuclei are combined to form a heavier nucleus, the nuclear reaction is said to be a *fusion reaction* (see Fig. 1.1). The opposite process, in which reactant nuclei are split into lighter nuclei, is known as a *fission reaction*. Both in fusion and fission nuclear reactions, the relativistic energy of the system, E_{rel}, is conserved. Therefore,

$$E_{rel} = \sum_{i=1}^{i=M} \left[m_0 \left(\frac{v^2}{2} + c^2 \right) \right]_{r_i} = \sum_{j=1}^{j=N} \left[m_0 \left(\frac{v^2}{2} + c^2 \right) \right]_{p_j}, \tag{1.2}$$

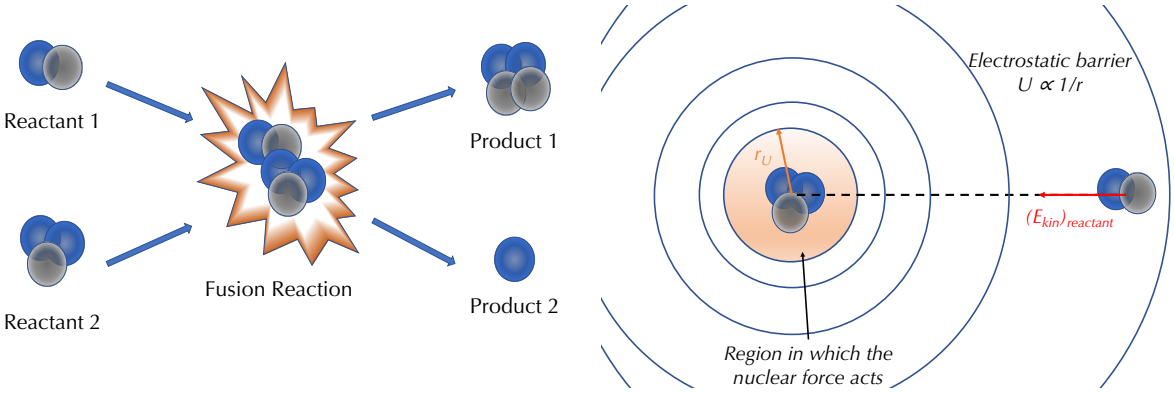

Figure 1.1: Schematic of the D-T fusion reaction (on the left) and the Coulombic electrostatic barrier (on the right).

where m_0 is the rest mass, v is the velocity, c is the speed of light, and $[(\cdot)]_{r_i}$, $[(\cdot)]_{p_j}$ denote that the variable $(\cdot)$ corresponds to the i-th reactant or j-th product, respectively. Using the definition of kinetic energy, $E_{kin} = \frac{1}{2}m_0v^2$, equation (1.2) can be rewritten as follows,

$$\Delta E_{kin} = \sum_{i=1}^{i=M}\left[\frac{1}{2}m_0v^2\right]_{p_j} - \sum_{j=1}^{j=N}\left[\frac{1}{2}m_0v^2\right]_{r_i} = (\sum_{j=1}^{j=N}[m_0]_{r_i} - \sum_{i=1}^{i=M}[m_0]_{p_j})c^2, \qquad (1.3)$$

i.e., the variation of kinetic energy in the reaction, ΔE_{kin}, is proportional to the sum of the reactant rest masses minus the sum of the product rest masses. If $\Delta E_{kin} > 0$, the products gain kinetic energy with respect to the reactants, and such reaction is called *exothermic*. In an exothermic reaction, the difference in rest mass between reactants and products is transformed into kinetic energy. On the contrary, if $\Delta E_{kin} < 0$, the products have a lower kinetic energy than the reactants, and such reaction is called *endothermic*. In an endothermic reaction, there is an increase in rest mass of the products with respect to that of the reactants. For energy production purposes, exothermic reactions are much more interesting than endothermic reactions, as the increase in kinetic energy through the reaction can be transformed into other types of energy, like for example thermal energy or electrical energy. The final goal of the current fusion-science research program is to achieve significant exothermic fusion reactions in order to produce electrical energy.

Some exothermic fusion reactions of interest, together with their kinetic energy gains, are given by

$$\mathrm{D} + \mathrm{T} \rightarrow {}^{4}\mathrm{He} + \mathrm{n}, \quad (\Delta E_{kin} = 17.6 \text{ MeV}) \tag{1.4}$$

$$\mathrm{D} + \mathrm{D} \rightarrow {}^{3}\mathrm{He} + \mathrm{n}, \quad (\Delta E_{kin} = 2.46 \text{ MeV}) \tag{1.5}$$

$$\mathrm{D} + {}^{3}\mathrm{He} \rightarrow {}^{4}\mathrm{He} + \mathrm{p}^{+}, \quad (\Delta E_{kin} = 18.3 \text{ MeV}) \tag{1.6}$$

where D is the deuterium nucleus (the hydrogen isotope composed by one proton and one neutron), sometimes referred to as deuteron, T is the tritium nucleus (hydrogen isotope composed by one proton and two neutrons), sometimes referred to as triton, n denotes a neutron, and p^{+} denotes a proton.

The mechanism of a nuclear fusion reaction cannot be understood without the two following forces: the Coulombic forces and the strong nuclear forces. On the one hand, the electrostatic Coulombic forces are repulsive between like-charged particles, so they make the positively-charged nuclei particles repel each other just like the positive (or negative) ends of two magnets. On the other hand, the strong nuclear forces bind the nuclei particles together. The strong nuclear forces are much more powerful than the Coulombic forces, but are also extremely short-range (only relevant at distances within the order of a nucleus size). For a fusion reaction to happen, the reactant particles must overcome the repulsive Coulombic forces experienced by their positively-charged nuclei (the so-called Coulombic barrier, see Fig. 1.1), and come close enough so that the strong nuclear forces bind them together.

Overcoming the Coulombic barrier requires that the reactants have very high kinetic energies. For the heavier elements, this may result in an endothermic fusion reaction. In general, lighter elements are more likely to yield exothermic fusion reactions. A simple estimate of the kinetic energy required for fusion can be obtained for single-charged ions using the electrostatic potential, $U = \frac{q_e^2}{4\pi\epsilon_0 r_U}$, where q_e is the electron charge, ϵ_0 is the vacuum electrical permittivity, and r_U is the characteristic distance at which the strong nuclear force acts. If r_U is taken as the radius of the proton, whose order of magnitude is 10^{-15} m, then the order of magnitude of U is 100 keV. However, significant fusion reactions can happen at lower temperatures, within the order of 10 keV. This can be explained by means of quantum mechanics

and the so-called *quantum tunneling* phenomenon, which predicts that subatomic particles can overcome potential barriers that could not be overcome according to classical mechanics, and is due to the particle-wave duality of subatomic particles.

The likelihood for fusion reactions to happen is quantified in nuclear physics by means of the so-called *reactivity*, $\langle \sigma v \rangle$, which is a function of the kinetic energy of the reactants, or their temperature[1], T. Approximate $\langle \sigma v \rangle$ values for the fusion reactions in (1.4)-(1.6) are shown in Fig. 1.2, within the range $T = [1, 100]$ keV [3].

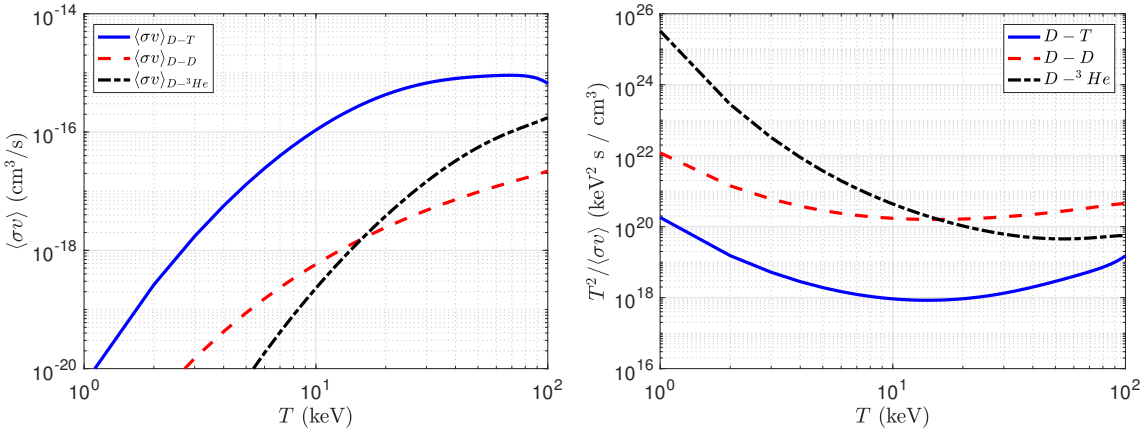

Figure 1.2: Reactivities $\langle \sigma v \rangle$ and $T^2/\langle \sigma v \rangle$ for D-T, D-D and D-^{3}He fusion reactions.

It can be seen that the D-T reaction (1.4) presents the highest $\langle \sigma v \rangle$ at the given temperature range, so it is the most interesting for energy production purposes. The fusion power-density produced by D-T reactions, denoted by Q_{fus}, is given by

$$Q_{fus} = \Delta E_{kin} n_D n_T \langle \sigma v \rangle, \tag{1.7}$$

where n_D and n_T are the D and T densities, respectively, and $\Delta E_{kin} = 17.6$ MeV is the energy gain in every D-T reaction, as indicated in (1.4). Approximately 4/5 of Q_{fus} is carried by the neutron, whereas the remaining 1/5 is carried by the α particle (^{4}He).

[1]The kinetic-energy requirements for fusion can be expressed in terms of the temperature of the reactants. The reactivity, $\langle \sigma v \rangle$, is the average over a Maxwellian particle-distribution of the reaction cross-section, σ, multiplied by the velocity of the particles, v. The relationship between the temperature of the Maxwellian distribution, T, and the average kinetic energy of the particles in a three-dimensional Maxwellian distribution, E_{av}, is given by $E_{av} = \frac{3}{2}KT$, where K is the Boltzmann's constant. More details can be found in [2].

1.1.3 Fusion Science and Plasma Physics

As it can be seen in Fig. 1.2, the temperature required to achieve fusion is extremely high even for the lightest atoms, hydrogen and its isotopes (1 keV corresponds to approximately 10^7 K). At such extreme temperatures, the reactants are found in *plasma state*, in which ions and electrons are dissociated. Therefore, fusion science and plasma physics are fields of study that are inherently interconnected.

Such connection makes fusion science an even more challenging field. In addition to the technological difficulties associated with achieving the required temperatures, plasmas behave in unexpected ways, specially when compared to non-ionized gases. Because charged particles move within plasmas, electrical currents can be driven through them. Moreover, charged particles can interact with magnetic fields. A plasma within a prescribed magnetic field experiences a Lorentz force that modifies the momentum of the particles, and therefore the electrical currents within the plasma. In turn, such currents create magnetic fields that modify the externally created magnetic field. Even to the untrained eye, it would not be difficult to hint that such a system might be hard to understand from an intuitive physical standpoint. As a matter of fact, some of the plasma instabilities observed cannot be fully explained by the existing physical theories.

1.1.4 Feasibility of a Fusion Power Plant

A schematic of a possible D-T fusion reactor is shown in Fig. 1.3. The reactant plasma would preferably be a D-T mix, although a D-D reactor would function in an analogous way. Deuterium can be obtained from sea water and is virtually inexhaustible, but tritium cannot be found in nature. It can be synthesized from lithium by neutron bombardment according to the following fission reactions,

$$\mathrm{n} + {}^{6}\mathrm{Li} \rightarrow \mathrm{T} + {}^{4}\mathrm{He}, \quad \mathrm{n} + {}^{7}\mathrm{Li} \rightarrow \mathrm{n} + \mathrm{T} + {}^{4}\mathrm{He}. \tag{1.8}$$

A lithium blanket would be placed around the reacting plasma, so that the high energetic neutrons released in the fusion reactions collide with the blanket and provide the reactor with the necessary T for its operation. The heat arising from neutron

bombardment of the lithium blanket would be employed to generate electrical energy by means of a turbine, as in any conventional thermal plant. On the other hand, the α particles (^{4}He) would remain within the plasma providing the necessary heating to sustain the required fusion temperatures. In addition, auxiliary power sources would be employed to provide additional heating during the operation phases in which it may be needed.

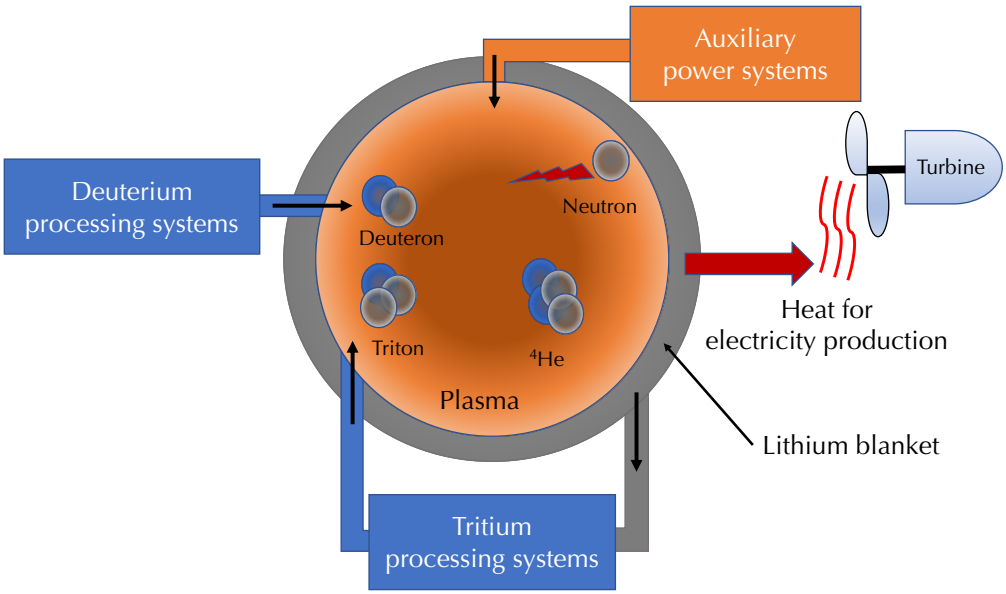

Figure 1.3: Schematic of a D-T fusion reactor with lithium blanket.

A parameter of interest in fusion power plants is the so-called fusion gain, $Q \triangleq P_{fus}/P_{aux}$, i.e., the ratio of fusion power produced, P_{fus}, to auxiliary power injected, P_{aux}. Ideally, P_{aux} would be needed only to initiate the fusion reactions or for thermal control during small periods of time, so that the plasma temperature is maintained mostly by means of α-heating power. This operating point, in which $Q \to \infty$, is known as *ignition* by analogy to fossil-fuel power plants. A less exigent but still relevant operating point would be that in which $Q = 1$, that is, the power produced from fusion reactions is the same as the power injected by the auxiliary sources. The condition $Q = 1$ is known as *breakeven*. However, a value of $Q = 1$ would not be enough to ensure the economical feasibility of a power plant because the conversion between P_{fus} and electrical power cannot be done with 100% efficiency.

Fusion reactors would be much safer than fission reactors because they have no risk of meltdown and their radioactive waste is short-lived. They would also have the typical advantages of other clean sources of energy: they do not produce CO_2 and their fuel is almost unlimited[2]. However, other technological and economical difficulties, such as the partial lack of physics understanding, the difficulties associated with tritium processing and steady-state operation, or the high construction cost of fusion plants, are drawbacks that need to be overcome for fusion reactors to become viable power plants.

1.1.5 Lawson's Criterion

The expression for P_{fus} in equation (1.7) indicates that, in addition to reaching the high temperatures required for significant fusion to occur, it is also necessary to sustain them at high enough density. Moreover, the time during which the particles remain within the confined plasma must be maximized. Temperature, density, and confinement time characterize the so-called *plasma confinement*. In an ignited plasma (i.e., $Q \to \infty$, $P_{aux} = 0$) under steady-state conditions, the α-heating power density, Q_α, must be equal to the power-density losses, Q_{loss}. For a D-T plasma, both magnitudes are given by

$$Q_\alpha = \Delta E^\alpha_{kin} n_D n_T \langle \sigma v \rangle, \tag{1.9}$$

$$Q_{loss} = \frac{3}{2}\frac{(n_D + n_T)KT_i + n_e KT_e}{\tau_E} \approx \frac{3}{2}\frac{(n_D + n_T + n_e)KT}{\tau_E}, \tag{1.10}$$

where $\Delta E^\alpha_{kin} = 3.52 MeV$ is the energy carried by the α particle in the D-T reaction, and τ_E is the energy confinement time. It is assumed that the temperature of the ions, T_i, and electrons, T_e, is similar, $T_i \approx T_e \approx T$. The quasi-neutrality condition[3] for a D-T plasma with small or no α and impurity content is given by $n_D + n_T =$

[2]There is a growing concern that there will be a shortage of lithium due to an increasing demand from the electronics industry [4], although it is unclear whether this will affect the future development of nuclear fusion as a feasible way of producing clean energy.

[3]Plasmas are *quasi-neutral*: although ions and electrons are dissociated, the overall electrical charge remains approximately zero.

$n_i = n_e$, where n_i and n_e are the ion and electron densities, respectively. Using the quasi-neutrality condition and assuming $n_D = n_T$, the condition $Q_\alpha = Q_{loss}$ can be written as[4]

$$n_e T \tau_E = \frac{12T^2}{\Delta E^\alpha_{kin} \langle \sigma v \rangle}. \tag{1.11}$$

Equation (1.11) is sometimes referred to as *triple product* or *Lawson's criterion*. It gives an approximate estimation of the minimum requirements for ignition in terms of T, n_e, and τ_E. The function $T^2/\langle \sigma v \rangle$ has a minimum at around $T \approx 15$ keV (see Fig. 1.2), at which $T^2/\langle \sigma v \rangle \approx 10^{18}$ keV^2 s/m^3, so (1.11) can be rewritten as

$$n_e T \tau_E \geq 3 \times 10^{21} \text{ keV s/m}^3. \tag{1.12}$$

It must be noted that, instead of $Q \to \infty$, high Q (i.e., $P_{fus} >> P_{aux} \neq 0$) may suffice to fulfill the energy-production objectives of a fusion reactor. In the case with $P_{aux} \neq 0$, the condition $Q_\alpha = Q_{loss}$ is written as $Q_\alpha + Q_{aux} = Q_{loss}$ instead, where $Q_{aux} \propto P_{aux}$ is the auxiliary power-density. This yields

$$n_e T \tau_E = \frac{12T^2}{\Delta E^\alpha_{kin} \langle \sigma v \rangle} \left(1 - Q_{aux} \frac{\tau_E}{3 n_e T} \right), \tag{1.13}$$

which represents a less exigent requirement than (1.11). However, thus far, fusion plasmas have demonstrated worse confinement (and therefore, a lower triple product) than it was initially predicted by scientists in the early stages of nuclear fusion research [2], and neither (1.11) nor (1.13) have been attained yet. However, $1 << Q < \infty$ operation may be attainable and is the focus of the fusion-energy research programs around the world.

1.2 The Tokamak Concept

Within the aforementioned magnetic-confinement approach to fusion, the tokamak is one of the most promising devices that has been designed thus far [5]. Invented by Soviet Union scientists in the 1950's, the tokamak is a torus-shaped device in which

[4] To simplify the notation used, T is employed instead of KT for the remaining of this Section.

a plasma is confined by means of helical magnetic fields, as shown in Fig. 1.4. Moreover, electrical current is inductively driven through the plasma, which acts as the secondary of a transformer. Because of this transformer-like principle of operation, the tokamak was originally designed as an inherently pulsed device. However, the addition of auxiliary current sources into most tokamak designs and the discovery of the self-generated *bootstrap current* [5] may make up for the loss of inductively-driven current, possibly allowing tokamak operation in steady-state regimes.

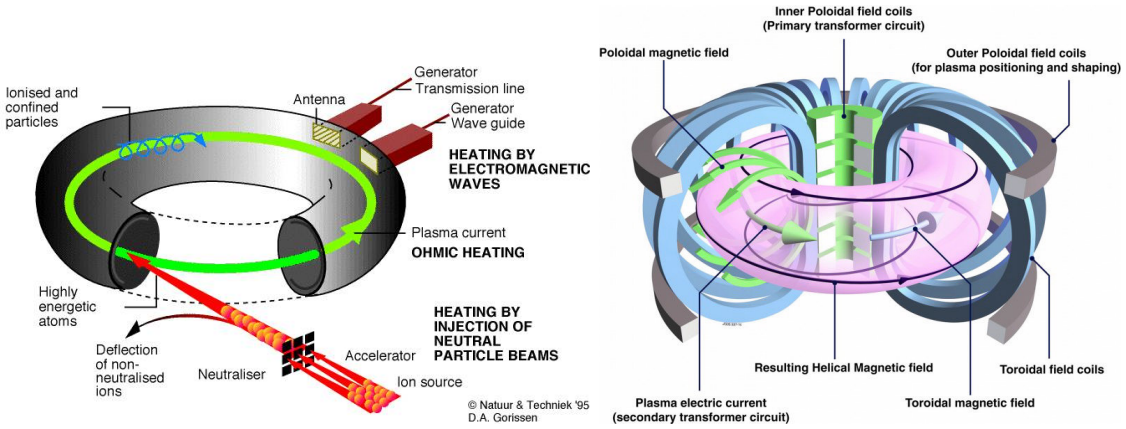

Figure 1.4: The tokamak: on the left, main types of heating and current drive methods employed; on the right, the magnetic configuration and coils.

Nowadays, tens of tokamaks operate around the world. Currently, the biggest tokamak and the only one that operates with D-T plasmas during some periods of its experimental campaigns is the Joint European Torus (JET), in the United Kingdom, that achieved the highest Q ever attained ($Q \approx 0.67$). However, the triple-product world record belongs to the JT-60 tokamak, in Japan, that achieved $n_e T \tau_E \approx 1.5 \times 10^{21}$ keV s/m^3. Other medium-size tokamaks are WEST in France, ASDEX-U in Germany, or DIII-D in the United States of America. A major milestone in the development of fusion science is ITER, the next-generation tokamak currently under construction in France. ITER is approximately two times the size of JET, and its main mission is to demonstrate the feasibility of nuclear fusion as a means of producing energy, as well as providing a benchmark for future commercial-grade fusion reactors.

1.2.1 Basic Description of the Tokamak Operation

A tokamak pulse, also known as plasma discharge, starts with the injection of a gas (normally D in present devices, but ideally a D-T mix in future devices) into the tokamak vacuum chamber. In the initial phase, also known as *breakdown*, the gas is ionized and becomes a plasma by means of the ohmic coil. The ohmic coil acts as the primary of a transformer, whereas the plasma behaves as the secondary. During this initial phase, the plasma is very conductive and its temperature raises due to ohmic heating. After the breakdown phase, the total plasma current, denoted by I_p, is normally ramped-up until it reaches a more or less stationary value. The evolution of I_p is regulated by controlling the current in the ohmic coil. After some time at an approximately constant I_p, the plasma discharge finishes with an I_p ramp-down. The stationary value of I_p and the duration of the stationary phase depend on the particular design of the tokamak in question. Based on the evolution of I_p, a plasma discharge is normally divided into three phases: *ramp-up* phase, *flat-top* phase, and *ramp-down* phase.

As the discharge evolves in the ramp-up and flat-top phases, most present-day tokamaks employ auxiliary sources to supply additional Heating and Current Drive (H&CD) to the plasma (see Fig. 1.4). This is due to the fact that as the plasma temperature raises, its conductivity decreases, making the ohmic-heating method much more inefficient. Auxiliary H&CD methods commonly used are Neutral Beam Injection (NBI), that employs neutral particles that collide with the plasma particles and get ionized while transferring their energy, and electromagnetic waves, such as Electron-Cyclotron (EC), Ion-Cyclotron (IC) or Lower-Hybrid (LH) waves, that excite the EC, IC or LH plasma frequencies [2]. Also, additional gas is normally injected into the vacuum chamber to increase the plasma density. As of now, two fueling methods are used in tokamaks: gas puffing, that injects gas at the plasma edge by means of a system of valves and conducts open to the tokamak's first wall, and pellet injection, that injects high velocity pellets directly into the plasma core.

As introduced above, the plasma particles are confined within a tokamak by means of magnetic fields. The primary magnetic field in a tokamak is the toroidal

magnetic field (see Fig. 1.4). The toroidal field coils distributed along the tokamak are responsible for the creation of the toroidal field. Present medium and large-size tokamaks operate with toroidal fields within the order of a few teslas. The current through the toroidal coils is kept approximately constant, so that the external toroidal field is also constant. An order of magnitude smaller, but still indispensable to make the plasma column stable within a tokamak, is the poloidal magnetic field[5]. It is mainly generated by I_p, but it is also affected by the poloidal field coils that are used for plasma shape and position control within the vacuum chamber (see Fig. 1.4). The combination of the toroidal and poloidal magnetic fields results in helical magnetic-field lines. Other additional magnetic coils are sometimes available, depending on the design of the tokamak in question. They receive different denominations depending on their configuration. For example, the coils whose location is inside the tokamak's vacuum vessel are sometimes denominated in-vessel coils, whereas the coils located outside the vacuum vessel denominated ex-vessel coils. In DIII-D, the in-vessel coils are referred to as I-coils, whereas the ex-vessel coils are referred to as C-coils. The coils may also be named after their purpose, like for example in ITER, in which edge-localized mode (ELM) coils, field-correction coils, and vertical-stability (VS) coils are found[6].

The time evolution of some plasma magnitudes (I_p, line-average[7] n_e, and P_{aux}) in a plasma discharge for the DIII-D tokamak (shot 147634), is illustrated in Fig. 1.5, together with the electron temperature and pressure[8] profiles, T_e and p_e, respectively. At the flat-top phase, the values for I_p, line-average n_e, and P_{aux} are approximately 1 MA, 4.5×10^{19} m^{-3}, and 14 MW, respectively, whereas T_e and p_e are within the order of a few keV (10^7 K) and KJ/m^3 (10^{-3} atm), respectively, illustrating the high temperature and low pressure ranges in which present tokamaks operate.

[5]For a deeper explanation on why the poloidal magnetic field is necessary, see Section 2.1 or [5].

[6]See Section 1.3 for a brief introduction on the ELM, field-correction and vertical-stability control problems in which these coils are employed.

[7]The line-average density is the average density measured along a line or beam, normally defined from the diagnostics employed. See Section 1.3.6 and/or [6] for more details.

[8]The pressure of a particular plasma species is the product of its density and temperature. It is formally introduced in Section 2.1.5.

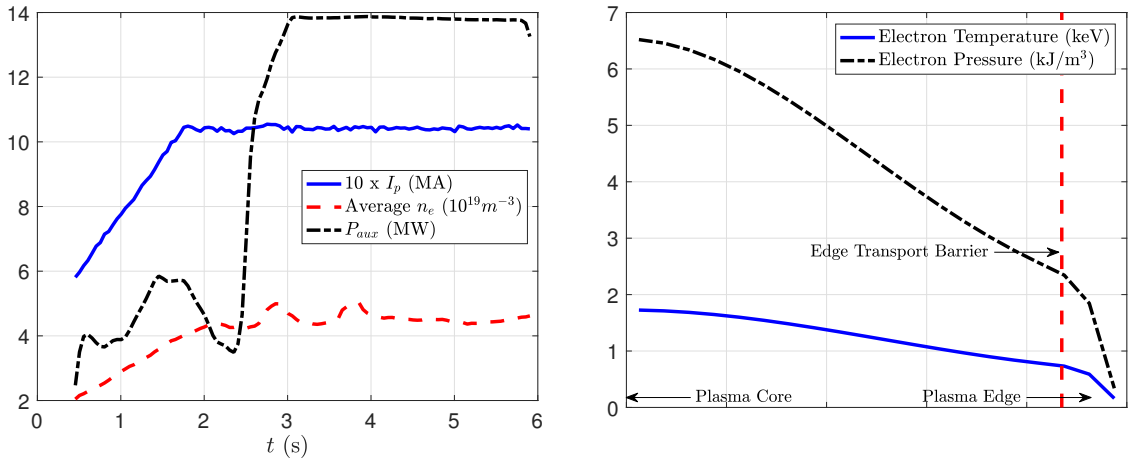

Figure 1.5: Magnitude evolutions during a tokamak H-mode discharge (DIII-D shot 147634): on the left, I_p, P_{aux}, and average n_e; on the right, electron temperature and pressure profiles.

1.2.2 Tokamak-Plasma Confinement Modes

From the creation of the tokamak until the 1980's, it was an experimental fact that increasing the heating power in a tokamak plasma implied a decrease in τ_E. The plasma was turbulent from its core to the edge, and applying a higher P_{aux} resulted in an increased turbulence and particle transport, worsening the plasma confinement. However, during some experiments in the ASDEX tokamak [7] in 1982, it was observed that if the heating power was above a certain threshold, then the plasma transitioned into an improved-confinement mode with higher τ_E (improved by a factor of about 2). Such improved-confinement mode was denominated *H-mode* ("high" confinement mode), whereas the previous confinement mode was denominated *L-mode* ("low" confinement mode).

The H-mode is characterized by a reduced turbulence at the plasma edge, which creates an edge transport barrier and reduces the overall plasma transport. This effect rises the plasma kinetic variables (such as the temperature or density) at the core, whereas at the edge transport barrier, the kinetic variables suffer a sudden drop as depicted in Fig. 1.5. However, a new type of plasma instabilities known as edge-localized modes (ELMs) were observed in H-mode discharges, possibly due to the steep pressure gradient at the edge. During an ELM, a sudden current burst (with the associated energy and particle loss) takes place, spoiling the plasma

confinement and possibly damaging the tokamak's first wall. Substantial research is being carried out to minimize the negative impact of ELMs by mitigating or fully suppressing them.

In any case, the H-mode is a desirable confinement mode and the basis for most current tokamak-plasma research due to its improved confinement when compared to L-mode. Also, a number of H-mode regimes with particular characteristics have been discovered throughout the years, such as the *QH-mode* ("quiescent" H-mode, which does not show ELM activity [8]), or the *super H-mode* (which has an even higher confinement than the "conventional" H-mode, and was theoretically predicted before its experimental demonstration [9]).

1.2.3 Tokamak Operating Scenarios

A tokamak *operating scenario* is defined as the sequence of events executed during tokamak operation to prepare and initiate the plasma, raise I_p to its flat-top value, inject gas, employ H&CD auxiliary sources, and finally terminate the plasma in a controlled and safe way [10]. Generally speaking, tokamak scenarios are divided into two broad categories attending to the amount of inductive/non-inductive current that they operate with:

- *Conventional* or *Inductive Scenarios*, characterized by a high fraction of inductive current. These scenarios are in principle easier to explore and operate, but have an inherently pulsed nature.

- *Advanced* or *Non-Inductive Scenarios*, characterized by a high fraction of non-inductive current, and therefore, of longer duration than inductive scenarios. Ideally, the non-inductive fraction would be equal to 1, and steady-state operation would be possible. However, these scenarios have been proven to be more difficult to achieve and operate than conventional scenarios.

Within these two general categories, there are lots of particular tokamak scenarios that are being studied at the different tokamaks existing in the world [10]. In particular, for ITER, two main scenarios are envisioned: an inductive scenario (sometimes

referred to as the *ITER baseline scenario*) with $P_{fus} = 500$ MW and $P_{aux} = 50$ MW (i.e., $Q = 10$), and a long-pulse or steady-state scenario with $Q = 5$.

1.3 Control Problems in Tokamak Plasmas

Different control problems arise in tokamak plasmas for which a solution is needed. Fig. 1.6 shows a basic schematic of the different elements present in tokamak control problems. As in any control problem, the objective is to drive a particular set of measurable variables (known as the system's *output* in the control jargon) towards a desired trajectory (normally known as the output *target*, sometimes also as *reference*) by regulating a particular set of variables (known as the *controllable input*). The *plant* is the to-be-controlled subject (i.e., the tokamak and/or the plasma), and the *system* is the combination of the plant and a controller. Controllers for tokamak plasmas are implemented in the so-called plasma control systems (PCSs). The minimum set of variables that describes the state of the system at any given time is the so-called *system state*. Sometimes, it may be desirable to control the system state, but it may not be measurable and/or controllable. In addition, there are some variables that affect the system but cannot be controlled (known as the *non-controllable input*). Finally, the *system dynamics* is characterized by a mathematical model that describes the relationship between the system's state, input (controllable or not), and output, and defines the state and output time evolutions once the state initial condition and the input trajectory are given.

An example of a critical control problem that has been introduced in Section 1.2.1 is controlling I_p by means of the ohmic-coil current. In this example, it can be considered that the output is I_p, the controllable input is the ohmic-coil current, and the target is defined by the ramp-up rate and flat-top values of I_p. The controller employs I_p and the target information to generate the controllable input signal (the ohmic-coil current) which is sent to the plant (the tokamak). The dynamical model relates how the ohmic-coil current and other non-controllable inputs affect I_p, i.e., it models the relationship between inputs, outputs, and state (u, y, and x in Fig. 1.6).

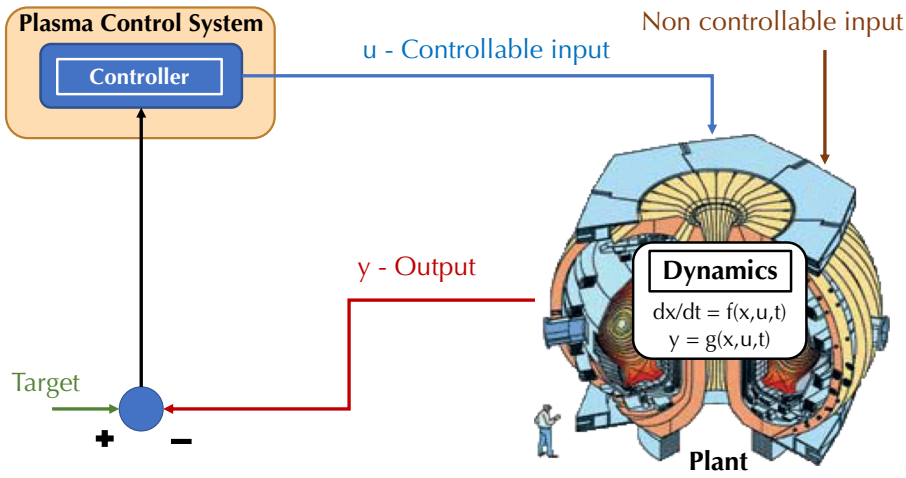

Figure 1.6: Schematic of the elements existing in tokamak control problems.

Tokamak-plasma control problems are normally categorized depending on the nature of the variables involved. If the to-be-controlled magnitudes are kinetic variables such as the ion/electron temperature, density, pressure, velocity, and/or energy, the problem is classified as a *kinetic control* problem. On the other hand, when magnetic variables such as the magnetic field, electric field, and/or electrical current are involved, the problem is classified as a *magnetic control* problem. A third category corresponds to *instability control* problems[9], i.e., control problems in which the final goal is the mitigate or suppress a particular type of plasma instability. It has to be noted that the distinction between kinetic, magnetic and instability control problems is somewhat arbitrary because, more often than not, the dynamics of the kinetic and magnetic variables and plasma instabilities are tightly coupled.

1.3.1 Kinetic Control

Control of the tokamak kinetic variables (velocity, temperature, density, etc.) is known as kinetic control. Actuators normally employed for kinetic control include auxiliary power injection (NBI, ECH, ICH, etc.) and fueling by means of gas puffing or pellet injection. Also, other actuation methods that affect magnetic variables can

[9] Although *instability control* is a term normally employed by nuclear-fusion physicists, control engineers may find it more appropriate to use the term *instability suppression*.

be employed for kinetic control in an "indirect" fashion. For instance, it is known that modifying the plasma shape and/or the plasma current profile has a direct effect on the plasma confinement, so actuators such as the magnetic coils (which modify the external magnetic fields, and therefore the plasma shape) or auxiliary current-drive injection by means of NBI and ECCD (which modify the plasma current profile) could also be employed for kinetic control.

Some important kinetic-control problems in tokamaks are:

- *β control.* The parameter β is a metric of the confinement efficiency in a tokamak[10], as it measures how much kinetic pressure, p, can be confined by means of a given magnetic field, B. Maximizing β for a given tokamak design is a prime goal in fusion science. Moreover, β is related to certain plasma instabilities, such as the neoclassical tearing modes (NTMs) [2], which are treated later during this dissertation.

- *Toroidal-rotation control.* The toroidal momentum of the ions is a variable of interest due to its close relationship with plasma performance. For example, it is observed that a particular type of plasma instabilities called Resistive Wall Modes (RWMs) are stabilized with increasing rotation. Also, toroidal rotation improves NTM rotation, preventing that these modes lock and terminate the confined plasma. NBI and some magnetic coils are actuators that can be employed to vary the torque injected into the plasma, respectively, and regulate the toroidal rotation in present-day tokamaks. However, it is unclear to what extent it will be possible to control the toroidal rotation in future fusion reactors due to their higher volume and plasma inertia.

- *Burn control.* The main objective in this control problem is to regulate the plasma temperature and density around a given target (which defines the so-called *burn condition*) to obtain a desired amount of fusion power. Also, possible thermal instabilities may arise which need suppression by means of

[10] β is defined as the ratio of kinetic pressure p to "magnetic" pressure $B^2/(2\mu_0)$, where μ_0 is the vacuum magnetic permeability. The definition of β is derived in Chapter 2.

burn control. Although present tokamaks also require density and temperature control, these are not high enough to produce relevant fusion power. Therefore, the burn control problem is only relevant for ITER and future burning-plasma tokamaks.

Other kinetic control problems are related to the tokamak *divertor(s)*[11] (like radiation/heat-flux control), electron-density control, fast-particle dynamics, and Alfven eigenmodes control [11].

1.3.2 Magnetic Control

Control of the tokamak magnetic variables (magnetic field, electric field, currents, etc.) is known as magnetic control. Actuators normally employed for magnetic control are auxiliary current-drive injection (NBI, ECCD, ICCD, etc.), ohmic coil-current modulation, and modulation of other magnetic-coil currents. Also, changes in the kinetic variables may affect the evolution of certain magnetic variables, and "indirect" magnetic control is possible, for example, by modifying the plasma resistivity through the electron temperature by using auxiliary heating sources.

Some magnetic control problems in tokamaks are:

- *Plasma shape and position control.* As introduced above, the poloidal field coils are employed sometimes in conjunction with some other magnetic coils[12] to achieve and maintain a desired plasma shape and position within the tokamak. The plasma shape is chosen so that the plasma performance is optimized. For example, it is known that plasmas with high elongation, κ (a measure of how "tall" the plasma column is when compared to its width), have an improved confinement. On the other hand, the positioning of the plasma is important to avoid plasma contact with the vessel walls. Control of the plasma shape and position is one of the most mature control problems in tokamaks, and it

[11] The divertor is a tokamak structural component that serves to "capture" plasma particles that escape the closed magnetic-field lines. More information can be found in Section 2.1.3 or in [5].

[12] One of the magnetic coils normally employed for shape and position control is the ohmic-coil, so the I_p control problem and the shape & position control problems are closely coupled.

is routinely carried out in present-day tokamaks. For example, in JET, the plasma shape and position can be controlled with errors within the order of a few centimeters [12].

- *Current profile control.* The different auxiliary sources can be employed to modify the plasma resistivity (indirectly by means of the electron temperature, T_e), the auxiliary-source current driven, and the self-generated bootstrap current. These different mechanisms would, in principle, allow for controlling the current profile in tokamak plasmas. Sometimes, instead of the current profile, the variable of interest is the so-called safety factor, q, which is a measure of the pitch of the magnetic field lines, and is closely related to the current profile. For example, control of the q profile is particularly important in advanced scenarios because of the following feedback mechanism. The high bootstrap-current fraction found in advanced scenarios may lead to q profiles with negative magnetic shear, s, at the center of the plasma core (s is a measure of the gradient of q, see Fig. 1.7). In plasmas with $s < 0$ at the plasma core, an improvement in the plasma confinement is found due to the formation of an internal transport barrier (ITB). Therefore, at the ITB, the pressure gradient increases dramatically and so does the bootstrap current, closing the feedback mechanism. This loop requires active q-profile control (sometimes in conjunction with β control) to avoid too high pressure values and the possible triggering of plasma instabilities. Also, $q > 1$ values avoid the so-called sawtooth instability, which is highly deleterious for the plasma confinement [5].

Other magnetic problems of interest can be the vertical stabilization problem, a well-known instability that happens in highly elongated plasmas and destroys the plasma confinement, or the error (magnetic) field correction problem, whose final goal is to eliminate any magnetic field asymmetries. Also, control of the magnetic configuration in the divertor region is a problem of interest.

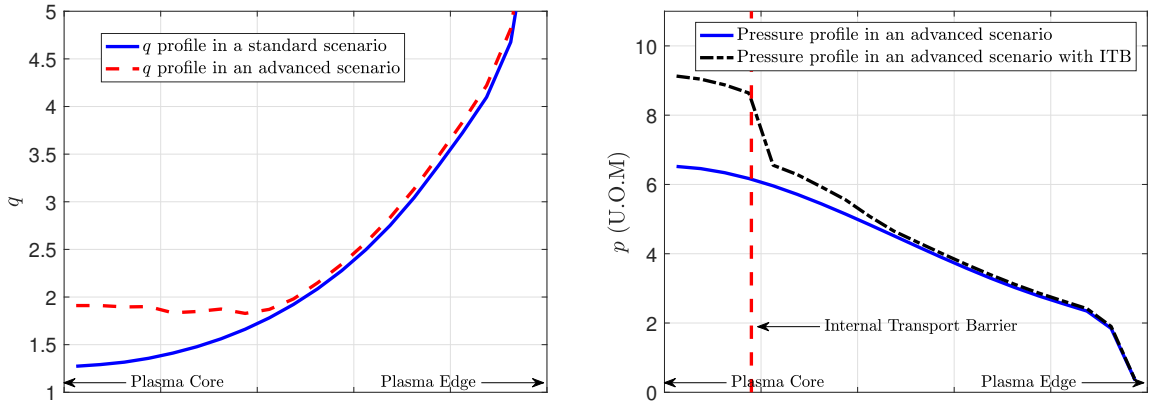

Figure 1.7: Typical q and p profiles: on the left, standard (no reversed shear) q profile and advanced (reversed shear) q profile; on the right, advanced p profile (no ITB) and advanced p profile with ITB.

1.3.3 Instability Control

Mitigation and/or suppression of the plasma instabilities is an essential part of the existing tokamak-plasma control problems. Some instability control problems of interest are:

- *NTM control.* NTMs are current and pressure driven MagnetoHydroDynamic (MHD) instabilities [5] that modify the tokamak-plasma equilibrium, allowing for particles to escape. Therefore, NTMs spoil the plasma confinement. The physics behind the development of NTMs is not totally understood thus far, but active NTM suppression has been achieved by means of ECCD deposition at the NTM location [13]. Also, it is possible that particular q profiles improve the plasma resilience against NTMs. In the worst case scenario, NTMs not only degrade the plasma confinement, but may also lock (causing what is known as a "locked mode") and suddenly terminate the plasma. Increased plasma rotation improves plasma resilience against NTM locking.

- *ELM control.* Mitigation or total suppression of the ELMs (previously introduced in Section 1.2.2) is a need in tokamaks to avoid the associated deterioration of the plasma confinement, and also to prevent damage to the tokamak's first wall and divertor due to the heat load arising from the ELM

current bursts. Actuation methods commonly employed for ELM control are impurity pellet injection and magnetic coils that produce non-axisymmetric magnetic-field perturbations [14].

- *RWM control.* The RWM is a pressure-driven kink MHD stability[13] whose growth rate is slowed down due to the electrical resistance of the tokamak's first wall. This instability limits the achievable β and decreases the plasma performance. It is experimentally observed that increasing toroidal rotation reduces the RWM strength, making the RWM control problem be closely coupled with the rotation control problem. RWM stabilization is carried out by means of both passive methods (i.e., machine designs with nearby conducting walls that slow down the RWM growth rate) and active methods (i.e., feedback control). Actuators normally employed for active RWM control are NBI or non-axisymmetric magnetic coils.

1.3.4 Coupled Dynamics in Tokamak Plasmas

As introduced above, a tokamak plasma is a highly coupled dynamical system in which the evolution of the magnetic and kinetic variables and plasma instabilities are interlaced. A diagram illustrating some of the main dynamics coupling between magnetic and kinetic variables and some MHD instabilities is shown in Fig. 1.8.

Regarding the kinetic variables, it can be seen that the velocity of the particles, v, is related to their density, n, and temperature, T, by means of the mass, momentum, and energy balance equations (for example, the general balance equations shown in Fig. 1.8). Both n and T are related to the pressure, p, by means of a state equation. In turn, p enters the definition of β. A relationship between kinetic and magnetic variables is given by the physical fact that if a particle with velocity v has electric charge, q_{elec}, then there exists a current density, j, which is proportional to q_{elec}, v and n. Moreover, also j will exist in any media which is subject to an electric field, E, as long as this has a finite electrical resistivity, η (in a plasma, a simple analysis

[13] A kink instability is a particular type of MHD instability that causes the plasma column to deform transversally. More details can be found in [5].

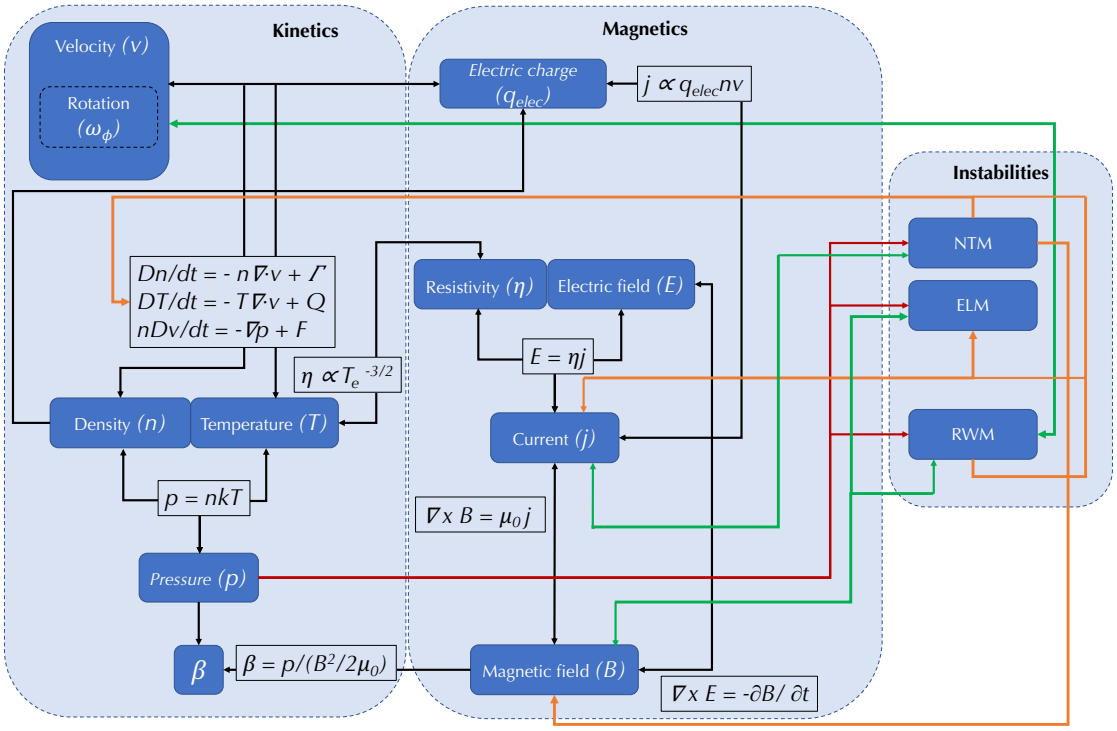

Figure 1.8: Dynamical coupling in a tokamak plasma. Black arrows represent relationships in terms of physical laws or definitions. Red lines represent triggering mechanisms, orange lines represent deterioration mechanisms, and green lines represent suppression mechanisms.

assuming Coulomb collisions are dominant [2], it is found that η is proportional to $T_e^{-3/2}$). Both j and E are related to the magnetic field B by means of Ampere's and Faraday's laws, respectively. Finally, B also enters the definition of β. Regarding the instabilities, NTMs deteriorate the plasma confinement by increasing particle and energy transport, and also modify B, i.e., the magnetic configuration. On the other hand, NTMs can be suppressed by j deposition. Both ELMs and RWMs deteriorate the plasma confinement by means of current bursts and transport modification. The ELM and RWM effects can be minimized by means of B modifications, whereas RMWs are also diminished by plasma toroidal rotation, ω_ϕ.

The simplified schematic in Fig. 1.8 is only illustrative and does not include all the coupled effects existing in plasmas (like, for instance, the relationship between momentum transport and B due to the Lorentz force, the relationship between n

and E due to the electric density in Gauss's law of electricity, or the possibility to mitigate ELMs by pellet injection that modifies n).

1.3.5 The Need for Integrated Control Solutions

There are some general characteristics of the plasma dynamics that determine the nature of the control problems found in tokamaks. First, complex physics phenomena occur in tokamak plasmas, and as a result, the dynamics of many variables is nonlinear. Second, the evolutions of many plasma variables are not independent of each other, i.e., the dynamics of such plasma variables are coupled. Third, in general, tokamaks are underactuated devices: the number of avxailable controllable inputs does not suffice to drive the plasma state/output to any arbitrary target. Finally, as of now, much of the physics that describes the plasma behavior is not well understood and there is almost always some degree of uncertainty involved in the modeling of the plasma dynamics. Section 1.3.4 may provide a first impression on the level of variety, complexity and coupling that exist in tokamak control problems.

As a result of all these characteristics, one may in principle deduce that *nonlinear, robust, multi-input multi-output (MIMO) controllers* will have an edge over any other type of controller because they take into account the nonlinearity and uncertainty of the model, and employ multiple coupled outputs and inputs. However, sometimes, the complexity of the theoretical plasma models makes it impractical or even impossible to carry out such nonlinear, robust MIMO control designs. Data-driven modeling, approximate linearization and/or model reduction are control techniques customarily employed in the synthesis of tokamak-plasma controllers.

Regardless of the control approach employed, it seems reasonable to assure that future reactor-grade PCSs will employ a variety of MIMO controllers (if possible, model-based, nonlinear, and robust controllers) dedicated to specific tasks. It is envisioned that these controllers will be embedded in what are normally referred to as *integrated-control architectures*, i.e., architectures composed of controllers that work with a certain degree of communication (integration) amongst themselves, rather

than isolated from each other. These integrated architectures should have *actuator management and sharing* capabilities, i.e., the ability to decide and coordinate which actuators can be used and/or shared for each specific control task. Therefore, *Supervisory and Exception Handling* (S&EH) algorithms must be available to perform real-time surveillance, actuator sharing and management tasks, and controlled shutdown when possible damage to the device may occur.

The development of such tokamak-plasma integrated-control strategies is a new control aspect in the fusion field that needs to be solved for ITER [11, 15] and, thus far, the necessary degree of integration that will be required is not clear. Regarding actuator management and sharing, two main types have been considered [15]: simultaneous multiple mission (SMM) sharing and repurposing (RP) sharing. The first type of actuator sharing consists in using a given actuator by two or more controllers that have different purposes, whereas the second approach consists in transferring that actuator (as requested by a S&EH system) from one controller to another without simultaneous use of it. Both actuator sharing schemes will most likely be necessary in ITER and future commercial tokamaks. An example of SMM sharing would be the use of the poloidal-field coils for position and shape control in conjunction with vertical stabilization, whereas a RP example would be the asynchronous use of EC to control both the q profile and suppress NTMs.

An example in which an integrated control architecture is absolutely necessary is as follows. Assume a tokamak that operates using a controller for active q-profile control. If no β, ω_ϕ, or instability control or surveillance are carried out, the q-profile controller may drive β and/or ω_ϕ towards values that trigger RWMs or NTMs, deteriorating the plasma confinement and possibly terminating the plasma. Even if β, ω_ϕ, or instability control is performed, but the q-profile controller is isolated from the rest of the existing controllers, the efficiency and performance of the q-profile controller would be reduced. Ideally, an (integrated) PCS would be capable of regulating more than just the q profile and/or communicating all the existing controllers, and also have the capability of doing actuator management and sharing, like for example, RP actuator sharing by using ECCD to suppress NTMs in case they developed.

1.3.6 Tokamak Diagnostics for Control

Some of the most relevant tokamak diagnostics employed for control are summarized in this Section. The most basic diagnostics provide an estimation of the local magnetic field and/or flux based on *magnetic probes* (see Fig. 1.9). These basically consist of a small coil in which the voltage between its ends, V_{emf}, is measured, allowing for estimating the magnetic flux Φ_B through its circular cross section S_B by means of Faraday's induction law,

$$\frac{\partial \vec{B}}{\partial t} = -\nabla \times \vec{E} \implies \frac{\partial}{\partial t} \iint_{S_B} \vec{B} \cdot d\vec{S}_B = -\iint_{S_B} (\nabla \times \vec{E}) \cdot d\vec{S}_B = -\int_{\Gamma_B} \vec{E} \cdot d\vec{l}$$
$$\implies \frac{\partial \Phi_B}{\partial t} = -NV_{emf}, \quad (1.14)$$

where Stoke's integral theorem has been employed, $\Phi_B \triangleq \iint_{S_B} \vec{B} \cdot d\vec{S}_B$, $V_{emf} \triangleq \int_{\Gamma_B} \vec{E} \cdot d\vec{l}$, Γ_B is the boundary of S_B, $d\vec{l}$ is a differential element in such boundary, and N is the number of turns in the coil. Employing the magnetic flux, an estimation of the magnetic field along the axis of the probe can be obtained as well, $B \approx \Phi_B / S_B$. Using the same concept, the so-called *flux loops* and *saddle loops* provide an estimation of the magnetic flux through the surface that they bound (note that the flux loop surface coincides with the surface S depicted in Fig. 2.3, and therefore the flux they estimate the important magnitude known as *poloidal flux*, Ψ, defined later in Section 2.1.3, "The Tokamak Magnetic Configuration"). However, the bigger size of the flux and saddle loops does not provide a good estimation of B.

A *Rogowski coil* provides an estimation of I_p by means of a combination of B estimations using magnetic probes in a circular closed loop (see Fig. 1.9) and Ampere's law,

$$\nabla \times \vec{B} = \mu_0 \vec{j} \implies \iint_{S_{I_p}} (\nabla \times \vec{B}) \cdot d\vec{S}_{I_p} = \mu_0 \iint_{S_{I_p}} \vec{j} \cdot d\vec{S}_{I_p}$$
$$\implies \int_{\Gamma_{I_p}} \vec{B} \cdot d\vec{S}_B = \mu_0 I_p, \quad (1.15)$$

where Stoke's integral theorem has been employed, $I_p \triangleq \iint_{S_{I_p}} \vec{j} \cdot d\vec{S}_{I_p}$, and μ_0 is the vacuum permeability. Magnetic measurements for B, I_p and magnetic fluxes allow

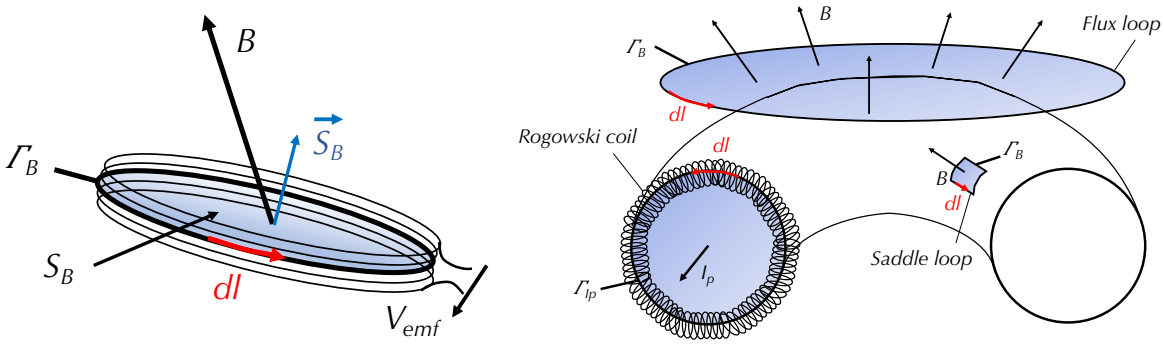

Figure 1.9: Basic magnetic diagnostics in a tokamak: on the left, a schematic of a magnetic probe; on the right, schematics for a flux loop, a saddle loop, and a Rogowski coil.

for plasma equilibrium reconstruction (see Section 2.1.3), and therefore, they play a key role in the plasma shape and position control problem and in the q-profile control problem.

The aforementioned basic magnetic measurements can only be placed outside the plasma domain due to evident technological constraints. Internal measurements for B were not possible until more advanced techniques were discovered, like for example, Motional Stark Effect (MSE) techniques. MSE techniques employ hydrogen or deuterium neutrals injected at high velocities (for example, by means of NBI), which produce a very characteristic line-emission pattern as they penetrate the strong E that exists in a tokamak. Information about such emissions allows for estimating the strength and/or direction of B. MSE measurements are commonly added as constraints in the equilibrium reconstruction problem, substantially increasing the accuracy of such reconstruction.

Local measurements of temperature and density can be obtained using different techniques, like for example Thomson scattering techniques. Thomson scattering is the elastic scattering of a photon by a charged particle, normally an electron. The spectrum of the scattered photons can be measured using both non-perturbative or laser-based techniques, and the information it carries allows for determining the temperature and density of the electrons. For ions, Charge-Exchange Recombination (CER) techniques are often employed, which infer the temperature and density from the spectrum of the photons emitted in charge-exchange collision between neutrals

and ions,

$$A^0 + B^Z \rightarrow A^+ + B^{Z-1}, \tag{1.16}$$

where A is the neutral, B is the ion, and Z is the ion atomic number. CER techniques also allow for estimating the toroidal rotation velocity of the ions. Measurements of the ion/electron density and temperature are essential in kinetic control problems, and employed in magnetic or instability control problems as well.

Other methods employed to measure the magnetic field, and ion/electron density and temperature are interferometry/polarimetry techniques (based on lasers that are driven through the plasma and whose changes in refractive indexes and polarization angles allow for inferring magnetic field and density properties), reflectometry techniques (which works as a radar sending electromagnetic waves taking advantage of the cutoff phenomena found in plasmas [2], to measure, for example, the line-average n_e), or Electron-Cyclotron Emission (ECE) techniques (to measure the electron temperature, using information from the electron-cyclotron emissions due to the helical movement of the electrons in a magnetic field, see Section 2.1.1). Comprehensive information about tokamak-plasma diagnostics can be found in [6].

1.4 Dissertation Outline

The main contribution of this dissertation work is the design and development of integrated control strategies for tokamak plasmas. The integrated-control solutions tackle many of the control problems introduced in Section 1.3, and mostly employ model-based nonlinear-robust control techniques. Some of those control solutions have been experimentally tested in the DIII-D tokamak. In addition, control-oriented, physics-based models that characterize some specific aspects of the plasma dynamics have been employed to further develop COTSIM (Control-Oriented Transport SIMulator), a 1D control-oriented fast code for controller testing and tuning created by the Lehigh University Plasma Control Group. COTSIM has been employed for validation testing of most of the controllers presented in this dissertation work.

This dissertation is organized as follows:

- **Chapter 2** describes some concepts of plasma physics required to understand the basic behavior of a plasma, together with the models employed throughout this dissertation for both simulation and control synthesis.

- **Chapter 3** describes the Control-Oriented Transport SIMulator (COTSIM) code, which is a key tool employed in the validation of plasma controllers via simulation.

- **Chapter 4** focuses on the burn control problem, for which a nonlinear, robust controller based on Lyapunov techniques is proposed. Some of the steps in this controller are integrated using a RP actuator-sharing approach. The controller is tested in simulations.

- **Chapter 5** focuses on the simultaneous q-profile + β control problem, for which two control solutions are proposed. The first control approach focuses on central safety factor and β control under zero NBI torque, and is based on approximate linearization techniques. The controller is tested both in simulations and experimentally on the DIII-D tokamak. The second control approach focuses on q-profile + β control by using feedback linearization and Lyapunov redesign techniques. Both approaches use a SMM actuator-sharing approach. This controller is tested in COTSIM simulations.

- **Chapter 6** focuses on the individual-scalars control problem using a SMM actuator-sharing approach. A nonlinear, robust, integrated-control scheme with an actuator management algorithm is designed for the regulation of individual-scalar variables. The control scheme is tested in 0D simulations using the control-oriented models, and in 1D simulations using COTSIM.

- **Chapter 7** focuses on the problem of simultaneously controlling plasma profiles/scalars and suppressing NTMs using a RP actuator-sharing approach. An integrated control approach with actuator management capabilities is employed. Experimental results are reported for the q-profile + β control problem

with NTM suppression, whereas 1D simulations using COTSIM are included for individual-scalars + NTM control.

- **Chapter 8** summarizes the contributions of this dissertation and discusses future work directions.

- **Appendices** are also included with basic theorems, additional computations, and demonstrations related to the different modeling and control approaches.

It can be noted that the control problems treated during this dissertation work (Chapters 4 through 7) can be classified according to the physical (kinetic, magnetic, instabilities) or mathematical (scalars or profiles) nature of the to-be-controlled variables, as well as the type of actuator sharing carried out (SMM or RP). A summary is shown in Fig. 1.10.

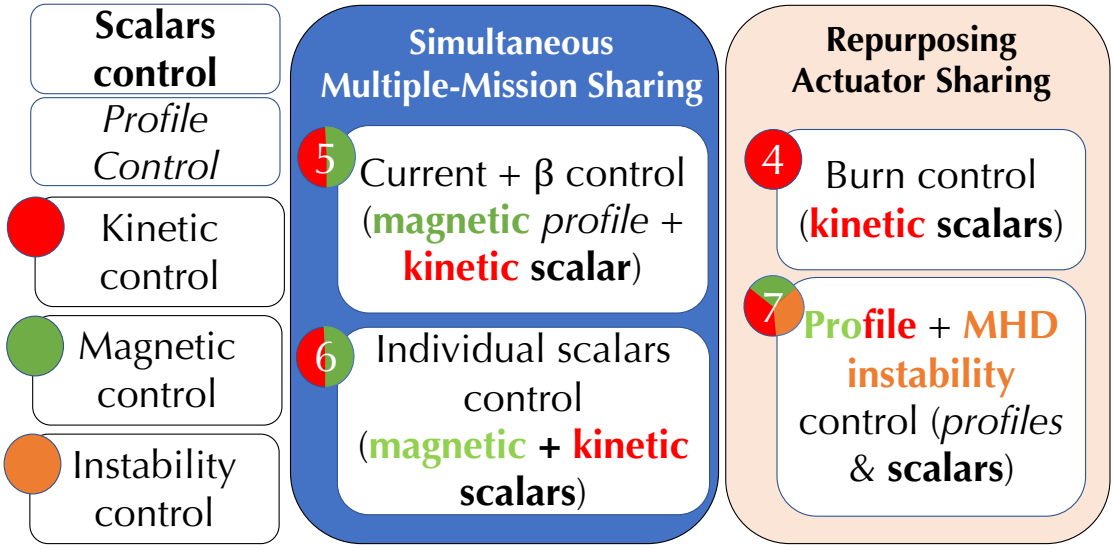

Figure 1.10: Classification of the control problems treated in this dissertation work. Scalar control problems are highlighted using **bold text**, whereas profile control problems are highlighted using *italics*. Kinetic problems are marked with a red bullet, magnetic problems are marked with a green bullet, and instability problems are marked with an orange bullet. Chapters 5 and 6 belong to SMM sharing problems, whereas 4 and 7 belong to RP sharing problems.

Chapter 2

Basic Plasma Physics and Modeling for Control Applications

The objective of this Chapter is to introduce the plasma-response models utilized in the control problems treated in this dissertation. First, Section 2.1 introduces some essential plasma-physics concepts that are necessary for a basic understanding of the aforementioned plasma-response models. The experienced reader is advised to go directly to Sections 2.2 and 2.3, where the one-dimensional (1D) and zero-dimensional (0D) models for control applications are presented.

2.1 Basic Plasma Physics

2.1.1 Particle Trajectories and Drifts

A particle with electrical charge q and mass m subject to a constant, unidirectional (uniform) magnetic field B describes a gyrating motion as depicted in Fig. 2.1 due to the Lorentz force that it experiences. The velocity of the particle in the ϕ direction, v_ϕ, remains constant because the Lorentz force is always contained within the r-z (perpendicular) plane. The equations of motion in the r-z plane are given by

$$r = r_0 + r_L \sin(\omega_c t + \psi), \quad z = z_0 \pm r_L \cos(\omega_c t + \psi), \tag{2.1}$$

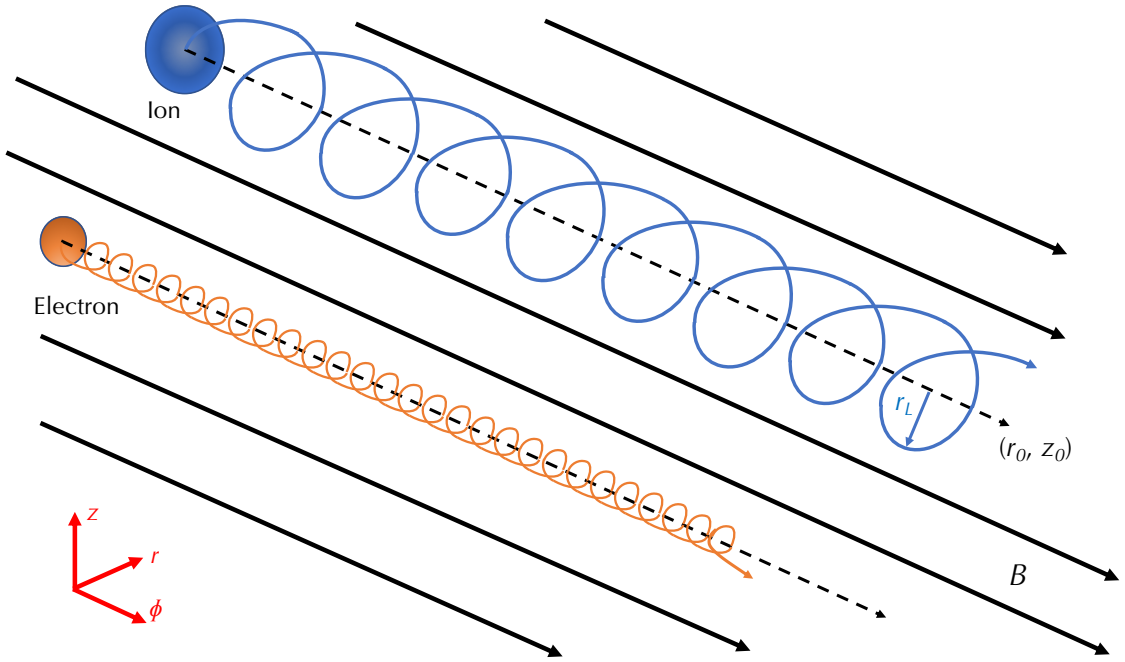

Figure 2.1: Particle trajectories in a uniform magnetic field. Ions (plotted in blue) are more massive than electrons (plotted in orange), so the ion Larmor radius (r_L) is larger than the electron r_L, whereas ω_c is smaller for ions than for electrons. Also, because of their different electric charge, ions and electrons gyrate in opposite directions (see equation (2.1)).

where r and z are the radial and vertical coordinates, respectively, r_0 and z_0 are constants that define the so-called *guiding center*, $\omega_c \triangleq |q|B/m$ is the so-called *cyclotron frequency*, $r_L \triangleq v_{\perp,0}/\omega_c$ is the so-called *Larmor radius*, $v_{\perp,0}$ is the initial velocity in the r-z plane, and ψ is a constant. The $\pm$ sign in the expression for z in (2.1) is the same as the sign of q.

In the case of a curved magnetic field $\vec{B}$ in a vacuum, particles experience a drift due to the centrifugal force F_c (also known as *curvature drift*) plus a drift due to the gradient of B (also known as *grad-B drift*). The total drift, $\vec{v}_c$, is approximately given by [2]

$$\vec{v}_c = \frac{m}{q}\frac{\vec{r}\times\vec{B}}{rB^2}\left(v_\phi^2 + \frac{1}{2}(v_r^2 + v_z^2)\right), \tag{2.2}$$

where v_ϕ, v_r, and v_z are the velocity components in the coordinates ϕ-r-z shown in

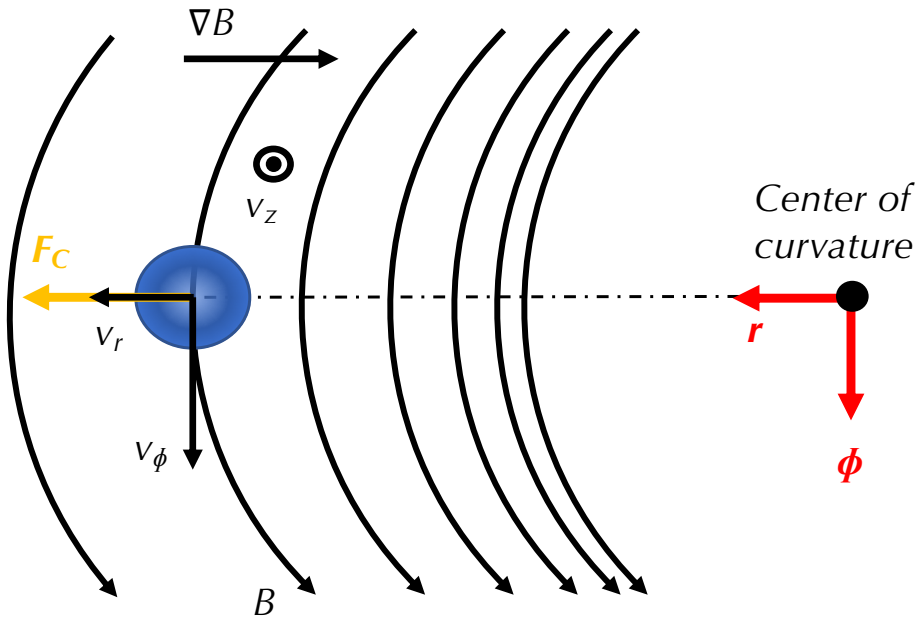

Figure 2.2: Schematic of the velocity field components in a curved magnetic field.

Fig. 2.2. The toroidal velocity, v_ϕ, is tangent to the magnetic field lines, whereas v_r is the velocity in the radial direction, r, and v_z is the velocity in the vertical direction, z.

When subject to a uniform $\vec{B}$ plus a uniform electric field, $\vec{E}$, a particle experiences the so-called $\vec{E} \times \vec{B}$ *drift*, denoted by $\vec{v}_E$, which is given by

$$\vec{v}_E = \frac{\vec{E} \times \vec{B}}{B^2}. \tag{2.3}$$

As it will be seen in Section 2.1.3, the existence of the grad-B + curvature drift (2.2) and the $\vec{E} \times \vec{B}$ drift (2.3) defines the magnetic configuration of a tokamak. For a more complete derivation of the equations presented in this Section, see Appendix A.1 and/or [2].

2.1.2 The MHD Theory

The description given in Section 2.1.1 approximately represents the situation of the plasma particles in a tokamak vacuum: the externally created $\vec{B}$ has a main direction

(the toroidal direction) and is approximately constant. However, the description presented is substantially oversimplified in the sense that the electric and magnetic fields are prescribed. This is not the real situation in a tokamak. As the charged particles move within the plasma, they create electric currents that in turn induce internally-generated magnetic fields. The motion of the particles is subject to both the external and "internal" magnetic fields that the particles themselves generate. Therefore, an accurate model of the particles trajectory cannot assume prescribed E and B. Instead, a valid description should resolve the problem self-consistently.

A self-consistent theory that explains many of the physics phenomena occurring in a plasma is the so-called *MHD theory* (see Appendix A.2). It is composed of a set of continuity and momentum equations, together with Maxwell's equations for electromagnetism, and a generalized Ohm's law. The MHD continuity equation is given by

$$\frac{Dn}{Dt} = -n\nabla \cdot \vec{v}, \tag{2.4}$$

where $n_e \approx n_i \triangleq n$ (n_e and n_i are the electron and ion densities, respectively), and $\vec{v} \triangleq (m_i\vec{v}_i + m_e\vec{v}_e)/(m_i + m_e)$, where m_i and m_e are the ion and electron masses, respectively, and $\vec{v}_i$ and $\vec{v}_e$ are the ion and electron velocities, respectively. The MHD momentum equation is given by

$$n(m_i + m_e)\frac{D\vec{v}}{Dt} = -\nabla p + \vec{j} \times \vec{B}, \tag{2.5}$$

where $p = p_i + p_e$ is the total pressure field (which is the addition of the ion pressure, p_i, and electron pressure, p_e), and $\vec{j} = n(q_i\vec{v}_i + q_e\vec{v}_e)$ is the current density, where q_i and q_e are the ion and electron charges, respectively. Maxwell's equations for a plasma are given by,

$$\nabla \cdot \vec{E} = \frac{\sigma}{\epsilon_0}, \quad \nabla \times \vec{E} = -\frac{\partial \vec{B}}{\partial t}, \quad \nabla \cdot \vec{B} = 0, \quad \nabla \times \vec{B} = \mu_0 \left(\vec{j} + \epsilon_0 \frac{\partial \vec{E}}{\partial t} \right), \tag{2.6}$$

where ϵ_0 is the vacuum electric permittivity, μ_0 is the vacuum magnetic permeability, and $\sigma = q_i n_i + q_e n_e$ is the charge density. The so-called generalized Ohm's law is given by

$$\vec{E} + \vec{v} \times \vec{B} = \eta\vec{j} + \frac{1}{nq_i}(\vec{j} \times \vec{B} - \nabla p_e), \tag{2.7}$$

where η is the plasma resistivity, which is given by $\eta = \nu_{e,i}\frac{m_e}{nq_e^2}$, where $\nu_{e,i}$ is the electron-ion collision frequency.

If the plasma is in equilibrium, (2.5) yields

$$\nabla p = \vec{j} \times \vec{B}. \tag{2.8}$$

Equation (2.8) describes the plasma equilibrium under MHD conditions. Two conclusions can be drawn from (2.8). First, taking internal product with $\vec{B}$, it is found that $\nabla p \cdot \vec{B} = 0$, i.e., the $\vec{B}$-field lines have constant p. Also, if the internal product is taken with $\vec{j}$, then it can be seen that the $\vec{j}$-field lines also have constant p. These characteristics of the MHD plasma equilibrium are key to understand the tokamak magnetic configuration, Section 2.1.3.

2.1.3 The Tokamak Magnetic Configuration

In this Section, the magnetic configuration of a tokamak is introduced and characterized. MHD equilibrium conditions are assumed, as well as axial symmetry in the ϕ direction (see Fig. 2.3, in which the r-ϕ-z frame is defined so that z is aligned with the vertical direction, r with the radial direction, and ϕ with the toroidal direction).

As it has been previously introduced in Chapter 1, Section 1.2.1, the tokamak magnetic field $\vec{B}$ has two components: the toroidal field, $\vec{B}_\phi$, and the poloidal field, $\vec{B}_\theta$, so that $\vec{B} = \vec{B}_\phi + \vec{B}_\theta$. The poloidal field $\vec{B}_\theta$ is absolutely necessary to guarantee that the plasma column stays within the tokamak due to the $\vec{E} \times \vec{B}$ and grad-B + curvature drifts introduced in Section 2.1.1. In a pure toroidal field $\vec{B} = \vec{B}_\phi$, the grad-B + curvature drift (see equation (2.2)) would make the ions drift in the $\vec{z}$ direction and the electrons drift in the $-\vec{z}$ direction, creating an electric field $\vec{E}$ in the $-\vec{z}$ direction. Such $\vec{E}$ would make both ions and electrons drift in the $\vec{r}$ direction as well (see equation (2.3)). Therefore, the particles would never stay confined within the tokamak magnetic field. The addition of the poloidal field $\vec{B}_\theta$ to the toroidal field $\vec{B}_\phi$ helps to correct the drifts and improves the plasma confinement, resulting in helical magnetic field lines. This is known as *rotational transform*.

In order to characterize the magnetic configuration of a tokamak, the so-called *magnetic-flux surfaces* play a key role. A magnetic-flux surface can be defined as

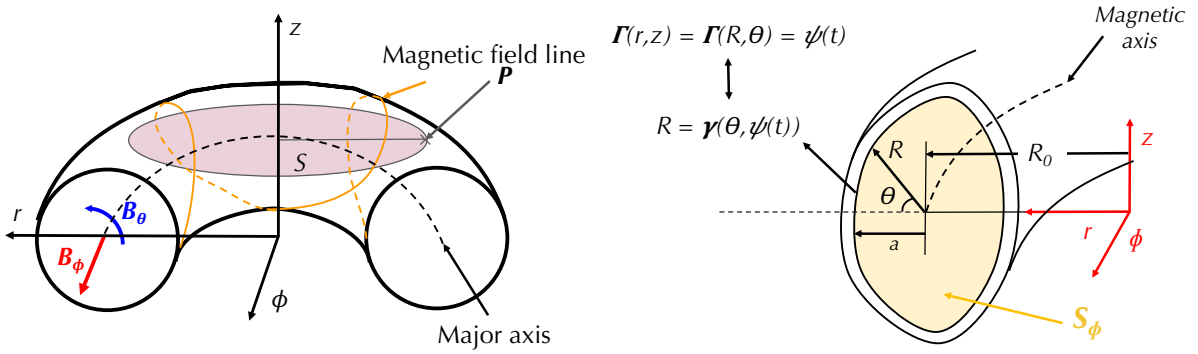

Figure 2.3: Tokamak magnetic geometry: on the left, definition of S together with magnetic field components, $\vec{B}_\phi$ and $\vec{B}_\theta$; on the right, definition of S_ϕ together with the magnetic-flux contour equation, Γ, and the tokamak major and minor radiuses, R_0 and a.

the set of points P with the same value of poloidal flux, Ψ, defined as

$$\Psi = \iint_S B_\theta dS, \tag{2.9}$$

where S is the surface that is perpendicular to the z-axis and whose boundary is defined by the circumference passing through P (see Fig. 2.3). Alternatively, the poloidal stream function, $\psi = \Psi/(2\pi)$, is commonly employed. The contour of a given magnetic-flux surface is defined by the equation $\psi = \Gamma(r,z)$, or alternatively, $R = \gamma(\theta,\psi)$ (R and θ are the radial and poloidal angle coordinates shown in Fig. 2.3). The magnetic-flux surface that collapses to a line is known as *magnetic axis*. Its position is characterized by the so-called tokamak major radius, R_0, which is normally very close to the geometric major radius (i.e., the position of the major axis in Fig. 2.3).

Using the MHD theory, it can be shown that other variables are also constant within a magnetic-flux surface (see Appendix A.3). Such variables are referred to as *flux functions*. Possible flux functions are the plasma pressure, p, the toroidal magnetic flux, Φ, the effective minor radius, ρ, or the safety factor, q. The toroidal magnetic flux, Φ, through a toroidal surface S_ϕ, is defined as

$$\Phi = \iint_{S_\phi} B_\phi dS_\phi, \tag{2.10}$$

where S_ϕ is the surface enclosed by a magnetic-flux surface and is perpendicular to the ϕ-axis, as depicted in Fig. 2.3 and Fig. 2.4. The minor effective radius, ρ, is defined as

$$\Phi = B_{\phi,0}\pi\rho^2, \tag{2.11}$$

where $B_{\phi,0}$ is the reference (normally taken as the vacuum) magnetic field at the magnetic axis. It is customary to employ the normalized minor effective radius, $\hat{\rho}$, which is defined as $\hat{\rho} = \rho/\rho_b$, where ρ_b is the value of ρ at the last-closed magnetic-flux surface (see Fig. 2.4). Finally, the safety factor, q, is a measure of the pitch of the magnetic field lines, and it is defined as

$$q \triangleq -\frac{d\Phi}{d\Psi} = -\frac{B_{\phi,0}\rho_b^2\hat{\rho}}{\partial\psi/\partial\hat{\rho}}. \tag{2.12}$$

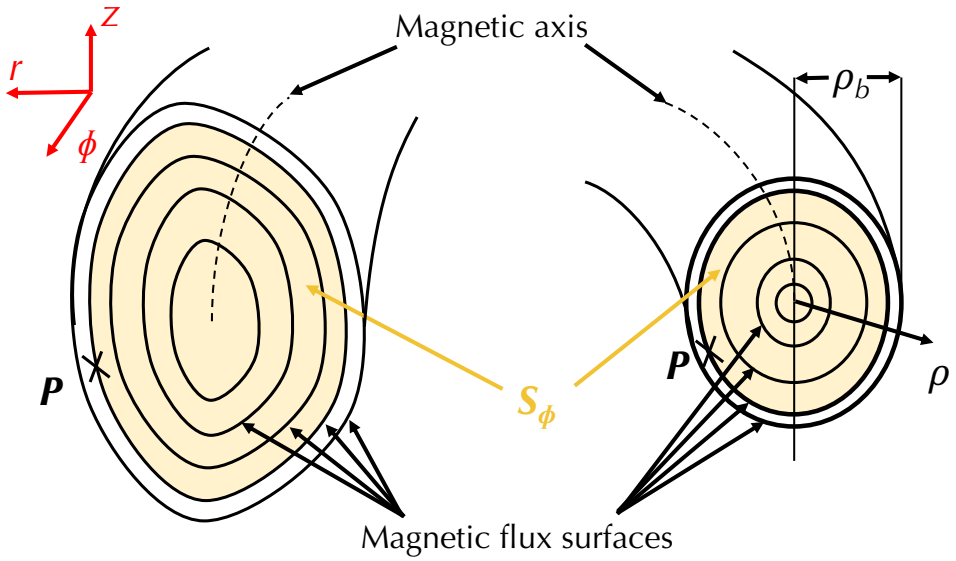

Figure 2.4: Tokamak magnetic geometry: magnetic-flux surfaces under ideal MHD conditions, and reduction from 3D to 1D using the flux function ρ.

A particular branch of the MHD theory is the so-called *ideal MHD theory*, which assumes that $\eta \to 0$. According to the ideal MHD theory, the magnetic-flux surfaces are nested around the magnetic axis (see Fig. 2.4). The last-closed magnetic-flux surface defines the *plasma boundary*. In the first tokamak designs, the position of

the plasma boundary was defined by a first-wall component in contact with the confined plasma, normally referred to as *limiter*. The numerous disadvantages of using limiters (impurity sputtering[1], limiter erosion, etc.) led to the development of *diverted* configurations, in which the plasma boundary separates[2] two regions: a region of confined plasma in which the magnetic-flux surfaces are closed, and a region with open magnetic-flux surfaces, also known as the scrape-off layer (SOL). The latter is the region in contact with the so-called *divertor*, normally located on or very close to the tokamak's first-wall. Diverted configurations avoid direct contact between the confined plasma and any structural component of the tokamak, minimizing the chance that impurities get into the confined plasma region, and solving many of the problems of the limited configurations. Still, maintaining a given magnetic configuration in diverted configurations is a challenging problem, and divertors also suffer from erosion due to the high heat loads and particle fluxes to which they are exposed. Fig. 2.5 shows a schematic of the magnetic-flux surfaces in both limited and diverted configurations.

Regardless of the particular limited/diverted configuration, the magnetic-flux surfaces can be indexed by any of the aforementioned flux functions. This fact, together with the assumption of toroidal symmetry (i.e., in the ϕ direction), reduces the three dimensions (3D) in space to 1D (for example, going from r-ϕ-z coordinates to ρ coordinates as depicted in Fig. 2.4). This reduction from 3D to 1D greatly simplifies the analysis of magnetic problems in tokamaks, because any flux function f can be used to write $\nabla(\cdot) = \frac{\partial(\cdot)}{\partial f} df$, for a particular variable $(\cdot)$. One of the most illustrative examples is the equation that relates p and ψ under MHD equilibrium conditions, which can be obtained from (2.8) as

$$r\frac{\partial}{\partial r}\left(\frac{1}{r}\frac{\partial \psi}{\partial r}\right) + \frac{\partial^2 \psi}{\partial z^2} = -\mu_0 r^2 \frac{dp}{d\psi} - \frac{1}{2}\frac{d(rB_\phi)}{d\psi}, \tag{2.13}$$

[1]Sputtering is the process in which particles leave a solid surface due to bombardment of energetic particles. In a tokamak, this effect may be important due to the plasma-particles bombardment of the tokamak's first wall, limiter or divertor.

[2]The plasma boundary is also known as *separatrix* in diverted configurations. It has the characteristic that the poloidal magnetic field, B_θ, is zero.

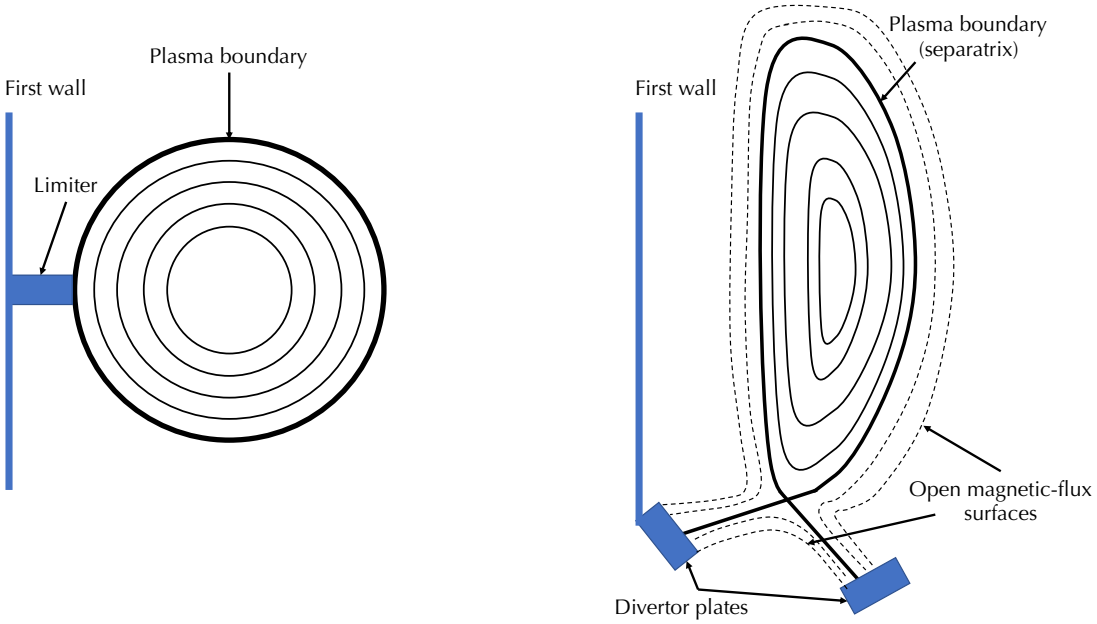

Figure 2.5: Tokamak magnetic geometry: limited and diverted configurations.

where the chain rule $\nabla(\cdot) = \frac{\partial(\cdot)}{\partial\psi} d\psi$ has been employed. Equation (2.13) is known as *Grad-Shafranov equation*, and is extensively used to reconstruct the plasma MHD equilibrium in tokamaks from magnetic measurements and either p measurements or some theoretical estimation of the shape of the p profile. Equilibrium reconstruction allows for estimating the plasma shape and position within the vacuum chamber, and plays a key role in magnetic control problems such as shape and position control or q-profile control.

2.1.4 Particle Transport in Tokamak Plasmas

The MHD continuity equation (2.4) describes the transport of particles within the plasma domain according to the principles of Continuum Mechanics. It can be seen that if $\vec{v}$ is known, then (2.4) univocally determines[3] the evolution of n. Equation

[3]With the exception of points in the plasma domain in which there exists an external source of particles. In such case, an expression for those sources would be necessary to close the model.

(2.4) can be rewritten as

$$\frac{\partial n}{\partial t} = -\nabla \cdot (n\vec{v}). \tag{2.14}$$

The volume-average plasma density, n^{av}, is defined as

$$n^{av} \triangleq \frac{1}{V_p} \iiint_{V_p} n dV_p, \tag{2.15}$$

where V_p is the plasma volume enclosed within the last-closed magnetic-flux surface (see Fig. 2.6). Multiplying by dV_p, integrating over the whole plasma domain V_p, and dividing by V_p, (2.14) becomes

$$\frac{1}{V_p} \int_{V_p} \frac{\partial n}{\partial t} dV_p = -\frac{1}{V_p} \int_{V_p} \nabla \cdot (n\vec{v}) dV_p, \tag{2.16}$$

and utilizing the Reynold's transport theorem, equation (2.16) becomes

$$\frac{dn^{av}}{dt} + \frac{n^{av}}{V_p}\frac{dV_p}{dt} - \frac{1}{V_p} \int_{S_p} n(\vec{v}_p \cdot \vec{R}) dS_p = -\frac{1}{V_p} \int_{V_p} \nabla \cdot (n\vec{v}) dV_p, \tag{2.17}$$

where S_p is the area that encloses V_p, $\vec{v}_p$ is the velocity of S_p, and $\vec{R}$ is the unit vector in the R direction, which is normal to S_p (see Fig. 2.6).

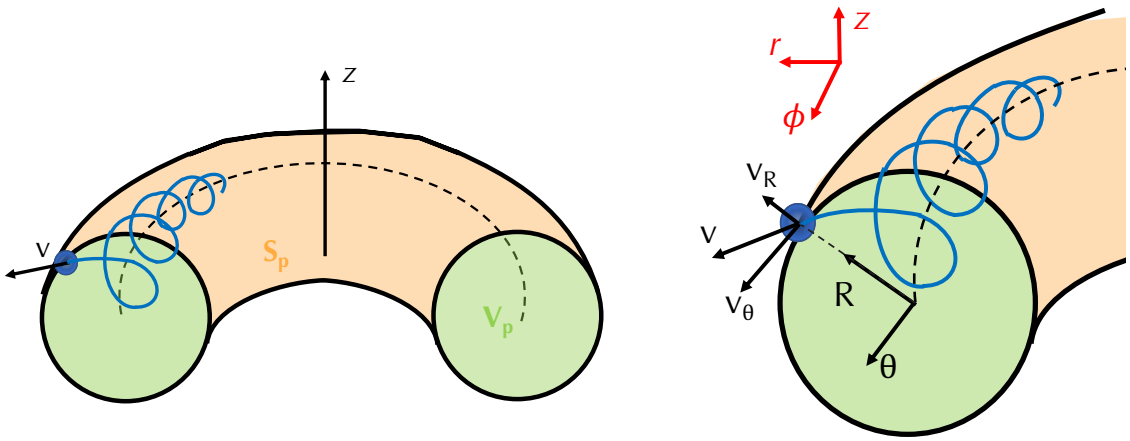

Figure 2.6: Schematic for the plasma volume, V_p, and plasma surface, S_p, together with the particle velocities.

Re-arranging terms, using Gauss's divergence's theorem, and adding a general source/sink of particles within the plasma (for example, due to NBI injection,

gas/impurity puffing and pellet injection, etc.), denoted by Γ_n, equation (2.17) becomes

$$\frac{dn^{av}}{dt} = -\frac{n^{av}}{V_p}\frac{dV_p}{dt} + \frac{1}{V_p}\int_{S_p} n(\vec{v}_p - \vec{v}) \cdot \vec{R} dS_p + \Gamma_n. \tag{2.18}$$

In fact, because it is derived from first principles, equation (2.18) may model the transport of any type of particle within a tokamak. This equation can also be employed to model the transport of other scalar magnitudes, like energy, as long as Γ_n represents a source/sink of power.

Employing the MHD momentum equation and generalized Ohm's law, equations (2.5) and (2.7), the velocity in the R-θ plane, $\vec{v}_\perp = \vec{v}_R + \vec{v}_\theta$ (see Fig. 2.6), can be estimated as [2],

$$\vec{v}_\perp = \frac{\vec{E} \times \vec{B}}{B^2} - \frac{\eta_\perp}{B^2}\nabla p, \tag{2.19}$$

where $\eta_\perp$ is the resistivity in the R direction. If $\vec{E}$ only has a radial component along R, then the first term (which is nothing but the $\vec{E} \times \vec{B}$ drift) only has a component along the θ direction, and transport is determined by the term $\frac{\eta_\perp \nabla p}{B^2}$. Such prediction is normally referred to as *classical transport*, which however has been proven to estimate a much lower transport in tokamaks than what is experimentally observed. The *neoclassical theory* provides an explanation for more complex transport processes due to particle trapping in banana orbits because of the magnetic mirror[4] created by the magnetic field decay in the radial direction of a toroidal device like the tokamak [16]. Although the transport estimate given by the neoclassical theory is normally higher than the one given by the classical theory, it still underestimates the transport experimentally found in magnetically confined plasmas. This difference between the classical/neoclassical predictions and the experimentally observed transport is known as *anomalous transport*. Recent research suggests that plasma turbulence created by micro-instabilities may be responsible for this anomalous transport, although no conclusive proof or complete physical theory that explains such phenomena have been demonstrated thus far.

[4]The magnetic-mirror effect is the reduction in velocity that a particle experiences as it moves in decreasing magnetic field (as is the case in the outward radial direction, r, in a tokamak). It is due to the invariance of the magnetic moment, $\frac{1}{2}\frac{mv_\perp^2}{B}$. More details can be found in [2]

2.1.5 Plasma Performance Parameters

The ion and electron temperature fields, denoted by T_i and T_e respectively, are related to p_i and p_e by means of the state equations

$$p_i = Kn_iT_i, \quad p_e = Kn_eT_e. \tag{2.20}$$

The ion and electron thermal energies per volume unit, denoted by E_i and E_e, are given by

$$E_i = \frac{3}{2}Kn_iT_i, \quad E_e = \frac{3}{2}Kn_eT_e, \tag{2.21}$$

where K is Boltzmann's constant. The total thermal stored energy, W, is given by

$$W = \iiint_{V_p} (E_i + E_e) dV_p, \tag{2.22}$$

and is a magnitude of importance to assess the plasma performance, as it includes both density and temperature in its definition (two of the three parameters in Lawson's criteria, see Section 1.1.5). The relationship between p and W is given by

$$W = \frac{3}{2} \iiint_{V_p} p \, dV_p, \tag{2.23}$$

which can be easily obtained from (2.20), (2.21), and (2.22).

A figure of merit which is thoroughly used in fusion science is the plasma β, which is given by

$$\beta = \frac{p}{B^2/(2\mu_0)}. \tag{2.24}$$

Its definition is derived from the MHD equations in Appendix A.4. It can be seen that β measures the efficiency of the plasma confinement: it quantifies how much thermal pressure p is achieved by means of a given "magnetic" pressure $B^2/(2\mu_0)$ (or magnetic field B). Related to β, the toroidal beta, β_t, the poloidal beta, β_p, and normalized beta, β_N, are often employed. These are defined as

$$\beta_t = \frac{p}{B_\phi^2/(2\mu_0)}, \quad \beta_p = \frac{p}{B_\theta^2/(2\mu_0)}, \quad \beta_N = \beta[\%]\frac{aB}{I_p}, \tag{2.25}$$

where a is the minor radius (see Fig. 2.3). The volume-average approximation of β, denoted by β^{av}, is given by

$$\beta^{av} = \frac{1}{V_p} \iiint_{V_p} \beta dV_p \approx \frac{\frac{2}{3} W/V_p}{B^2/(2\mu_0)} [\%]. \tag{2.26}$$

where (2.23) has been employed.

2.2 One-dimensional Plasma Models for Control Applications

Once that the basic plasma-physics concepts have been introduced in Section 2.1, the present Section introduces three 1D models for the dynamics of plasma variables of interest in control problems: the magnetic diffusion equation, which is employed to model the dynamics of ψ (and, therefore, of other related variables such as q), the electron heat-transport equation, which is employed to model the dynamics of T_e, and the toroidal rotation equation, which is employed to model the dynamics of the ions toroidal angular velocity, $\omega_\phi \triangleq v_{\phi,i}/r$, where $v_{\phi,i}$ is the toroidal component of $\vec{v}_i$ (see Section 2.1.2). The three models are based on partial differential equations (PDEs) in t and $\hat{\rho}$. Additional models are also included to characterize the dynamics of some plasma variables, like for example η, the electron heat-sources or the ion torque-sources.

2.2.1 The Magnetic Diffusion Equation

The magnetic diffusion equation (MDE) describes the dynamics of ψ. It can be obtained from Maxwell's equations as illustrated in [17], and it is given by

$$\frac{\partial \psi}{\partial t} = \frac{\eta}{\mu_0 \rho_b^2 \hat{F}^2} \frac{1}{\hat{\rho}} \frac{\partial}{\partial \hat{\rho}} \left(\hat{\rho} \hat{F} \hat{G} \hat{H} \frac{\partial \psi}{\partial \hat{\rho}} \right) + R_0 \hat{H} \eta \frac{\langle \vec{j}_{ni} \cdot \vec{B} \rangle}{B_{\phi,0}}, \tag{2.27}$$

together with the boundary conditions,

$$\left. \frac{\partial \psi}{\partial \hat{\rho}} \right|_{\hat{\rho}=0} = 0, \quad \left. \frac{\partial \psi}{\partial \hat{\rho}} \right|_{\hat{\rho}=1} = -\frac{\mu_0 R_0}{2\pi G(\hat{\rho}=1) H(\hat{\rho}=1)} I_p, \tag{2.28}$$

where $\vec{j}_{ni}$ is the non-inductive current density (i.e., due to auxiliary sources, such as NBI, ECH&CD, etc., and the bootstrap current), and $\hat{F}$, $\hat{G}$, and $\hat{H}$ are geometric factors that can be calculated for a particular plasma equilibrium, and are given by

$$\hat{F} = \frac{R_0 B_{\phi,0}}{r B_\phi}, \quad \hat{G} = \langle \frac{R_0^2}{r^2} |\nabla \rho|^2 \rangle, \quad \hat{H} = \frac{\hat{F}}{\langle R_0^2 / r^2 \rangle}, \tag{2.29}$$

where $\langle \cdot \rangle$ is the average of a given magnitude $(\cdot)$ on a magnetic-flux surface [16]. Control-level models for η and $\frac{\langle \vec{j}_{ni} \cdot \vec{B} \rangle}{B_{\phi,0}}$ are employed [18]. For η, a Spitzer-like resistivity model is employed in this work,

$$\eta = \frac{Z_{eff} k_{sp}^{prof}}{T_e^{3/2}}, \tag{2.30}$$

where Z_{eff} is the effective atomic number of the plasma ions, and k_{sp}^{prof} is a fixed profile that characterizes the spatial variation of Z_{eff}. For $\frac{\langle \vec{j}_{ni} \cdot \vec{B} \rangle}{B_{\phi,0}}$, the contributions from the auxiliary sources and bootstrap current are modeled separately, so that

$$\frac{\langle \vec{j}_{ni} \cdot \vec{B} \rangle}{B_{\phi,0}} = \sum_{i=1}^{N_{aux}} \frac{\langle \vec{j}_{aux,i} \cdot \vec{B} \rangle}{B_{\phi,0}} + \frac{\langle \vec{j}_{BS} \cdot \vec{B} \rangle}{B_{\phi,0}}, \tag{2.31}$$

where $\frac{\langle \vec{j}_{aux,i} \cdot \vec{B} \rangle}{B_{\phi,0}}$ is the contribution of the i-th auxiliary source for a total of N_{aux} auxiliary sources, and $\frac{\langle \vec{j}_{BS} \cdot \vec{B} \rangle}{B_{\phi,0}}$ is the bootstrap current contribution. The contribution of the i-th auxiliary source is modeled as

$$\frac{\langle \vec{j}_{aux,i} \cdot \vec{B} \rangle}{B_{\phi,0}} = j_{aux,i}^{dep} \frac{T_e^{\delta_{aux,i}}}{n_e} P_{aux,i}, \tag{2.32}$$

where $j_{aux,i}^{dep}$, $\delta_{aux,i}$, and $P_{aux,i}$ are the current-deposition profile, the efficiency constant, and the power of the i-th auxiliary source, respectively. Equation (2.32) reflects the experimental evidence that the current-drive efficiency increases with T_e, whereas it decreases with n_e. The bootstrap current [5] is created by momentum transfer between the particles trapped in banana orbits and the passing particles, and is modeled as

$$\frac{\langle \vec{j}_{BS} \cdot \vec{B} \rangle}{B_{\phi,0}} = \frac{R_0}{\hat{F}} \left(\frac{\partial \psi}{\partial \hat{\rho}} \right)^{-1} \left[2\mathcal{L}_{31} T_e \frac{\partial n_e}{\partial \hat{\rho}} + \left(2\mathcal{L}_{31} + \mathcal{L}_{32} + \alpha \mathcal{L}_{34} \right) n_e \frac{\partial T_e}{\partial \hat{\rho}} \right], \tag{2.33}$$

where α, $\mathcal{L}_{31}$, $\mathcal{L}_{32}$, and $\mathcal{L}_{34}$ are profiles corresponding to a particular plasma equilibrium [19].

The safety factor profile, q, has been defined in equation (2.12). Because $B_{\phi,0}$ and ρ_b are machine parameters that can be estimated, it can be seen that the MDE model determines the dynamics of q.

Table 2.1: Variables in MDE model

Variable	Description	Scalar/Profile	Variable type
ψ	Poloidal stream function	Profile	State
n_e, T_e	Electron density & temperature	Profile	Input
$\hat{F}$, $\hat{G}$, $\hat{H}$, $\mathcal{L}_{31}$, $\mathcal{L}_{32}$, $\mathcal{L}_{34}$, α	Profiles from magnetic equilibrium	Profile	Model parameter
Z_{eff}	Effective atomic number	Scalar	Model parameter
k_{sp}^{prof}	Resistivity profile	Profile	Model parameter
$\delta_{aux,i}$	Current-drive efficiency constant	Scalar	Model parameter
$j_{aux,i}^{prof}$	Current-deposition profiles for auxiliary sources	Profile	Model parameter
R_0	Major radius	Scalar	Model parameter
ρ_b	ρ at last closed magnetic-flux surface	Scalar	Model parameter
$P_{aux,i}$	Auxiliary source powers	Scalar	Controllable input
I_p	Plasma current	Scalar	Controllable input

A summary of the variables involved in this model is shown in Table 2.1, together with a brief description, whether the variable is a scalar or a profile, and whether it is considered to be a state variable, an input, a controllable input, or a model parameter. For example, T_e is an input to this MDE model that can be prescribed (for example, from experimental data like Thomson scattering measurements) or obtained from a separate model (like the electron heat-transport model, see Section 2.2.2, or the 0.5D models described next [18]), whereas $P_{aux,i}$ are considered directly controllable inputs. It must be kept in mind that certain variables which are considered as model parameters in this work could be considered as inputs in a

different model. For example, Z_{eff} is considered as a model parameter in this MDE model, but it could be modified by using impurity injection, and therefore, it may be an input or even a controllable input in a different model.

Alternatively to the model summarized in Table 2.1, a closed MDE model that does not need the n_e and T_e inputs can be obtained if these are modeled as proposed in [18], i.e.,

$$n_e = n_e^{prof}\bar{n}_e, \;\; T_e = T_e^{prof} I_p^{\gamma} P_{tot}^{\epsilon} n_e^{\zeta}, \tag{2.34}$$

where n_e^{prof} is a fixed spatial profile that characterizes the spatial distribution of n_e, $\bar{n}_e$ is the line-average electron density, T_e^{prof} is a fixed spatial profile that characterizes the spatial distribution of T_e, P_{tot} is the total power injected into the plasma (whose model is described below), and γ, ϵ, and ζ are constants that model how T_e scales with the I_p, P_{tot}, and n_e, respectively. The total power, P_{tot}, is given by

$$P_{tot} = P_{\alpha} + \sum_{i=1}^{i=N_{aux}} P_{aux,i} + P_{Ohm} - P_{rad}, \tag{2.35}$$

where P_{α} is the α-heating power (only different from zero in plasmas that produce fusion energy, also known as *burning plasmas*), $\sum_{i=1}^{i=N_{aux}} P_{aux,i} \triangleq P_{aux}$ is the total auxiliary power, P_{Ohm} is the ohmic power and P_{rad} is the radiative power. The α-heating power, P_{α}, is given by

$$P_{\alpha} = \iiint_{V_p} Q_{\alpha} dV_p = \Delta E_{kin}^{\alpha} \iiint_{V_p} n_D n_T \langle \sigma v \rangle dV_p, \tag{2.36}$$

where $\Delta E_{kin}^{\alpha} = 3.52$ MeV is the energy carried by the α particles in the D-T reaction. The ohmic power, P_{Ohm}, is given by

$$P_{Ohm} = \iiint_{V_p} \eta j_{\phi}^2 dV_p, \tag{2.37}$$

where j_{ϕ} is the toroidal component of current density, that can be calculated if ψ and the plasma equilibrium are known (see Appendix A.3, equation (A.30)). The radiated power, P_{rad}, is assumed to be given mainly by Bremsstrahlung radiation, and it is taken as

$$P_{rad} = k_{brem} \iiint_{V_p} Z_{eff} n_e^2 \sqrt{T_e} dV_p, \tag{2.38}$$

where k_{brem} is the Bremsstrahlung radiation constant.

Table 2.2 summarizes the additional variables employed in the MDE model if (2.34) are used. The approximate models for n_e and T_e in (2.34) exploit the fact the characteristic time in which the kinetic variables change is much smaller than that of the magnetic variables, so the plasma temperature and density are always in quasi-equilibrium on the time scale of the ψ (or q) evolution. These models are referred to as 0.5D models. This approach for the modeling of n_e and T_e is an approximation that may be suitable for q-profile control design as long as it is envisioned that the T_e and n_e spatial distributions will not change a lot (despite q-profile control actuation) in a given plasma scenario.

Table 2.2: Additional variables in MDE model if 0.5D models for T_e and n_e are used

Variable	Description	Scalar/Profile	Variable type
n_e^{prof}	Density profile	Profile	Model parameter
T_e^{prof}	Temperature profile	Profile	Model parameter
γ, ϵ, ζ	Temperature scaling constants	Scalar	Model parameter
$\bar{n}_e$	Line-average electron density	Scalar	Input
n_D, n_T	D and T densities	Profile	Input

2.2.2 The Electron Heat-Transport Equation

The electron heat-transport equation (EHTE) describes the dynamics of $E_e = \frac{3}{2} n_e T_e$ (see equation (2.21)). It can be derived by applying the magnetic-flux surface average, $\langle(\cdot)\rangle$, to equation (2.14) using E_e instead of n, and adding sources of electron heating, denoted by Q_e. The version of the EHTE employed in this dissertation and its boundary conditions are given by

$$\frac{\partial \left(\frac{3}{2} n_e T_e\right)}{\partial t} = \frac{1}{\rho_b^2 \hat{H} \hat{\rho}} \frac{\partial}{\partial \hat{\rho}} \left(\frac{\hat{G} \hat{H}^2}{\hat{F}} n_e \chi_e \frac{\partial T_e}{\partial \hat{\rho}} \right) + Q_e, \tag{2.39}$$

$$\left. \frac{\partial T_e}{\partial \hat{\rho}} \right|_{\hat{\rho}=0} = 0, \qquad T_e(\hat{\rho}=1) \to 0, \tag{2.40}$$

where the boundary condition at $\hat{\rho} = 1$ reflects the physical fact that T_e is much lower at the boundary than at the rest of the plasma domain, and χ_e is the electron thermal diffusivity, which is given by

$$\chi_e = \chi_e^{classical} + \chi_e^{neoclassical} + \chi_e^{anomalous}, \tag{2.41}$$

where the two first terms, $\chi_e^{classical}$ and $\chi_e^{neoclassical}$, are the contributions from classical and neoclassical transport, respectively, and $\chi_e^{anomalous}$ is the contribution from anomalous transport. Because $\chi_e^{classical}$ and $\chi_e^{neoclassical}$ are normally several orders of magnitude smaller than $\chi_e^{anomalous}$ in present tokamak experiments, the latter is the main contribution to the total χ_e. Based on dimensional analysis and along the lines of some previous work [20–22], the anomalous electron diffusion in tokamaks $\chi_e^{anomalous}$ is modeled as

$$\chi_e^{anomalous} = \chi_e^{Bohm} F_{\chi_e}\left(\rho_*, q, \frac{a\nabla p_e}{p_e}, \hat{\rho}, s, \left.\frac{a\nabla T_e}{T_e}\right|_{\hat{\rho}=\hat{\rho}_{TB}}\right), \tag{2.42}$$

where χ_e^{Bohm} is the Bohm diffusivity, which is given by

$$\chi_e^{Bohm} = \frac{T_e(eV)}{B_{\phi,0}}, \tag{2.43}$$

and F_{χ_e} is a function of various non-dimensional variables: the normalized gyroradius, $\hat{\rho}_* \triangleq \sqrt{m_i T_e}/(|q_e|aB)$, the safety factor, q, the normalized electron-pressure gradient, $\frac{a\nabla p_e}{p_e}$, the normalized effective minor radius, $\hat{\rho}$, the magnetic shear, $s \triangleq \frac{r}{q}\frac{dq}{dr}$, and the normalized electron-temperature gradient, $\frac{a\nabla T_e}{T_e}$, at the edge transport barrier position, $\hat{\rho}_{TB}$ (in H-mode scenarios only). It is proposed that F_{χ_e} scales with the different variables as

$$F_{\chi_e} = {\rho_*}^{\lambda_0} \left(\frac{a\nabla p_e}{p_e}\right)^{\lambda_1} q^{\lambda_2}\, f_q(\hat{\rho})\, g_s(s) \left(\left.\frac{T_e}{a\nabla T_e}\right|_{\hat{\rho}=\hat{\rho}_{TB}}\right)^{\lambda_3}, \tag{2.44}$$

where λ_i are constant parameters that depend on a particular plasma scenario (it is assumed that $\lambda_0 = 0$ or 1, i.e., the χ_e scaling is either purely Bohm-like or gyro-Bohm-like [20], and $\lambda_i > 0$), the function f_q is taken as an ad-hoc term given by

$$f_q(\hat{\rho}) = \left(1 - \frac{1}{1 + e^{-C_0(\hat{\rho}-\hat{\rho}_{TB})}}\right)\left(C_1 + C_2\hat{\rho} + C_3\hat{\rho}^2\right), \tag{2.45}$$

where C_i are constant model parameters, and the function f_q models the spatial variation of χ_e at or near the H-mode edge. The function g_s models the confinement improvement found in reversed-shear scenarios, and is also an ad-hoc term given by

$$g_s(s) = \frac{1}{1 + e^{D_0(D_1 - s)}}, \tag{2.46}$$

where D_i are constant model parameters.

Different contributions to the electron heating are considered,

$$Q_e = Q_{aux} + Q_{Ohm} - Q_{rad} + Q_{collisions}, \tag{2.47}$$

where Q_{aux} is the electron-heating produced by auxiliary heating methods (NBI, ECH, etc.), Q_{Ohm} is the ohmic heating power, Q_{rad} represents the radiation losses, and $Q_{collisions}$ is the energy gain/loss of the electrons due to collisions with ions[5]. The auxiliary heating, Q_{aux}, is modeled as

$$Q_{aux} = \sum_{i=1}^{i=N_{aux}} Q_{aux,i}^{prof} P_{aux,i}, \tag{2.48}$$

where $Q_{aux,i}^{prof}$ is the heating-deposition profile corresponding to the i-th auxiliary source. The ohmic heating, Q_{Ohm}, is modeled as

$$Q_{Ohm} = \eta j_\phi^2, \tag{2.49}$$

where η is modeled as in (2.30). As in the MDE model, the radiative losses, Q_{rad}, are considered to be mainly due to Bremsstrahlung losses, which are modeled as

$$Q_{rad} = k_{brem} Z_{eff} n_e^2 \sqrt{T_e}. \tag{2.50}$$

Finally, the collision-associated heating, $Q_{collisions}$, is modeled as

$$Q_{collisions} = \nu_{e,i} n_e \left(T_i - T_e\right), \tag{2.51}$$

where $\nu_{e,i}$ is electron-ion collisionality, which is modeled as $\nu_{e,i} = 0.041 n_e/(T_e^{3/2} A_i)$, where A_i is the effective mass of the plasma ions.

[5]This implies that either a fully ionized plasma is assumed (so the population of neutrals is neglected) or that the ion-electron collisions dominate versus the neutral-electron collisions.

A summary of the variables in this EHTE model is shown in Table 2.3. As in the MDE model, the different inputs can be either prescribed from experimental data or estimated using some other model (for example, 0.5D models like (2.34) for T_i and n_e, or the MDE model to estimate the magnetic variables likes q, s, or j_ϕ).

Table 2.3: Variables in EHTE model

Variable	Description	Scalar/Profile	Variable type
T_e	Electron temperature	Profile	State
n_e, T_i	Electron density & ion temperature	Profile	Input
q, s, j_ϕ	Safety factor, magnetic shear & toroidal current	Profile	Input
$\hat{F}$, $\hat{G}$, $\hat{H}$	Profiles from magnetic equilibrium	Profiles	Model parameter
$B_{\phi,0}$, a	Vacuum magnetic field & minor radius	Scalar	Model parameter
Z_{eff}	Effective atomic number	Scalar	Model parameter
k_{sp}^{prof}	Resistivity profile	Profile	Model parameter
λ_i, C_i, D_i	Parameters in χ_e scaling	Scalars	Model parameter
$\hat{\rho}_{TB}$	Edge transport barrier position	Scalar	Model parameter
A_i	Effective mass of the plasma ions	Scalar	Model parameter
ρ_b	ρ at last closed magnetic-flux surface	Scalar	Model parameter
$Q_{aux,i}^{prof}$	Heating-deposition profiles for auxiliary sources	Profiles	Model parameter
$P_{aux,i}$	Auxiliary source powers	Scalar	Controllable input

2.2.3 The Toroidal Rotation Equation

The toroidal rotation equation (TRE) is employed to describe the dynamics of the toroidal angular velocity of the ions, defined as

$$\omega_\phi \triangleq \frac{v_{\phi,i}}{r}. \tag{2.52}$$

The TRE can be obtained by applying the magnetic-flux surface average to the toroidal component of the ion momentum equation multiplied by the radial coordinate r (see, for example, Appendix A.2, equation (A.12), and/or [23]). The TRE and boundary conditions employed in this dissertation are given by [24]

$$m_i\langle r^2\rangle\frac{\partial(n_i\omega_\phi)}{\partial t} = \frac{1}{\hat{\rho}\hat{H}}\frac{\partial}{\partial\hat{\rho}}\left[\hat{\rho}\hat{H}n_i m_i\chi_\phi\langle r^2(\nabla\hat{\rho})^2\rangle\frac{\partial\omega_\phi}{\partial\hat{\rho}}\right] + t_\omega, \tag{2.53}$$

$$\left.\frac{\partial\omega_\phi}{\partial\hat{\rho}}\right|_{\hat{\rho}=0} = 0, \qquad \omega_\phi(\hat{\rho}=1)\to 0, \tag{2.54}$$

where the boundary condition at $\hat{\rho}=1$ just reflects the physical fact that ω_ϕ is much lower at the boundary than at the rest of the plasma domain, χ_ϕ is the toroidal momentum diffusivity, and t_ω is the torque deposition averaged over a flux-surface.

For χ_ϕ, the simplification $\chi_\phi = f_\phi\chi_e$ is employed, where f_ϕ is a fixed profile that is determined for the applicable plasma scenario. Three torque contributions are considered,

$$t_\omega = \sum_{i=1}^{i=N_{NBI}} t_{NBI,i} + t_{int} + t_{NRMF}, \tag{2.55}$$

where $t_{NBI,i}$ is the torque injected by the i-th NBI and N_{NBI} is the total number of NBIs, t_{int} is the intrinsic torque source [25], and t_{NRMF} is the torque generated by actuation of magnetic coils that generate non-axisymmetric magnetic perturbations, in particular, non-resonant magnetic field (NRMF) perturbations[6]. Control-level models are employed for $t_{NBI,i}$, t_{int}, and t_{NRMF} [24],

$$t_{NBI,i} = t^{prof}_{NBI,i} n_i^{\alpha_{n,NBI}} T_i^{\alpha_{T,NBI}} P_{NBI,i}, \tag{2.56}$$

$$t_{int} = t^{prof}_{int}\frac{E_i + E_e}{I_p}, \tag{2.57}$$

$$t_{NRMF} = t^{prof}_{NRMF}(\omega_\phi - \omega^\star_\phi) n_i^{\alpha_{n,NRMF}} T_i^{\alpha_{T,NRMF}} \omega_E^{\alpha_\omega} I^2_{NRMF}, \tag{2.58}$$

where $t^{prof}_{NBI,i}$ is the torque-deposition profile for the i-th NBI, $\alpha_{n,NBI}$ and $\alpha_{T,NBI}$ are constants that model the NBI torque-deposition efficiency as a function of n_i and

[6] In general, non-axisymmetric perturbations can be resonant (with the same helicity, i.e., same q as the non-perturbed $\vec{B}$) or non-resonant (different helicity from the non-perturbed $\vec{B}$.). More information can be found, for example, in [26].

T_i, respectively, t_{int}^{prof} is a profile that characterizes the spatial distribution of the intrinsic torque, t_{NRMF}^{prof} is a profile that characterizes the spatial distribution of the NRMF torque, $\alpha_{n,NRMF}$ and $\alpha_{T,NRMF}$ are constants that model the NRMF torque-deposition efficiency as a function of n_i and T_i, respectively, $\omega_\phi^\star$ is an offset rotation profile for the NRMF torque, ω_E is the toroidal component of the $\vec{E} \times \vec{B}$ drift, and I_{NRMF} is the current through the coils that generate the NRMF perturbations.

A summary of the variables in this TRE model is shown in Table 2.4, together with a brief description, if they are a scalar or a profile, and whether the applicable variable is considered to be the state, an input, or a model parameter. Just as before, variables like n_e, n_i, T_e, or T_i can be prescribed or estimated by other models.

Table 2.4: Variables in TRE model

Variable	Description	Scalar/Profile	Variable type
ω_ϕ	Toroidal angular rotation	Profile	State
n_e, n_i, T_e, T_i	Electron & ion density/temperature	Profile	Input
χ_e	Electron thermal diffusivity	Profile	Input
V_p, $\langle r^2 \rangle$, $\langle r^2 (\nabla \hat{\rho})^2 \rangle$	Plasma volume	Profile	Model parameter
f_ϕ	Profile in χ_ϕ scaling	Profile	Model parameter
$\alpha_{n,(\cdot)}$, $\alpha_{T,(\cdot)}$, α_ω	Parameters in NBI & NRMF torque scalings	Scalar	Model parameter
$t_{NBI,i}^{prof}$, t_{int}^{prof}, t_{NRMF}^{prof}	Torque-deposition profiles for NBI, intrinsic torque & NRMF	Profile	Model parameter
$\omega_\phi^\star$	Offset rotation profile for NRMF torque	Profile	Model parameter
ω_E	Toroidal component in $\vec{E} \times \vec{B}$ drift	Profile	Model parameter
$P_{aux,i}$	Auxiliary source powers	Scalar	Controllable input
I_p	Plasma current	Scalar	Controllable input
I_{NRMF}	NRMF coil current	Scalar	Controllable input

2.3 Zero-dimensional Plasma Models for Control Applications

This Section presents 0D models for some scalar plasma-variables: the stored thermal energy, W, volume-average particle densities, bulk toroidal rotation, Ω_ϕ, central and edge safety factors, q_0 and q_{edge}, and NTM island width, w. The 0D models are based on the basic plasma-physics concepts presented in previous Sections, although they are substantially reduced and/or simplified in order to serve their control-design purpose.

2.3.1 Plasma Energy Balance

A 0D balance for the evolution of the stored thermal energy, W, defined in (2.22), can be derived from 1D energy balances for ions and electrons. The energy-balance equations for ions and electrons can be obtained from applying equation (2.14) to both E_i and E_e, and are given by

$$\frac{\partial E_i}{\partial t} + \nabla \cdot (E_i \vec{v}_i) = Q_i, \tag{2.59}$$

$$\frac{\partial E_e}{\partial t} + \nabla \cdot (E_e \vec{v}_e) = Q_e, \tag{2.60}$$

where Q_i and Q_e are generic sources/sinks of ion and electron power density, respectively (Q_e is the same term that appears in the EHTE, equation (2.39)). Adding equations (2.59) and (2.60), it is found that

$$\frac{\partial (E_i + E_e)}{\partial t} + \nabla \cdot (E_i \vec{v}_i) + \nabla \cdot (E_e \vec{v}_e) = Q_i + Q_e. \tag{2.61}$$

Integrating over the plasma domain V_p, using Gauss's theorem and Reynold's transport theorem as in Section 2.1.4, and re-arranging terms, (2.61) becomes

$$\frac{dW}{dt} = -W\frac{dV_p}{dt} - \iint_{S_p} [E_i(\vec{v}_p - \vec{v}_i) + E_e(\vec{v}_p - \vec{v}_e)] \cdot \vec{R} dS_p + \iiint_{V_p} (Q_i + Q_e) dV_p. \tag{2.62}$$

The first term on the right hand side of (2.62) represents the change in W due to plasma volume varations. If V_p is constant in time or its change in time is negligible, this first term vanishes. The last term on the right hand side of (2.62) is, by definition, the total power injected to the plasma, P_{tot}. The second term on the right hand side of (2.62) represents the ion and electron losses through the plasma boundary S_p, just as introduced in Section 1.1.5, equation (1.10), so it is approximated as

$$\iint_{S_p} [E_i \vec{v}_i + E_e \vec{v}_e] \cdot \vec{R} dS_p \approx \frac{1}{\tau_E} \iiint_{V_p} (E_i + E_e) dV_p = -\frac{W}{\tau_E}. \tag{2.63}$$

Equation (2.62) becomes the 0D power-balance equation thoroughly employed in fusion science,

$$\frac{dW}{dt} = -\frac{W}{\tau_E} + P_{tot}, \tag{2.64}$$

where P_{tot} is modeled as in (2.35)-(2.38), and τ_E is estimated using the IPB98(y,2) empirical scaling [27],

$$\tau_E = 0.0562 H_H I_p^{0.93} B_{\phi,0}^{0.15} R_0^{1.97} \kappa^{0.78} \epsilon^{0.58} A_i^{0.19} P_{tot}^{-0.69} \bar{n}_{e,19}^{0.41}, \tag{2.65}$$

where H_H is the so-called H-factor or confinement factor, I_p must be given in MA, κ is the plasma elongation, $\epsilon = a/R_0$ is the inverse aspect ratio, A_i is the effective mass of the plasma ions in a.m.u., P_{tot} must be given in MW, and $\bar{n}_{e,19}$ is the line-average electron density in 10^{19} m^{-3}. For convenience, τ_E is written as

$$\tau_E = k H_H I_p^{0.93} P_{tot}^{-0.69} \bar{n}_{e,19}^{0.41}, \tag{2.66}$$

where $k = 0.0562 B_{\phi,0}^{0.15} R_0^{1.97} \kappa^{0.78} \epsilon^{0.58} A_i^{0.19}$. The H-factor, H_H, is a scalar that represents the uncertainty of the IPB98(y,2) scaling under different scenarios and operating conditions. A value of $H_H = 1$ yields the best fit to experimental data in the international database. It can also be seen as a measurement of the plasma confinement quality which comprises effects not explicitly included in the IPB98(y,2) scaling. Amongst those effects, perturbations in the axisymmetric magnetic configuration can be considered. In particular, non-axisymmetric magnetic perturbations intentionally created by the aforementioned in-vessel magnetic coils have a

proven impact on H_H in DIII-D plasmas with relatively low $\nu_{e,i}$ and n_e (normalized $\nu_{e,i} \approx 0.1$, $n_e \approx 3.5 \times 10^{19} m^{-3}$) [28]. In these experiments, activation of the in-vessel coils implied a decrease in H_H and, consequently, a decrease in τ_E. Tokamak plasmas with higher $\nu_{e,i}$ and n_e, on the contrary, did not show H_H variations under application of non-axisymmetric magnetic fields [14]. Using the experimental data available for DIII-D plasma with with ITER-like plasma shapes [14, 28], the following control-oriented scaling is used to account for the influence of the in-vessel-coil current, denoted by I_{coil}, on H_H,

$$H_H = H_H^{nom} + \left(\frac{n_e^{av}}{n_{e,0}^{av}}\right)^{-\lambda_{1,coil}} \left(\frac{\nu_{e,i}^{av}}{\nu_{e,i0}^{av}}\right)^{-\lambda_{2,coil}} \left(C_{2,coil} I_{coil}^2 + C_{1,coil} I_{coil}\right), \qquad (2.67)$$

where H_H^{nom} is a known, nominal value for H_H without activation of the in-vessel coils, n_e^{av} is the volume-average electron density (although any other scalar, reference value for n_e can be employed), $\nu_{e,i}^{av}$ is the volume-average electron-ion collisionality, $n_{e,0}^{av}$ and $\nu_{e,i0}^{av}$ are the volume-average electron density and electron-ion collisionality, respectively, corresponding to a nominal working point for which experimental data is available, and $\delta > 0$, $\lambda_{i,coil} > 0$, and $C_{i,coil}$ are constants that are determined from experimental data. Because the in-vessel coils can only reduce H_H with the experimental configurations considered [14, 28], the term $\left[C_{2,coil} I_{coil}^2 + C_{1,coil} I_{coil}\right] \leq 0$, for any $I_{coil} \geq 0$.

In order to design controllers that are as effective as possible, the dynamic model includes different types of uncertainties. First, an uncertainty δ_{H_H} is added to H_H in (2.67) to yield

$$H_H = H_H^{nom} + \left(\frac{n_e^{av}}{n_{e,0}^{av}}\right)^{-\lambda_{1,coil}} \left(\frac{\nu_{e,i}^{av}}{\nu_{e,i0}^{av}}\right)^{-\lambda_{2,coil}} \left(C_{2,coil} I_{coil}^2 + C_{1,coil} I_{coil}\right) + \delta_{H_H}. \quad (2.68)$$

The uncertainty δ_{H_H} reflects the aforementioned variations in confinement quality which are often observed in tokamaks. In addition, an uncertain power source is added on the right hand side of (2.64), denoted by δ_P, so it becomes

$$\frac{dW}{dt} = -\frac{W}{\tau_E} + P_{tot} + \delta_P. \qquad (2.69)$$

The uncertainty δ_P models unknown variations in P_{tot} such as, for example, unmodeled radiative losses or inefficient auxiliary heating.

Finally, equation (2.69) can be rewritten as

$$\frac{dW}{dt} = -\frac{W}{\tau_E^{nom}} + P_{tot} + \delta_W, \tag{2.70}$$

where the dependence on t has been dropped in all variables to ease notation, τ_E^{nom} is the value of τ_E when $\delta_{H_H} = 0$, and δ_W is an uncertain term that bundles all the uncertainties in the 0D model for W, and is given by

$$\delta_W = \frac{W}{\tau_E^{nom}} - \frac{W}{\tau_E} + \delta_P. \tag{2.71}$$

A summary of the variables in this 0D model for W is shown in Table 2.5. All variables considered are scalars. Because P_{tot} depends on $P_{aux,i}$ (see equation (2.35)), it is considered that P_{tot} is a partially controllable input.

Table 2.5: Variables in 0D model for W

Variable	Description	Variable type
W	Stored thermal energy	State
$B_{\phi,0}$, R_0, a, κ, A_i	Toroidal field, major and minor radiuses, elongation and effective mass	Model parameter
H_H^{nom}	Nominal H-factor	Model parameter
$C_{i,coil}$, $n_{e,0}^{av}$, $\nu_{e,i0}$, $\lambda_{i,coil}$	Parameters in H_H model	Model parameter
$\bar{n}_e$	Line-average density	Input
$\nu_{e,i}$, n_e^{av}	Electron-ion collision frequency & volume-average electron density	Input
P_{tot}	Total power	Input (Partially controllable)
I_p	Plasma current	Controllable input
I_{coil}	In-vessel coil current	Controllable input
δ_{H_H}, δ_P	Uncertain terms	Uncertainties

2.3.2 Plasma Particles Balance

In this section, 0D models for the evolution of the volume-average densities of the different types of plasma particles are presented [29]. These models focus on D-T plasmas, and can be obtained from 1D mass balances for each type of particles by

following the same approach as in Sections 2.1.4 and 2.3.1. The main purpose of these models is the design and simulation testing of controllers for burn control (i.e., *burn controllers*) in conjunction with the 0D model for W presented in Section 2.3.1, as well as providing a simplified model for the evolution of the volume-average electron density, n_e^{av}. This modeling work considers a plasma in which deuterium (D), tritium (T), α particles (α's) and impurities are present. For each type of particle, (2.18) is employed, and the transport term across the plasma surface S_p is expressed in terms of a confinement time in the same way as in (2.63). Unless explicitly stated, the variables involved in this Section are volume-average variables.

The α-particle balance equation is given by

$$\frac{dn_\alpha}{dt} = -\frac{n_\alpha}{\tau_\alpha} + S_\alpha, \tag{2.72}$$

where n_α is the α-particle average density, τ_α is the α's confinement time, and S_α is the source of α's arising from fusion reactions, which is given by

$$S_\alpha = n_D n_T \langle \sigma v \rangle_{DT}, \tag{2.73}$$

where n_D and n_T are the D and T ions densities, respectively, and $\langle \sigma v \rangle_{DT}$ is the D-T reactivity. The function $\langle \sigma v \rangle_{DT}$ depends on the ion temperature, T_i, as introduced in Section 1.1.2 and shown in Fig. 1.2. In this 0D model, an average temperature T_i is employed. It is not defined as an integral of T_i over the plasma volume, but instead it can be obtained from the volume-average version of equation (2.22),

$$\frac{3}{2}\left(n_i T_i + n_e T_e\right) = \frac{W}{V_p}, \tag{2.74}$$

where n_i is the ion density, which is given by

$$n_i = n_\alpha + n_D + n_T + n_I, \tag{2.75}$$

and n_e can be obtained from the quasi-neutrality condition,

$$n_e = n_D + n_T + 2n_\alpha + Z_I n_I, \tag{2.76}$$

where Z_I is the atomic number of the impurities.

The D and T particle balance equations are given by

$$\frac{dn_D}{dt} = -\frac{n_D}{\tau_D} - S_\alpha + f_{eff} S_D^R + S_D^{inj}, \tag{2.77}$$

$$\frac{dn_T}{dt} = -\frac{n_T}{\tau_T} - S_\alpha + f_{eff} S_T^R + S_T^{inj}, \tag{2.78}$$

where τ_D and τ_T are the D and T confinement times, respectively, S_D^{inj} and S_T^{inj} are the D and T injection rates, respectively, S_D^R and S_T^R are the D and T recycling sources, respectively, and f_{eff} is the efficiency with which the incoming recycling fluxes fuel the plasma core. These recycling sources arise from particles trapped in the tokamak's first-wall and SOL that cross the last-closed magnetic-flux surface and come back into the plasma core. The recycling terms S_D^R and S_T^R are modeled as in [29],

$$S_D^R = \frac{f_{ref}\frac{n_D}{\tau_D} + (1-\gamma_{PFC})\left[\frac{(1-f_{ref}(1-f_{eff}))R_{eff}}{1-R_{eff}(1-f_{eff})} - f_{ref}\right]\left(\frac{n_D}{\tau_D} + \frac{n_T}{\tau_T}\right)}{1 - f_{ref}(1-f_{eff})}, \tag{2.79}$$

$$S_T^R = \frac{f_{ref}\frac{n_T}{\tau_T} + \gamma_{PFC}\left[\frac{(1-f_{ref}(1-f_{eff}))R_{eff}}{1-R_{eff}(1-f_{eff})} - f_{ref}\right]\left(\frac{n_D}{\tau_D} + \frac{n_T}{\tau_T}\right)}{1 - f_{ref}(1-f_{eff})}, \tag{2.80}$$

where f_{ref}, R_{eff} and γ_{PFC} are recycling parameters that characterize the recycling effects. Fig. 2.7 shows a schematic illustrating how the recycling effects work and the meaning of each of the parameters. More details can be found in [29].

In ITER, the two fueling techniques existing in present-day devices will be considered: gas puffing and pellet injection. Present-day tokamaks normally use gas puffing as the primary fueling technique. However, in higher densities and H-mode regimes with steep edge pressure-gradients, it is predicted that gas puffing will have a poor fueling efficiency [30]. Pellet injection, on the contrary, has a higher capability to penetrate the magnetic fields and deposit particles into the plasma core due to the high velocity of the particles injected, and is planned to be the primary fueling technique in ITER. Gas puffing will mainly be used to fuel the plasma edge in order to enhance impurity transport out of the plasma core and keep optimal divertor conditions [30]. Two pellet injectors will be available in the initial phase of ITER. Each of these pellet injectors will be able to produce pellets made of both D and T,

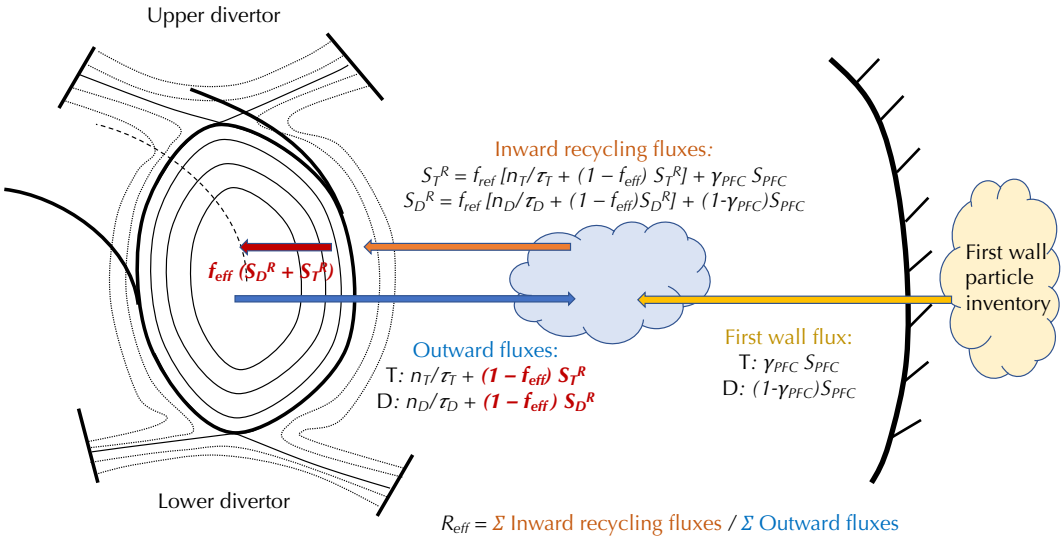

Figure 2.7: Recycling effects in 0D model for particle transport.

with a concentration of up to 90% T. It is envisioned that one of the pellet injectors is set up to inject pellets made of D only, and that the other pellet injector injects pellets with the highest possible concentration of T. In this modeling work, the first pellet injector is denoted as D pellet injector, whereas the second pellet injector is denoted as D-T pellet injector. Although the nominal concentrations for these lines are 100% D and 10%D - 90%T, respectively, the D-T concentration of those pellets may vary over time. This is mainly due to the fact that T tends to permeate very easily through the plasma facing components (PFCs), and also through the tritium exhaust and re-processing system [31]. Most PFCs will be made of Beryllium (like the vacuum vessel walls), Tungsten (divertor components) or Carbon, whereas the tritium exhaust and re-processing systems will include materials such as ceramics, different kinds of steel, and Aluminum alloys. The T permeability and solubility in all these materials is variable, so part of the T will inevitably diffuse into the materials which are more susceptible at a rate which will be difficult to estimate during operation. As a result, keeping a constant D-T concentration in the pellets may be just impossible. Variations in the D-T pellet concentration, which may be in turn hard or impossible to measure in real time, can decrease the burning plasma

performance to unacceptable levels. To deal with this problem in the design of burn controllers, S_D^{inj} and S_T^{inj} are modeled as

$$S_D^{inj} = (1 - \gamma_{D-line})S_{D-line}^{inj} + (1 - \gamma_{DT-line})S_{DT-line}^{inj}, \tag{2.81}$$

$$S_T^{inj} = \gamma_{D-line}S_{D-line}^{inj} + \gamma_{DT-line}S_{DT-line}^{inj}, \tag{2.82}$$

where S_{D-line}^{inj} and $S_{DT-line}^{inj}$ are the injection rates of the D pellet injector and D-T pellet injector, respectively, and γ_{D-line} and $\gamma_{DT-line}$ are uncertain parameters that characterize the D-T concentration in the pellets of the D pellet injector and D-T pellet injector, respectively. Although uncertain, the values of the two parameters γ_{D-line} and $\gamma_{DT-line}$ are between 0 and 1, so that 0 represents a 0% concentration in T and 1 represents a 100% concentration in T. Both γ_{D-line} and $\gamma_{DT-line}$ are expressed in this model as

$$\gamma_{D-line} = \gamma_{D-line}^{nom} + \delta_{D-line}, \tag{2.83}$$

$$\gamma_{DT-line} = \gamma_{DT-line}^{nom} + \delta_{DT-line}, \tag{2.84}$$

where $\gamma_{D-line}^{nom} = 0$ and $\gamma_{DT-line}^{nom} = 0.9$ are the known, nominal values corresponding to a 0% and 90% T concentration in the corresponding pellet injectors, respectively, and δ_{D-line} and $\delta_{DT-line}$ are uncertain variables.

The impurities balance equation is given by

$$\frac{dn_I}{dt} = -\frac{n_I}{\tau_I} + S_I^{sp} + S_I^{inj}, \tag{2.85}$$

where n_I is the impurity-ions average density, τ_I is the impurity confinement time, S_I^{sp} is the source of impurities arising from sputtering, and S_I^{inj} is the impurity injection rate, which is considered to be a controllable input in this model. Although only one type of impurity is considered, this model can be easily extended to include different kinds of impurities as the ones mentioned above (Carbon, Tungsten, Beryllium, etc.). The term S_I^{sp} is modeled as

$$S_I^{sp} = f_I^{sp}\left(\frac{n_e}{\tau_I} + \frac{dn_e}{dt}\right), \tag{2.86}$$

where n_e is the volume-average electron density, and $f_I^{sp} << 1$ is a constant parameter that characterizes the intensity of the sputtering effects.

To model the confinement times of the different particles, it is assumed that all of them scale with τ_E as

$$\tau_\alpha = k_\alpha \tau_E, \tau_D = k_D \tau_E,\ \tau_T = k_T \tau_E,\ \tau_I = k_I \tau_E, \tag{2.87}$$

where k_α, k_D, k_T, and k_I are constant parameters.

A summary of the variables in this 0D model for the particle densities is shown in Table 2.6. All variables considered are scalars.

Table 2.6: Variables in 0D model for n_α, n_D, n_T, and n_I

Variable	Description	Variable type
n_α, n_D, n_T, n_I	α, D, T, and impurity volume-average densities	State
W	Stored energy	Input
τ_E	Energy-confinement time	Input
k_α, k_D, k_T, k_I	Confinement constants	Model parameter
f_{eff}, f_{ref}, R_{eff}, γ_{PFC}	Constants for recycling effects	Model parameter
V_p	Plasma volume	Model parameter
$\gamma^{nom}_{DT-line}$, γ^{nom}_{D-line}	Nominal pellet concentrations	Model parameter
f_I^{sp}	Constant for sputtering effects	Model parameter
Z_I	Impurities atomic number	Model parameter
$S^{inj}_{DT-line}$, S^{inj}_{D-line}, S^{inj}_I	Injection rates	Controllable input
$\delta_{DT-line}$, δ_{D-line}	Uncertain pellet concentrations	Uncertainties

2.3.3 Electron Density Balance

To develop a 0D model for the evolution of the volume-average n_e, the balance equations presented in Section 2.3.2 for the different types of particles are employed. Taking time derivative in (2.76), using the balance equations (2.72), (2.77), (2.78), and (2.85) together with equations (2.86) and (2.87), and solving for dn_e/dt, the following expression is found

$$\frac{dn_e}{dt} = -\frac{1}{(1 - Z_I f_I^{sp})\tau_E}\left(\frac{n_D}{k_D} + \frac{n_T}{k_T} + 2\frac{n_\alpha}{k_\alpha} + Z_I \frac{n_I - f_I^{sp} n_e}{k_I}\right) + \frac{1}{1 - f_I^{sp}}\left(f_{eff}(S_D^R + S_T^R) + S_D^{inj} + S_T^{inj} + Z_I S_I^{inj}\right). \tag{2.88}$$

In order to have a model for the n_e evolution that is as simplified as possible to facilitate control synthesis, a few extra assumptions are made. First, it is assumed that $k_D \approx k_T \approx k_{DT}$, i.e., that τ_D and τ_T are the same. This implies that both D and T are assumed to diffuse out of the plasma core at a similar rate. Second, it is assumed that $n_I << n_e$ and $n_\alpha << n_e$, i.e., the impurities and α's presence in the plasma is negligible when compared to the D and T content[7]. Using these assumptions and some basic algebra, the first term in (2.88) can be rewritten as

$$\begin{aligned}
&\frac{1}{(1-Z_I f_I^{sp})\tau_E}\left(\frac{n_D}{k_D}+\frac{n_T}{k_T}+2\frac{n_\alpha}{k_\alpha}+Z_I\frac{n_I-f_I^{sp}n_e}{k_I}\right)= \\
&\quad\frac{1}{(1-Z_I f_I^{sp})k_{DT}\,\tau_E}\left(n_D+n_T+2n_\alpha\frac{k_{DT}}{k_\alpha}+Z_I n_I\frac{k_{DT}}{k_I}-Z_I\frac{f_I^{sp}k_{DT}n_e}{k_I}\right)= \\
&\quad\frac{1}{(1-Z_I f_I^{sp})k_{DT}\,\tau_E}\left(n_D+n_T+2n_\alpha+Z_I n_I-Z_I\frac{f_I^{sp}k_{DT}n_e}{k_I}\right. \\
&\qquad\left.-2n_\alpha\frac{k_\alpha-k_{DT}}{k_\alpha}-Z_I n_I\frac{k_I-k_{DT}}{k_I}\right)= \\
&\frac{1}{(1-f_I^{sp})k_{DT}\,\tau_E}\left(\left(1-Z_I\frac{f_I^{sp}k_{DT}}{k_I}\right)n_e-2n_\alpha\frac{k_\alpha-k_{DT}}{k_\alpha}-Z_I n_I\frac{k_I-k_{DT}}{k_I}\right)\approx \\
&\qquad\approx\frac{\left(1-Z_I f_I^{sp}\frac{k_{DT}}{k_I}\right)}{(1-Z_I f_I^{sp})k_{DT}\,\tau_E}n_e, \quad (2.89)
\end{aligned}$$

so the electron-density balance equation, (2.88), becomes

$$\frac{dn_e}{dt}=-\frac{n_e}{\tau_e}+\frac{1}{1-Z_I f_I^{sp}}\left(f_{eff}(S_D^R+S_T^R)+S_D^{inj}+S_T^{inj}+Z_I S_I^{inj}\right), \quad (2.90)$$

where τ_e is the electron confinement-time, which is given by

$$\tau_e \triangleq \frac{(1-Z_I f_I^{sp})k_{DT}\,\tau_E}{\left(1-Z_I f_I^{sp}\frac{k_{DT}}{k_I}\right)}. \quad (2.91)$$

A summary of the variables in this 0D model for the volume-average electron density is shown in Table 2.7. All variables considered are scalars.

[7]Such assumption is not totally arbitrary. The ideal operation of a burning plasma in tokamaks envisions low contents of α's and impurities.

Table 2.7: Variables in 0D model for n_e

Variable	Description	Variable type
n_e	Electron volume-average density	State
τ_E	Energy-confinement time	Input
n_D, n_T	D and T densities	Inputs
k_{DT}	D-T confinement constant	Model parameter
f_{eff}, f_{ref}, R_{eff}, γ_{PFC}	Constants for recycling effects	Model parameter
$\gamma^{nom}_{DT-line}$, γ^{nom}_{D-line}	Nominal pellet concentrations	Model parameter
f^{sp}_I	Constant for sputtering effects	Model parameter
Z_I	Impurities atomic number	Model parameter
$S^{inj}_{DT-line}$, S^{inj}_{D-line}, S^{inj}_I	Injection rates	Controllable input
$\delta_{DT-line}$, δ_{D-line}	Uncertain pellet concentrations	Uncertainties

For present-day devices with low impurity content, the n_e model can be simplified even further because most present-day tokamaks do not work with T, so equation (2.76) becomes $n_e \approx n_D$, and equation (2.90) becomes

$$\frac{dn_e}{dt} = -\frac{n_e}{\tau_e} + \frac{1}{1 - Z_I f_I^{sp}} \left(f_{eff} S_D^R + S_D^{inj} + Z_I S_I^{inj} \right), \tag{2.92}$$

which is still a more sophisticated model than just using a balance equation like (2.77) with $n_D = n_e$ and $S_\alpha = 0$, because equation (2.92) includes the impurity sputtering effects (which affect the confinement time, τ_e, and D injection rate, S_D^{inj}), together with impurity injection.

2.3.4 Central Safety Factor Evolution

The central safety factor, q_0, is the value of q at the magnetic axis, i.e., $\hat{\rho} = 0$, and is given by

$$q_0 \triangleq - \left. \frac{B_{\phi,0} \rho_b^2 \hat{\rho}}{\partial \psi / \partial \hat{\rho}} \right|_{\hat{\rho}=0}. \tag{2.93}$$

Using the definition for the poloidal flux gradient, θ, which is given by

$$\theta \triangleq \frac{\partial \psi}{\partial \hat{\rho}}, \tag{2.94}$$

and using L'Hopital's rule and the boundary condition at $\hat{\rho} = 0$, (2.28), equation (2.93) can be rewritten as

$$q_0 = -\frac{B_{\phi,0}\rho_b^2}{\theta_0'}, \tag{2.95}$$

where $\theta_0' = \frac{\partial\theta}{\partial\hat{\rho}}|_{\hat{\rho}=0}$. The derivative θ_0' is approximated as

$$\theta_0' \approx \frac{\theta_1 - \theta_0}{\Delta\hat{\rho}}, \tag{2.96}$$

where θ_0 is the value of θ at $\hat{\rho} = 0$, θ_1 is the value of θ at $\hat{\rho} = \Delta\hat{\rho}$, and $\Delta\hat{\rho}$ is taken such that $\Delta\hat{\rho} << 1$. Using (2.96), and the boundary condition at $\hat{\rho} = 0$ (2.28), equation (2.95) can be rewritten as

$$q_0 = -\frac{B_{\phi,0}\rho_b^2\Delta\hat{\rho}}{\theta_1}, \tag{2.97}$$

and taking time derivative in (2.97), it is possible to write

$$\frac{dq_0}{dt} = \frac{B_{\phi,0}\rho_b^2\Delta\hat{\rho}}{\theta_1^2}\frac{d\theta_1}{dt}. \tag{2.98}$$

The evolution of θ_1 can be obtained by taking derivative with respect to $\hat{\rho}$ in the MDE (2.27), and particularizing at $\hat{\rho} = \Delta\hat{\rho}$. The evolution equation for θ_1 would be given by

$$\frac{d\theta_1}{dt} = \frac{\partial}{\partial\hat{\rho}}\left[\frac{\eta}{\mu_0\rho_b^2\hat{F}^2}\frac{1}{\hat{\rho}}\frac{\partial}{\partial\hat{\rho}}\left(\hat{\rho}\hat{F}\hat{G}\hat{H}\theta\right) + R_0\hat{H}\eta\frac{\langle\vec{j}_{ni}\cdot\vec{B}\rangle}{B_{\phi,0}}\right]_{\hat{\rho}=\Delta\hat{\rho}}. \tag{2.99}$$

To facilitate the control synthesis using this 0D model for q_0, it is assumed that the plasma equilibrium does not change in time, i.e., that no time dependence is found in ρ_b, $\hat{F}$, $\hat{G}$, $\hat{H}$, or other parameters. This, evidently, is not the real situation found in a tokamak. Changes in θ will affect $\vec{j}$ (see Appendix A.3, equation (A.30)), and therefore, the pressure field p will reorganize until a new equilibrium is achieved (so that (2.8) is fulfilled). Therefore, changes in θ always imply changes in the plasma shape. However, for q_0 control design, it is assumed that the plasma shape and position controllers will keep an approximately constant plasma shape and position, and also that the variations in the profiles related to the magnetic configuration can

be neglected. For η and $\langle \vec{j}_{ni} \cdot \vec{B} \rangle / B_{\phi,0}$, the same models as introduced in Section 2.2.1 are employed, whereas T_e and n_e are modeled using the 0.5D approximation [18].

The following spatial profiles are defined for convenience and clarity,

$$f_\eta = \frac{1}{\mu_0 \rho_b^2 \hat{F}^2} \frac{k_{sp}^{prof} Z_{eff}}{\left(T_e^{prof} \, (n_e^{prof})^\zeta \right)^{3/2}}, \quad f_{diff,1} = f_\eta \left(\frac{D_\psi}{\hat{\rho}} + \frac{\partial D_\psi}{\partial \hat{\rho}} \right), \tag{2.100}$$

$$f_{diff,2} = f_\eta D_\psi, \quad f_{aux,i} = \frac{R_0 \hat{H} k_{sp}^{prof} Z_{eff} j_{aux,i}^{prof} \left(T_e^{prof} (n_e^{prof})^\zeta \right)^{\delta_{NBI}}}{\left(T_e^{prof} \, (n_e^{prof})^\zeta \right)^{3/2} n_e^{prof}}, \tag{2.101}$$

$$f_{BS} = \frac{\hat{H} R_0^2 k_{sp}^{prof} Z_{eff}}{\hat{F} \left(T_e^{prof} \, (n_e^{prof})^\zeta \right)^{3/2}} \left[2\mathcal{L}_{31} T_e^{prof} (n_e^{prof})^\zeta \frac{\partial n_e^{prof}}{\partial \hat{\rho}} \right. \tag{2.102}$$

$$\left. + \left(2\mathcal{L}_{31} + \mathcal{L}_{32} + \alpha \mathcal{L}_{34} \right) \frac{\partial (T_e^{prof} (n_e^{prof})^\zeta)}{\partial \hat{\rho}} n_e^{prof} \right], \tag{2.103}$$

where $D_\psi \triangleq \hat{F} \hat{G} \hat{H}$. Also, the following function of the inputs I_p, P_{tot}, $\bar{n}_e$ and $P_{aux,i}$ are defined (they will be referred to as "virtual inputs" to the system),

$$u_\eta = (I_p^\gamma P_{tot}^\epsilon \bar{n}_e^\zeta)^{-3/2}, \tag{2.104}$$

$$u_{aux,i} = (I_p^\gamma P_{tot}^\epsilon \bar{n}_e^\zeta)^{(-3/2+\delta_{aux,i})} \bar{n}_e^{-1} P_{aux,i}, \tag{2.105}$$

$$u_{BS} = (I_p^\gamma P_{tot}^\epsilon \bar{n}_e^\zeta)^{-1/2} \bar{n}_e. \tag{2.106}$$

Introducing the definitions (2.100)-(2.106), (2.99) is rewritten as

$$\frac{d\theta_1}{dt} = \frac{\partial}{\partial \hat{\rho}} \left[\left(f_{diff,1} \theta + f_{diff,2} \frac{\partial \theta}{\partial \hat{\rho}} \right) u_\eta + \sum_{i=1}^{i=N_{aux}} f_{aux,i} u_{aux,i} + \frac{1}{\theta} f_{BS} u_{BS} \right]_{\hat{\rho}=\Delta\hat{\rho}}, \tag{2.107}$$

and using the chain rule to compute the partial derivative with respect to $\hat{\rho}$, equation (2.107) becomes

$$\frac{d\theta_1}{dt} = \left\{ \left[f'_{diff,1} \theta + \left(f_{diff,1} + f'_{diff,2} \right) \theta' + f_{diff,2} \theta'' \right] u_\eta + \right.$$
$$\left. \sum_{i=1}^{i=N_{aux}} f'_{aux,i} u_{aux,i} + \left(\frac{1}{\theta} f'_{BS} - \frac{\theta'}{\theta^2} f_{BS} \right) u_{BS} \right\}_{\hat{\rho}=\Delta\hat{\rho}}, \tag{2.108}$$

where $(\cdot)' \triangleq \partial(\cdot)/\partial\hat{\rho}$. The first and second derivatives of θ at $\hat{\rho} = \Delta\hat{\rho}$, θ_1' and θ_1'', are discretized as $\theta_1' \approx (\theta_2 - \theta_0)/(2\Delta\hat{\rho})$, $\theta_1'' \approx (\theta_2 + \theta_0 - 2\theta_1)/\Delta\hat{\rho}^2$, where $\theta_2 \triangleq \theta(\hat{\rho} = 2\Delta\rho)$. By defining the following constants,

$$\lambda_{diff,1} = f'_{diff,1}(\hat{\rho} = \Delta\hat{\rho}) - 2\frac{f_{diff,2}(\hat{\rho} = \Delta\hat{\rho})}{\Delta\hat{\rho}^2}, \tag{2.109}$$

$$\lambda_{diff,2} = \frac{f_{diff,1}(\hat{\rho} = \Delta\hat{\rho}) + f'_{diff,2}(\hat{\rho} = \Delta\hat{\rho})}{2\Delta\hat{\rho}} + \frac{f_{diff,2}(\hat{\rho} = \Delta\hat{\rho})}{\Delta\hat{\rho}^2}, \tag{2.110}$$

it is possible to rewrite (2.108) as

$$\frac{d\theta_1}{dt} = (\lambda_{diff,1}\theta_1 + \lambda_{diff,2}\theta_2)u_\eta + \sum_{i=1}^{i=N_{aux}} f'_{aux,i}(\hat{\rho} = \Delta\hat{\rho})u_{aux,i} + \left[\frac{1}{\theta_1}f'_{BS}(\hat{\rho} = \Delta\hat{\rho}) - \frac{\theta_2}{\theta_1^2}\frac{f_{BS}(\hat{\rho} = \Delta\hat{\rho})}{2\Delta\hat{\rho}}\right]u_{BS}. \tag{2.111}$$

Plugging (2.111) into (2.98), it is found that

$$\frac{dq_0}{dt} = \frac{B_{\phi,0}\rho_b^2\Delta\hat{\rho}}{\theta_1}\left[\lambda_{diff,1} + \lambda_{diff,2}\frac{\theta_2}{\theta_1}\right]u_\eta + \frac{B_{\phi,0}\rho_b^2\Delta\hat{\rho}}{\theta_1^2}\sum_{i=1}^{i=N_{aux}} f'_{aux,i}(\hat{\rho} = \Delta\hat{\rho})\, u_{aux,i} + \frac{B_{\phi,0}\rho_b^2\Delta\hat{\rho}}{\theta_1^3}\left[f'_{BS}(\hat{\rho} = \Delta\hat{\rho}) - \frac{\theta_2}{\theta_1}\frac{f_{BS}(\hat{\rho} = \Delta\hat{\rho})}{2\Delta\hat{\rho}}\right]u_{BS}, \tag{2.112}$$

and using the definition (2.97) for q_0, then (2.112) can be rewritten as

$$\frac{dq_0}{dt} = -q_0\left(\lambda_{diff,1} + \lambda_{diff,2}\frac{\theta_2}{\theta_1}\right)u_\eta + q_0^2\sum_{i=1}^{i=N_{aux}}\lambda_{aux,i}u_{aux,i} - q_0^3\left(\lambda_{BS,1} + \lambda_{BS,2}\frac{\theta_2}{\theta_1}\right)u_{BS}, \tag{2.113}$$

where $\lambda_{(\cdot)}$ are given by

$$\lambda_{aux,i} = \frac{f'_{aux,i}(\hat{\rho} = \Delta\hat{\rho})}{B_{\phi,0}\rho_b^2\Delta\hat{\rho}}, \quad \lambda_{BS,1} = \frac{f'_{BS}(\hat{\rho} = \Delta\hat{\rho})}{(B_{\phi,0}\rho_b^2\Delta\hat{\rho})^2}, \quad \lambda_{BS,2} = -\frac{f_{BS}(\hat{\rho} = \Delta\hat{\rho})}{2(B_{\phi,0}\rho_b^2)^2\Delta\hat{\rho}^3}. \tag{2.114}$$

It is assumed that $\frac{\theta_2}{\theta_1}$ is uncertain and given by

$$\frac{\theta_2}{\theta_1} = \left.\frac{\theta_2}{\theta_1}\right|_{nom} + \delta_\theta, \tag{2.115}$$

where $\frac{\theta_2}{\theta_1}|_{nom}$ is a nominal, known value, and δ_θ is an uncertain term. This assumes that the influence of the rest of the q-profile on q_0 is uncertain. In addition, δ_θ can model any other source of unknown dynamics in the q_0 subsystem. Equation (2.113) is rewritten as

$$\frac{dq_0}{dt} = -q_0 \left(\lambda_{diff,1} + \lambda_{diff,2} \left. \frac{\theta_2}{\theta_1} \right|_{nom} \right) u_\eta + q_0^2 \sum_{i=1}^{i=N_{aux}} \lambda_{aux,i} u_{aux,i} - q_0^3 \left(\lambda_{BS,1} + \lambda_{BS,2} \left. \frac{\theta_2}{\theta_1} \right|_{nom} \right) u_{BS} + \delta_{q_0}, \quad (2.116)$$

where $\delta_{q_0} = -(q_0 \lambda_{diff,2} u_\eta + q_0^3 \lambda_{BS,2} u_{BS}) \delta_\theta$ is a term that bundles the uncertainties in the q_0 subsystem.

A summary of the variables in this 0D model for q_0 is shown in Table 2.8. All variables considered are scalars.

Table 2.8: Variables in 0D model for q_0

Variable	Description	Variable type
q_0	Central safety factor	State
$\lambda_{diff,i}$	Diffusion constants	Model parameter
$\lambda_{aux,i}$	Auxiliary CD constants	Model parameter
$\lambda_{BS,i}$	Bootstrap current constants	Model parameter
$\left. \frac{\theta_2}{\theta_1} \right\|_{nom}$	Nominal θ_2/θ_1 evolution	Model parameter
γ, ϵ, ζ	Temperature scaling constants	Model parameter
$\bar{n}_e$	Line-average density	Input
P_{tot}	Total power	Controllable input
I_p	Plasma current	Controllable input
$P_{aux,i}$	Auxiliary source powers	Controllable input
δ_{q_0}	Uncertain q_0 dynamics	Uncertainty

2.3.5 Edge Safety Factor Evolution

The model for q_{edge} is based on the boundary condition at $\hat{\rho} = 1$ for the MDE (2.28), which can be written in terms of θ at $\hat{\rho} = 1$ as,

$$\theta(\hat{\rho} = 1) = -k_{I_p} I_p, \quad (2.117)$$

where $k_{I_p} \triangleq \frac{\mu_0 R_0}{2\pi G(\hat{\rho}=1) H(\hat{\rho}=1)}$. The definition for q_{edge} is given by

$$q_{edge} = -\frac{B_{\phi,0}\rho_b^2}{\theta(\hat{\rho}=1)}. \tag{2.118}$$

Combining (2.117) and (2.118), and taking time derivative (as in the q_0 case, it is assumed that $B_{\phi,0}$ and ρ_b are constant in time), it is found that

$$\frac{dq_{edge}}{dt} = \frac{B_{\phi,0}\rho_b^2}{(k_{I_p} I_p)^2}\left(\frac{dk_{I_p}}{dt} I_p + k_{I_p}\frac{dI_p}{dt}\right). \tag{2.119}$$

The variable k_{I_p} is a model parameter that depends on the plasma magnetic configuration and/or the position of the magnetic axis (it depends on $\hat{G}$, $\hat{H}$, and R_0). It is modeled as

$$k_{I_p} = k_{I_p}^{nom} + \delta_{k_{I_p}}, \tag{2.120}$$

where $k_{I_p}^{nom}$ is a constant, known value of k_{I_p}, and $\delta_{k_{I_p}}$ is an uncertain term, representing unknown variations in the plasma magnetic configuration and position.

Because of the definition of the separatrix ($B_\theta = 0$) in diverted plasmas, it can be noted that there is a singularity at the edge that produces $q_{edge} \to \infty$. In diverted configurations, the model presented in this Section must be seen as a model for q at some point near the edge/separatrix, but not right at it. Alternatively, q_{95}, which denotes q at the flux surface that encloses 95% of the toroidal flux Φ, is a magnitude widely used within the fusion community that is often employed instead of q_{edge}.

Table 2.9: Variables in 0D model for q_{edge}

Variable	Description	Variable type
q_{edge}	Edge safety factor	State
$k_{I_p}^{nom}$	Nominal BC constant	Model parameter
$B_{\phi,0}$	Vacuum toroidal field	Model parameter
ρ_b	ρ at last closed magnetic-flux surface	Model parameter
P_{tot}	Total power	Controllable input
I_p	Plasma current	Controllable input
$\delta_{k_{I_p}}$	Uncertain BC constant	Uncertainty

A summary of the variables in this 0D model for q_{edge} is shown in Table 2.9. All variables considered are scalars.

2.3.6 Global Toroidal Rotation Balance

The derivation of this model starts with the definition of the bulk toroidal rotation of the ions, Ω_ϕ. The ion velocity field $\vec{v}_i$ can be decomposed as a toroidal velocity field, $\vec{v}_{\phi,i}$, plus a perpendicular velocity field, $\vec{v}_{\perp,i}$, such that $\vec{v}_i = \vec{v}_{\phi,i} + \vec{v}_{\perp,i}$ (see Fig. 2.8). Whereas $\vec{v}_{\perp,i}$ is contained in the r-z plane and represents the particles rotation around the ϕ direction in Fig. 2.8 (i.e., the Larmor gyration), $\vec{v}_{\phi,i}$ represents the particles rotation around the z-axis (toroidal rotation). Then, $v_{\phi,i}$ and $v_{\perp,i}$ are related to the angular velocity vector, $\vec{\omega}$, by

$$\vec{\omega} \times \vec{r} = \vec{\omega} \times (\vec{R}_0 + \vec{\xi}) = \vec{v}_{\phi,i} + \vec{v}_{\perp,i}, \tag{2.121}$$

where $\vec{R}_0 = R_0\vec{r}$ and $\vec{\xi} = \xi_r\vec{r} + \xi_z\vec{z}$ are the vectors that define the position in space of a particular ion, as depicted in Fig. 2.8.

The three components of the vector equation (2.121) are given by

$$\omega_c \xi_z = \vec{v}_{\perp,i} \cdot \vec{r} \triangleq v_{r,i}, \tag{2.122}$$

$$\omega_\phi(\xi_r + R_0) = v_{\phi,i}, \tag{2.123}$$

$$-\omega_c(\xi_r + R_0) = \vec{v}_{\perp,i} \cdot \vec{z} \triangleq v_{z,i}, \tag{2.124}$$

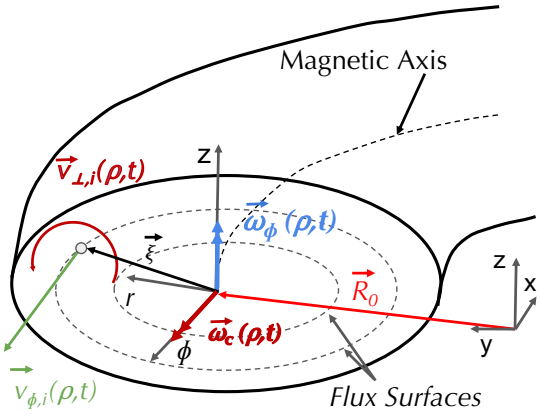

Figure 2.8: Schematic of the linear and angular velocity components.

where ω_c is the angular velocity around the ϕ axis, and ω_ϕ is the angular velocity around the z axis, i.e., the toroidal angular velocity. It can be noted that no radial angular velocity is considered in the model ($\omega_r \equiv 0$), due to the axisymmetry around the z-axis. Equations (2.122) and (2.124) describe the Larmor rotation around the magnetic axis direction, ϕ (thus the notation employed for its angular velocity, ω_c, i.e., the ion-cyclotron frequency), whereas equation (2.123) describes to the toroidal rotation. Then, from (2.123),

$$\omega_\phi = \frac{v_{\phi,i}}{R_0 + \xi_r}. \tag{2.125}$$

The bulk toroidal rotation, Ω_ϕ, is defined in this work as the average toroidal rotation of the ions inside the plasma, and it is given by

$$\Omega_\phi \triangleq \frac{1}{N_p} \iiint_{V_p} n\ \omega_\phi dV_p, \tag{2.126}$$

where N_p is the total number of ions within the plasma, which is given by

$$N_p = \iiint_{V} n dV_p. \tag{2.127}$$

Using the system's symmetry around the z-axis and the magnetic axis, and equation (2.125), it is possible to rewrite (2.126) as

$$\Omega_\phi = 2\pi R_0 \frac{\int_{\rho=0}^{\rho=\rho_b} \left[\oint_\Gamma n\, v_{\phi,i} \frac{d\Gamma}{R_0+\xi_r} \right] d\rho}{N_p}, \tag{2.128}$$

where Γ is the contour equation for a magnetic flux surface (see Fig. 2.3). Measurements of both $v_{\phi,i}$ or n are available in some tokamaks, for example from CER measurements (see Section 1.3.6), allowing for the computation of Ω_ϕ as long as information about the magnetic geometry (i.e., Γ) is available, for example, from equilibrium reconstruction codes. An easier, control-oriented approach that allows for finding an analytic expression for Ω_ϕ without having to reconstruct the plasma equilibrium can be found in Appendix B.1.

The model proposed in this work to estimate the time evolution of Ω_ϕ is simplified but based on first principles. In the same way that a particle of mass m and position vector $\vec{r}$ would have an angular momentum given by $\vec{L} = \vec{r} \times m\frac{d\vec{r}}{dt}$, the plasma is assumed to have an angular momentum Γ in the z-direction given by

$$\Gamma = m_p R_0^2 \Omega_\phi, \tag{2.129}$$

where m_p is the plasma mass contained within the last closed magnetic-flux surface, which neglecting the electrons contribution is given by

$$m_p = \frac{m_D}{N_{Av}} N_p, \tag{2.130}$$

where m_D is the molar mass of the plasma, and N_{Av} is Avogadro's number. The plasma is regarded as a particle with the same mass as the total plasma mass which

is rotating around the z-axis with angular velocity $\vec{\Omega}_\phi = \Omega_\phi \vec{z}$, and at a distance R_0. The angular momentum varies in time due to the external torque sources as

$$\frac{d\Gamma}{dt} = R_0^2 \frac{d\left(m_p \Omega_\phi\right)}{dt} = \sum_{i=1}^{N_{NBI}} T_{NBI,i} + T_{NRMF} + T_{int}, \tag{2.131}$$

where $T_{NBI,i}$ is the volume-average torque injected by the i-th NBI, T_{NRMF} is the volume-average torque created by NRMFs, and T_{int} is the volume-average intrinsic-torque source. Expanding the time derivative in (2.131), and rearranging terms,

$$\frac{d\Omega_\phi}{dt} = -\Omega_\phi \frac{1}{m_p}\frac{dm_p}{dt} + \sum_{i=1}^{N_{NBI}} \frac{T_{NBI,i}}{m_p R_0^2} + \frac{T_{NRMF}}{m_p R_0^2} + \frac{T_{int}}{m_p R_0^2}. \tag{2.132}$$

The first term, $-\Omega_\phi \frac{1}{m_p}\frac{dm_p}{dt}$, represents the diffusion of toroidal rotation. By defining the global rotation confinement time, τ_{Ω_ϕ}, as

$$\tau_{\Omega_\phi} \triangleq \frac{m_p}{dm_p/dt}, \tag{2.133}$$

the Ω_ϕ dynamics equation (2.132) can be rewritten as

$$\frac{d\Omega_\phi}{dt} = -\frac{\Omega_\phi}{\tau_{\Omega_\phi}} + \sum_{i=1}^{N_{NBI}} \frac{T_{NBI,i}}{m_p R_0^2} + \frac{T_{NRMF}}{m_p R_0^2} + \frac{T_{int}}{m_p R_0^2}. \tag{2.134}$$

Control-oriented models for τ_{Ω_ϕ}, $T_{NBI,i}$, T_{NRMF}, and T_{int} are employed. The confinement time τ_{Ω_ϕ} is taken as $\tau_{\Omega_\phi} = k_\Omega \tau_E$, where $k_\Omega > 0$ is a dimensionless parameter. For $T_{NBI,i}$, the following model is employed,

$$T_{NBI,i} = k_{NBI,i} P_{NBI,i}, \tag{2.135}$$

where $k_{NBI,i}$ are constant parameters that depend on the type of NBI. For example, co-current and counter-current NBIs have $k_{NBI,i}$ with opposite signs. The NRMF torque, T_{NRMF}, is modeled as

$$T_{NRMF} = k_{NRMF}\left(\Omega_\phi - \Omega_\phi^\star\right) I_{NRMF}^2, \tag{2.136}$$

where k_{NRMF} is a constant parameter, and $\Omega_\phi^\star$ is an offset bulk rotation. Finally, the intrinsic torque is modeled as

$$T_{int} = k_{int} \frac{W}{I_p}, \tag{2.137}$$

where k_{int} is a constant parameter.

In addition to the uncertainty in τ_Ω through H_H, an unknown source/sink of torque δ_T is added on the right hand side of (2.134) to account for uncertain/unmodeled effects such as inefficient torque injection, uncertainty in the model parameters ($k_{NBI,i}$, k_{int}, etc.), or inaccurate measurements of the state/inputs. Equation (2.134) can be rewritten as

$$\frac{d\Omega_\phi}{dt} = -\frac{\Omega_\phi}{k_\Omega H_H^{nom} k {P_{tot}}^{-0.69}} + \sum_{i=1}^{N_{NBI}} \frac{T_{NBI,i}}{m_p R_0^2} + \frac{T_{NRMF}}{m_p R_0^2} + \frac{T_{int}}{m_p R_0^2} + \delta_{\Omega_\phi}, \qquad (2.138)$$

where $\delta_{\Omega_\phi} = \frac{\Omega_\phi}{k_\Omega k {P_{tot}}^{-0.69}}(\frac{1}{H_H^{nom}} - \frac{1}{H_H}) + \delta_T$ is a term that bundles all the uncertain terms of the Ω_ϕ-subsystem. The model given by (2.138) describes relevant physical effects observed in tokamaks. For example, the influence of $\sum_i T_{NBI,i}$ on the Ω_ϕ dynamics decreases as the machine size is increased (i.e., as m_p, R_0, and/or $T_{int} \propto W$ increase).

A summary of the variables in this 0D model for Ω_ϕ is shown in Table 2.10. All variables considered are scalars.

Table 2.10: Variables in 0D model for Ω_ϕ

Variable	Description	Variable type
Ω_ϕ	Bulk toroidal rotation	State
τ_E	Energy-confinement time	Input
W	Stored thermal energy	Input
$\bar{n}_e$	Line-average density	Input
k_Ω	Confinement constant	Model parameter
$k_{NBI,i}$, k_{NRMF}, k_{int}	NBI, NRMF & intrinsic torque constants	Model parameter
V_p, R_0	Plasma volume & major radius	Model parameter
$P_{aux,i}$	Auxiliary source powers	Controllable input
I_p	Plasma current	Controllable input
I_{NRMF}	NRMF coil current	Controllable input
δ_T	Uncertain torque	Uncertainty

2.3.7 The Modified Rutherford Equation

In this Section, a 0D model for the evolution of the width of an NTM island is presented. As introduced in Section 1.3, NTMs modify the magnetic configuration of a tokamak so that not all the magnetic-flux surfaces are nested around the magnetic axis as predicted by the ideal MHD theory. Such modification in the magnetic-field topology gives place to the so-called *magnetic islands*, regions with their own separatrix in which the magnetic-flux surfaces tear and reconnect. Inside the magnetic island, the plasma resistivity η cannot be neglected, and particle escape producing a flattening of the pressure profile, p. This implies an undesired decrease in the overall plasma performance.

Due to the helical magnetic-field configuration in a tokamak, NTMs have a geometry as depicted in Fig. 2.9. The magnetic islands are found at rational surfaces with $q = m/n$, where m and n are integers that are denominated poloidal and toroidal mode numbers, respectively. The island O-point corresponds to the radial location, r, corresponding to its maximum width, w, whereas the island X-point is located at the singularity of its separatrix.

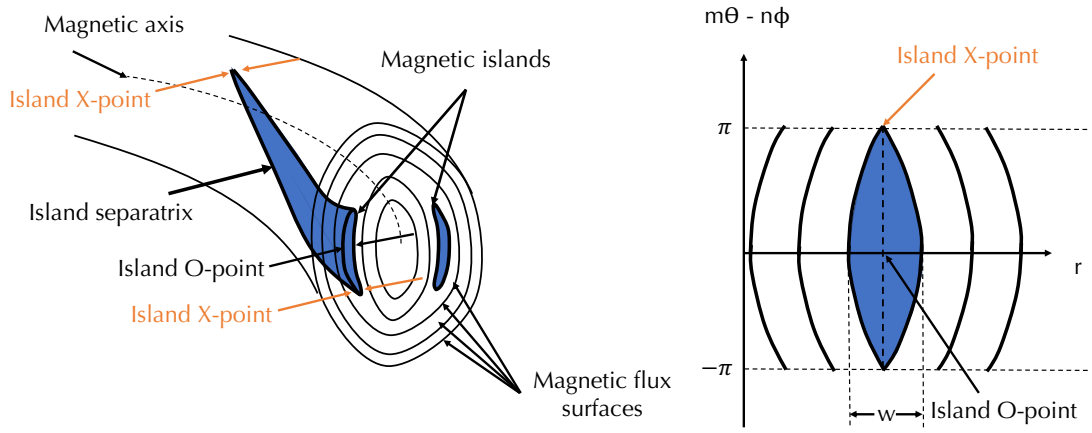

Figure 2.9: Diagram of the an NTM magnetic island showing the island width as a function of the radial coordinate, r, and helical angle, $m\theta - n\phi$, together with the X-point and O-point locations.

The 0D model employed to estimate the size of an NTM island is based on one version of the Modified Rutherford Equation (MRE) [5] given by

$$\frac{\tau_R}{r}\frac{dw}{dt} = \Delta' r + a_2 \frac{j_{BS}}{j_\phi}\frac{L_q}{w}\left[1 - \frac{w_{marg}^2}{3w^2} - K_{EC}(\Delta\rho_{NTM})\frac{j_{EC}^{max}}{j_{BS}}\right], \tag{2.139}$$

where w is the magnetic-island radial width, τ_R is the island's resistive diffusion time, $\Delta' r$ is the NTM stability parameter, a_2 is a geometric factor, j_{BS} is the local bootstrap current density, j_ϕ is the local toroidal current density, j_{EC}^{max} is the maximum EC current density, $L_q \triangleq q/(dq/dr)$ is the local magnetic shear length, w_{marg} is the marginal island width (i.e., the island width with the maximum dw/dt), and $K_{EC}(\Delta\rho_{NTM})$ is a parameter that characterizes the efficiency of EC to replace the bootstrap current loss due to local flattening of the pressure profile, and depends on $\Delta\rho_{NTM} = \rho_{NTM} - \rho_{EC}$, where ρ_{NTM} is the position of the rational surface and ρ_{EC} is the position of the EC current peak. It is assumed that ECCD can be steered toward different locations in the plasma domain, so that ρ_{EC} is a controllable input, together with j_{EC}^{max}, which can be modified by varying the EC power injected, P_{EC}.

The island's resistive diffusion time, τ_R, is modeled as

$$\tau_R = \frac{\mu_0 \pi r w}{1.22\eta}, \tag{2.140}$$

where η is the local resistivity, i.e., $\eta(\hat{\rho}_{NTM})$. The NTM stability parameter is modeled as

$$\Delta' r = \Delta_0' r + \delta\Delta' r, \tag{2.141}$$

where $\Delta_0' r$ is the classical stability index, and $\delta\Delta' r$ is the variation in $\Delta' r$ due to EC. For an NTM located at the $q = m/n$ rational surface, $\Delta_0' r = -m$. For $\delta\Delta' r$, the following model is employed [32],

$$\delta\Delta' r = -\frac{5\pi^{3/2}}{32} a_2 \frac{L_q}{\delta_{EC}^w} F_{EC}(\Delta\rho_{NTM})\frac{j_{EC}^{max}}{j_\phi}, \tag{2.142}$$

where δ_{EC}^w characterizes the width of the EC current deposition, and $F_{EC}(\Delta\rho_{NTM})$ is an alignment function. The parameter a_2 is modeled as

$$a_2 = -\Delta_0' r \frac{w_{sat}}{L_q}\frac{j_\phi}{j_{BS}}, \tag{2.143}$$

where w_{sat} is the saturated island width, which is the maximum value for w. It is assumed that an estimation for w_{sat} is available. The marginal island width, w_{marg}, is modeled as

$$w_{marg} = 2\epsilon^{1/2}\rho_{\theta,i}, \tag{2.144}$$

where ϵ is the inverse aspect ratio, and $\rho_{\theta,i}$ is the ion banana-orbit width, which is given by

$$\rho_{\theta,i} = \sqrt{\frac{2m_iT_i}{|q_e|B_\theta^2}}. \tag{2.145}$$

Using (2.140), (2.141), and (2.142), the MRE in (2.139) becomes

$$\frac{\mu_0\pi w}{1.22\eta}\frac{dw}{dt} = \Delta_0' r + a_2\frac{j_{BS}}{j_\phi}\frac{L_q}{w}\left[1 - \frac{w_{marg}^2}{3w^2} - \left(K_{EC} + \frac{5\pi^{3/2}}{32}F_{EC}\frac{w}{\delta_{EC}}\right)\frac{j_{EC}^{max}}{j_{BS}}\right], \tag{2.146}$$

and using (2.143),

$$\frac{\mu_0\pi w}{1.22\eta}\frac{dw}{dt} = \Delta_0' r\left\{1 - \frac{w_{sat}}{w}\left[1 - \frac{w_{marg}^2}{3w^2} - \left(K_{EC} + \frac{5\pi^{3/2}}{32}F_{EC}\frac{w}{\delta_{EC}}\right)\frac{j_{EC}^{max}}{j_{BS}}\right]\right\}. \tag{2.147}$$

A summary of the variables in this 0D model for w is shown in Table 2.11. All variables considered are scalars.

Table 2.11: Variables in 0D model for w

Variable	Description	Variable type
w	NTM island width	State
η	Plasma resistivity	Input
j_{BS}	Bootstrap current density	Input
w_{marg}	Marginal island width	Input
ρ_{NTM}	NTM location	Input
$\Delta_0' r$	Classical stability index	Model parameter
w_{sat}	Saturated island width	Model parameter
δ_{EC}^w	ECCD profile width	Model parameter
K_{EC}, F_{EC}	ECCD efficiency functions for NTM suppression	Model parameter
ρ_{ECCD}	ECCD deposition location	Controllable input
j_{EC}^{max}	Maximum EC current density	Controllable input

2.4 Conclusions

A brief physical description of plasmas, with special emphasis on tokamak plasmas, has been presented in this Chapter. In addition, the physics-based models employed during this dissertation for control-oriented simulation and control design have been introduced. These models have different levels of complexity and accuracy, ranging from 1D, first-principles models to 0D, heuristic models. In principle, the 1D models are more sophisticated than the simplified 0D models, so the former should be able to describe the real plasma behavior with better accuracy than the latter. However, it must be kept in mind that modeling with different complexity levels is needed for control development. Models with a higher degree of mathematical complexity may be more suitable to reproduce confidently the observed plasma phenomena (and will have an edge for simulation purposes), but may not allow for a practical design of plasmas controllers, as the difficulty of the control synthesis substantially increases with the mathematical complexity of the model.

A key part of the reduced modeling process is the inclusion of uncertainties. In a field such as nuclear fusion science, where plasmas behave in unexpected ways almost as if they had life of their own, uncertainty modeling is of major relevance. A successful control design must take into account the possible inaccuracies or unknown physics in the model in order to ensure that the system's performance is within acceptable limits. In other words, *it is important that we know and quantify "how much we do not know" about our system*, and carry out a consequent control design with which we can still fulfill the control objective. This is the reason why so many uncertainties have been included in the modeling process detailed in this Chapter. When bounds and/or other characteristic of the uncertainties can be estimated, techniques such as *robust control* can be utilized to guarantee the appropriate plasma behavior.

Chapter 3

COTSIM: a Simulation Code for Control Applications

3.1 Introduction

The synthesis and development of a control algorithm for tokamak plasmas consists of different steps. The first step is the *modeling* stage, in which mathematical models are sought for the dynamics of to-be-controlled plasma variables. In Chapter 2, Sections 2.2 and 2.3, 1D models for the dynamics of ψ (or, equivalently, q), T_e, and ω_ϕ were presented together with 0D models for the dynamics of W, volume-average particle densities, kinetic and magnetic individual scalars (Ω_ϕ, q_0, q_{edge}), and NTM magnetic-island width, w. These models are derived from first principles, and are complemented by control-oriented models for some specific plasma variables, together with some simplifications. The second step is the *controller synthesis*, which is presented in Chapters 4, 5, 6, and 7 for different control problems: burn control, q-profile control, β and/or W control, individual scalar control (q_0, q_{edge}, Ω_ϕ), and NTM suppression. The third step is the *simulation testing* of the controller by means of codes that emulate the plasma behavior. Testing by means of simulation is necessary in order to ensure the correct implementation of the applicable control algorithm before its experimental testing, helping to foresee possible software and/or

numerical problems, as well as to assess the controller's performance and tune the necessary design parameters involved. The fourth stage is the *experimental testing* of the algorithm, in which the actual capability of the controller to regulate the plasma variables of interest can be shown during the actual operation of the machine.

A key issue in the third stage introduced above is the choice of the simulation code. Tokamak-plasma simulation codes can be classified according to the level of complexity of the plasma-response models that they employ. If the controller is a model-based controller, the first and lowest level of complexity would correspond to codes that employ the same models as those utilized for control synthesis. Although this type of simulation allows, in principle, for a fast check and tuning of the controller, the accuracy of these models, which are normally reduced and/or simplified to enable the controller synthesis, may not be enough to assess the controller's capability to regulate the plasma in real experiments. A second level of complexity would correspond to control-oriented simulation codes with model implementations that are more sophisticated than the models employed for control synthesis, but still allow for fast simulations (within the order of seconds to a few minutes). The computation time of this type of codes is a critical aspect: they must be computationally inexpensive so that efficient, quick control tuning can be carried out without having to wait for hours or days until the simulation finishes. At the same time, this second-level codes should be flexible enough to allow for easy programming of the to-be-tested algorithms, and also be highly configurable to create different simulation conditions. Example of this type of codes are COTSIM, METIS, and RAPTOR [33]. The third and final level of complexity would correspond to codes such as TRANSP [34] or ASTRA [35], with model implementations that try to capture as many relevant aspects of the plasma dynamics as possible, and therefore, in principle, produce much more extensive and accurate results at the cost of taking several hours or even days to finish the simulation of a single plasma discharge.

In this Chapter, the Control Oriented Transport SIMulator (COTSIM) is presented. COTSIM is a simulation code previously developed by the Lehigh University Plasma-Control Group, and expanded thoroughly during this dissertation work. It is a control-oriented, computationally inexpensive, 1D (in space) code that evolves

certain plasma variables such as ψ, T_e, and ω_ϕ. In addition, the evolution of some 0D magnitudes is computed as well, like W or the NTM island width, w. With the models currently available, COTSIM would fall within the second-level category of simulation codes described above. However, due to its modular and highly configurable structure, models with a higher degree of computational complexity could be implemented. The code is developed in MATLAB® mainly due to the availability of its graphical programming environment Simulink®, which allows for a practical implementation and testing of models and controllers. Using COTSIM, feedback simulations can be run within the order of seconds, providing a powerful tool for fast testing and tuning of tokamak-plasma controllers.

3.2 Control Oriented Transport SIMulator (COTSIM)

3.2.1 Dynamics Modeling within COTSIM

The most significative developments in COTSIM carried out during this dissertation work include the implementation and coupling of 1D kinetic models (for T_e and ω_ϕ) and 0D MHD instability models (for w), as well as their coupling with the previously implemented 1D magnetic model (MDE). Other important advancements include the implementation of T_i and n_i evolution modules (in which 0.5D models are currently implemented, that will be substituted by 1D models in the future) and thermal/momentum diffusivity ($\chi_{(\cdot)}$) modules (in which mixed Bohm/Gyro-Bohm models are currently implemented, but different transport models can be included). This version of COTSIM allows predictive simulation of the following 1D variables:

- *Magnetics:* ψ and/or q profiles, by means of the MDE, equation (2.27), using a model as the one introduced in Chapter 2, Section 2.2.1, in which the plasma resistivity, η, is estimated using a Spitzer-like model, whereas the non-inductive current-density source $\langle \vec{j}_{ni} \cdot \vec{B} \rangle / B_{\phi,0}$ is estimated using physics-based control-oriented models.

- *Kinetics:* the T_e profile, by means of the EHTE, equation (2.39), using a model as the one introduced in Chapter 2, Section 2.2.2, and the ω_ϕ profile, by means of the TRE, equation (2.53), using a model as the one introduced in Chapter 2, Section 2.2.3. Mixed Bohm/Gyro-Bohm models are employed for the thermal and momentum diffusivities, χ_e and χ_ϕ, whereas physics-based control-oriented models are employed to estimate the heat and torque sources, Q_e and t_ω.

From table 2.1, it can be seen that T_e affects the ψ dynamics. Such coupling is due to η and $\langle \vec{j}_{ni} \cdot \vec{B} \rangle / B_{\phi,0}$ (as they depend on T_e). In turn, from table 2.3, it can be seen that ψ affects the T_e dynamics as well, due to χ_e and Q_{Ohm} (which depend on q, s, and j_ϕ). The controllable inputs $P_{aux,i}$ directly affect both ψ and T_e. Therefore, it can be seen that there is a tight coupling between the MDE and EHTE models implemented in COTSIM. On the other hand, from table 2.4, it can be seen that the dynamics of ω_ϕ is affected by ψ and T_e through χ_ϕ and t_ω. In this version, ω_ϕ does not affect the ψ and T_e dynamics in COTSIM. To close the simulation model, 0.5D models are employed for n_e, n_i, and T_i as the ones introduced in (2.34). Also, if simulating a burning-plasma tokamak discharge, then the n_D and n_T profiles must be available as inputs to the simulation in order to compute P_α.

In addition, COTSIM simulates the evolution of the following 0D variables:

- *Kinetics:* W, using a model as the one introduced in Chapter 2, Section 2.3.1. It can be appreciated that this model employs the IPB98(y,2) scaling to estimate the confinement time τ_E, whereas simplified models are employed for the volume-average energy sources.

- *MHD instabilities:* NTM island width w, by means of the MRE, equation (2.139), using a model as the one introduced Chapter 2, Section 2.3.7. Because NTMs do not happen simultaneously at different $q = m/n$ surfaces, only one type of NTM is simulated within COTSIM for a single discharge.

In this version, the implementation of the 0D kinetic simulation for W is not coupled with the other simulated variables in COTSIM. On the other hand, from

table 2.11, it can be seen that the w-dynamics is coupled with the ψ-T_e dynamics through η, j_{BS}, w_{marg}, $\Delta\rho_{NTM}$, and j_{EC}^{max}. Also, as it has already been introduced in Sections 1.3 and 2.3.7, it is a well-known experimental fact that the development of NTMs (i.e, w) affects transport. In COTSIM, this coupling is made through χ_e, so that

$$\chi_e = f_{NTM}(w)\chi_e^{anomalous}, \tag{3.1}$$

where $\chi_e^{anomalous}$ is modeled as in (2.42), and f_{NTM} is a function that increases with w in order to characterize the confinement deterioration as NTMs develop.

3.2.2 The Structure of COTSIM

COTSIM is structured in three main files: the setup file, the configuration file, and the simulation file. These files interact with a Graphical User Interface (GUI) and data repositories for inputs, models, controller, outputs, and others. A simplified schematic is showed in Fig. 3.1.

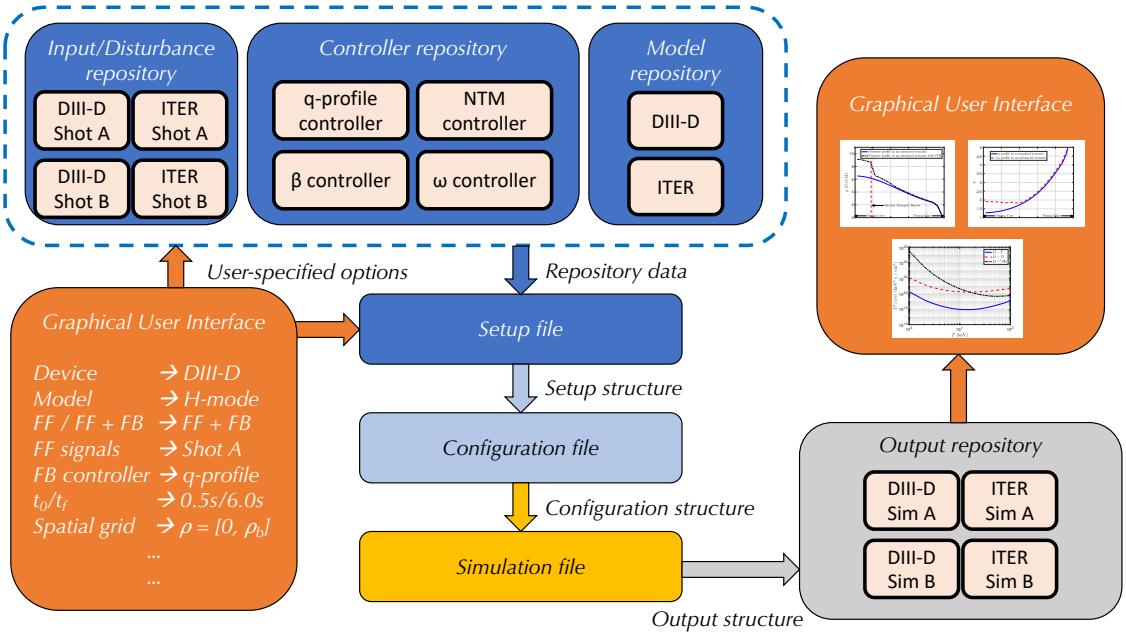

Figure 3.1: COTSIM structure.

The *setup file* is the only file that can be modified by the user, who can specify characteristics of the simulation such as the model and/or tokamak employed, the type of simulation (feedforward, feedforward + feedback), the spatial or time grids, the feedforward inputs to be employed, the type of feedback controller, the initial conditions, disturbances/noise, etc. Such information can be specified using the GUI or directly modifying the setup file. The corresponding data can be either uploaded from external files located in a repository, or introducing the data directly.

The *configuration file* employs the information provided in the setup file to import all the necessary data to run the simulation. For example, it imports the feedforward signals, the model profiles and parameters, and the controller file. It creates a MATLAB® structure that is used as the input to the simulation file.

The *simulation file* is the core of COTSIM, as it evolves the plasma dynamics by using the configuration structure in conjunction with the required functions implemented as part of the source code that simulate the system dynamics (described above in Section 3.2.1). The simulation-file output is stored in an output repository from which the GUI reads the applicable data and allows for visualizing the results.

3.3 Validation of the 1D COTSIM Prediction for DIII-D Shot 147634

In this Section, COTSIM results are presented for a simulation in which the inputs corresponds to the experimental values from DIII-D shot 147634. Relevant machine parameters and model constants for this scenario are $B_{\phi,0} = 1.65$ T, $R_0 = 1.69$ m, $a = 0.6$ m, $Z_{eff} = 1.75$, $\delta_{NBI,i} = 0.5$, and $\delta_{EC} = 1$.

COTSIM results for q, T_e, and ω_ϕ are compared to the corresponding TRANSP data for shot 147634 in Fig. 3.2, Fig. 3.3, and Fig. 3.4, respectively. It can be seen that, although the match is not perfect, the agreement between COTSIM and TRANSP is reasonable during most of the simulation time, and therefore, good enough for control synthesis and simulation testing purposes.

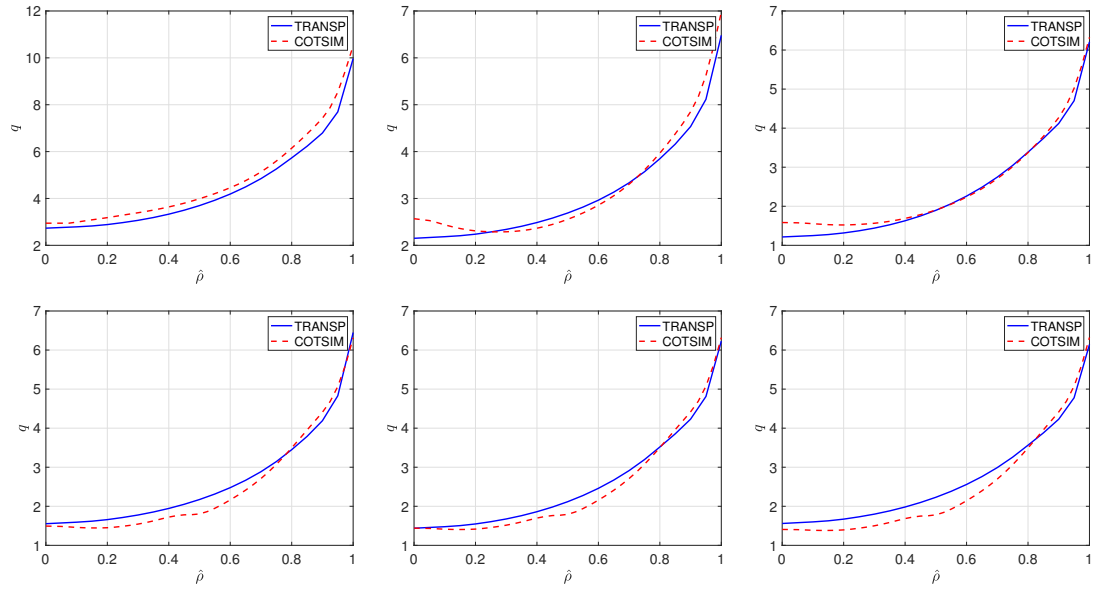

Figure 3.2: COTSIM results for the q profile corresponding to shot 147634, and compared to TRANSP data, at $t = 0.6$, 1.5, 2.5, 3.5, 4.5, and 5.5 seconds.

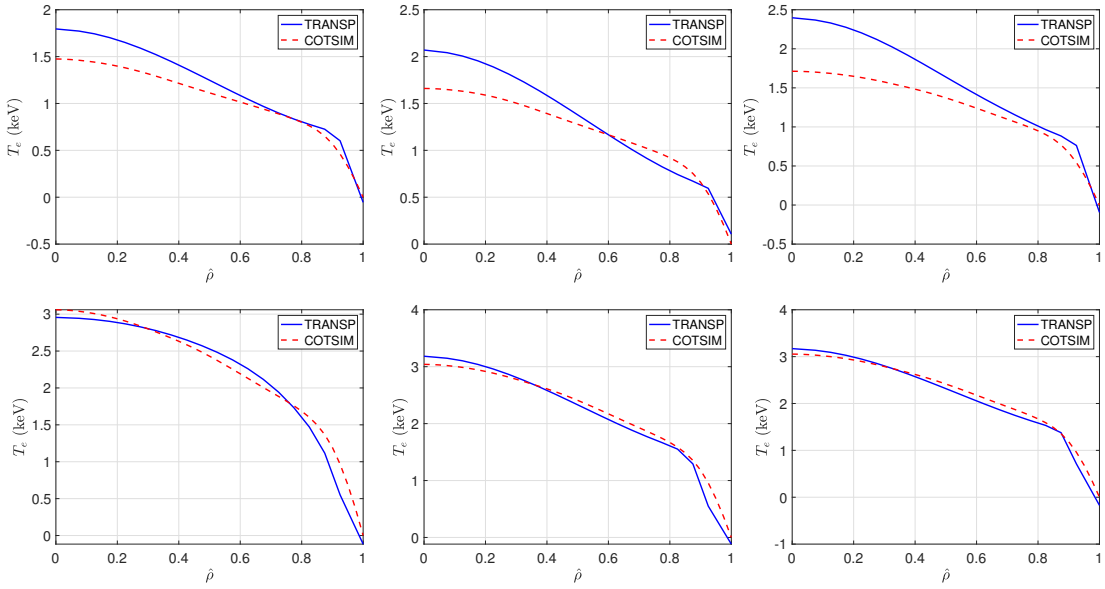

Figure 3.3: COTSIM results for the T_e profile corresponding to shot 147634, and compared to TRANSP data, at $t = 0.6$, 1.5, 2.5, 3.5, 4.5, and 5.5 seconds.

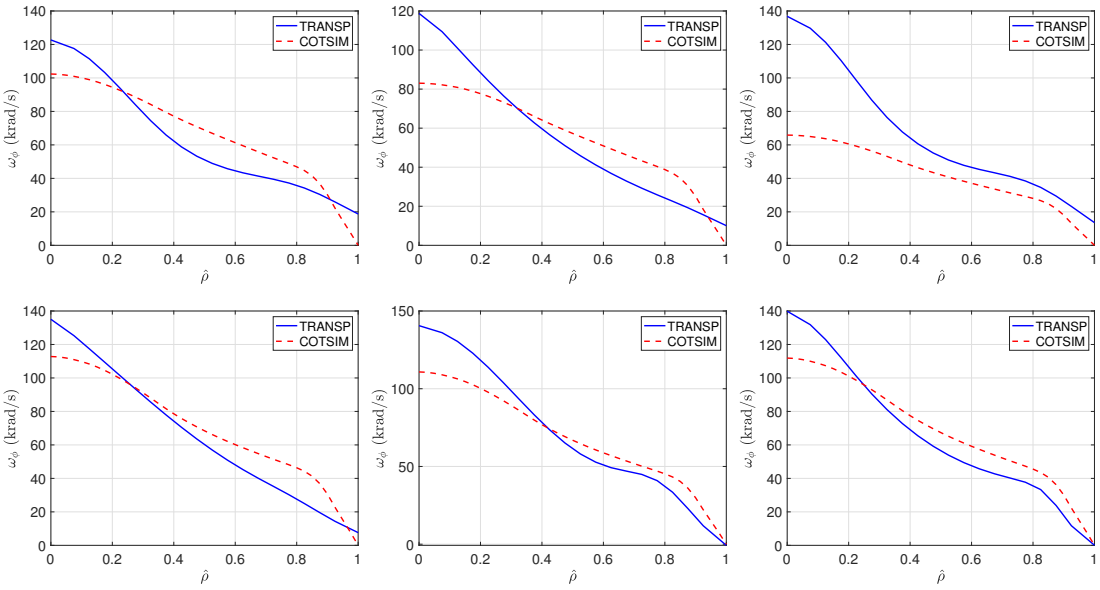

Figure 3.4: COTSIM results for the ω_ϕ profile corresponding to shot 147634, and compared to TRANSP data, at $t = 0.6$, 1.5, 2.5, 3.5, 4.5, and 5.5 seconds.

3.4 Conclusions

COTSIM, a tokamak-plasma simulation code for control applications, has been further developed during the course of this dissertation work. It is specially envisioned to permit fast and easy implementation of tokamak-plasma controllers, as well their simulation testing and tuning. In this version, COTSIM employs physics-based control-oriented models derived from first principles. Moreover, the kinetic, magnetic, and MHD instability aspects of the plasma dynamics have a high coupling degree, giving the implemented model a significant increase in complexity when compared to reduced models that are normally utilized for control synthesis. The model coupling also makes COTSIM a valuable tool for integrated-control testing. Finally, COTSIM can simulate a great variety of control conditions, such as noise, disturbances, or dynamic uncertainties that are unknown to the controllers.

Still, further work is needed within COTSIM to finalize the plasma-models coupling, specially that of the 0D MHD instability model with the 1D kinetics and

magnetics, and that of the 1D rotation with the rest of the models. In addition, future developments will consist in the implementation of 1D models for kinetic variables such as n_e, n_i, or T_i, as well as the inclusion of different transport models for $\chi_{(\cdot)}$.

Chapter 4

Integrated Kinetic Control: the Burn Control Problem

4.1 Introduction and Previous Work

For tokamaks to be commercially competitive, stable operation for long periods of time with a large fusion gain Q will be necessary. Such performance cannot be achieved without accurate control of the ion/electron temperatures and densities, as these variables determine the total amount of fusion power produced, P_{fus}, which can be obtained by integrating equation (1.7) over the plasma volume V_p as

$$P_{fus} = \iiint_{V_p} Q_{fus} dV_p = \Delta E_{kin} \iiint_{V_p} n_D n_T \langle \sigma v \rangle (T) dV_p. \tag{4.1}$$

In addition, and although thermally-stable operating points[1] will most likely be found in future burning-plasma tokamaks such as ITER [36], thermal instabilities may happen that can drive the plasma to a different operating point [37], substantially deteriorating the plasma performance and possibly damaging the tokamak vacuum vessel. The problem of controlling temperature and density in order to control Q and/or P_{fus} while avoiding thermal instabilities is known as *burn control*.

[1] In this context, a thermally-stable operating point is such that small deviations in temperature or energy do not make the system drift away from such operating point.

The burn control problem can be seen as an integrated kinetic-control problem, as the control objective is to control several kinetic variables (temperature and densities of the different plasma species, whose particular values define the so-called *burn condition*) by means of a combination of actuators. Previous work on the burn control area considered different actuators: auxiliary power modulation, fueling rate modulation, and controlled impurity injection. Each of these actuation methods has its own advantages and drawbacks, and these must be considered when designing burn controllers that integrate multiple actuation methods.

Burn controllers that only make use of auxiliary power modulation have been proposed in [38–40]. Such approach is suitable as long as the auxiliary power required to stabilize the burning-plasma system is not too close to either the minimum auxiliary power required for H&CD purposes, P_{aux}^{min}, or the maximum auxiliary power available, P_{aux}^{max}. In the first situation ($P_{aux} \to P_{aux}^{min}$), a reduction in P_{aux} would have a very limited effect on the total power injected, P_{tot}, and positive excursions in the plasma energy may be unavoidable if no backup actuators are used to further decrease the plasma energy. In the second situation ($P_{aux} \to P_{aux}^{max}$), it would not be possible to reject a negative perturbation in the plasma energy, leading to a complete thermal quench. In such case, it may be necessary to either upgrade the machine to install more auxiliary power, i.e., to increase P_{aux}^{max}, or to enhance the tokamak design by modifying the machine parameters (B_T, flat-top I_p, R_0, a, κ, and so on) in order to improve the energy-confinement time, τ_E (see equation (2.65)). An alternative option when $P_{aux} \to P_{aux}^{max}$ would be operating the tokamak at a different scenario with a lower P_{aux} requirement than the original scenario.

Burn controllers based on fueling rate modulation can be found in [41–45]. While this approach allows for working at operating points close to P_{aux}^{min} or P_{aux}^{max}, it also has its own shortcomings. Accurate density control by modulation of the fueling rates is complicated due to the highly nonlinear dynamics of the particle densities, in which effects such as particle recycling, sputtering, and other complex phenomena are present (see Section 2.3.2). By using fueling rate modulation, particles can be injected into the plasma core, but they leave the plasma in a characteristic time within the order of the the particles confinement times. Such times may be too

long or too short for the control requirements of a particular scenario. Another aspect that must be taken into account is that certain tokamak systems cannot be employed when the plasma density is too high (like for example, EC H&CD), limiting the applicability of this control method to either scenarios without EC H&CD actuation or scenarios with low enough density. In addition, plasma density limits exist in tokamaks at which plasma instabilities are triggered. For example, exceeding the Greenwald density limit, $n_{GW} \triangleq I_p/(\pi a^2)$ (I_p has to be given in MA, and n_{GW} is obtained in 10^{20} m^{-3}) may terminate the confined plasma [46]. Lastly, it is difficult to control P_{fus} just by controlling the plasma density, as the plasma temperature may increase or decrease, depending on the scenario, in response to the same variation in the plasma density. Combined modulation of the auxiliary power and fueling rates could overcome some of these limitations, as shown in [47], where the fusion power is successfully regulated using a proportional-integral-derivative (PID) controller in a scenario with high impurity content, whereas a controller that only employs fueling rate modulation fails.

Another actuation method that has been considered is impurity injection. This method has normally been suggested as a backup to auxiliary power modulation [48, 49]. Injecting particles with high atomic number, Z_I, produces an increase in Z_{eff}, and therefore the radiative losses P_{rad} are enhanced (see equation (2.38)), reducing the total power injected into the plasma. This is translated into an effective reduction of the plasma energy, allowing for rejecting positive plasma energy perturbations. The main drawback of this actuation method is that, for large energy perturbations, it may be necessary to inject too large amounts of impurities. Due to their high atomic number, these impurities normally have large confinement times, and they can remain in the plasma for long periods of time. This would produce excessive radiative power losses, which must be counteracted by increasing P_{aux} reducing Q. Damage to the divertor and/or the first wall may also occur as a result of too high P_{rad} values.

An additional actuator that can be considered is coil-current modulation. Recent experiments in the DIII-D tokamak suggested the possibility of using the in-vessel coils for burn control purposes [28]. When electric current is driven through the

in-vessel coils, these generate non-axisymmetric magnetic fields that modify the original magnetic configuration of the tokamak. In [28], the capability of the in-vessel coils to modify τ_E and control the plasma energy is shown in low collisionality, low density discharges. Reductions in τ_E were observed after activation of the in-vessel coils, together with decreases in the pedestal[2] electron density. Changes in the plasma shape and ELM activity were small after application of non-axisymmetric magnetic fields. Other previous experiments in DIII-D [14], TEXT [50] and Tore Supra [51] also showed a degradation in τ_E and/or electron density reduction after application of non-axisymmetric magnetic fields. However, in discharges with higher plasma collisionality and higher density, reductions in the plasma-energy confinement time or pedestal electron density may not be found [14]. The effects of non-axisymmetric fields on confinement degradation are still under research as, in general, these affect the ELM dynamics and the plasma shape. In any case, as low collisionalities will be expected in ITER [52], it seems reasonable to include in-vessel coil-current modulation as a potential actuator for burn control. The main drawback of employing this actuator for burn control is its interference with other control tasks, such as ELM mitigation/suppression and/or toroidal rotation control.

Due to the advantages and disadvantages of each actuation method, an integrated control scheme with as many actuators as possible seems to be the best solution for future burning-plasma tokamaks. Previous work in which auxiliary power modulation, fueling rate modulation, and impurity injection were used to design model-based linear controllers includes [48, 49, 53–55]. These controllers are synthesized by applying approximate linearization techniques to the nonlinear burning-plasma dynamics. However, the complex nonlinear physics involved in the burning-plasma-dynamics modeling, in which some relevant plasma magnitudes cannot be determined without significant uncertainty, suggests that nonlinear, robust controllers will have an improved performance when compared to non-robust controllers obtained by approximate linearization techniques. Other previous work made use of non-model based control techniques, like neural networks [56, 57]. This

[2]The pedestal is the region between the edge transport barrier and the last-closed magnetic-flux surface in H-mode plasmas (see Fig. 1.5).

work based on neural networks does not use linearization techniques. In [37], a nonlinear, model-based controller was presented in which modulation of the auxiliary power and fueling rates are employed in a combined actuation strategy, using impurity injection as a backup actuator. The controller is synthesized using Lyapunov theory. The nonlinear nature of the controller extends its applicability to reject large perturbations and drive the system between different working points during operation. Such performance is not expected in linear controllers. In [37], a zero-dimensional model that assumed an optimal 50:50 D-T mix was used. Other previous work [29] followed a similar modeling and control design approach to the one in [37], but with the significant novelties of incorporating a more complex model with separate evolutions for the deuterium and tritium particle densities [58], as well as recycling effects from particle inventories existing in the tokamak's first wall and scrape-off layer (SOL). Also, fueling rate modulation was used in [29] to control the mix of deuterium and tritium by using the so-called isotopic fuel tailoring approach [59], which controls the α-power, P_α, by reducing the tritium fraction, $\gamma \triangleq n_T/(n_D + n_T)$.

In this Chapter, the work in [60–62], which converged to the final design described in [63], is reported in a summarized fashion. A similar modeling approach to the one in [29] is followed, with separate modeling of the D and T particle evolutions, and inclusion of recycling effects (see Section 2.3.2 of this dissertation). One of the main novelties in this work is the inclusion of a control-oriented model to account for the influence of the in-vessel-coil current on the plasma-energy confinement time based on DIII-D experimental data [14, 28, 52]. This model has been presented in Chapter 2, Section 2.3.1, and takes into account the different impact of the in-vessel coils on τ_E when the plasma collisionality and density vary. A control law for τ_E regulation using the in-vessel coils has been designed [60, 61, 63] based on such model. Another key novelty is the modeling of D-T concentration uncertainties in the pellets employed for fueling [62, 63]. As introduced in Chapter 2, Section 2.3.2, two pellet injectors will be available in the initial phase of ITER. Each of these pellet injectors will be able to produce pellets made of both deuterium (D) and tritium (T), with a concentration of up to 90% T. Although the nominal concentrations

for these lines are 100% D and 10%D - 90%T, respectively, the D-T concentration of those pellets may vary over time in an uncertain manner. These concentration variations, which may be in turn hard or impossible to measure in real time, can decrease the burning plasma performance to unacceptable levels. In order to avoid such situation, an integrated burn-controller is developed which is robust to D-T pellet-concentration variations and combines auxiliary power modulation, in-vessel coil-current modulation, isotopic fueling (controlling γ and n_e), D and T density control, and impurity injection as the actuation methods for burn control.

4.2 Burning Plasma Model

The model employed both for control design and simulation testing is a 0D model in which all the variables can be considered as volume-average quantities. The model can be divided in two parts: the plasma energy balance equation, described in Chapter 2, Section 2.3.1, and the particle balance equations, described in Chapter 2, Section 2.3.2. Some slight modifications and additional assumptions are introduced as described next.

First, instead of W, the thermal energy density, E, is employed, $E \triangleq W/V_p$, where V_p is assumed to be a constant. Also, in (2.64) and (2.68), it is assumed that $\delta_{H_H} = 0$ and $\delta_P = 0$, respectively. Therefore, no uncertainty is assumed within the energy subsystem. The balance equation (2.64) is rewritten as

$$\frac{dE}{dt} = -\frac{E}{\tau_E} + \frac{P_{tot}}{V_p}. \tag{4.2}$$

Second, the contributions to the total power density, P_{tot}/V_p, are modeled is a slightly different way. Power-density versions of the equations (2.35)-(2.38) are employed. Dividing (2.35) by V_p, it is found that

$$\frac{P_{tot}}{V_p} = \frac{P_\alpha + P_{aux} + P_{Ohm} - P_{rad}}{V_p}, \tag{4.3}$$

where $P_\alpha/V_p = \Delta E^\alpha_{kin} n_D n_T \langle \sigma v \rangle$ is the α-heating power density, P_{aux}/V_p is the auxiliary power density, which is considered as a controllable input, $P_{Ohm}/V_p =$

$2.8 \times 10^{-9}(Z_{eff} I_p^2)/(a^4 T^{3/2})$ is the ohmic power density, where Z_{eff} is not considered a model parameter as in the MDE or EHTE models (see tables 2.1 and 2.3), but is computed as

$$Z_{eff} = \frac{4n_\alpha + n_D + n_T + Z_I^2 n_I}{n_e}, \tag{4.4}$$

and $P_{rad}/V_p = (P_{brem} + P_{line} + P_{rec})/V_p$ is the radiative power density, that has three contributions: P_{brem} is the Bremsstrahlung term, P_{line} is the line radiation term, and P_{rec} is the recombination term. Each term is given by $P_{brem}/V_p = 4.8 \times 10^{-37}\big(\sum_j n_j Z_j^2\big) n_e \sqrt{T}$, $P_{line}/V_p = 1.8 \times 10^{-38}\big(\sum_j n_j Z_j^4\big) n_e T^{-1/2}$, and $P_{rec}/V_p = 4.1 \times 10^{-40}\big(\sum_j n_j Z_j^6\big) n_e T^{-3/2}$, where the summation in j is done for all types of ions in the plasma, and T has to be given in keV [64]. For simplicity, all power densities, $P_{(\cdot)}/V_p$, will just be denoted as $P_{(\cdot)}$ for the remaining of this Chapter.

Third, it is assumed that the volume-average temperatures for ions and electrons are the same, $T_i = T_e = T$. Using this assumption and the definition for E, equation (2.74) becomes

$$T = \frac{E}{\frac{3}{2}(n_e + n_i)}. \tag{4.5}$$

Lastly, it has to be taken into account that A_i, which enters the formula for τ_E (2.65), is not considered as a model parameter, but is estimated as $A_i = (2n_D + 3n_T)/(n_D + n_T)$.

The variables employed in this model can be found in Table 4.1.

As a summary, the state-space representation of the burning plasma model is given by

$$\frac{dx}{dt} = f(x, u), \tag{4.6}$$

where $x = [n_\alpha, n_D, n_T, n_I, E]^T$ is the state, $u = [P_{aux}, I_{coil}, S_{D-line}^{inj}, S_{DT-line}^{inj}, S_I^{inj}]^T$ is the input, and $f \in \mathbb{R}^{5\times 1}$ is a nonlinear function whose components are given by (2.72), (2.77), (2.78), (2.85), and (4.2). However, because isotopic fueling controls E by regulating γ, and stability limits exist for n_e, it may be convenient to control $n \triangleq n_i + n_e$ and γ instead of n_D and n_T when using this fueling technique. From the definitions $\gamma \triangleq n_T/(n_D + n_T)$ and $n \triangleq n_i + n_e$, and the balance equations (2.72), (2.77), (2.78), and (2.85), it is possible to write the balance equations for n and γ,

Table 4.1: Model variables.

Symbol	Description	Type of variable
n_α, n_D, n_T, n_I	Particle densities	State
E	Plasma energy density	State
γ	Tritium fraction	Intermediate variable
n_e, n_i, n	Electron, ion, and total density	Intermediate variable
Z_{eff}	Effective atomic number	Intermediate variable
M	Plasma effective mass	Intermediate variable
T	Plasma temperature	Intermediate variable
β_t, β_N	Toroidal and normalized beta	Intermediate variable
S_α	Source of α particles from fusion	Intermediate variable
$\langle\sigma v\rangle$	Reactivity	Intermediate variable
S_D^R, S_T^R	Recycling D and T sources	Intermediate variable
S_D^{inj}, S_T^{inj}	Injected D and T sources	Intermediate variable
S_I^{sp}	Sputtering source	Intermediate variable
P_α, P_{Ohm}, P_{rad}	α, Ohmic, and radiative powers	Intermediate variable
τ_E, τ_α, τ_D, τ_T, τ_I	Confinement times	Intermediate variable
S_{D-line}^{inj}, $S_{DT-line}^{inj}$	D and DT pellet injection rates	Controllable input
S_I^{inj}	Impurity injection rate	Controllable input
I_{coil}	In-vessel coil current	Controllable input
P_{aux}	Auxiliary heating	Controllable input
I_p, R, a, B_T, κ_{95}, V, ν_e	Machine parameters	Machine parameter
a_i, r	Reactivity constants	Model parameter
Z_I	Impurity atomic number	Model parameter
k_α, k_D, k_T, k_I	Confinement time constants	Model parameter
f_{eff}, R_{eff}, f_{ref}, γ_{PFC}, f_I^{sp}	Recycling & sputtering constants	Model parameter
$H_{H,0}$, C_i, λ, δ, $n_{e,0}$, $\nu_{e,0}$	In-vessel coil-model constants	Model parameter
γ_{D-line}^{nom}, $\gamma_{DT-line}^{nom}$	Nominal pellet concentrations	Model parameter
δ_{D-line}, $\delta_{DT-line}$	Uncertain pellet concentrations	Uncertain variables

which are given by

$$\frac{dn}{dt} = 3\left(-\frac{n_\alpha}{\tau_\alpha} + S_\alpha\right) + \left[3n_\alpha + (1+Z_I)\,n_I - n\right]\left(\frac{1-\gamma}{\tau_D} + \frac{\gamma}{\tau_T}\right) + 2f_{eff}\left(S_D^R + S_T^R\right) - 4S_\alpha + 2(S_{D-line}^{inj} + S_{DT-line}^{inj}) + (1+Z_I)\left(-\frac{n_I}{\tau_I} + S_I^{inj} + S_I^{sp}\right), \tag{4.7}$$

$$\frac{d\gamma}{dt} = \gamma(1-\gamma)\left(\frac{1}{\tau_D} - \frac{1}{\tau_T}\right) + \frac{2}{n - 3n_\alpha - (1+Z_I)\,n_I}\left[f_{eff}S_T^R - S_\alpha + \gamma_{D-line}S_{D-line}^{inj} + \gamma_{DT-line}S_{DT-line}^{inj} - \gamma\left(f_{eff}\left(S_D^R + S_T^R\right) - 2S_\alpha + S_{D-line}^{inj} + S_{DT-line}^{inj}\right)\right]. \tag{4.8}$$

Therefore, if the state is chosen as $x = [n_\alpha, n, \gamma, n_I, E]^T$, then the components of f are (2.72), (4.7), (4.8), (2.85), and (4.2).

4.3 Plasma Operating Points and Control Objective

When the state is chosen as $x = [n_\alpha, n_D, n_T, n_I, E]^T$, the equilibrium of the balance equations (2.72), (2.77), (2.78), (2.85), and (4.2) define the operating points of the burning-plasma tokamak. Such equilibrium is given by the solution of

$$0 = -\frac{\bar{n}_\alpha}{\bar{\tau}_\alpha} + \bar{S}_\alpha, \tag{4.9}$$

$$0 = -\frac{\bar{n}_D}{\bar{\tau}_D} + f_{eff}\bar{S}_D^R - \bar{S}_\alpha + (1-\gamma_{D-line}^{nom})\bar{S}_{D-line}^{inj} + (1-\gamma_{DT-line}^{nom})\bar{S}_{DT-line}^{inj}, \tag{4.10}$$

$$0 = -\frac{\bar{n}_T}{\bar{\tau}_T} + f_{eff}\bar{S}_T^R - \bar{S}_\alpha + \gamma_{D-line}^{nom}\bar{S}_{D-line}^{inj} + \gamma_{DT-line}^{nom}\bar{S}_{DT-line}^{inj}, \tag{4.11}$$

$$0 = -\frac{\bar{E}}{\bar{\tau}_E} + \bar{P}_\alpha + \bar{P}_{Ohm} - \bar{P}_{rad} + \bar{P}_{aux}, \tag{4.12}$$

$$0 = -\frac{\bar{n}_I}{\bar{\tau}_I} + \bar{S}_I^{sp}, \tag{4.13}$$

where the bar in all variables indicates equilibrium values. As no controlled impurity injection is desired at equilibrium, $\bar{S}_I^{inj} \equiv 0$ is set. In addition, at any operating point, it is desirable that $\bar{\tau}_E$ is as large as possible, thus $\bar{I}_{coil} \equiv 0$ is imposed. Then, system (4.9)-(4.13) is composed by 5 equations with 8 unknowns (5 state variables + 3 inputs), so 3 variables must be specified in order to find a unique solution. If the state is chosen as $x = [n_\alpha, n, \gamma, n_I, E]^T$, a similar analysis could be done, obtaining the same conclusion: 3 variables must be specified to define an operating point.

The variables fixed in this dissertation to solve for the equilibrium are $T = \bar{T}$, $\gamma = \bar{\gamma}$, and $\beta_N = \bar{\beta}_N$, where β_N is obtained from (2.25) and (2.26) as

$$\beta_N = \frac{\frac{4}{3}\mu_0 E a}{B I_p}[\%] \approx \frac{\frac{4}{3}\mu_0 E a}{B_{\phi,0} I_p}[\%], \tag{4.14}$$

where the approximation $B \approx B_{\phi,0}$ has been taken.

By defining the equilibrium state and input trajectories, $\bar{x} \triangleq [\bar{n}_\alpha, \bar{n}_D, \bar{n}_T, \bar{n}_I, \bar{E}]^T$ and $\bar{u} \triangleq [\bar{P}_{aux}, 0, \bar{S}_{D-line}^{inj}, \bar{S}_{DT-line}^{inj}, 0]^T$, respectively, which fulfill $f(\bar{x}, \bar{u}) = 0$, (4.6) can be rewritten in terms of the state error, $\tilde{x} \triangleq x - \bar{x}$, as

$$\frac{d\tilde{x}}{dt} = f(\bar{x} + \tilde{x}, \bar{u} + \tilde{u}) - f(\bar{x}, \bar{u}) = f(\bar{x} + \tilde{x}, \bar{u} + \tilde{u}), \tag{4.15}$$

so that the error-dynamic equations are given by

$$\frac{d\tilde{n}_\alpha}{dt} = -\frac{\bar{n}_\alpha}{\tau_\alpha} - \frac{\tilde{n}_\alpha}{\tau_\alpha} + S_\alpha, \tag{4.16}$$

$$\frac{d\tilde{n}_D}{dt} = -\frac{\bar{n}_D}{\tau_D} - \frac{\tilde{n}_D}{\tau_D} + f_{eff}S_D^R - S_\alpha + (1-\gamma_{D-line})S_{D-line}^{inj} + (1-\gamma_{DT-line})S_{DT-line}^{inj}, \tag{4.17}$$

$$\frac{d\tilde{n}_T}{dt} = -\frac{\bar{n}_T}{\tau_T} - \frac{\tilde{n}_T}{\tau_T} + f_{eff}S_T^R - S_\alpha + \gamma_{D-line}S_{D-line}^{inj} + \gamma_{DT-line}S_{DT-line}^{inj}, \tag{4.18}$$

$$\frac{d\tilde{n}_I}{dt} = -\frac{\bar{n}_I}{\tau_I} - \frac{\tilde{n}_I}{\tau_I} + S_I^{inj} + S_I^{sp}, \tag{4.19}$$

$$\frac{d\tilde{E}}{dt} = -\frac{\bar{E}}{\tau_E} - \frac{\tilde{E}}{\tau_E} + P_\alpha + P_{Ohm} - P_{rad} + P_{aux}, \tag{4.20}$$

if $\tilde{x} = [\tilde{n}_\alpha, \tilde{n}_D, \tilde{n}_T, \tilde{n}_I, \tilde{E}]^T$. If $\tilde{x} = [\tilde{n}_\alpha, \tilde{n}, \tilde{\gamma}, \tilde{n}_I, \tilde{E}]^T$, then (4.17) and (4.18) are substituted by

$$\begin{aligned}
\frac{d\tilde{n}}{dt} &= 3\left(-\frac{\tilde{n}_\alpha}{\tau_\alpha} - \frac{\bar{n}_\alpha}{\tau_\alpha} + S_\alpha\right) + 2f_{eff}\left(S_D^R + S_T^R\right) - 4S_\alpha \\
&\quad + \left[3\left(\bar{n}_\alpha + \tilde{n}_\alpha\right) + (1+Z_I)(\bar{n}_I + \tilde{n}_I) - (\bar{n} + \tilde{n})\right]\left(\frac{1-(\bar{\gamma}+\tilde{\gamma})}{\tau_D} + \frac{(\bar{\gamma}+\tilde{\gamma})}{\tau_T}\right) \\
&\quad + 2(S_{D-line}^{inj} + S_{DT-line}^{inj}) + (1+Z_I)\left(-\frac{\bar{n}_I}{\tau_I} - \frac{\tilde{n}_I}{\tau_I} + S_I^{inj} + S_I^{sp}\right),
\end{aligned} \tag{4.21}$$

$$\begin{aligned}
\frac{d\tilde{\gamma}}{dt} &= (\bar{\gamma}+\tilde{\gamma})(1-(\bar{\gamma}+\tilde{\gamma}))\left(\frac{1}{\tau_D} - \frac{1}{\tau_T}\right) \\
&\quad + \frac{2}{\bar{n} + \tilde{n} - 3(\bar{n}_\alpha + \tilde{n}_\alpha) - (1+Z_I)\left(\bar{n}_I + \tilde{n}_I\right)}\left\{f_{eff}S_T^R - S_\alpha\right. \\
&\quad + \gamma_{D-line}S_{D-line}^{inj} + \gamma_{DT-line}S_{DT-line}^{inj} \\
&\quad \left. - (\bar{\gamma}+\tilde{\gamma})\left[f_{eff}\left(S_D^R + S_T^R\right) - 2S_\alpha + S_{D-line}^{inj} + S_{DT-line}^{inj}\right]\right\}.
\end{aligned} \tag{4.22}$$

The control objective is to drive the state error $\tilde{x}$ to zero, i.e., to drive the state x to its equilibrium value $\bar{x}$. It is assumed that the state is available for feedback control (either measured by plasma diagnostics or estimated by a state observer). A diagram of the model and its connection with the controller is show in Fig. 4.1.

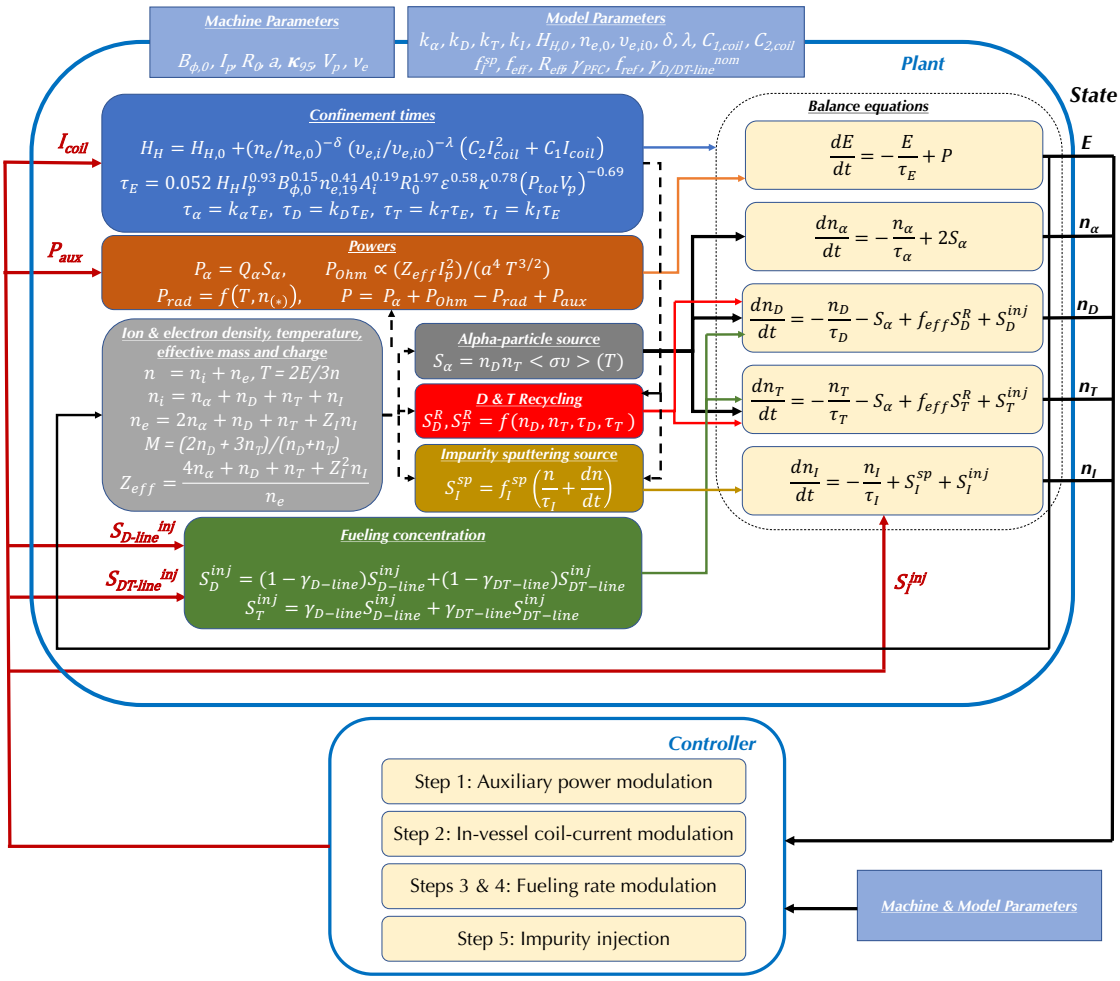

Figure 4.1: Diagram for the burning-plasma plant and its connection with the controller.

4.4 Integrated Burn-Controller Design

4.4.1 Nominal Control Law ($\delta_{D-line} = 0$, $\delta_{DT-line} = 0$)

A controller for the nominal system ($\delta_{D-line} = 0$, $\delta_{DT-line} = 0$) is designed in this Section by using Lyapunov techniques (see Appendix C.1.1 and/or [65]). Each actuation method is employed in accordance with the flowchart shown in Fig. 4.2. First, the nominal controller attempts to regulate $\tilde{E}$ by using auxiliary power modulation. If P_{aux} saturates, then in-vessel coil-current modulation is used. If in-vessel

coil-current modulation saturates as well, then fueling rate modulation is used to attempt to control $\tilde{E}$ and $\tilde{n}$ by isotopic fueling. On the other hand, if auxiliary power modulation and/or in-vessel coil-current modulation suffice to regulate $\tilde{E}$ without saturation, then fueling rate modulation is used to control $\tilde{n}_D$ and $\tilde{n}_T$, except if too high values of n are found. In order to prevent n from reaching excessively high values that may trigger instabilities, isotopic fueling is used when the Greenwald density limit, denoted as n_{GW}, is close to be reached. Finally, in case isotopic fueling is used but $\tilde{E}$ and $\tilde{n}$ regulation cannot be ensured, impurity injection is employed to regulate $\tilde{E}$. Stability proofs are provided to show that if $\tilde{E}$, $\tilde{n}_D$, and $\tilde{n}_T$ (or, alternatively, $\tilde{E}$, γ, and $\tilde{n}$ when isotopic fueling is used) are successfully regulated, then $\tilde{n}_\alpha$ and $\tilde{n}_I$ converge to zero as well.

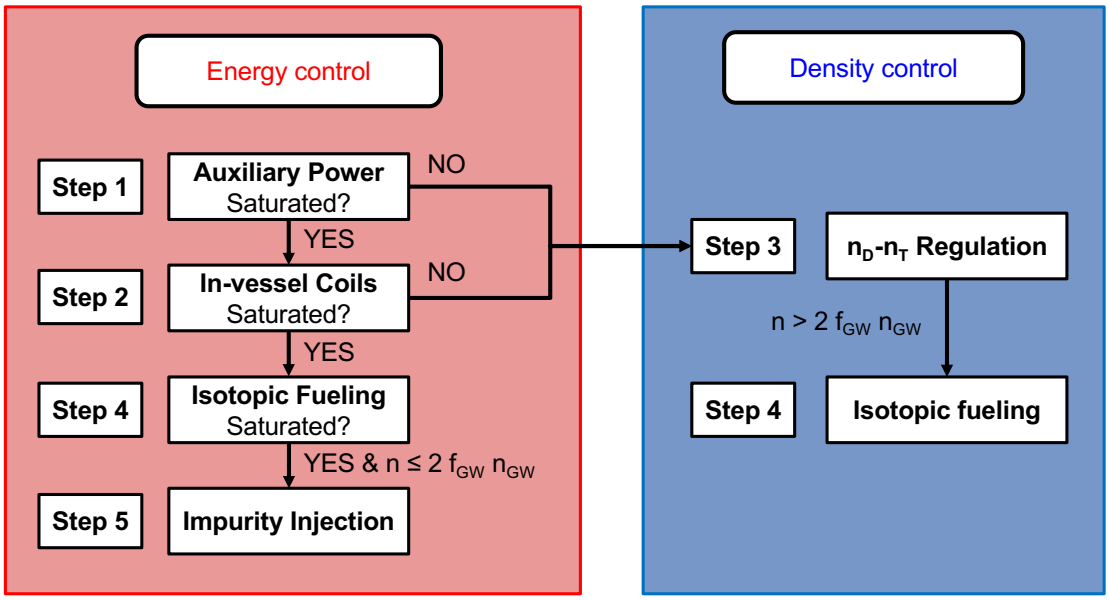

Figure 4.2: Utilization of the different actuation methods within the burn controller. Each actuation method is associated with a particular step of the algorithm.

Step 1: Auxiliary Power Modulation. If P_{aux} is set to

$$P_{aux}^{unsat} = \frac{\bar{E}}{\tau_E} - P_\alpha - P_{Ohm} + P_{rad} - K_P \tilde{E}, \tag{4.23}$$

where $K_P > 0$ is a design parameter, then (4.20) is reduced to $d\tilde{E}/dt = -\left(1/\tau_E + K_P\right)\tilde{E}$, and using a Lyapunov function $V_{\tilde{E}} = \frac{1}{2}\tilde{E}^2 > 0$, yields $\dot{V}_{\tilde{E}} =$

$-\left(1/\tau_E + K_P\right)\tilde{E}^2 < 0$. This ensures global asymptotical stability for $\tilde{E}$ (i.e., $\tilde{E} \to 0$). Equation (4.23) represents the control law for P_{aux}. When $P_{aux} = P_{aux}^{unsat}$, neither in-vessel coil-current modulation (Step 2) nor impurity injection (Step 5) are used, i.e., $I_{coil} \equiv 0$ and $S_I^{inj} \equiv 0$. Moreover, $\tilde{n}_D$ and $\tilde{n}_T$ are controlled by fueling rate modulation (Step 3) as long as $n \leq 2 f_{GW} n_{GW}$, where $n_{GW} = \frac{I_p}{\pi a^2} 10^{20} m^{-3}$ is the Greenwald density limit (I_p in MA), and $0 < f_{GW} \leq 1$ is a design parameter. Otherwise, $\tilde{n}_D$ and $\tilde{n}_T$ are controlled by isotopic fueling (Step 4). However, it may not be possible to set $P_{aux} = P_{aux}^{unsat}$ as requested by (4.23) because there exist saturation limits, P_{aux}^{max} and P_{aux}^{min}. If $P_{aux}^{unsat} > P_{aux}^{max}$, the control algorithm keeps $P_{aux} = P_{aux}^{max}$, but it cannot be ensured that $\tilde{E} \to 0$. The only possible ways to cope with this limitation are either increasing P_{aux}^{max} or improving the machine parameters (I_p, B_T, R, a, κ, etc.) to enhance confinement. On the other hand, if $P_{aux}^{unsat} < P_{aux}^{min}$, the control algorithm keeps $P_{aux} = P_{aux}^{min}$, but it cannot be ensured that $\tilde{E} \to 0$. In that case, the controller is designed to use in-vessel coil-current modulation (Step 2), isotopic fueling (Step 4), and/or impurity injection (Step 5) to regulate $\tilde{E}$, in this order.

Step 2: In-vessel Coil-current Modulation. If τ_E is set to

$$\tau_E^{unsat} = \frac{\bar{E}}{P^{min} + K_{\tau_E}\tilde{E}}, \tag{4.24}$$

where $P^{min} = P_\alpha + P_{Ohm} - P_{rad} + P_{aux}^{min}$, and $K_{\tau_E} > 0$ is a design parameter, then (4.20) is reduced to $d\tilde{E}/dt = -\left(1/\tau_E + K_{\tau_E}\right)\tilde{E}$. Using $V_{\tilde{E}} = \frac{1}{2}\tilde{E}^2 > 0$, then $\dot{V}_{\tilde{E}} = -\left(1/\tau_E + K_{\tau_E}\right)\tilde{E}^2 < 0$, which ensures global asymptotical stability for $\tilde{E}$ (i.e., $\tilde{E} \to 0$). The required value I_{coil}^{unsat} to set τ_E as in (4.24) is obtained from (2.65), (2.68), and (4.24) by solving the following nonlinear equation,

$$C_{2,coil}(I_{coil}^{unsat})^2 + C_{1,coil} I_{coil}^{unsat} = \left(\frac{\tau_E^{unsat}}{K_{IPB98(y,2)}} - H_H^{nom}\right)\left(\frac{n_e}{n_{e,0}}\right)^{-\lambda_{1,coil}}\left(\frac{\nu_{e,i}}{\nu_{e,i0}}\right)^{-\lambda_{2,coil}}, \tag{4.25}$$

where $K_{IPB98(y,2)} = 0.0562 I_p^{0.93} B_{\phi,0}^{0.15} R_0^{1.97} \kappa^{0.78} \epsilon^{0.58} A_i^{0.19} (P^{min})^{-0.69} V^{-0.69} n_{e,19}^{0.41}$. As in Step 1, the right hand side of (4.25) can be computed, providing the

control law for I_{coil}. When $I_{coil} = I_{coil}^{unsat}$, $\tilde{n}_D$ and $\tilde{n}_T$ are controlled by fueling rate modulation (Step 3), except if $n > 2f_{GW}n_{GW}$, when again isotopic fueling (Step 4) is activated. However, it may not be possible to set $I_{coil} = I_{coil}^{unsat}$ because there exist saturation limits, i.e., $0 \leq I_{coil} \leq I_{coil}^{max}$. $I_{coil}^{unsat} \leq 0$ is an indication that indeed there is no need to decrease τ_E. In this case, in-vessel coil-current modulation is not necessary and the controller makes $I_{coil} \equiv 0$. On the other hand, if $I_{coil}^{unsat} > I_{coil}^{max}$, the controller sets $I_{coil} = I_{coil}^{max}$ and uses isotopic fueling (Step 4) and impurity injection (Step 5) to further regulate $\tilde{E}$.

Step 3: Fueling Rate Modulation ($\tilde{n}_D$ and $\tilde{n}_T$ control). Setting S_D^{inj}, S_T^{inj} as

$$S_D^{inj,unsat} = -f_{eff}S_D^R + S_\alpha + \frac{\bar{n}_D}{\tau_D} - K_D\tilde{n}_D, \tag{4.26}$$

$$S_T^{inj,unsat} = -f_{eff}S_T^R + S_\alpha + \frac{\bar{n}_T}{\tau_T} - K_T\tilde{n}_T, \tag{4.27}$$

where $K_D > 0$ and $K_T > 0$ are design parameters, then (4.17) and (4.18) are reduced to $d\tilde{n}_D/dt = -\left(1/\tau_D + K_D\right)\tilde{n}_D$ and $d\tilde{n}_T/dt = -\left(1/\tau_T + K_T\right)\tilde{n}_T$, respectively. Using $V_{\tilde{n}_D} = \frac{1}{2}\tilde{n}_D^2$ and $V_{\tilde{n}_T} = \frac{1}{2}\tilde{n}_T^2$, it is found that $\dot{V}_{\tilde{n}_D} = -\left(1/\tau_D + K_D\right)\tilde{n}_D^2$ and $\dot{V}_{\tilde{n}_T} = -\left(1/\tau_T + K_T\right)\tilde{n}_T^2 < 0$, thus both $\tilde{n}_D$ and $\tilde{n}_T$ evolutions are globally asymptotically stable (i.e., $\tilde{n}_D \to 0$ and $\tilde{n}_T \to 0$). The stabilizing values for S_{D-line}^{inj} and $S_{DT-line}^{inj}$ are obtained by solving (2.81)-(2.84) together with (4.26), (4.27), and are given by

$$\begin{aligned} S_{D-line}^{inj,unsat} \frac{1}{\gamma_{DT-line}^{nom} - \gamma_{D-line}^{nom}} \Bigg(& \gamma_{DT-line}^{nom}(-f_{eff}S_D^R + S_\alpha + \frac{\bar{n}_D}{\tau_D} - K_D\tilde{n}_D) \\ & - \gamma_{D-line}^{nom}(-f_{eff}S_T^R + S_\alpha + \frac{\bar{n}_T}{\tau_T} - K_T\tilde{n}_T) \Bigg), \end{aligned} \tag{4.28}$$

$$\begin{aligned} S_{DT-line}^{inj,unsat} = \frac{1}{\gamma_{DT-line}^{nom} - \gamma_{D-line}^{nom}} \Bigg(& \gamma_{DT-line}^{nom}(-f_{eff}S_D^R + S_\alpha + \frac{\bar{n}_D}{\tau_D} - K_D\tilde{n}_D) \\ & - \gamma_{D-line}^{nom}(-f_{eff}S_T^R + S_\alpha + \frac{\bar{n}_T}{\tau_T} - K_T\tilde{n}_T) + f_{eff}(S_D^R - S_T^R) \\ & + \frac{\bar{n}_T}{\tau_T} - \frac{\bar{n}_D}{\tau_D} + K_D\tilde{n}_D - K_T\tilde{n}_T \Bigg). \end{aligned} \tag{4.29}$$

Equations (4.28) and (4.29) are the nominal control laws for $S_{DT-line}^{inj}$ and S_{D-line}^{inj}, respectively, when Step 3 is activated. Nonetheless, as before, it

may not be possible to set $S^{inj}_{D-line} = S^{inj,unsat}_{D-line}$ and/or $S^{inj}_{DT-line} = S^{inj,unsat}_{DT-line}$ because there exist physical saturation limits, that are denoted by $S^{inj,max}_{D-line}$, $S^{inj,min}_{D-line}$, $S^{inj,max}_{DT-line}$, and $S^{inj,min}_{DT-line}$. If $S^{inj}_{D-line}/S^{inj}_{DT-line}$ is larger or smaller than its applicable saturation limits, the controller keeps $S^{inj}_{D-line}/S^{inj}_{DT-line}$ at the saturation limit that has been violated, and no further steps in the control algorithm are activated. The asymptotic stability of $\tilde{n}_D$ and/or $\tilde{n}_T$ cannot be ensured unless the controller recovers from the saturation limits. This is not an inherent problem of the control algorithm but just a physical limitation in the actuation capability of the tokamak.

Finally, it can be shown that, if $\tilde{E}$, $\tilde{n}_D$, and $\tilde{n}_T$ are driven to zero, i.e. if $E = \bar{E}$, $n_D = \bar{n}_D$, and $n_T = \bar{n}_T$, then $\tilde{n}_\alpha$ and $\tilde{n}_I$ are also driven to zero as $t \to \infty$ provided that $S^{inj}_I \equiv 0$. First, by defining $\hat{n}_I \triangleq n_I - f^{sp}_I n$, (2.85) can be rewritten as

$$\frac{d\hat{n}_I}{dt} + f^{sp}_I \frac{dn}{dt} = -\frac{\hat{n}_I + f^{sp}_I n}{\tau_I} + S^{sp}_I, \tag{4.30}$$

and using (2.86), it is found that

$$\frac{d\hat{n}_I}{dt} = -\frac{\hat{n}_I}{\tau_I}. \tag{4.31}$$

Thus, $\hat{n}_I$ goes to zero as $t \to \infty$ because $\tau_I > 0$, which implies that

$$\lim_{t\to\infty} n_I = f^{sp}_I \lim_{t\to\infty} n, \tag{4.32}$$

regardless of any condition other than $S^{inj}_I \equiv 0$. It can be noted from (4.12), i.e. $0 = -\frac{\bar{n}_I}{\bar{\tau}_I} + \bar{S}^{sp}_I$, and (2.86), i.e. $\bar{S}^{sp}_I = \frac{f^{sp}_I \bar{n}}{\bar{\tau}_I}$, that $\bar{n}_I = f^{sp}_I \bar{n}$, which is consistent with (4.32). Using the definition of n and (4.32), it is found that

$$\lim_{t\to\infty} n = \frac{3\lim_{t\to\infty} n_\alpha + 2\bar{n}_D + 2\bar{n}_T}{1 - f^{sp}_I(1 + Z_I)}. \tag{4.33}$$

So, if $\lim_{t\to\infty} n_\alpha = \bar{n}_\alpha$, n tends to its equilibrium value as well, and so does n_I. Then, it is necessary to inspect the terms on the right-hand side of (4.16). The first term, $-(\bar{n}_\alpha + \tilde{n}_\alpha)/\tau_\alpha = -n_\alpha/\tau_\alpha$, decreases with an increase in n_α, and vice versa, it increases with a decrease in n_α. The second term, S_α, can

be written as $S_\alpha = \bar{n}_D \bar{n}_T \langle \sigma v \rangle_{DT}$. To see the dependence of S_α with n_α, it is necessary to analyze $\langle \sigma v \rangle_{DT}$, which is a positive, increasing function of T for the range of temperatures in which tokamaks operate ([3], see Fig. 1.2). Using (4.5), it is found that

$$T = \frac{E}{\frac{3}{2}n} = \frac{\bar{E}}{\frac{3}{2}(3n_\alpha + 2\bar{n}_D + 2\bar{n}_T)} \left(1 - f_I^{sp}(1 + Z_I) \right), \tag{4.34}$$

where the definition of n has been employed, and $E = \bar{E}$, $n_D = \bar{n}_D$, $n_T = \bar{n}_T$, and $n_I = f_I^{sp} n$ due to $S_I^{inj} \equiv 0$. Therefore, increases in n_α imply decreases in T, which imply decreases in $\langle \sigma v \rangle_{DT}$ and in S_α. On the other hand, decreases in n_α imply increases in T, which imply increases in $\langle \sigma v \rangle_{DT}$ and in S_α. Thus, due to the particular dependence of the right-hand-side terms of equation (4.16) with n_α, it is possible to write that

$$\frac{d\tilde{n}_\alpha}{dt} \propto -\tilde{n}_\alpha, \tag{4.35}$$

and it can be concluded that the $\tilde{n}_\alpha \to 0$ as $t \to \infty$. Then, n_α tends to $\bar{n}_\alpha$, n tends to $\bar{n}$, and n_I tends to $\bar{n}_I$, and the control objective is fully achieved.

Step 4: Fueling Rate Modulation ($\hat{\gamma}$ and $\tilde{n}$ Control). By using isotopic fueling, the controller attempts to drive $\gamma \to \gamma^*$ to make $\tilde{E}$ asymptotically stable by exploiting the dependence of S_α on γ, which can be obtained from (2.73) and the definition of γ as $S_\alpha = \gamma(1-\gamma)(n_D + n_T)^2 \langle \sigma v \rangle_{DT}$. The γ^* value is obtained by solving the nonlinear equation

$$\gamma^*(1 - \gamma^*) = \frac{\frac{\bar{E}}{\tau_E} - P_{Ohm} - P_{aux} + P_{rad} - K_{\gamma,1}\tilde{E}}{Q_\alpha (n_D + n_T)^2 \langle \sigma v \rangle_{DT}}, \tag{4.36}$$

where $K_{\gamma,1} > 0$ is a design parameter. In this case, (4.20) reduces to $d\tilde{E}/dt = -\left(1/\tau_E + K_{\gamma,1}\right)\tilde{E}$, and using the same Lyapunov function $V_{\tilde{E}} = \frac{1}{2}\tilde{E}^2 > 0$ as before, global asymptotical stability of $\tilde{E}$ is ensured because

$$\dot{V}_{\tilde{E}} = -\left(1/\tau_E + K_{\gamma,1}\right)\tilde{E}^2 < 0. \tag{4.37}$$

For stability analysis, it is convenient to define $\hat{\gamma} \triangleq \gamma - \gamma^*$ since making $\hat{\gamma} \to 0$ is equivalent to making $\gamma \to \gamma^*$. Taking S_T^{inj} as

$$S_T^{inj,unsat} = \frac{\gamma[f_{eff}(S_D^R + S_T^R) - 2S_\alpha + S_D^{inj,unsat}] + S_\alpha - f_{eff}S_T^R + v}{1-\gamma}, \quad (4.38)$$

and using the definition for $\hat{\gamma}$ and (4.8), it is possible to write

$$\frac{d\hat{\gamma}}{dt} = \gamma(1-\gamma)\left(\frac{1}{\tau_D} - \frac{1}{\tau_T}\right) + \frac{v}{n_D + n_T} + \frac{d\gamma^*}{dt}. \quad (4.39)$$

By taking

$$v = -(n_D + n_T)\left[\gamma(1-\gamma)\frac{1}{\tau_D} + \frac{\gamma^2 - \gamma^*}{\tau_T} + K_{\gamma,2}\hat{\gamma} + \frac{d\gamma^*}{dt}\right], \quad (4.40)$$

where $K_{\gamma,2} > 0$ is a design parameter, it is found that

$$\frac{d\hat{\gamma}}{dt} = -\left(1/\tau_T + K_{\gamma,2}\right)\hat{\gamma}. \quad (4.41)$$

Then, using $V_{\hat{\gamma}} = \frac{1}{2}\hat{\gamma}^2$, it is found that $\dot{V}_{\hat{\gamma}} = -\left(1/\tau_T + K_{\gamma,2}\right)\hat{\gamma}^2 < 0$. Thus, global asymptotical stability of $\hat{\gamma}$ is ensured. Taking S_D^{inj} as

$$S_D^{inj,unsat} = \frac{n_D}{\tau_D} + \frac{n_T}{\tau_T} - f_{eff}(S_D^R + S_T^R) + 2S_\alpha - S_T^{inj,unsat} + w, \quad (4.42)$$

and using (4.7), it is possible to write

$$\frac{d\tilde{n}}{dt} = 3\left(-\frac{n_\alpha}{\tau_\alpha} + S_\alpha\right) + (1 + Z_I)\left(-\frac{n_I}{\tau_I} + S_I^{inj} + S_I^{sp}\right) + 2w, \quad (4.43)$$

where $\tilde{n} \triangleq n - \bar{n}$. By taking

$$w = -\frac{1}{2}\left[3\left(-\frac{n_\alpha}{\tau_\alpha} + S_\alpha\right) + (1 + Z_I)\left(-\frac{n_I}{\tau_I} + S_I^{inj} + S_I^{sp}\right) + K_n\tilde{n}\right], \quad (4.44)$$

where $K_n > 0$ is a design parameter, it is found that $d\tilde{n}/dt = -K_n\tilde{n}$. Using $V_{\tilde{n}} = \frac{1}{2}\tilde{n}^2$ ensures global asymptotical stability of $\tilde{n}$ because $\dot{V}_{\tilde{n}} = -K_n\tilde{n}^2 < 0$. Solving (4.38) and (4.42) for $S_D^{inj,unsat}$ and $S_T^{inj,unsat}$ yields

$$S_D^{inj,unsat} = (1-\gamma)\left(\frac{n_D}{\tau_D} + \frac{n_T}{\tau_T} + w\right) + S_\alpha - f_{eff}S_D^R - v, \quad (4.45)$$

$$S_T^{inj,unsat} = \gamma\left(\frac{n_D}{\tau_D}+\frac{n_T}{\tau_T}+w\right)+S_\alpha-f_{eff}S_T^R+v. \tag{4.46}$$

The stabilizing values for S_{D-line}^{inj} and $S_{DT-line}^{inj}$ are obtained from solving (2.81)-(2.84) together with (4.45)-(4.46), and are given by

$$\begin{aligned} S_{D-line}^{inj,unsat} = \frac{1}{\gamma_{DT-line}^{nom}-\gamma_{D-line}^{nom}}\Bigg[&\gamma_{DT-line}^{nom}(1-\gamma)\left(\frac{n_D}{\tau_D}+\frac{n_T}{\tau_T}+w\right)\\ &-\gamma_{D-line}^{nom}\gamma\left(\frac{n_D}{\tau_D}+\frac{n_T}{\tau_T}+w\right)+(\gamma_{DT-line}^{nom}-\gamma_{D-line}^{nom})\left(S_\alpha-f_{eff}(S_D^R+S_T^R)\right)\\ &-v(\gamma_{DT-line}^{nom}+\gamma_{D-line}^{nom})\Bigg], \end{aligned} \tag{4.47}$$

$$\begin{aligned} S_{DT-line}^{inj,unsat} = \frac{1}{\gamma_{DT-line}^{nom}-\gamma_{D-line}^{nom}}\Bigg[&(\gamma_{DT-line}^{nom}-1)(1-\gamma)\left(\frac{n_D}{\tau_D}+\frac{n_T}{\tau_T}+w\right)\\ &+(\gamma_{DT-line}^{nom}-1)(S_\alpha-f_{eff}S_D^R-v)+(1-\gamma_{D-line}^{nom})\gamma\left(\frac{n_D}{\tau_D}+\frac{n_T}{\tau_T}+w\right)\\ &+(1-\gamma_{D-line}^{nom})(S_\alpha-f_{eff}S_T^R+v)\Bigg]. \end{aligned} \tag{4.48}$$

Equations (4.47) and (4.48) are the nominal control laws for $S_{DT-line}^{inj}$ and S_{D-line}^{inj}, respectively, when Step 4 is activated. If the saturation limits $S_{D-line}^{inj,max}$, $S_{D-line}^{inj,min}$, $S_{DT-line}^{inj,max}$, and $S_{DT-line}^{inj,min}$ are reached, then the controller keeps S_{D-line}^{inj} / $S_{DT-line}^{inj}$ at the saturation limit that has been violated (i.e., same procedure as in Step 3). The stability of the $\tilde{E}$, $\tilde{n}$, and/or $\hat{\gamma}$ cannot be ensured in this case until the controller recovers from the saturation limits. Again, this is not a problem of the control algorithm but just a natural limitation imposed by the available actuation capability. However, in this case, impurity injection is activated for $\tilde{E}$ regulation (Step 5), as long as $n \leq 2f_{GW}n_{GW}$. If $n > 2f_{GW}n_{GW}$, impurity injection is never used, as it always increases n.

Finally, by following arguments similar to those used for Step 3, it can be shown that, if $\tilde{E}$, $\tilde{n}$, and $\tilde{\gamma}$ are driven to zero, i.e. if $E=\bar{E}$, $n=\bar{n}$, and $\gamma=\bar{\gamma}$, then $\tilde{n}_\alpha$ and $\tilde{n}_I$ are also driven to zero as $t\to\infty$ provided that $S_I^{inj}\equiv 0$, and the control objective is fully achieved.

Step 5: Impurity Injection. By using impurity injection, the controller attempts to drive $n_I \to n_I^*$ such that the $\tilde{E}$ evolution is asymptotically stable by exploiting the dependence of P_{rad} on n_I. This n_I^* value is obtained by solving the nonlinear equation

$$P_{rad}(n_I^*) = -\frac{\bar{E}}{\tau_E^{min}} + P_\alpha^{min} + P_{Ohm} + P_{aux}^{min} + K_{n_I}\tilde{E}, \tag{4.49}$$

where $K_{n_I} > 0$ is a design parameter, and P_α^{min} is the α heating achieved by isotopic fueling. Note that $P_{aux} = P_{aux}^{min}$, $\tau_E = \tau_E^{min}$, and $P_\alpha = P_\alpha^{min}$, which means that impurity injection is used only when the combination of auxiliary power modulation (Step 1), in-vessel coil-current modulation (Step 2) and isotopic fueling (Step 3) is not enough to asymptotically stabilize $\tilde{E}$. In this case, (4.20) reduces to $d\tilde{E}/dt = -\left(1/\tau_E^{min} + K_{n_I}\right)\tilde{E}$. By using $V_{\tilde{E}} = \frac{1}{2}\tilde{E}^2 > 0$ as before, global asymptotical stability of $\tilde{E}$ is ensured because $\dot{V}_{\tilde{E}} = -\left(1/\tau_E^{min} + K_{n_I}\right)\tilde{E}^2 < 0$. It is convenient to define $\hat{n}_I \triangleq n_I - n_I^*$ for stability analysis since making $\hat{n}_I \to 0$ is equivalent to making $n_I \to n_I^*$. By using both this definition and (2.85), and by taking S_I^{inj} equal to

$$S_I^{inj,unsat} = \frac{n_I^*}{\tau_I} - S_I^{sp} - K_I\hat{n}_I + \frac{dn_I^*}{dt}, \tag{4.50}$$

where $K_I > 0$ is a design parameter, it is possible to write

$$\frac{d\hat{n}_I}{dt} = -\left(1/\tau_I + K_I\right)\hat{n}_I. \tag{4.51}$$

Taking $V_{\hat{n}_I} = \frac{1}{2}\hat{n}_I^2$, it is found that $\dot{V}_{\hat{n}_I} = -(1/\tau_I + K_I)\hat{n}_I^2 < 0$, which implies $\hat{n}_I \to 0$. Therefore, it can be ensured that $n_I \to n_I^*$ and $\tilde{E} \to 0$. Equation (4.50) is the control law for S_I^{inj}. Because of the upper saturation limit that exists for S_I^{inj}, denoted as $S_I^{inj,max}$ (note that $S_I^{inj,min} \equiv 0$), $\tilde{E} \to 0$ cannot be guaranteed until after the controller recovers from saturation.

4.4.2 Robust Control Law ($\delta_{D-line} \neq 0$, $\delta_{DT-line} \neq 0$)

The control laws obtained for the nominal system are robustified in this Section for the uncertain system ($\delta_{D-line} \neq 0$, $\delta_{DT-line} \neq 0$) by following a Lyapunov redesign approach (see Appendix C.2.1 and/or [65]). The robust controller uses the same order and logic followed by the nominal controller for the activation of the actuators. Because the uncertainties are only found in the n_D-n_T balance equations, or alternatively, in the n-γ balance equations, the control laws for auxiliary power modulation, in-vessel coil-current modulation, and controlled impurity injection do not need to be modified. On the other hand, the control laws for S^{inj}_{D-line} and $S^{inj}_{DT-line}$, either controlling $\tilde{n}_D$ and $\tilde{n}_T$ (4.28)-(4.29), or controlling $\tilde{E}$ (through $\hat{\gamma}$) and $\tilde{n}$ (4.47)-(4.48), need to be modified to make them robust against the model uncertainties. Then, only Steps 3 and 4 need to be considered for redesign.

Step 3: Robust Fueling Rate Modulation ($\tilde{n}_D$ and $\tilde{n}_T$ Control). Equations (4.17) and (4.18) can be written in matrix form as

$$\begin{bmatrix} \dot{\tilde{n}}_D \\ \dot{\tilde{n}}_T \end{bmatrix} = f + G\big[u + \delta\big], \tag{4.52}$$

where

$$f = \begin{bmatrix} -\frac{\bar{n}_D}{\tau_D} - \frac{\tilde{n}_D}{\tau_D} + S^R_D - S_\alpha \\ -\frac{\bar{n}_D}{\tau_T} - \frac{\tilde{n}_T}{\tau_T} + S^R_T - S_\alpha \end{bmatrix}, \tag{4.53}$$

$$G = \begin{bmatrix} 1-\gamma^{nom}_{DT-line} & 1-\gamma^{nom}_{D-line} \\ \gamma^{nom}_{DT-line} & \gamma^{nom}_{D-line} \end{bmatrix}, \tag{4.54}$$

$$u = \begin{bmatrix} S^{inj}_{DT-line} \\ S^{inj}_{D-line} \end{bmatrix}, \tag{4.55}$$

$$\delta = G^{-1} \begin{bmatrix} -(\delta_{DT-line} S^{inj}_{DT-line} + \delta_{D-line} S^{inj}_{D-line}) \\ \delta_{DT-line} S^{inj}_{DT-line} + \delta_{D-line} S^{inj}_{D-line} \end{bmatrix}. \tag{4.56}$$

The nominal control law for $\tilde{n}_D$-$\tilde{n}_T$, (4.28)-(4.29), is denoted by ψ_n. For the nominal $\tilde{n}_D$-$\tilde{n}_T$ subsystem, given by (4.52) with $\delta = 0$, it has been shown

that $u = \psi_n$ is a stabilizing control law, i.e. the Lyapunov function $V_{\tilde{n}_{DT}} = V_{\tilde{n}_D} + V_{\tilde{n}_T} = \frac{1}{2}\tilde{n}_D^2 + \frac{1}{2}\tilde{n}_T^2$ yields $\dot{V}_{\tilde{n}_{DT}} = -\big(\frac{1}{\tau_D} + K_D\big)\tilde{n}_D^2 - \big(\frac{1}{\tau_T} + K_T\big)\tilde{n}_T^2$, which is strictly negative for all $\tilde{n}_D, \tilde{n}_T \neq 0$. A control law

$$u = \psi_n + v_{rob} \tag{4.57}$$

is now sought for the uncertain $\tilde{n}_D$-$\tilde{n}_T$ subsystem, given by (4.52) with $\delta \neq 0$, where v_{rob} is the part to be designed for robustness. Using a Lyapunov-redesign approach, v_{rob} is taken as

$$v_{rob} = \begin{cases} -\frac{\kappa_0 \|\psi_n\|_2}{1-\kappa_0} \frac{w_{rob}}{\|w_{rob}\|_2} \text{ if } \kappa_0 \|\psi_n\|_2 \|w_{rob}\|_2 \geq \epsilon, \\ \\ -\left(\frac{\kappa_0 \|\psi_n\|_2}{1-\kappa_0}\right)^2 \frac{w_{rob}}{\epsilon} \text{ if } \kappa_0 \|\psi_n\|_2 \|w_{rob}\|_2 < \epsilon, \end{cases} \tag{4.58}$$

where ϵ is a small positive design parameter that is needed to prevent a potential singularity of the control law at $\tilde{n}_D = \tilde{n}_T \equiv 0$, and w_{rob} is given by $w_{rob}^T = [\frac{\partial V_{\tilde{n}_{DT}}}{\partial \tilde{n}_D}, \frac{\partial V_{\tilde{n}_{DT}}}{\partial \tilde{n}_T}]G$, where $\kappa_0 = \sqrt{2(\delta_{DT-line}^{max})^2 + (\delta_{D-line}^{max})^2}/|\gamma_{DT-line}^{nom} - \gamma_{D-line}^{nom}|$ is a positive constant that is obtained by finding a bound to δ of the form $\|\delta(\psi_n + v_{rob})\|_2 \leq \kappa_0(\|\psi_n\|_2 + \|v_{rob}\|_2)$. This bound can be relatively easily obtained by using the triangular and the Cauchy-Schwarz inequalities (see Appendix D.1). The modified control laws (4.57)-(4.58) do not assure that $\tilde{n}_D \to 0$ and $\tilde{n}_T \to 0$ in time, but they guarantee that $|\tilde{n}_D|$ and $|\tilde{n}_T|$ are bounded by class $\mathcal{K}$ functions[3] of ϵ. Therefore, it is critical to carefully choose ϵ so that it is small enough. Finally, using similar arguments to those used for the nominal system, it can be shown that if $\tilde{E}$ is driven to zero, $|\tilde{n}_\alpha|$ and $|\tilde{n}_I|$ are also bounded by class $\mathcal{K}$ functions of ϵ provided that $S_I^{inj} \equiv 0$. The proof is included in Appendix D.2.

Step 4: Robust Fueling Rate Modulation ($\hat{\gamma}$ and $\tilde{n}$ Control). Equations (4.21) and (4.22) can be written in matrix form as

$$\begin{bmatrix} \dot{\tilde{n}} \\ \dot{\hat{\gamma}} \end{bmatrix} = f^\star + G^\star\big[u + \delta^\star\big], \tag{4.59}$$

[3] A continuous function $f(x)$ is said to be a class $\mathcal{K}$ function if: (1) it is a strictly increasing function of x, and (2) $f(0) = 0$.

where

$$f^\star = \begin{bmatrix} f_1^\star \\ f_2^\star \end{bmatrix}, \tag{4.60}$$

$$f_1^\star = 3\left[-\frac{n_\alpha}{\tau_\alpha} + S_\alpha\right] + \left(3n_\alpha + (1+Z_I)\,n_I - n\right)\left(\frac{1-\gamma}{\tau_D} + \frac{\gamma}{\tau_T}\right) + 2f_{eff}\left(S_D^R + S_T^R\right) - 4S_\alpha + (1+Z_I)\left[-\frac{n_I}{\tau_I} + S_I^{sp}\right], \tag{4.61}$$

$$f_2^\star = \gamma(1-\gamma)\left(\frac{1}{\tau_D} - \frac{1}{\tau_T}\right) + \frac{2}{n - 3n_\alpha - (1+Z_I)\,n_I}\left\{f_{eff}S_T^R - S_\alpha - \gamma\left[f_{eff}\left(S_D^R + S_T^R\right) - 2S_\alpha\right]\right\}, \tag{4.62}$$

$$G^\star = \begin{bmatrix} 2 & 2 \\ 2\frac{\gamma_{DT-line}^{nom} - \gamma}{n-3n_\alpha-(1+Z_I)n_I} & 2\frac{\gamma_{D-line}^{nom} - \gamma}{n-3n_\alpha-(1+Z_I)n_I} \end{bmatrix}, \tag{4.63}$$

$$\delta^\star = (G^\star)^{-1}\begin{bmatrix} 0 \\ 2\frac{\delta_{DT-line}S_{DT-line}^{inj}}{n-3n_\alpha-(1+Z_I)n_I} + 2\frac{\delta_{D-line}S_{D-line}^{inj}}{n-3n_\alpha-(1+Z_I)n_I} \end{bmatrix}. \tag{4.64}$$

The nominal control law for $\hat{\gamma}$-$\tilde{n}$ (isotopic fueling), (4.47)-(4.48), is denoted by $\psi_n^\star$. For the nominal $\tilde{n}_D$-$\hat{\gamma}$ subsystem, given by (4.59) with $\delta = 0$, it has been shown that $u = \psi_n^\star$ is a stabilizing control law, i.e. the Lyapunov function $V_{\tilde{n},\hat{\gamma}} = V_{\tilde{n}} + V_{\hat{\gamma}} = \frac{1}{2}\tilde{n}^2 + \frac{1}{2}\hat{\gamma}^2$ yields $\dot{V}_{\tilde{n},\hat{\gamma}} = -K_n\tilde{n}_D^2 - \left(\frac{1}{\tau_T} + K_{\gamma,2}\right)\hat{\gamma}^2$, which is strictly negative for all $\tilde{n}_D, \hat{\gamma} \neq 0$. A control law

$$u = \psi_n^\star + v_{rob}^\star, \tag{4.65}$$

is now sought for the uncertain $\tilde{n}_D$-$\hat{\gamma}$ subsystem, given by (4.59) with $\delta \neq 0$, where $v_{rob}^\star$ is the part to be designed for robustness. Using a Lyapunov-redesign approach, $v_{rob}^\star$ is taken as

$$v_{rob}^\star = \begin{cases} -\frac{\kappa_0^\star \|\psi_n^\star\|_2}{1-\kappa_0^\star}\frac{w_{rob}^\star}{\left\|w_{rob}^\star\right\|_2} \text{ if } \kappa_0^\star \left\|\psi_n^\star\right\|_2 \left\|w_{rob}^\star\right\|_2 \geq \epsilon^\star, \\ \\ -\left(\frac{\kappa_0^\star \|\psi_n^\star\|_2}{1-\kappa_0^\star}\right)^2 \frac{w_{rob}^\star}{\epsilon^\star} \text{ if } \kappa_0^\star \left\|\psi_n^\star\right\|_2 \left\|w_{rob}^\star\right\|_2 < \epsilon^\star, \end{cases} \tag{4.66}$$

where $\epsilon^\star$ is a small positive design parameter that is needed to prevent a potential singularity of the control law at $\tilde{n} = \hat{\gamma} \equiv 0$, and $w_{rob}^\star$ is given by

$(w^\star_{rob})^T = [\frac{\partial V_{\tilde{n},\hat{\gamma}}}{\partial \tilde{n}}, \frac{\partial V_{\tilde{n},\hat{\gamma}}}{\partial \hat{\gamma}}]G^\star$, where $\kappa^\star_0 = \kappa_0$ is a constant that is obtained by finding a bound to $\delta^\star$ of the form $\|\delta^\star(\psi^\star_n + v^\star_{rob})\|_2 \leq \kappa^\star_0(\|\psi^\star_n\|_2 + \|v^\star_{rob}\|_2)$. As in the case for Step 3, this bound can be relatively easily obtained by using the triangular and the Cauchy-Schwarz inequalities (see Appendix D.1). The modified control laws (4.65)-(4.66) do not assure that $\tilde{n} \to 0$ and $\hat{\gamma} \to 0$ in time, but they guarantee that $|\tilde{n}|$ and $|\hat{\gamma}|$ are bounded by class $\mathcal{K}$ functions of $\epsilon^\star$. As before, ϵ^* must be chosen small enough. Finally, following similar arguments as in Appendix D.2, it can be shown that $|\tilde{n}_\alpha|$ and $|\tilde{n}_I|$ are also bounded by class $\mathcal{K}$ functions of $\epsilon^\star$ if $\tilde{E}$ is driven to zero as long as $S^{inj}_I \equiv 0$.

A summary of the variables employed in this Section is shown in Table 4.2.

Table 4.2: Controller variables.

Symbol	Description	Type of variable
$\bar{(\cdot)}$	Equilibrium variable	Reference
$\tilde{(\cdot)}$	Deviation variable	Error
P^{unsat}_{aux}	Unsaturated auxiliary power	Control law variable
I^{unsat}_{coil}	Unsaturated in-vessel coil current	Control law variable
$S^{inj,unsat}_{D/DT-line}$, $S^{inj,unsat}_{D/DT-line}$	Unsaturated D, DT pellet injection	Control law variable
$S^{inj,unsat}_I$	Unsaturated impurity injection rate	Control law variable
P^{max}_{aux}, P^{min}_{aux}, I^{max}_{coil}	Max/min P_{aux} and I_{coil}	Saturation level
$S^{inj,max}_{D/DT-line}$, $S^{inj,min}_{D/DT-line}$	Max/min D and DT injection rates	Saturation level
$S^{inj,max}_I$	Max impurity injection rate	Saturation level
K_P, K_{τ_E}, K_D, K_T	Nominal controller gains	Design parameter
$K_{\gamma,1}$, $K_{\gamma,2}$, K_n, K_{n_I}, K_I	Nominal controller gains	Design parameter
f_{GW}	Greenwald density proximity constant	Design parameter
n_{GW}	Greenwald density	Intermediate variable
P^{min}	P with minimum P_{aux}	Intermediate variable
τ^{min}_E	τ_E with minimum I_{coil}	Intermediate variable
$\hat{n}_I$	n_I deviation w.r.t. steady-state value	Intermediate variable
γ^*, $\hat{\gamma}$	γ and error for isotopic fueling	Intermediate variable
n^*_I, $\hat{n}_I$	n_I and error for impurity injection	Intermediate variable
f, G, u, δ	Matrices for n_D-n_T uncertain model	Intermediate variable
$f^\star$, $G^\star$, u, $\delta^\star$	Matrices for n-γ uncertain model	Intermediate variable
ψ_n, $\psi^\star_n$, v, w	Functions for nominal fueling control	Intermediate variable
v_{rob}, $v^\star_{rob}$, w_{rob}, $w^\star_{rob}$	Functions for robust fueling control	Intermediate variable
κ_0, $\kappa^\star_0$	Constants from bounds to δ and $\delta^\star$	Model parameter
ϵ, $\epsilon^\star$	Constants for robust fueling control	Design parameter

4.5 Simulation Study

The performance of the proposed burn controller is tested in this Section for two different scenarios. In the first scenario, a first operating point with high density is used to test the controller performance when isotopic fueling (i.e. $\tilde{n}$-$\hat{\gamma}$ control) is employed to regulate the plasma density n, while a second operating point with lower density is used to test the controller performance when switching between isotopic fueling and $\tilde{n}_D$-$\tilde{n}_T$ control. No recycling and a relatively small amount of impurities are considered in this first simulation case. In the second scenario, operating points with lower density are chosen so that $\tilde{n}_D$-$\tilde{n}_T$ control is used during most of the simulation, only using isotopic fueling as a backup to decrease the plasma energy when needed. Also, recycling effects are included and a higher amount of impurities is introduced in this second simulation case in order to test the controller in a more demanding situation. In both scenarios, perturbations in the D-T concentrations of the fueling lines are emulated to test the robustness of the controller under the presence of the uncertainties $\delta_{DT-line}$ and δ_{D-line}. It is very important to emphasize that such perturbations in the D-T concentrations with respect to the nominal case are totally unknown to the controller during the simulations studies. The saturation limits imposed are shown in Table 4.3. Also, the following parameters are used: $k_\alpha = 5$, $k_D = 2.5$, $k_T = 2.5$, and $k_I = 8$.

Table 4.3: Actuator limits

Symbol	Description	Value
P_{aux}^{max}	Maximum power	73 MW
P_{aux}^{min}	Minimum power	35 MW
S_D^{max}	Maximum D fueling rate	3×10^{19} m^{-3}s^{-1}
$\dot{S}_D^{max}$	Maximum D fueling ramp rate	3×10^{19} m^{-3}s^{-2}
S_T^{max}	Maximum T fueling rate	3×10^{19} m^{-3}s^{-1}
$\dot{S}_T^{max}$	Maximum T fueling ramp rate	3×10^{19} m^{-3}s^{-2}
I_{coil}^{max}	Maximum in-vessel coil current	4 kA

4.5.1 Scenario 1: Combined isotopic and D-T fueling, no recycling, low impurity

In this first scenario, recycling effects are neglected ($f_{eff} = 0$), and it is considered that the content of impurities in the plasma is relatively low ($f_I^{sp} = 0.005$). Also, only Beryllium impurities are considered ($Z_I = 4$), and the H-factor without activation of the in-vessel coils is taken as $H_H^{nom} = 1.1$. Regarding the uncertainties (see equations (2.83)-(2.84)), a constant negative 30 % drop in the T concentration of the D-T pellet injector is emulated during the whole simulation, i.e. $\delta_{DT-line} = -0.3$, whereas no T is assumed in the D pellet injector (as in the nominal case), i.e. $\delta_{D-line} = 0$. Firstly, the controller attempts to regulate the system around a first operating point defined by $\bar{T} = 10$ keV, $\bar{\beta}_N = 2$, and $\bar{\gamma} = 0.5$, from $t = 0$ s till $t = 50$ s. The simulation study starts from a perturbed initial condition with respect to this first equilibrium point (+20% in n_α, +30% in n_D, −10% in n_T, and +20% in E (no perturbation is introduced in n_I)). Secondly, at $t = 50$ s, the controller attempts to drive the system to a different operating point defined by $\bar{T} = 12$ keV, $\bar{\beta}_N = 1.75$, and $\bar{\gamma} = 0.45$. Finally, from $t = 100$ s until $t = 150$ s, the controller tries to drive the system back to the first operating point. Because the first operating point is characterized by a value of n which is close to the Greenwald density limit, $f_{GW} = 0.8$ is taken so that n is regulated by isotopic fueling around such operating point in order to prevent instabilities related with too high density values.

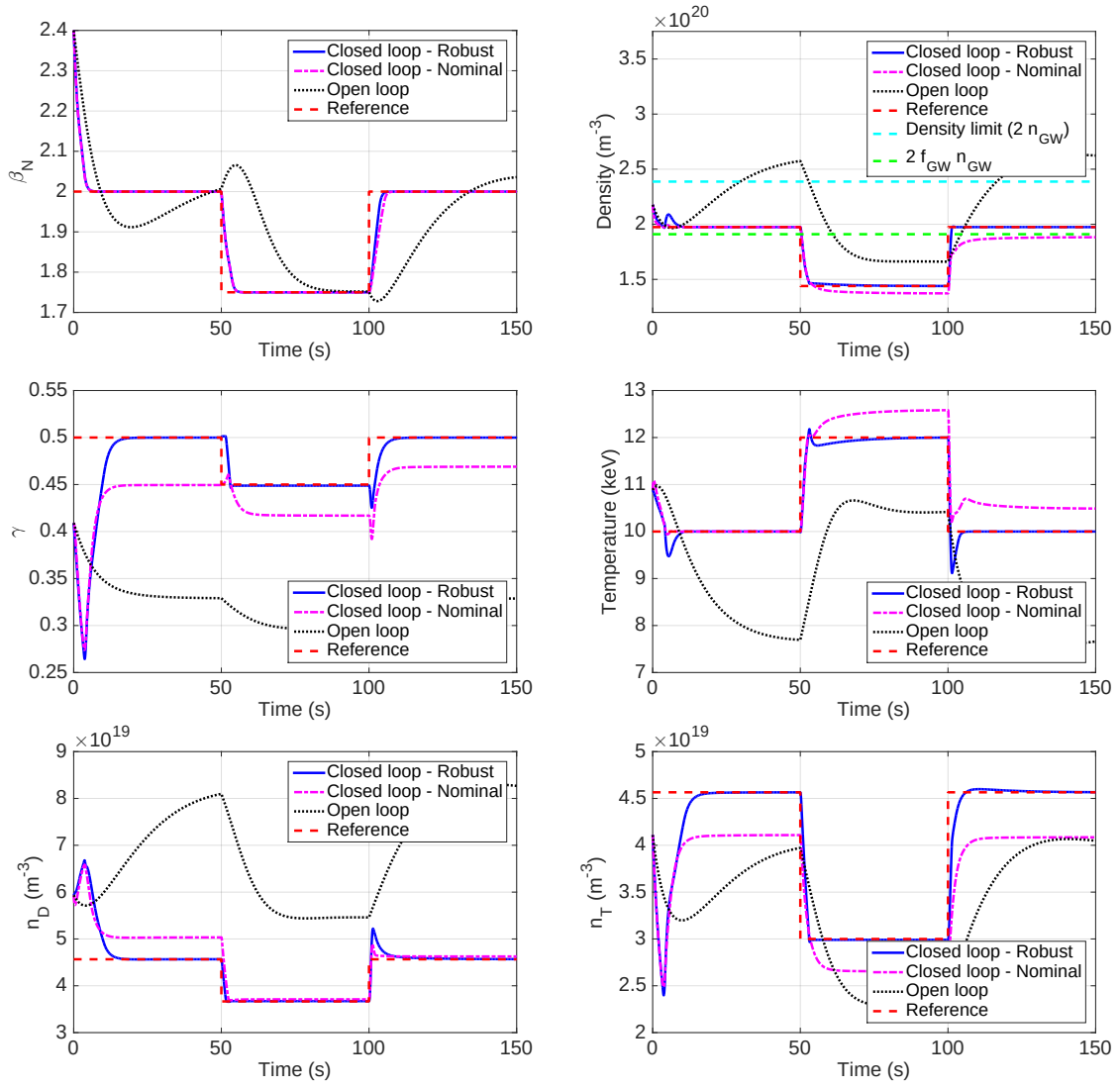

Figure 4.3: Time evolutions for β_N, n, γ, T, n_D, and n_T in Scenario 1 under robust feedback control law (solid blue), nominal feedback control law (magenta dashed-dotted), and feedforward control law (black dotted), together with the reference signals (red dashed).

Simulation results for the evolutions of β_N, n, γ, T, n_D and n_T together with their corresponding targets are shown in Fig. 4.3 for three different cases: i- open loop (no control), ii- closed loop under the nominal control law, iii- closed loop under the robust control law. The inputs S_D^{inj}, S_T^{inj}, S_{D-line}^{inj}, $S_{DT-line}^{inj}$, I_{coil} and P_{aux} are shown in Fig. 4.4. In the case of nominal D-T fuel concentration, the reference actuator

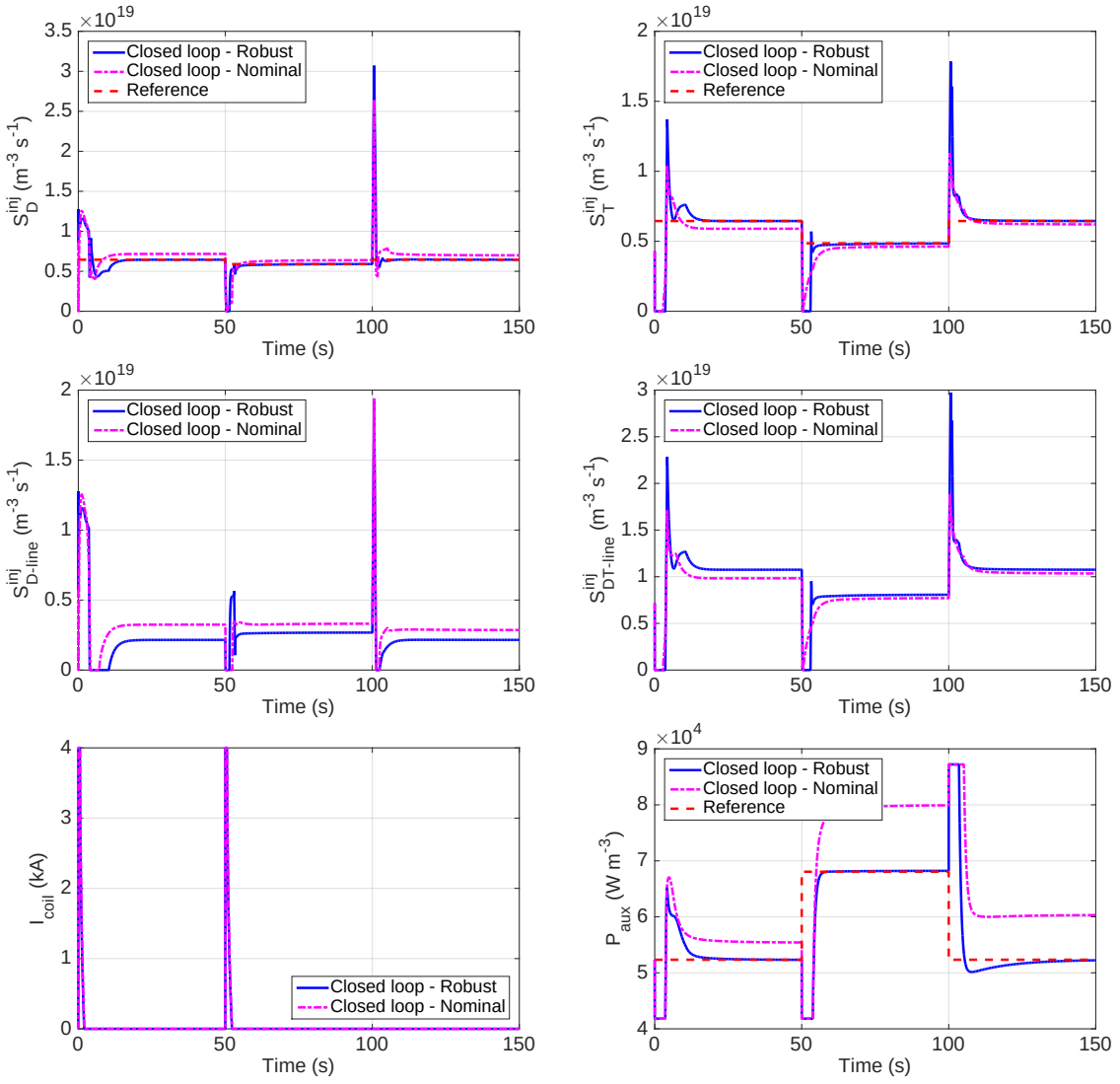

Figure 4.4: Time evolutions for S_D^{inj}, S_T^{inj}, S_{D-line}^{inj}, $S_{DT-line}^{inj}$, I_{coil}, and P_{aux} in Scenario 1 under robust (solid blue) and nominal (magenta dashed-dotted) control laws, together with the actuator reference (red dashed).

signals (red dashed) shown in Fig. 4.4 are designed to achieve in open loop the desired reference states (red dashed) shown in Fig. 4.3. However, in presence of the emulated bias in the T concentration of the D-T pellet injector, the variables evolve in open loop (black dotted) to values that are different from the desired references (red dashed) as shown in Fig. 4.3. Under the nominal control law, β_N is driven to

the desired operating points during the whole simulation (see Fig. 4.3(a)), whereas n and T can only be driven to the first operating point; at $t = 50$ s, the nominal control law is unable to accurately drive n and T to the second operating point, and it is also unable to drive n and T back to the first operating point at $t = 100$ s (see Fig. 4.3(b) and Fig. 4.3(d)). Because $n > 2f_{GW}n_{GW}$ between $t = 0$ s and $t \approx 50$ s, and later between $t \approx 100$ s and $t \approx 150$ s, isotopic fueling is employed during those time intervals (Fig. 4.3(b)), while $\tilde{n}_D$-$\tilde{n}_T$ control is used between $t \approx 50$ s and $t \approx 100$ s. In open loop, n goes beyond the Greenwald stability limit, while the nominal and robust control laws avoid violating such limit. Still, the nominal control law cannot drive γ, n_D and n_T to the desired operating points during the entire simulation (see Fig. 4.3(c), Fig. 4.3(e) and Fig. 4.3(f)). On the other hand, the robust control law is able to successfully drive all the variables β_N, n, γ, T, n_D and n_T to the different operating points. Fig. 4.4 shows that the robust control law can correct the drifts in the DT concentration of the pellet injectors even though they are unknown to the controller, and drives P_{aux}, S_D^{inj} and S_T^{inj} to their equilibrium values (see Fig. 4.4(a), Fig. 4.4(b), and Fig. 4.4(f)). It must be emphasized that S_{D-line}^{inj} and $S_{DT-line}^{inj}$ are not expected to converge to their reference values due to the emulated bias. The in-vessel coils are utilized by both the nominal and robust control laws during the short periods of time in which P_{aux} is saturated to its minimum value, around $t = 0$ s and $t = 50$ s (see Fig. 4.4(e) and Fig. 4.4(f)). Impurity injection is not used at all by the controller due to the fact that, while isotopic fueling is employed, density limits are closed to be violated (i.e., $n > 2f_{GW}n_{GW}$).

4.5.2 Scenario 2: D-T fueling under recycling effects and high impurity content

In this second scenario, intense recycling effects ($f_{eff} = 0.3$, $f_{ref} = 0.65$, $R_{eff} = 0.85$, $\gamma_{PFC} = 0.5$) and a relatively high content of impurities in the plasma ($f_I^{sp} = 0.05$) are considered. Also, impurities with higher atomic number are considered (Carbon, $Z_I = 6$), and the H-factor without activation of the in-vessel coils is taken as $H_H^{nom} = 1.2$. For a more demanding test of the controller, the uncertain

terms γ_{D-line} and $\gamma_{DT-line}$ (see equations (2.83)-(2.84)) vary in time as shown in Fig. 4.6(h). Firstly, the controller attempts to regulate the system around a first operating point defined by $\bar{T} = 10$ keV, $\bar{\beta}_N = 1.5$, and $\bar{\gamma} = 0.5$, from $t = 0$ s till $t = 50$ s. The simulation study starts from a perturbed initial condition with respect to the equilibrium (+20% in n_α, −10% in n_D, +15% in n_T, and +20% in E (again, no perturbation is introduced in n_I)). Secondly, at $t = 50$ s, the controller attempts to drive the system to a different operating point defined by $\bar{T} = 11$ keV, $\bar{\beta}_N = 1.4$, and $\bar{\gamma} = 0.45$. Finally, from $t = 100$ s until $t = 150$ s, the controller attempts to drive the system to a third operating point defined by $\bar{T} = 10.5$ keV, $\bar{\beta}_N = 1.6$, and $\bar{\gamma} = 0.5$. Because the density values that characterize these three operating points are substantially lower than in the first simulation scenario, regulation of n due to closeness to the Greenwald density limit is not considered as a priority in this case. A value of $f_{GW} = 1$ is taken.

Simulation results for the evolutions of β_N, n, γ, T, n_D and n_T together with their corresponding targets are shown in Fig. 4.5 for three different cases: i- open loop (no control), ii- closed loop under the nominal control law, iii- closed loop under the robust control law. The inputs S_D^{inj}, S_T^{inj}, S_{D-line}^{inj}, $S_{DT-line}^{inj}$, I_{coil} and P_{aux} are shown in Fig. 4.6 together with γ_{D-line} and $\gamma_{DT-line}$. As in the previous simulation case, the reference actuator signals (red dashed) shown in Fig. 4.6 are designed to achieve in open loop the desired reference states (red dashed) shown in Fig. 4.5 for the case of nominal D-T fuel concentration. However, in presence of the emulated drifts in the T concentrations of both the D pellet injector and the D-T pellet injector, the variables evolve in open loop (black dotted) to values that are different from the desired references (red dashed) as shown in Fig. 4.5. Under the nominal control law, β_N is driven to the desired operating points during the whole simulation, and n_D is also successfully regulated, although with small constant drifts with respect to the desired targets (see Fig. 4.5(a) and Fig. 4.5(e)). However, the nominal control law cannot drive n, γ, T, and n_T to the desired operating points (see Fig. 4.5(b), Fig. 4.5(c), Fig. 4.5(d) and Fig. 4.5(f)). On the contrary, the robust control law is able to successfully drive all the variables β_N, n, γ, T, n_D and n_T to the different operating points. It is interesting to note that the high content of

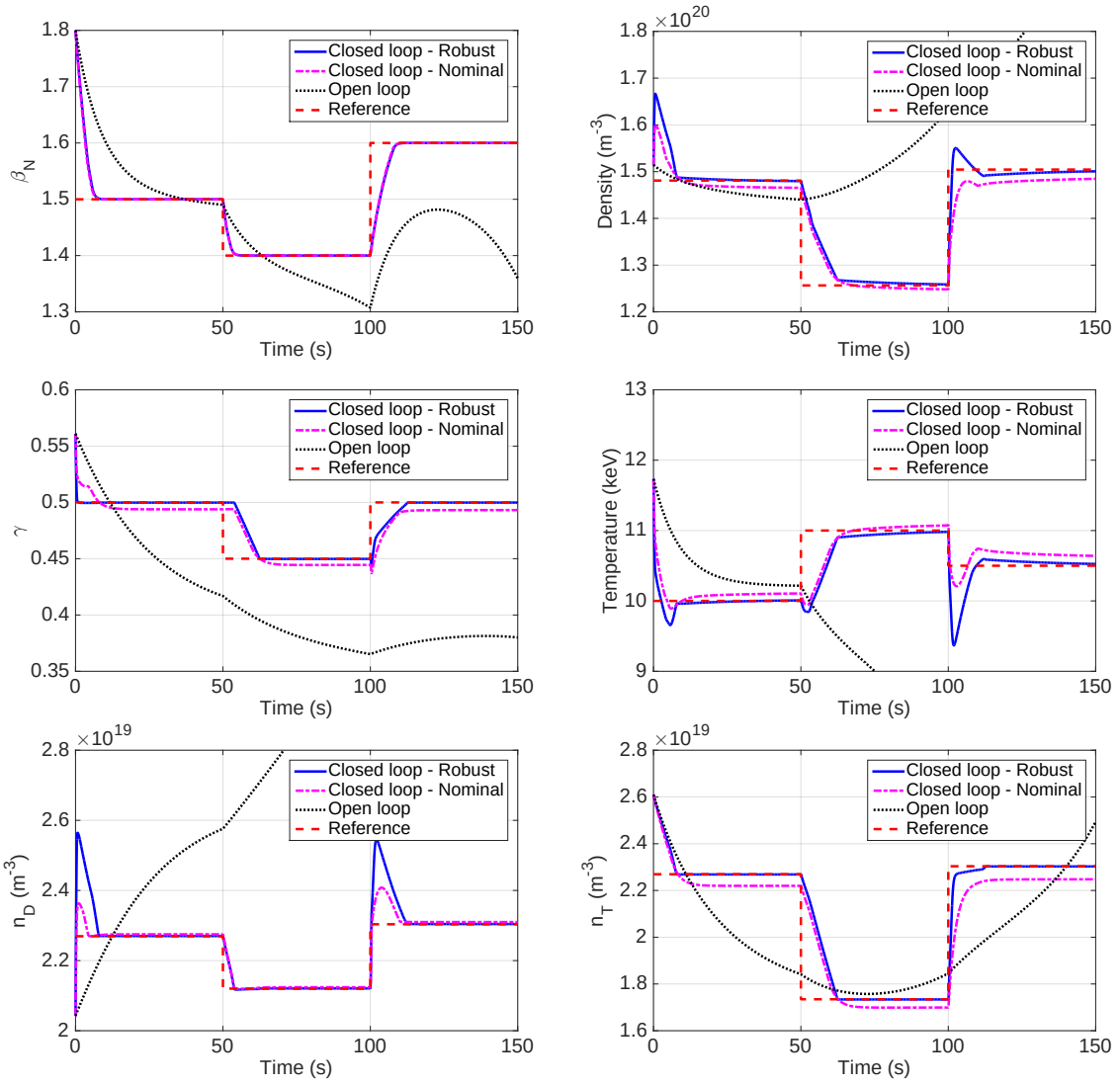

Figure 4.5: Time evolutions for β_N, n, γ, T, n_D, and n_T in Scenario 2 under robust feedback control law (solid blue), nominal feedback control law (magenta dashed-dotted), and feedforward control law (black dotted), together with the reference signals (red dashed).

impurities and the recycling effects slow down the n and T evolutions when compared to those in Scenario 1, even though the robust controller still regulates both n and T successfully. Fig. 4.6 shows how P_{aux}, S_D^{inj} and S_T^{inj} evolve to their equilibrium values both under the nominal and robust control laws (see Fig. 4.6(a), Fig. 4.6(b), and Fig. 4.6(f)). However, the S_D^{inj} and S_T^{inj} evolutions are slightly different, which

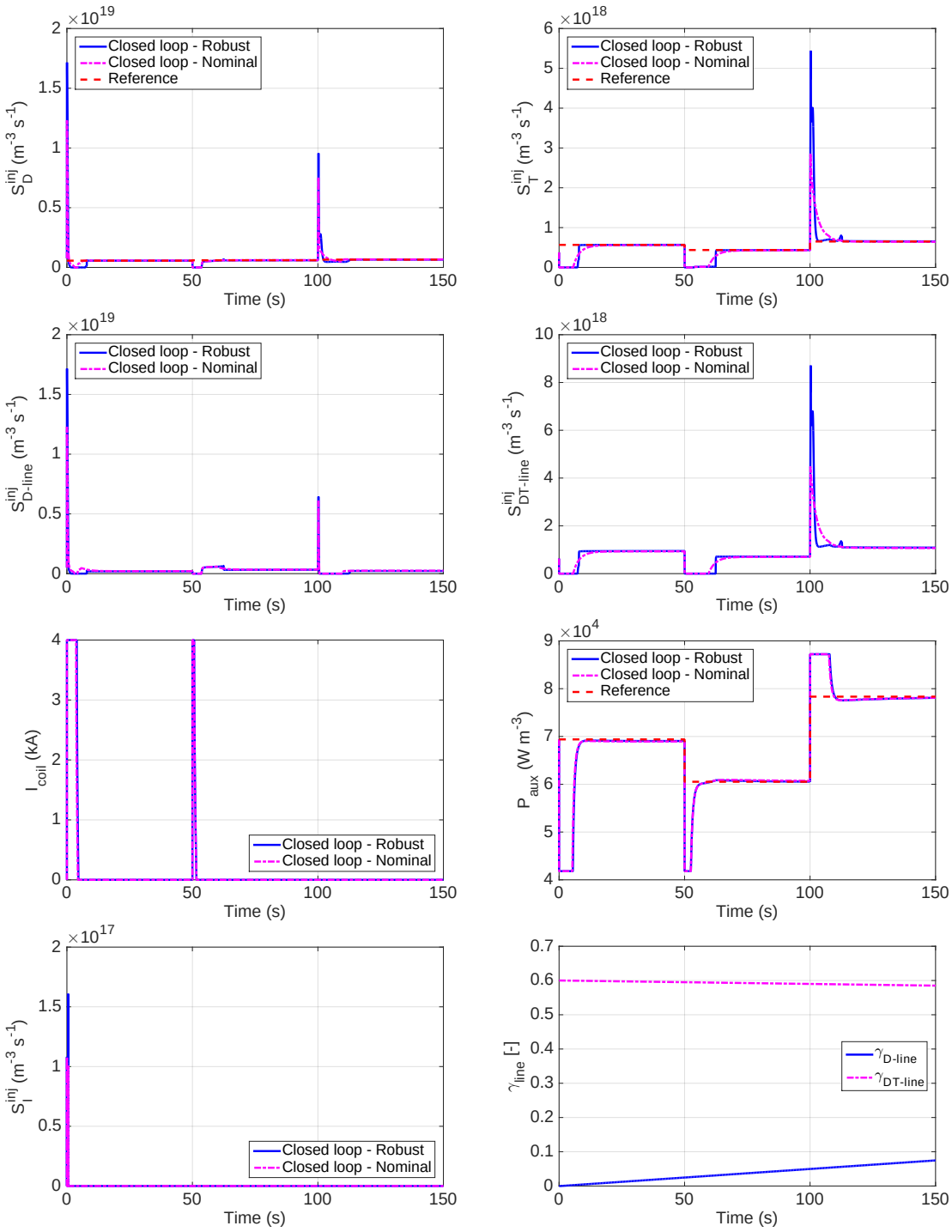

Figure 4.6: Time evolutions for S_D^{inj}, S_T^{inj}, S_{D-line}^{inj}, $S_{DT-line}^{inj}$, I_{coil}, P_{aux}, S_I^{inj}, γ_{D-line} and $\gamma_{DT-line}$ in Scenario 2 under robust (solid blue) and nominal (magenta dashed-dotted) control laws, and actuator reference (red dashed).

has an important impact on the state evolution due to the highly nonlinear nature of the system. The in-vessel coils are utilized by both the nominal and robust control laws during the short periods of time in which P_{aux} is saturated to its minimum value, around $t = 0$ s and $t = 50$ s (see Fig. 4.6(e) and Fig. 4.6(f)). Impurity injection is used only at the beginning of the simulation during a few seconds, in order to reject the initial perturbation in E.

4.6 Conclusions

In this Section, a nonlinear, robust burn controller has been presented which is capable of regulating the burning plasma around a desired equilibrium under the presence of large initial perturbations and uncertainties in the D-T concentration of the pellet injectors. The controller can be used to drive the burning plasma between different operating points, since the control-design process avoids model linearization around a particular equilibrium. Moreover, the algorithm combines all feasible actuators available in tokamaks for burn control (auxiliary power, in-vessel coil current, fueling rates, and impurity injection) in a comprehensive, integrated control strategy, which allows for a higher flexibility when choosing the most appropriate actuation methods in different scenarios. The integrated strategy follows a repurposing (RP) actuator-sharing approach, for example, using isotopic fueling in positive energy excursions (i.e., repurposing the fueling actuation for energy control). Also, the controller chooses isotopic fueling in scenarios in which disruptive density limits may be reached, whereas it chooses a more accurate D and T density control approach around operating points that are relatively far from disruptive density limits. It also employs the in-vessel coils as a backup actuator to decrease the plasma energy when positive thermal excursions cannot be avoided by means of auxiliary power. The inclusion of this actuator is an important novelty in this work with respect to previous work. The in-vessel coils may allow for fast, exception-handling actuation in situations in which other actuators may not suffice to regulate the plasma burn condition.

It is important to note that the nonlinear control laws for the different actuators are given as analytical functions of the measured or estimated states, which makes this control approach much less computationally demanding than any possible real-time nonlinear optimization approach and also much more robust since it is immune to feasibility and convergence issues. The controller performance has been studied in simulations for two different scenarios. The simulation study suggests both that the D-T pellet-concentration variations play a crucial role in the burning plasma dynamics and that robust burn controllers are necessary to effectively overcome their negative impact in ITER.

A simplified zero-dimensional, nonlinear model is used in this work for control synthesis and simulation. Even though these models are approximate, they capture the primary dynamics of the burning plasma that is needed for the synthesis of a robust controller whose control objective is defined in terms of zero-dimensional quantities such as the overall fusion power. However, as one-dimensional fueling actuation models become more mature, steps towards control simulations based on one-dimensional models are necessary because while the control objective is zero-dimensional, the to-be-controlled system is indeed one-dimensional. Future work also requires the incorporation of the actuator and sensor dynamics in the control-design process. It is anticipated that the proposed burn-control algorithm will need to be augmented to handle lags and delays associated with the actuators and sensors possibly by the use of backstepping and prediction techniques.

Chapter 5

Integrated Kinetic and Magnetic Control: Beta and Current Profile Control

5.1 Introduction and Previous Work

Regulation of β and/or the current profile[1] in tokamak plasmas is a control problem of significant interest in nuclear fusion research. As it has been previously introduced, β is a measurement of the plasma-confinement efficiency that characterizes the kinetic pressure p that can be attained my means of a particular magnetic field B. Higher β requires a lower B to maintain a given p, therefore reducing the cost of construction of a fusion power plant (which increases with B). On the other hand, if B is fixed, higher β yields higher p, hence a higher triple product can be achieved for the same τ_E (see equations (1.11) and (2.20)). Nonetheless, particular β values or evolutions may trigger MHD instabilities that normally decrease the plasma performance and may damage the vacuum vessel. High β values and efficient control can provide a cheaper fusion power plant with higher performance.

[1]The current profile is normally characterized in tokamaks by means of $\vec{j}$, ψ, q, or any other related magnitude. More details can be found in Chapter 2, Section 2.2.1.

The current profile plays a key role in the plasma equilibrium and performance (see the MHD equilibrium equation (2.8) or the Grad-Shafranov equation (2.13)). For example, advanced scenarios with high bootstrap current fractions may develop low or reversed magnetic-shear profiles ($s \to 0$ or $s < 0$, respectively) with ITBs that may drive β towards too high values (see Section 1.3). In such scenarios, q-profile regulation will most likely be needed.

As one may hint just from analyzing the Spitzer resistivity model (2.30), and the MDE and EHTE models presented in Sections 2.2.1 and 2.2.2 of Chapter 2, the q-profile and β dynamics are not independent. The electron temperature, T_e, enters the definition of β through p_e, but it also determines η, and therefore, affects the evolution of ψ and q. In turn, it is an experimental fact that q and s may affect the plasma transport (see, for example, the χ_e model proposed in (2.42), which is based on [20]), and therefore, also influence T_e and β. Another coupling effect that has not been considered in the models presented in this dissertation is the variation of the plasma equilibrium associated with changes in $\vec{j}$, ψ and/or q (see equations (2.8) and (2.13)), which in turn affects the plasma confinement, and T_e and/or β. The close coupling between the β and q-profile evolutions is the reason why their regulation is often treated as a single control problem.

The approach generally utilized in present-day devices to achieve some particular β and q evolutions is as follows. Auxiliary sources are customarily employed to achieve a particular β target by means of auxiliary power modulation, P_{aux}. The β target has an associated T_e evolution, and therefore, determines η as well. As a result, regulating both β and q independently by means of *diffusivity control* (i.e., by controlling η) is normally not possible, and the alternative is to modify the current driven through the plasma. This can be done by means of I_p or $\langle \vec{j}_{ni} \cdot \vec{B} \rangle / B_{\phi,0}$. In the control jargon, control by means of I_p is known as *boundary control*, whereas control by means of $\langle \vec{j}_{ni} \cdot \vec{B} \rangle / B_{\phi,0}$ is known as *interior control*. During the flat-top phase, it is normally desired to have a particular, approximately constant I_p value in order to achieve a particular q_{edge} evolution (or q_{95} in diverted plasmas), reducing the applicability of the boundary-control approach to the q-profile feedback-control problem. Moreover, high T_e values are normally found in high β scenarios because

of the large P_{aux} injected, and η is very small during the flat-top phase. The low η reduces the q-profile controllability by means of interior control during the flat-top phase ($\partial\psi/\partial t \propto \eta\langle\vec{j}_{ni}\cdot\vec{B}\rangle/B_{\phi,0}$), so the q profile can be regulated more efficiently during the ramp-up phase, when higher η values are found.

Significant effort has been carried out within the fusion community to find and test control algorithms for the regulation of the q profile [66–77]. Substantial work has also been done on simultaneous q-profile + β control [78–84]. Much of this work is non-model based (e.g., [66, 68]) or uses system-identification techniques (e.g., [78, 79, 82]). A common approach to model-based q-profile + β control in previous work is using an approximately linearized version of the system dynamics and/or applying linear control techniques at some point during the control design. For example, in previous work carried out by the Lehigh University Plasma-Control Group [80, 81], robust, linear controllers for the q-profile and W (in [80]) or T_e (in [81]) were designed based on linearized versions of the system dynamics. In [83, 84], a Model Predictive Control (MPC) scheme was proposed for the regulation of the q profile in conjunction with a PID control law for W. A linearized version of the q-profile dynamics is added as a constraint within the MPC scheme.

In this Chapter, two q + β control approaches are proposed. In both control designs, the models employed are the MDE model (Chapter 2, Section 2.2.1), together with 0.5D models for T_e and n_e, equations (2.34), and a 0D model for W (Chapter 2, Section 2.3.1). The first approach corresponds to the author's work presented in [85, 86], which employs approximate linearization techniques to design a controller for the central safety factor, q_0, and normalized beta, β_N. In [85], a control-oriented model of the q_0 dynamics is derived, and a PID controller is designed using approximate linearization techniques to regulate q_0 by means of P_{aux}. A key element in this control design is the addition of constraints to ensure that zero NBI torque is delivered. The work in [85] was extended to include simultaneous q_0 + β_N regulation with zero NBI torque, also by means of P_{aux}. The controller was tested in DIII-D experiments [86] with the final goal of facilitating access to QH-mode [8]. The second approach corresponds to the author's work presented in [87, 88]. This work eventually converged to the design proposed in [89], in which

a nonlinear, robust controller is synthesized for simultaneous q-profile + β control by means of feedback linearization and Lyapunov redesign techniques [65], that allows for synthesizing a nonlinear controller for q-profile regulation without recurring to approximate linearization techniques. This removes the natural limitations imposed by approximate linearization and/or linear techniques. The proposed controller employs I_p, NBI and EC power as the available actuators for control. First, control laws are designed for I_p and P_{aux} to control q_{edge} and β_N, respectively. These nonlinear, robust control laws for I_p and P_{tot} are based on Lyapunov redesign techniques, and can be easily embedded in the feedback-linearization scheme designed for q profile control. Second, a study is carried out to analyze under what conditions the q-profile subsystem is feedback linearizable, and if so, how many nodes of the q profile are controllable in conjunction with β_N by means of feedback linearization. It will be shown that the nominal system is in fact feedback linearizable as long as the auxiliary sources have different enough current-deposition profiles. Such analysis allows for a very intuitive assessment of the q-profile + β_N control capability within a tokamak. Third, a feedback-linearization nominal control law is synthesized to control the q profile at the interior nodes by means of the NBI and EC powers, assuming no uncertainty in the model employed for control design. Finally, the feedback-linearization nominal control law is robustified by means of Lyapunov redesign techniques, so that the controller is robust against unknown variations in T_e and n_e, which make η and $\langle \vec{j}_{ni} \cdot \vec{B} \rangle / B_{\phi,0}$ also uncertain.

5.2 $q_0 + \beta_N$ Control via Approximate Linearization Techniques under Zero NBI Torque

5.2.1 Modeling of the $q_0 + \beta_N$ Dynamics

The central safety factor, q_0, is defined in equation (2.93). The q_0 model employed for simulation and control design in this $q_0 + \beta_N$ control problem[2] is obtained by employing the MDE model described in Chapter 2, Section 2.2.1, together with the 0.5D models for T_e and n_e given by (2.34). The MDE (2.27) can be rewritten as

$$\frac{\partial \psi}{\partial t} = h_{diff}(\hat{\rho},t)\frac{\partial}{\partial \hat{\rho}}\left(\hat{\rho} D_\psi \frac{\partial \psi}{\partial \hat{\rho}}\right) + \sum_{i=1}^{N_{aux}} h_{aux,i}(\hat{\rho},t) P_{aux,i}(t) + h_{BS}(\hat{\rho},t)\left(\frac{\partial \psi}{\partial \hat{\rho}}\right)^{-1}, \quad (5.1)$$

where $D_\psi \triangleq \hat{F}\hat{G}\hat{H}$, and

$$h_{diff} = \frac{\eta^{prof}}{\mu_0 \rho_b^2 \hat{F}\hat{\rho}} k_{diff},\ \eta^{prof} = \frac{k_{sp}^{prof} Z_{eff}}{\left(T_e^{prof}\right)^{3/2}\left(n_e^{prof}\right)^{3\zeta/2}},\ k_{diff} = I_p^{-\frac{3}{2}\gamma} P_{tot}^{-\frac{3}{2}\epsilon} \bar{n}_e^{-\frac{3}{2}\zeta}, \quad (5.2)$$

$$h_{aux,i} = R_0 \eta^{prof} \hat{H} j_{aux,i}^{prof} \frac{\left(T_e^{prof}\right)^{\delta_{aux,i}}}{n_e^{prof}} k_{aux,i}, \quad (5.3)$$

$$k_{aux,i} = I_p^{\gamma(\delta_{aux,i}-\frac{3}{2})} P_{tot}^{\epsilon(\delta_{aux,i}-\frac{3}{2})} \bar{n}_e^{\zeta(\delta_{aux,i}-\frac{3}{2})-1}, \quad (5.4)$$

$$h_{BS} = \frac{\eta^{prof} R_0^2 \hat{H}}{\hat{F}}\left[2\mathcal{L}_{31} T_e^{prof}\frac{\partial n_e^{prof}}{\partial \hat{\rho}} + \left(2\mathcal{L}_{31} + \mathcal{L}_{32} + \alpha \mathcal{L}_{34}\right) n_e^{prof}\frac{\partial T_e^{prof}}{\partial \hat{\rho}}\right] k_{BS}, \quad (5.5)$$

$$k_{BS} = I_p^{-\frac{1}{2}\gamma} P_{tot}^{-\frac{1}{2}\epsilon} \bar{n}_e^{-\frac{1}{2}\zeta+1}, \quad (5.6)$$

where the auxiliary-source contributions are due to NBI and EC, so the second term on the right-hand side of (5.1) can be rewritten as

$$\sum_{i=1}^{N_{aux}} h_{aux,i}(\hat{\rho},t) P_{aux,i}(t) = \sum_{i=1}^{N_{NBI}} h_{NBI,i}(\hat{\rho},t) P_{NBI,i}(t) + h_{EC}(\hat{\rho},t) P_{EC}(t), \quad (5.7)$$

where $h_{NBI,i}$ and h_{EC} are analogous to the term given by (5.3), but particularized for $j_{aux,i}^{dep} = j_{NBI,i}^{dep}$ and $j_{aux,i}^{dep} = j_{EC}^{dep}$, respectively, and $\delta_{aux,i} = \delta_{NBI,i}$ and $\delta_{aux,i} = \delta_{EC}$, respectively.

[2]The model for q_0 described in Section 2.3.4 had not been developed by the time this $q_0 + \beta_N$ control design was carried out, hence a q_0 model was derived as reported in this Section.

The normalized plasma beta, β_N, can be obtained from (2.25) and (2.26), and its definition is given in (4.14). It can be rewritten in terms of W as

$$\beta_N = \frac{\frac{4}{3}\mu_0 W a}{B_{\phi,0} I_p V_p}[\%], \tag{5.8}$$

where V_p is assumed to be constant. The dynamics of W is estimated using the model presented in Chapter 2, Section 2.3.1. The additional assumption $P_{tot} \approx P_{aux}$ is employed, i.e., the α, ohmic, and radiative power contributions to P_{tot} can be neglected (see equation (2.35)). Also, it is assumed that there is no uncertainty in the W subsystem, i.e, $\delta_{H_H} = 0$ and $\delta_P = 0$.

In this model, ψ and W are utilized as states, whereas $P_{NBI,i}$ and P_{EC} are the controllable inputs. As a summary, the state-space representation of the nonlinear $q_0 + \beta_N$ dynamics is given by

$$\frac{d}{dt}\begin{bmatrix}\psi \\ W\end{bmatrix} = f(\psi, W, u, t), \quad \begin{bmatrix}q_0 \\ \beta_N\end{bmatrix} = g(\psi, W, t), \tag{5.9}$$

where $u = [P_{NBI,1}, ..., P_{NBI,N_{NBI}}, P_{EC}]^T$ is the vector of controllable inputs, f is the nonlinear state function whose first and second components are given by (5.1) and (2.64), respectively (where $\delta_P = 0$ and $\delta_{H_H} = 0$ are assumed), and g is the nonlinear output function whose first and second components are given by (2.93) and (5.8), respectively. The time dependence in f and g is due to I_p and $\bar{n}_e$, which are assumed to be non-controllable inputs in this $q_0 + \beta_N$ control problem.

5.2.2 Model Validation for a Reverse I_p DIII-D Scenario

The model given by (5.9) is tuned and validated for an H-mode, reverse plasma-current ($I_p < 0$) scenario in DIII-D. The control-oriented model is tailored to DIII-D shots 163518 through 163525, which all present similar conditions. Relevant machine parameters and model constants for this scenario are $B_{\phi,0} = 1.93$ T, $R_0 = 1.77$ m, $Z_{eff} = 3.5$, $H_H^{nom} = 1.1$, $\delta_{NBI,i} = 0.5$, $\delta_{EC} = 1$, $\gamma = 1$, $\epsilon = 0.5$ and $\zeta = 0$. It can be appreciated that the $q_0 + \beta_N$ model in (5.9) corresponds to the 1D model for ψ and 0D model for W implemented in COTSIM (see Chapter 3). Therefore, a COTSIM

simulation with the aforementioned models is run in open loop in order to carry out the validation of (5.9).

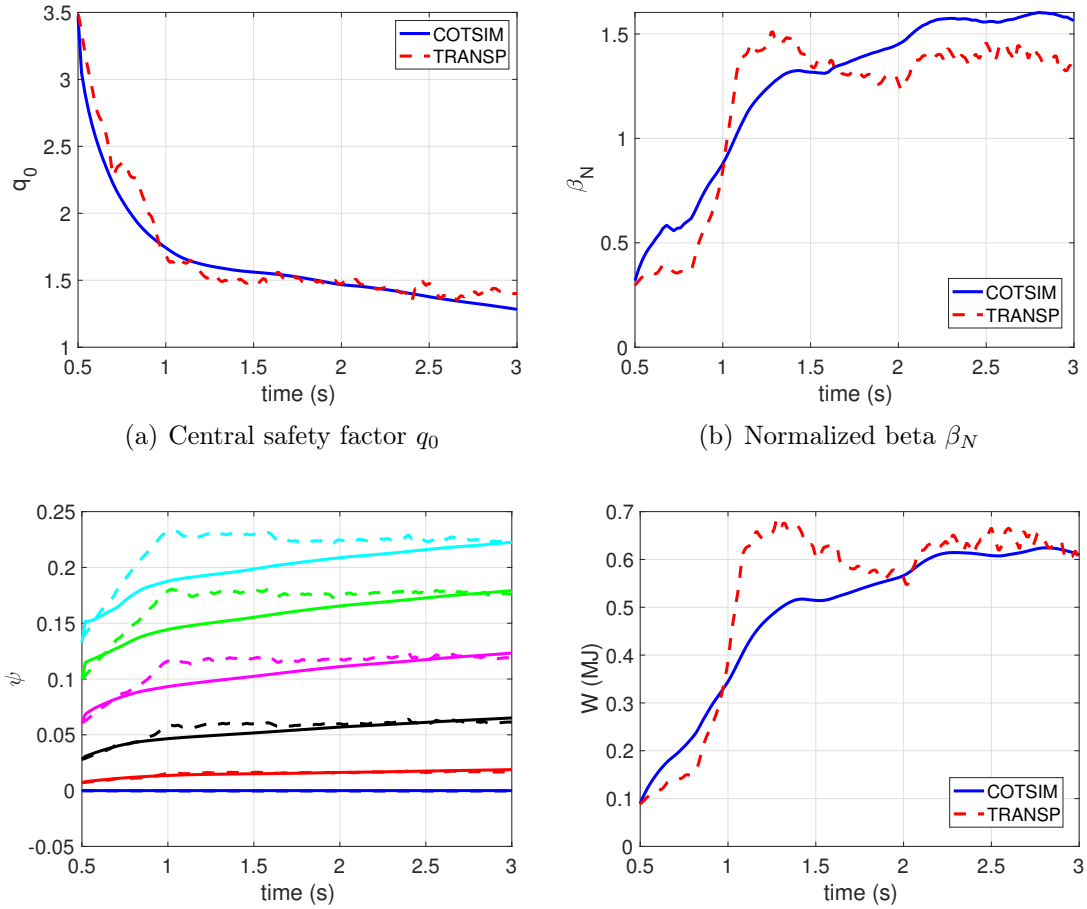

(a) Central safety factor q_0

(b) Normalized beta β_N

(c) Poloidal stream function ψ

(d) Thermal energy W

Figure 5.1: Validation of the $q_0 + \beta_N$ model: comparison between COTSIM and TRANSP data for shot 163521.

Fig. 5.1 shows the time evolution of the outputs q_0 and β_N together with the state ψ and W, when using the experimental inputs from shot 163521. The simulation is only run until $t = 3$ s because TRANSP data is only available within such time span. It can be seen that, although a perfect match between COTSIM and TRANSP results is not achieved, the same qualitative behavior is observed.

The most significant difference is found at the end of the ramp-up phase (around 1.25 s) with lower W, β_N, and ψ values predicted by the COTSIM simulation. This indicates that the models implemented in COTSIM may not be able to capture as many features of the plasma dynamics as TRANSP, which is expected from the different levels of complexity that these two codes employ. However, later in the simulation, it can be seen that all the variables follow trends that are very similar to those predicted by TRANSP.

5.2.3 Reduced, Linearized Model of the $q_0 + \beta_N$ Dynamics

To enable control design, the ψ-subsystem in (5.9) (i.e., the partial differential equation (5.1) and the definition (2.93)) is discretized in the $\hat{\rho}$-domain using finite differences to obtain a set of ordinary differential equations. A discretization grid with $N+1$ nodes in the interval $\hat{\rho} = [0, 1]$ is used. The value of ψ at each of the inner nodes is denoted by ψ_i, for $i = 1, ..., N-1$, and $\hat{\psi} = [\psi_1, ..., \psi_{N-1}]^T$ is a vector with all ψ_i. After spatially discretizing (5.1) and (2.93), together with the MDE boundary conditions (2.28), the $q_0 + \beta_N$ dynamics can be rewritten as

$$\dot{x} = f_x\big(x, t, u\big), \;\; y = g_x(x), \tag{5.10}$$

where $x = [\hat{\psi}, W] \in \mathbb{R}^{N\times 1}$ is the state vector and $y = [q_0, \beta_N]^T$ is the output vector. Linearizing with respect to a nominal trajectory of the system described by a state vector $\bar{x} = [\bar{\psi}, \bar{W}]^T$, input vector $\bar{u}$, and output vector $\bar{y} = [\bar{q}_0, \bar{\beta}_N]^T$, it is possible to write (5.10) as a MIMO linear time-varying (LTV) system given by

$$\dot{\tilde{x}} = A(t)\tilde{x} + \sum_{i=1}^{i=N_{NBI}} B_{1,i}(t)\tilde{P}_{NBI,i}(t) + B_2(t)\tilde{P}_{EC}(t), \tag{5.11}$$

$$\tilde{y} = C\tilde{x}, \tag{5.12}$$

where $\tilde{x} = x - \bar{x}$, $\tilde{u} = u - \bar{u} = [\tilde{P}_{NBI,1}, ..., \tilde{P}_{NBI,N_{NBI}}, \tilde{P}_{EC}]^T$, $\tilde{y} = y - \bar{y} = [\tilde{q}_0, \tilde{\beta}_N]^T$, $A(t) \in \mathbb{R}^{N\times N}$ is the time-varying state matrix, $B_{1,i}(t) \in \mathbb{R}^{N\times 1}$ is the time-varying input matrix associated to the i-th NBI, $B_2(t) \in \mathbb{R}^{N\times 1}$ is the time-varying input matrix associated to the EC source, and $C(t) \in \mathbb{R}^{2\times N}$ is the time-varying output

matrix. These matrices are computed as $A(t) = \partial f_x\big(\bar{x}+\tilde{x}, \bar{u}+\tilde{u}, t\big)/\partial\tilde{x}$, $B_{1,i}(t) = \partial f\big(\bar{x}+\tilde{x}, \bar{u}+\tilde{u}, t\big)/\partial\tilde{P}_{NBI,i}$, $B_2(t) = \partial f\big(\bar{x}+\tilde{x}, \bar{u}+\tilde{u}, t\big)/\partial\tilde{P}_{EC}$ and $C(t) = \partial g_x(\bar{x}+\tilde{x})/\partial\tilde{x}$, all of them evaluated at $\bar{x}(t)$, $\bar{u}(t)$.

5.2.4 NBI Configuration and Zero NBI-Torque in DIII-D

In the DIII-D tokamak, a total of 8 NBI's are available. These NBI's are denoted by 30L, 30R, 150L, 150R, 210L, 210R, 330L and 330R, and they are placed in the DIII-D tokamak as depicted in Fig. 5.2. Because a reverse I_p scenario is considered, it is found that 6 out of the 8 NBI's can drive current in the counter-current direction (30L, 30R, 150L, 150R, 330L and 330R, depicted in blue), whereas 2 NBI's can drive current in the co-current direction (210L and 210R, depicted in red).

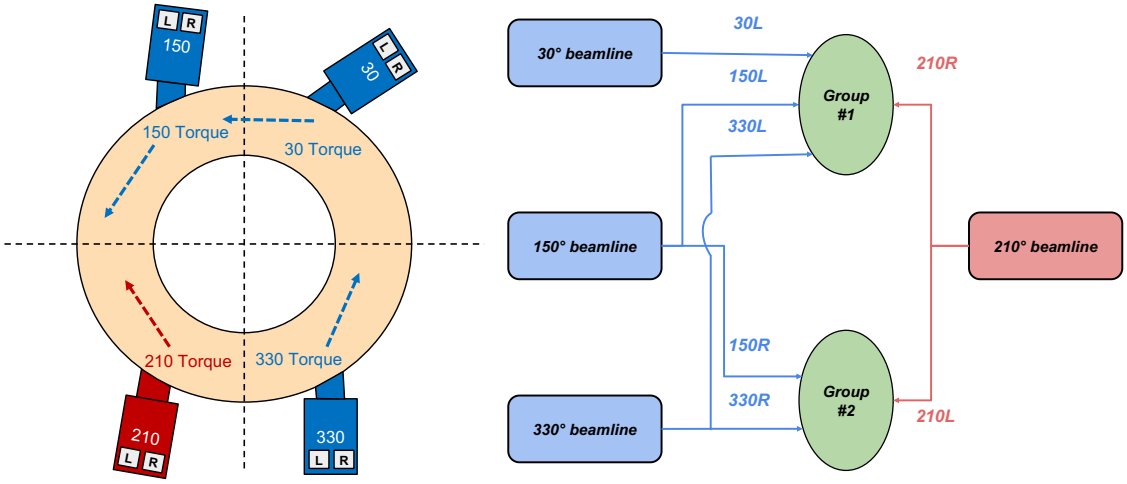

Figure 5.2: Geometry and balanced configuration of the NBIs in the DIII-D tokamak.

The torque injected by each of these NBI's is denoted in this Section as $T_{(\cdot)}$, where $(\cdot)$ is the designation of each NBI, i.e., $(\cdot) = 30L$, $(\cdot) = 30R$, etc. The total torque injected by the co-current NBI's is denoted by $T_{NBI,co}$, and it is given by

$$T_{NBI,co} = T_{210\mathrm{L}} + T_{210\mathrm{R}}. \tag{5.13}$$

The total torque injected by the counter-current NBI's is denoted by $T_{NBI,counter}$,

and it is given by

$$T_{NBI,counter} = T_{30\mathrm{L}} + T_{30\mathrm{R}} + T_{150\mathrm{L}} + T_{150\mathrm{R}} + T_{330\mathrm{L}} + T_{330\mathrm{R}}. \tag{5.14}$$

In order to produce a zero input-torque, the torque injected by the co-current NBI's must be equal to the torque injected by counter-current NBI's, i.e.,

$$T_{NBI,co} = T_{NBI,counter}. \tag{5.15}$$

Condition (5.15) is achieved by using the NBI's in balanced groups (see Fig. 5.2). A balanced group is composed by three co-current NBI and one counter-current NBI that inject the same torque. For any group of balanced NBI's with a similar physical dimension and same ion source, the input-torque is close to zero if the power delivered to them is similar. In the DIII-D tokamak, the 150 beamline is physically smaller than the rest (its design facilitates the off-axis injection of particles), and also the ion source is different. For the 150 beamline to deliver the same input-torque as the other beamlines by means of the same power, its voltage would need to be adjusted. Although it is more convenient to pair the NBI's of the other three beamlines (30, 210, and 330) to produce zero input-torque because no voltage adjustment is required, the 150 beamline may also be employed, and is kept as a backup in case any of the other beamlines cannot be employed. Thus, two groups of balanced NBI's are considered: a first group composed by 30L, 150L, 330L and 210R, and a second group composed by 30R, 150R, 330R and 210L. In terms of the power injected, the zero input-torque condition is written as

$$P_{30\mathrm{L}} + P_{150\mathrm{L}} + P_{330\mathrm{L}} = P_{210\mathrm{R}}, \;\; P_{30\mathrm{R}} + P_{150\mathrm{R}} + P_{330\mathrm{R}} = P_{210\mathrm{L}}, \tag{5.16}$$

where $P_{(\cdot)}$ is the power injected by the $(\cdot)$ NBI.

By using the zero input-torque configuration, the model substantially changes because the current driven by the co-current and counter-current NBIs mostly cancels out. Then, there is no net current-density driven by the NBI's, i.e., the second term on the right hand side of (5.1) is zero, $\sum_{i=1}^{N_{NBI}} h_{NBI,i}(\hat{\rho},t)P_{NBI,i}(t) = 0$. The term $P_{NBI,i}$ only enters in (5.1) by affecting $P_{tot}(t)$ through the functions h_{diff}, h_{EC}

and h_{BS}, given by (5.2)-(5.6). Therefore, the relevant magnitude for q_0 control is the total NBI power, denoted by $P_{NBI} \triangleq \sum_i P_{NBI,i}$, instead of the individual powers of each NBI, $P_{NBI,i}$. Moreover, the same situation is found for the W dynamics, equation (2.64): P_{NBI} is the only relevant magnitude. With the previous arguments, equation (5.11) adopts a different shape given by

$$\dot{\tilde{x}} = A(t)\tilde{x} + B_1(t)\tilde{P}_{NBI}(t) + B_2(t)\tilde{P}_{EC}(t) = A(t)\tilde{x} + [B_1(t)\ B_2(t)] \begin{bmatrix} \tilde{P}_{NBI}(t) \\ \tilde{P}_{EC}(t) \end{bmatrix}, \quad (5.17)$$

where $B_1(t) \in \mathbb{R}^{N\times 1}$ is the time-varying input matrix associated to $\tilde{P}_{NBI}$. Then, the linearized system is still a MIMO LTV system, but with 2 controllable inputs instead of the $N_{NBI} + 1$ that were considered before taking into account the zero input-torque condition.

5.2.5 q_0 Control Law Design

In [85], only control of q_0 was considered. The control objective is to drive q_0 to its nominal trajectory $\bar{q}_0$, or equivalently, $\tilde{q}_0 \triangleq q_0 - \bar{q}_0$ to zero. Even though the q_0 subsystem in (5.17)-(5.12) is a time-varying system, the system matrices A, B_1, B_2, and C are particularized at a reference time t_{ref} for control design. The $\psi + q_0$ subsystem in (5.17)-(5.12) is given by

$$\dot{\tilde{\psi}} = A_\psi \tilde{\psi} + B_\psi \begin{bmatrix} \tilde{P}_{NBI}(t) \\ \tilde{P}_{EC}(t) \end{bmatrix}, \quad \tilde{q}_0 = C_\psi \tilde{\psi}, \quad (5.18)$$

where $\tilde{\psi} \triangleq \hat{\psi} - \bar{\psi}$, $A_\psi \in \mathbb{R}^{(N-1)\times(N-1)}$ is the subpart of $A(t_{ref})$ given by its first $N-1$ rows and columns, $B_\psi \in \mathbb{R}^{(N-1)\times 2}$ is the subpart of $[B_1(t_{ref})\ B_2(t_{ref})]$ given its first $N-1$ rows, and $C_\psi \in \mathbb{R}^{1\times(N-1)}$ is the subpart of $C(t_{ref})$ given by its first row. The control law for $\tilde{P}_{NBI}$ and $\tilde{P}_{EC}$ is given by

$$\begin{bmatrix} \tilde{P}_{NBI} \\ \tilde{P}_{EC} \end{bmatrix} = \begin{bmatrix} K_{p_1} \\ K_{p_2} \end{bmatrix} \tilde{q}_0 + \begin{bmatrix} 1/T_{i_1} \\ 1/T_{i_2} \end{bmatrix} \int_{t_0}^{t} \tilde{q}_0 dt + \begin{bmatrix} T_{d_1} \\ T_{d_2} \end{bmatrix} \frac{d\tilde{q}_0}{dt}, \quad (5.19)$$

where K_{p_1}, T_{i_1}, T_{d_1}, K_{p_2}, T_{i_2} and T_{d_2} are design parameters which are adopted to obtain a desired response of the closed-loop $\psi + q_0$ subsystem, which is given by

$$\dot{\tilde{\psi}} = [A_\psi + B_\psi K_p C_\psi]\,\tilde{\psi} + B_\psi K_i C_\psi \int_{t_0}^{t} \tilde{\psi} dt + B_\psi K_d C_\psi \frac{d\tilde{\psi}}{dt}, \tag{5.20}$$

where $K_p = [K_{p_1} \;\; K_{p_2}]^T$, $K_i = [1/T_{i_1} \;\; 1/T_{i_2}]^T$, $K_d = [T_{d_1} \;\; T_{d_2}]^T$, and t_0 is the initial time in which the integral of the error starts to be computed. Once that $P_{NBI} = \bar{P}_{NBI} + \tilde{P}_{NBI}$ is computed, $P_{NBI,i}$ are computed using the zero input-torque condition given by (5.16). However, in general there are 8 NBI's available, but the control law (5.19) and the zero-torque condition only impose three constraints, so five additional conditions/constraints must be specified in order to univocally determine $P_{NBI,i}$ (i = 1, ..., 8) from P_{NBI}. These additional conditions are based on the requirements of each particular scenario. An example of the type of conditions imposed is shown in the simulation studies and experiments reported in [85, 86], and described in Sections 5.2.6, 5.2.8, and 5.2.9.

5.2.6 Simulation Testing of the q_0 Control Law

The simulation study for q_0-only control is carried out for a zero input-torque, H-mode, reverse plasma-current ($I_p < 0$) scenario in DIII-D (the same as in Section 5.2.2). Although the controller is ultimately synthesized from the linear model (5.18), it is tested based on the nonlinear model (5.9) by means of a COTSIM simulation which employs the q_0 model validated in Section 5.2.2. It can be noted that there are two controllable inputs (P_{NBI} and P_{EC}) to control only one output (q_0). Also, as the total available energy in the EC launchers (also known as *gyrotrons*) during a shot is limited, it may be convenient to use EC only in the most demanding situations. For such reasons, EC is only used as a backup actuator in this simulation study, so if P_{NBI} is not saturated, then $\tilde{P}_{EC} = 0$. Therefore, the control law used in simulation is slightly different from (5.19), as it includes some logic to detect saturation of $P_{NBI} = 0$ and set $\tilde{P}_{EC} = 0$.

It is necessary to specify the additional conditions for the zero-input torque configuration. First, the 150 beamline is only used as a backup line due to its

aforementioned special characteristics. Then, the controller sets $P_{150\mathrm{L}} = P_{150\mathrm{R}} = 0$ unless any of the other NBI fails, and extra power is needed to produce zero NBI input-torque. Second, in order to obtain real-time q-profile reconstruction in DIII-D by means of MSE, it is necessary to keep $P_{30\mathrm{L}} \geq 1$ MW. Then, it is chosen that the controller keeps $P_{30\mathrm{L}} = 1$ MW. Third, the 30R NBI is not used ($P_{30\mathrm{R}} = 0$) to reproduce the conditions of shot 163520. Equations (5.16) become

$$1 \text{ MW} + P_{330\mathrm{R}} = P_{210\mathrm{L}}, \tag{5.21}$$

$$P_{330\mathrm{L}} = P_{210\mathrm{R}}. \tag{5.22}$$

Finally, it is imposed that each group of balanced NBI's injects the same amount of power, except if $\tilde{P}_{NBI}$ as computed by the control law (5.19) is not high enough to ensure $P_{30\mathrm{L}} = 1$ MW. In such case, all the power is injected by the first group of balanced beams (where 30L belongs to) in order to ensure q-profile reconstruction. All the introduced conditions allow for univocally determining $\tilde{P}_{NBI,i}(t)$ ($i = 1, ..., 8$) once that $\tilde{P}_{NBI}(t)$ has been determined from the control law (5.19).

First, an open-loop, feedforward-only simulation is executed with the experimental inputs P_{NBI} and P_{EC} corresponding to the shot 163520, and the q_0 evolution obtained is denoted by q_0^{exp} . Based on q_0^{exp}, a target $\bar{q}_0$ is computed. The target $\bar{q}_0$ is taken as $+15\%$ of the q_0^{exp} evolution, i.e., $\bar{q}_0 = 1.15 q_0^{exp}$. Such choice is based upon the requirement $q_0 \geq 1$, necessary to avoid sawtooth instabilities. Second, a closed-loop simulation with disturbances is executed in which the controller attempts to regulate q_0 around $\bar{q}_0$. To make the simulation testing more challenging for the controller, a fictitious -20% decrease in j_{BS} is introduced during all the shot, representing some source of unknown variation in the bootstrap current density. Moreover, a constant -15% disturbance in q_0 is introduced between 4 s and 6 s, emulating some unexpected MHD activity. Finally, an open-loop, feedforward-only simulation using the previously described disturbances and experimental inputs is executed to explore the system's evolution with disturbances but without control.

Fig. 5.3(a) shows the q_0 evolution in open loop with disturbances (magenta dashed-dotted), in open loop without disturbances, q_0^{exp} (black dashed-dotted), and in closed loop with disturbances (blue solid), together with the target $\bar{q}_0$ (red

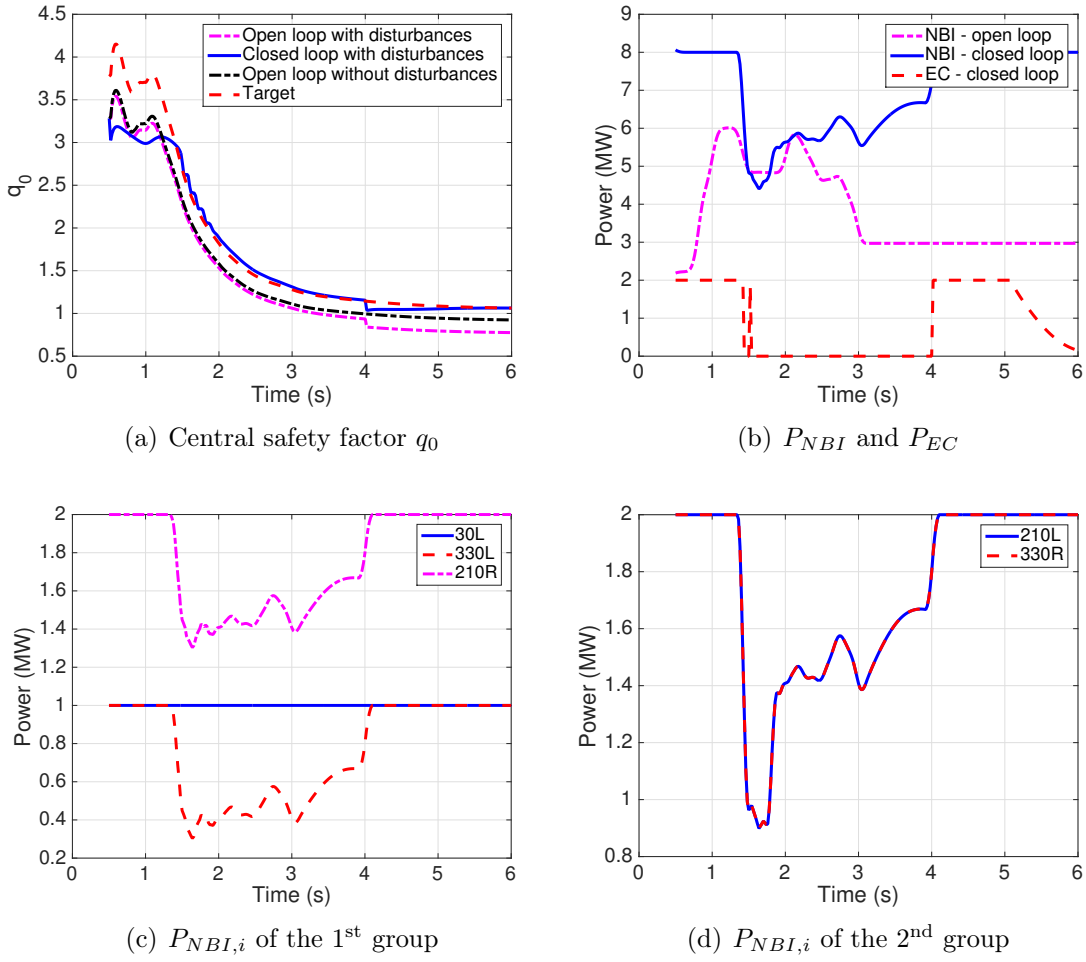

(a) Central safety factor q_0

(b) P_{NBI} and P_{EC}

(c) $P_{NBI,i}$ of the 1st group

(d) $P_{NBI,i}$ of the 2nd group

Figure 5.3: Simulation study for q_0 control: (a) q_0, (b) P_{NBI} and P_{EC}, (c) NBI powers in closed loop, 1^{st} balanced group: $P_{30\text{L}}$, $P_{330\text{L}}$ and $P_{210\text{R}}$, and (d) NBI powers in closed loop, 2^{nd} balanced group: $P_{330\text{R}}$ and $P_{210\text{L}}$.

dashed). Fig. 5.3(b) shows the evolution of P_{NBI} and P_{EC} during the open-loop and closed-loop simulations (note that P_{EC} is zero in open loop). Fig. 5.3(c) shows NBI powers in closed loop corresponding to the first balanced group, and Fig. 5.3(d) shows NBI powers in closed loop corresponding to the second balanced group. As it can be seen in Fig. 5.3(a), from the initial time till 4 s, the open-loop simulation with disturbances shows that q_0 is smaller than without disturbances, q_0^{exp}. Also, the controller successfully drives q_0 to $\bar{q}_0$ in closed loop till 4 s, when a sudden drop is suffered because of the constant q_0 disturbance introduced at that moment. After

4 s, the open-loop simulation with disturbances shows a constant drop in q_0, while the closed-loop simulation shows that the controller drives q_0 back to its reference value and is capable of keeping $q_0 \geq 1$, as desired. As it can be seen in Fig. 5.3(b), while P_{NBI} is modulated by the controller during the whole shot, P_{EC} is only used as a backup actuator when P_{NBI} is saturated between the beginning of the shot and ≈ 1.3 s (in order to achieve reference tracking), and between 4 s and ≈ 5.25 s (to recover from the sudden q_0 drop introduced as a disturbance).

5.2.7 $q_0 + \beta_N$ Control Design

As reported in [86], a controller for $q_0 + \beta_N$ was designed for experimental testing in DIII-D. The control objective is to drive $x = [q_0, \beta_N]^T$ to its nominal trajectory $\bar{x} = [\bar{q}_0, \bar{\beta}_N]^T$, or equivalently, $\tilde{x} \triangleq x - \bar{x}$ to zero. Similarly to the q_0-only control case, the control laws for $\tilde{P}_{NBI}$ and $\tilde{P}_{EC}$ are given by

$$\begin{bmatrix} \tilde{P}_{NBI} \\ \tilde{P}_{EC} \end{bmatrix} = K_p^* \begin{bmatrix} \tilde{q}_0 \\ \tilde{\beta}_N \end{bmatrix} + K_i^* \begin{bmatrix} \int_{t_0}^t \tilde{q}_0 dt \\ \int_{t_0}^t \tilde{\beta}_N dt \end{bmatrix}, \tag{5.23}$$

where K_p^* and K_i^* are 2×2 matrices designed to obtain a desired response of the closed-loop system, which is given by

$$\dot{\tilde{x}} = \left[A(t_{ref}) + B(t_{ref}) K_p^* C(t_{ref})\right] \tilde{x} + B(t_{ref}) K_i^* C(t_{ref}) \int_{t_0}^t \tilde{x} dt. \tag{5.24}$$

The constant matrices K_p^* and K_i^* ease the implementation of the controller in the DIII-D PCS. As before, once that $P_{NBI} = \bar{P}_{NBI} + \tilde{P}_{NBI}$ is computed, $P_{NBI,i}$ are computed using the zero input-torque condition given by (5.16) and additional conditions/constraints.

5.2.8 Simulation Testing of the $q_0 + \beta_N$ Control Law

In order to test the $q_0 + \beta_N$ controller in simulations before its experimental testing in DIII-D, a simulation study is carried out for the same scenario and using the same COTSIM models as in Section 5.2.2. In this case, the zero input-torque

conditions (5.21)-(5.22) are also employed, but P_{EC} is employed without logic to detect P_{NBI} saturation. First, an open loop simulation is run using essentially[3] the same experimental inputs as in Section 5.2.6 (without disturbances). A reference is then computed as $\bar{q}_0 = 1.15 q_0^{exp}$ and $\bar{\beta}_N = 1.2\beta_N^{exp}$, where β_N^{exp} is the open loop evolution for β_N obtained with the experimental inputs from shot 163520. Second, a closed-loop simulation is executed in which the controller attempts to regulate $q_0 + \beta_N$ around $\bar{q}_0$ and $\bar{\beta}_N$, respectively.

Fig. 5.4(a) shows the q_0 evolution in open loop, q_0^{exp} (magenta dashed-dotted), and closed loop (blue solid), together with the target $\bar{q}_0$ (red dashed). Fig. 5.4(b) shows the same signals for β_N. Fig. 5.4(c) shows NBI powers corresponding to the first balanced group, Fig. 5.4(d) shows the NBI powers corresponding to the second balanced group, and Fig. 5.4(e) shows P_{NBI} and P_{EC}, all in open loop and closed loop. Note that P_{EC} is zero in open loop, and almost zero for the entire simulation in closed loop. Good regulation of both q_0 and β_N can be appreciated, while maintaining the balanced NBI configuration.

5.2.9 Experimental Testing of the $q_0 + \beta_N$ Control Law

The algorithm derived in Section 5.2.7 was experimentally tested in the DIII-D tokamak in April, 2017. A shot that illustrates the controller's performance is 170685. Just like the scenario used for model validation and controller simulation testing, the experimental test was carried out in a reverse-I_p, H-mode scenario. The NBIs were configured in two groups: 30L and 330L balanced by 210R, and 150R (330R was not available during the experiment) balanced by 210L. The voltage of the 150R NBI was adjusted so that $P_{150R} = P_{210L}$ ensured zero input-torque. Also, in a similar fashion as in the simulation tests, $P_{30L} = 1.2$ MW and $P_{30R} = 0$ were imposed for MSE measurements and q-profile reconstruction.

Fig. 5.5 shows the q_0 and β_N evolutions with their respective targets during shot 170685, together with the ion toroidal velocity, $v_{\phi,i}$, energy confinement time and

[3]For numerical reasons, a slightly different initial condition for the experimental inputs (see Fig. 5.3(b) and Fig. 5.4(e)) is employed to avoid the initial bumps in the q_0 evolution in Fig. 5.3(a).

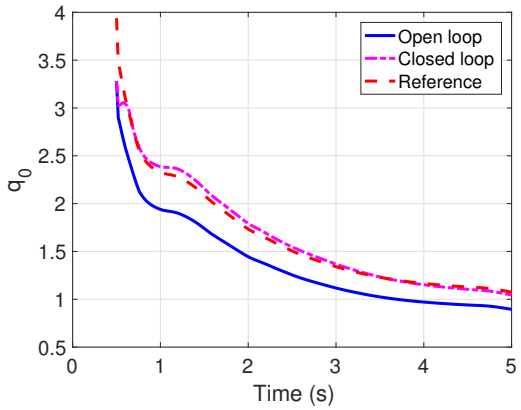

(a) Central safety factor q_0

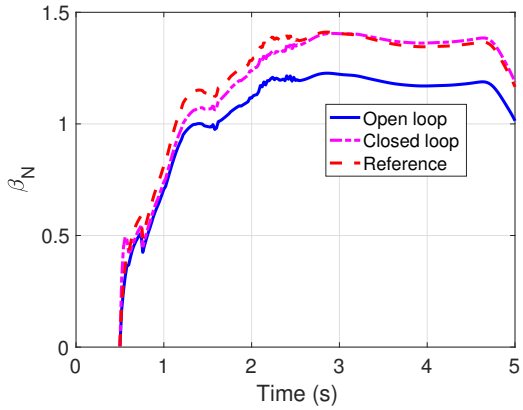

(b) Normalized beta β_N

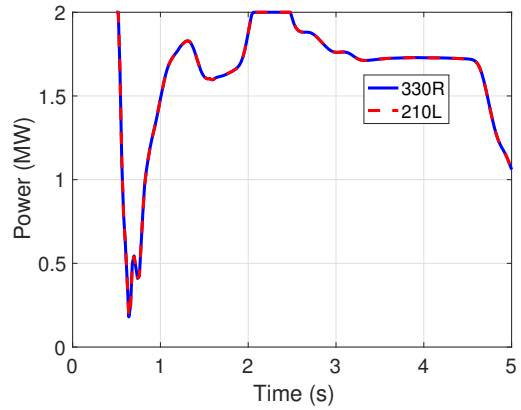

(c) $P_{NBI,i}$ of the 1st group

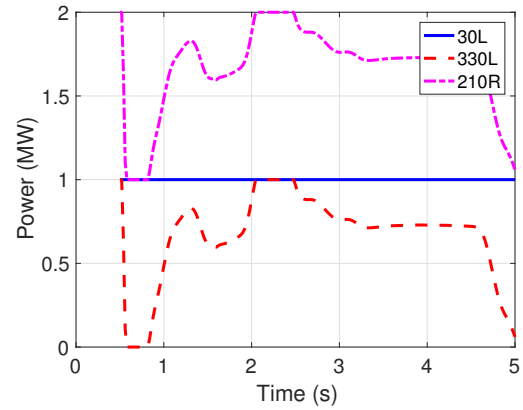

(d) $P_{NBI,i}$ of the 2nd group

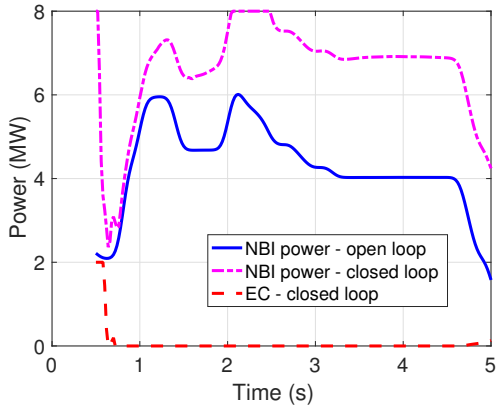

(e) P_{NBI} and P_{EC}

Figure 5.4: Simulation study for $q_0 + \beta_N$ control: (a) q_0, (b) β_N, (c) NBI powers in closed loop, 1^{st} balanced group: $P_{30\text{L}}$, $P_{330\text{L}}$ and $P_{210\text{R}}$, (d) NBI powers in closed loop, 2^{nd} balanced group: $P_{330\text{R}}$ and $P_{210\text{L}}$, and (e) P_{NBI} and P_{EC}.

H-factor, τ_E and H_H, NBI torque, T_{NBI}, and total EC and NBI powers, P_{NBI} and P_{EC}. As shown in Fig. 5.5(a) and Fig. 5.5(b), the controller is capable of regulating both q_0 and β_N around their targets during the initial stage of the shot. However, an NTM develops and possibly locks, see Fig. 5.6. Although the MHD activity starts at around 1.5 s (see the MHD $n = 2$ and $n = 3$ amplitudes in Fig. 5.6(a)), it seems that the NTM with the highest strength is the one with MHD $n = 1$ amplitude (most likely a $m/n = 2/1$ NTM), which develops at around 1.75 s. The development of the NTM affects β_N, which is decreased (see also the reduction in τ_E and H_H in Fig. 5.5(d)), but does not seem to have a strong impact on q_0, which can still be kept very close to its target. However, slightly after 2 s, the external saddle loop differenced (ESLD) signals indicate possible locking of the NTM (as appreciated by the sudden change in such signals, see Fig. 5.6(b), Fig. 5.6(c) and Fig. 5.6(d)), and q_0 drops and cannot recover despite employing the maximum available P_{EC}, see Fig. 5.5(f). From Fig. 5.5(c) and Fig. 5.5(e), it can also be seen that when T_{NBI} is driven to zero, $v_{\phi,i}$ substantially decreases (and possibly makes the NTM lock). Finally, Fig. 5.6(e) and Fig. 5.6(f) show how the controller keeps the balanced NBI configuration by imposing the conditions $P_{30L} + P_{330L} = P_{210L}$ and $P_{150R} = P_{210L}$.

5.2.10 Conclusions

A controller for simultaneous regulation of $q_0 + \beta_N$ has been designed during this dissertation work by using approximate linearization techniques. The controller is specially envisioned for zero NBI torque scenarios. It has been tested both in simulations using COTSIM and in experiments in the DIII-D tokamak. Although the controller's performance seems to be acceptable while MHD instabilities are not triggered, the experimental results obtained are not totally conclusive due to the small time window in which the plasma was free of NTMs. As a matter of fact, the $q_0 + \beta_N$ experimental test demonstrates that integrated control strategies will be required in future tokamaks, as they provide a much better performance than isolated controllers. In this case, the $q_0 + \beta_N$ controller could have been equipped with an NTM suppression algorithm to allow for better regulation of q_0 and β_N.

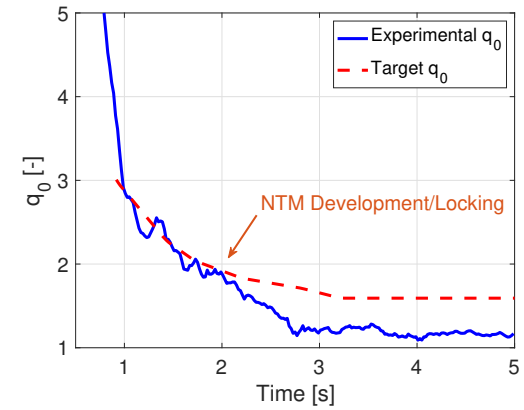

(a) Central safety factor q_0

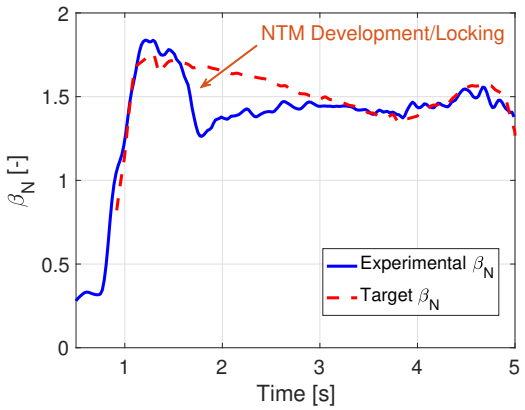

(b) Normalized beta β_N

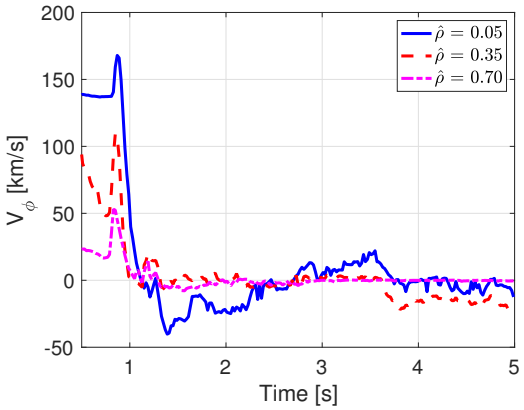

(c) Ion toroidal velocity $v_{\phi,i}$

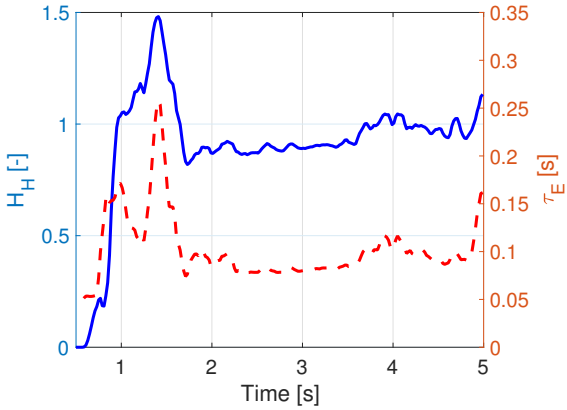

(d) τ_E and H_H

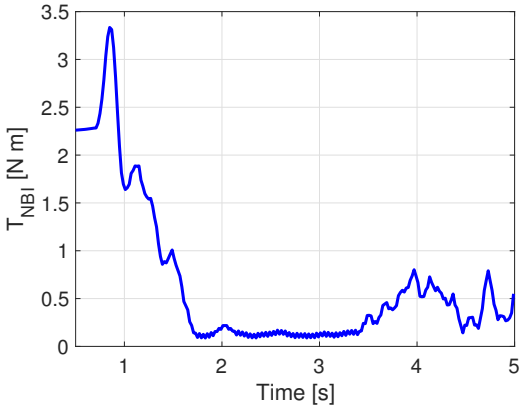

(e) NBI torque T_{NBI}

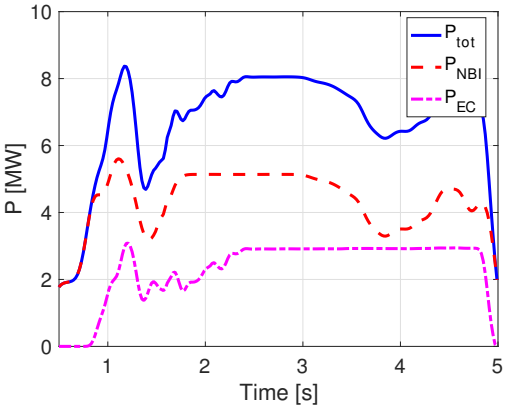

(f) P_{NBI} and P_{EC}

Figure 5.5: Experimental results for shot 170685: (a) q_0, (b) β_N, (c) ion toroidal rotation $v_{\phi,i}$ from CER measurements, (d) τ_E and H_H, (e) NBI torque, T_{NBI}, and (f) P_{NBI} and P_{EC}.

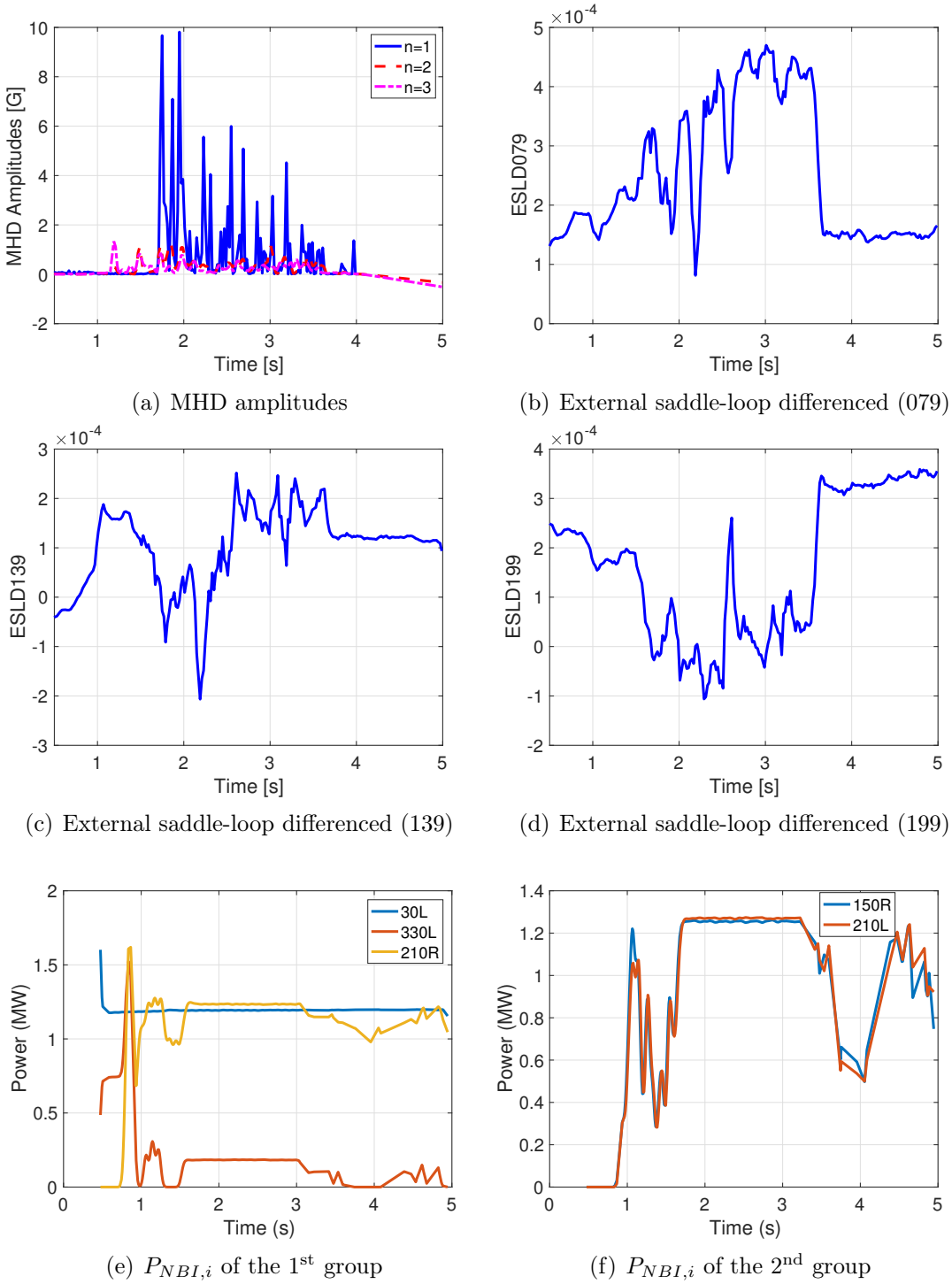

(a) MHD amplitudes

(b) External saddle-loop differenced (079)

(c) External saddle-loop differenced (139)

(d) External saddle-loop differenced (199)

(e) $P_{NBI,i}$ of the 1st group

(f) $P_{NBI,i}$ of the 2nd group

Figure 5.6: Experimental results for shot 170685: (a) MHD amplitudes, (b), (c) and (d) external-saddle loops (ESL) differenced signals, (e) 1^{st} balanced group: $P_{30\text{L}}$, $P_{330\text{L}}$ and $P_{210\text{R}}$, and (f) 2^{nd} balanced group: $P_{150\text{R}}$ and $P_{210\text{L}}$.

5.3 q-profile + β_N Control via Feedback Linearization and Lyapunov Redesign Techniques

5.3.1 Modeling of the q + β_N Dynamics

The model employed in this Section is basically the one introduced in Chapter 2, Section 2.2.1 (for q) and Section 2.3.1 (for β_N). In order to model uncertainties in T_e and n_e, the models given by (2.34) are modified as

$$T_e(\hat{\rho},t) = T_e^{prof}(\hat{\rho}) I_p(t)^{\gamma} P_{tot}(t)^{\epsilon} \bar{n}_e(t)^{\zeta} + \delta_{T_e}(\hat{\rho},t), \tag{5.25}$$

$$n_e(\hat{\rho},t) = n_e^{prof}(\hat{\rho}) \bar{n}_e(t) + \delta_{n_e}(\hat{\rho},t), \tag{5.26}$$

where δ_{T_e} and δ_{n_e} are uncertain terms to which a bound can be estimated based on experimental and physical constraints. Because η and $\langle \vec{j}_{ni} \cdot \vec{B} \rangle / B_{\phi,0}$ are functions of T_e and n_e, they can be written as

$$\eta(\hat{\rho},t) = \eta^{nom}(\hat{\rho},t) + \delta_{\eta}(\hat{\rho},t), \quad \langle \vec{j}_{ni} \cdot \vec{B} \rangle / B_{\phi,0}(\hat{\rho},t) = \langle \vec{j}_{ni} \cdot \vec{B} \rangle / B_{\phi,0}^{nom}(\hat{\rho},t) + \delta_{j_{ni}}(\hat{\rho},t), \tag{5.27}$$

where η^{nom} and $\langle \vec{j}_{ni} \cdot \vec{B} \rangle / B_{\phi,0}^{nom}$ are given by (2.30)-(2.31), and δ_{η} and $\delta_{j_{ni}}$ are uncertain terms to which a bound can be estimated because they are directly related to the uncertainties in (5.25)-(5.26). The MDE (2.27) can be rewritten as

$$\frac{\partial \psi}{\partial t} = \frac{\eta^{nom}}{\mu_0 \rho_b^2 \hat{F}^2 \hat{\rho}} \frac{\partial}{\partial \hat{\rho}} \left(\hat{\rho} D_{\psi} \frac{\partial \psi}{\partial \hat{\rho}} \right) + \eta^{nom} R_0 \hat{H} j_{ni}^{nom} + \delta_{\psi}, \tag{5.28}$$

where δ_{ψ} is an uncertain term given by

$$\delta_{\psi}(\hat{\rho},t) = \frac{\delta_{\eta}(\hat{\rho},t)}{\mu_0 \rho_b^2 \hat{F}(\hat{\rho})^2 \hat{\rho}} \frac{\partial}{\partial \hat{\rho}} \left(\hat{\rho} D_{\psi}(\hat{\rho}) \frac{\partial \psi(\hat{\rho},t)}{\partial \hat{\rho}} \right) + R_0 \hat{H}(\hat{\rho}) \left(\eta^{nom}(\hat{\rho},t) \delta_{j_{ni}}(\hat{\rho},t) + j_{ni}^{nom}(\hat{\rho},t) \delta_{\eta}(\hat{\rho},t) + \delta_{\eta}(\hat{\rho},t) \delta_{j_{ni}}(\hat{\rho},t) \right). \tag{5.29}$$

Finally, the 0D balance for W given in equation (2.70) is employed. It can be noted that uncertainties are found in both the ψ and W subsystems.

5.3.2 Model Validation for DIII-D Shot 147634

The nominal model (without uncertainties) given by (5.28)-(2.70) was tailored and validated for an H-mode, advanced DIII-D scenario (shot 147634) in previous work [18, 90]. This scenario is also employed in this work for control design and simulation testing, as it represents a feasible scenario in which q-profile + β_N may be needed. Therefore, the model tailoring and validation carried out in [18, 90] is utilized for this dissertation work.

5.3.3 Reduced Model of the q-profile + β_N Dynamics

By employing the definition of the poloidal flux gradient (2.94), taking derivative with respect to $\hat{\rho}$ in (5.28), and using the finite differences method over $N+1$ nodes (in a similar fashion as in Section 5.2.3, but using θ instead of ψ), the model composed by (5.28) and (2.70) can be rewritten as,

$$\frac{d}{dt}\begin{bmatrix} W \\ \hat{\theta} \end{bmatrix} = \begin{bmatrix} F(W, I_p, P_{NBI,i}, P_{EC}) \\ G(\hat{\theta}, I_p)u(I_p, P_{NBI,i}, P_{EC}) \end{bmatrix} + \begin{bmatrix} \delta_W \\ \hat{\delta}_\theta \end{bmatrix}, \tag{5.30}$$

where $\hat{\theta} = [\theta_1, ..., \theta_m, ..., \theta_{N-1}]^T$ is the vector of θ values at the interior discretization nodes, θ_m $(m = 1, ..., N-1)$, $\hat{\delta}_\theta = [\delta_{\theta,1}, ..., \delta_{\theta,N-1}]^T$ is the vector of δ_θ values at the interior discretization nodes, $\delta_{\theta,m}$, where $\delta_\theta = \partial\delta_\psi/\partial\hat{\rho}$, $F \triangleq -W/\tau_E^{nom} + P_{tot}$, and $u = [u_\eta, u_{NBI,1}, ..., u_{NBI,N_{NBI}}, u_{EC}, u_{BS}]^T$ is the virtual input vector, which is a function of the physical inputs to the system I_p, $P_{NBI,i}$ $(i = 1, ...N_{NBI})$, P_{EC}, and $\bar{n}_e$,

$$u_\eta = I_p^{-3\gamma/2} P_{tot}^{-3\epsilon/2} \bar{n}_e^{-3\zeta/2}, \tag{5.31}$$

$$u_{NBI,i} = I_p^{\gamma(\lambda_{NB}-\frac{3}{2})} P_{tot}^{\epsilon(\lambda_{NBI,i}-\frac{3}{2})} \bar{n}_e^{\zeta(\lambda_{NB}-\frac{3}{2})-1} P_{NBI,i}, \tag{5.32}$$

$$u_{EC} = I_p^{\gamma(\lambda_{EC}-\frac{3}{2})} P_{tot}^{\epsilon(\lambda_{EC}-\frac{3}{2})} \bar{n}_e^{\zeta(\lambda_{EC}-\frac{3}{2})-1} P_{EC}, \tag{5.33}$$

$$u_{BS} = I_p^{-\gamma/2} P_{tot}^{-\epsilon/2} \bar{n}_e^{1-\zeta/2}. \tag{5.34}$$

The matrix $G \in \mathbb{R}^{(N-1)\times(N_{NBI}+3)}$ was introduced in [87, 88], and is described next. For convenience, G can be divided into three subparts,

$$G(\hat{\theta}, I_p) = [G_\eta(\hat{\theta}, I_p), G_{aux}, G_{BS}(\hat{\theta}, I_p)]. \tag{5.35}$$

The first subpart, $G_\eta \in \mathbb{R}^{(N-1)\times 1}$, is associated with u_η, and is given by

$$G_\eta(\hat{\theta}, I_p) = \begin{bmatrix} \gamma_1\theta_1 + \beta_1\theta_2 \\ \alpha_2\theta_1 + \gamma_2\theta_2 + \beta_2\theta_3 \\ \vdots \\ \alpha_{N-2}\theta_{N-3} + \gamma_{N-2}\theta_{N-2} + \beta_{N-2}\theta_{N-1} \\ \alpha_{N-1}\theta_{N-2} + \gamma_{N-1}\theta_{N-1} - \beta_{N-1}k_{I_p}I_p \end{bmatrix}, \tag{5.36}$$

where $\gamma_{(\cdot)}$, $\beta_{(\cdot)}$ and $\alpha_{(\cdot)}$ are constants that depend on the model parameters and profiles. The second subpart, $G_{aux} \in \mathbb{R}^{(N-1)\times N_{aux}}$, is constant in time because it does not depend on θ. It is associated with $u_{NBI,i}$ and u_{EC}, and is given by

$$G_{aux} = \begin{bmatrix} h^1_{NBI,1} & \dots & h^1_{NBI,N_{NBI}} & h^1_{EC} \\ h^2_{NBI,1} & \dots & h^2_{NBI,N_{NBI}} & h^2_{EC} \\ \vdots & \ddots & \vdots & \vdots \\ h^{N-2}_{NBI,1} & \dots & h^{N-2}_{NBI,N_{NBI}} & h^{N-2}_{EC} \\ h^{N-1}_{NBI,1} & \dots & h^{N-1}_{NBI,N_{NBI}} & h^{N-1}_{EC} \end{bmatrix}, \tag{5.37}$$

where $h^{(\cdot)}_{NBI,i}$ and $h^{(\cdot)}_{EC}$ are constant parameters that depend on the deposition profiles associated with the $N_{aux} \triangleq N_{NBI} + 1$ auxiliary sources. The third subpart, $G_{BS} \in \mathbb{R}^{(N-1)\times 1}$, is associated with u_{BS}, and is given by

$$G_{BS}(\hat{\theta}, I_p) = \begin{bmatrix} \frac{h^1_{BS,1}}{\theta_1} - \frac{h^1_{BS,2}}{\theta_1^2}\frac{\theta_2}{2\Delta\hat{\rho}} \\ \frac{h^2_{BS,1}}{\theta_2} - \frac{h^2_{BS,2}}{\theta_2^2}\frac{\theta_3-\theta_1}{2\Delta\hat{\rho}} \\ \vdots \\ \frac{h^{N-2}_{BS,1}}{\theta_{N-2}} - \frac{h^{N-2}_{BS,2}}{\theta^2_{N-2}}\frac{\theta_{N-1}-\theta_{N-3}}{2\Delta\hat{\rho}} \\ \frac{h^{N-1}_{BS,1}}{\theta_{N-1}} - \frac{h^{N-1}_{BS,2}}{\theta^2_{N-1}}\frac{-k_{I_p}I_p-\theta_{N-2}}{2\Delta\hat{\rho}} \end{bmatrix}, \tag{5.38}$$

where $h_{BS,(\cdot)}$ are constants that depend on the model profiles and parameters related to the bootstrap current term. The relationship between the $\alpha_{(\cdot)}$, $\beta_{(\cdot)}$, $\gamma_{(\cdot)}$, and $h_{(\cdot)}$ functions and the MDE model profiles and parameters can be found in Appendix E.1.

Although θ and W compose the system's state vector, the outputs of interest are q and β_N. The relationship between q and θ can be easily obtained from their

definitions, equations (2.12) and (2.94), as

$$q = -\frac{B_{\phi,0}\rho_b^2\hat{\rho}}{\theta}, \tag{5.39}$$

whereas the relationship between W and β_N is given by (5.8). Hence, the system's output equation can be written as

$$\begin{bmatrix} \beta_N \\ \hat{q} \end{bmatrix} = \begin{bmatrix} h_1(W, I_p) \\ h_2(\hat{\theta}) \end{bmatrix}, \tag{5.40}$$

where $h_1 = \frac{\frac{4}{3}\mu_0 W a}{B_{\phi,0} I_p V_p}$, h_2 is defined by (5.39), and $\hat{q}$ is the vector of q values at the interior discretization nodes. As introduced above, the controllable inputs considered in this Section are I_p, $P_{NBI,i}$ $(i = 1, ...N_{NBI})$, and P_{EC}, whereas $\bar{n}_e$ is considered as a non-controllable input to the system.

Finally, the MDE boundary condition at $\hat{\rho} = 1$, (2.28), determines the evolution of the edge safety factor, q_{edge}. The boundary condition (2.28) and the relationship between $\theta(\hat{\rho} = 1) \triangleq \theta_N$ and q_{edge}, equation (2.118), can be rewritten as

$$\theta_N = -k_{I_p} I_p, \quad q_{edge} = -\frac{B_{\phi,0}\rho_b^2}{\theta_N}. \tag{5.41}$$

5.3.4 Boundary Control (q_{edge} Control) by Means of I_p Modulation

The first step in the control design is to synthesize a control law for I_p in order to regulate q_{edge} around a desired target value, $\bar{q}_{edge}$, or equivalently, to regulate θ_N around a desired value $\bar{\theta}_N = -B_{\phi,0}\rho_b^2/\bar{q}_{edge}$. From (5.41), it can be seen that if I_p is taken as

$$I_p = -\frac{\bar{\theta}_N}{k_{I_p}} = \frac{B_{\phi,0}\rho_b^2}{k_{I_p}\bar{q}_{edge}}, \tag{5.42}$$

then $q_{edge} = \bar{q}_{edge}$, fulfilling the desired control objective. As long as $\bar{q}_{edge}$ is known a priori, the control law (5.42) can actually be seen as a feedforward control law. This is due to the fact that q_{edge} has no dynamics in this model, as it can be seen from (5.41).

5.3.5 Energy Control (W Control) by Means of P_{tot} Modulation

The second step in the control design is to synthesize a control law for P_{tot} in order to regulate W around a desired target value, denoted by $\bar{W}$, or equivalently, to regulate β_N around a desired target value given by $\bar{\beta}_N \triangleq \frac{\frac{4}{3}\mu_0 \bar{W} a}{B_{\phi,0} I_p V_p}$. From this definition for $\bar{\beta}_N$, it is straightforward to see that $\bar{q}_{edge}$ and $\bar{\beta}_N$ are not independent because I_p is given by (5.42). Thus, W is employed instead of β_N for control design, because q_{edge} does not enter its definition. Lyapunov theory and redesign techniques are employed for the nominal and robust control laws, respectively (see Appendices C.1.2 and C.2.2, and/or [65]).

The derivation of the nominal control law for W follows the same ideas as the derivation of the E controller in Section 4.4.1. First, the nominal W-subsystem ($\delta_W = 0$) is considered,

$$\frac{dW}{dt} = -\frac{W}{\tau_E^{nom}} + P_{tot} \triangleq u_P, \tag{5.43}$$

where $u_P \triangleq -\frac{W}{\tau_E^{nom}} + P_{tot}$ is a virtual input defined just for the purpose of the control law derivation. If the right hand side of (5.43) is set as

$$u_P^{nom} = -\frac{W}{\tau_E^{nom}} + P_{tot} = -K_E \tilde{W} + \frac{d\bar{W}}{dt}, \tag{5.44}$$

where K_E is a design parameter and $\tilde{W} \triangleq W - \bar{W}$, then (5.43) is reduced to $d\tilde{W}/dt = -K_E \tilde{W}$, which ensures exponential stability of the nominal W-subsystem. The nominal energy confinement time, τ_E^{nom}, is a function only of the input P_{tot} (it has to be kept in mind that the control law (5.42) determines I_p, and that the machine parameters in (2.65) are assumed to be constant), thus the nonlinear equation (5.44) allows for computing the value of P_{tot} that stabilizes the nominal W-subsystem. Such value is denoted as P_{tot}^{nom}.

In the presence of the uncertainty δ_W, an extra term u_P^{rob} is added to u_P^{nom}, so that $u_P = u_P^{nom} + u_P^{rob}$ makes the W-subsystem robustly stable. The extra term u_P^{rob} is designed using Lyapunov redesign techniques. The W-subsystem dynamics

in (5.30) can be rewritten as

$$\frac{d\tilde{W}}{dt} = -\frac{d\bar{W}}{dt} - \frac{W}{\tau_E^{nom}} + P_{tot} + \delta_W \triangleq -\frac{d\bar{W}}{dt} + u_P + \delta_W, \tag{5.45}$$

where the definition of $\tilde{W}$ and u_P have been employed. Using the Lyapunov function $V_E = \frac{1}{2}\tilde{W}^2$, it is found that

$$\dot{V}_E = \tilde{W}\left(-\frac{d\bar{W}}{dt} + u_P^{nom}\right) + \tilde{W}\left(u_P^{rob} + \delta_W\right) = -K_E\tilde{W}^2 + \tilde{W}\left(u_P^{rob} + \delta_W\right), \tag{5.46}$$

where (5.44) has been employed. Taking $u_P^{rob} = -\eta_W\tilde{W}$, the second term on the right hand side of (5.46) becomes

$$\tilde{W}\left(u_P^{rob} + \delta_W\right) = -\tilde{W}^2\eta_W + \tilde{W}\delta_W \leq -\tilde{W}^2\eta_W + |\tilde{W}||\delta_W|, \tag{5.47}$$

which is ≤ 0 as long as $\eta_W \geq |\delta_W|/|\tilde{W}|$. If that is the case, the W-subsystem dynamics remains exponentially stable in the presence of δ_W. If an upper bound to δ_W is known, denoted by δ_W^{max}, then the control law

$$u_P^{rob} = -\delta_W^{max}\frac{\tilde{W}}{|\tilde{W}|} \tag{5.48}$$

ensures the global exponential stability of the W subsystem. The robust control law (5.48) needs to be modified to avoid division by zero when $|W| \to 0$. It can be shown that the control law

$$u_P^{rob} = -\delta_W^{max}\frac{\tilde{W}}{|\tilde{W}|}, \quad \text{if } \delta_W^{max}|W| \geq \epsilon, \tag{5.49}$$

$$u_P^{rob} = -(\delta_W^{max})^2\frac{\tilde{W}}{\epsilon}, \quad \text{if } \delta_W^{max}|W| < \epsilon, \tag{5.50}$$

where $\epsilon \to 0$ is a design parameter, ensures $|\tilde{W}| \leq f(\epsilon)$, where f is a class $\mathcal{K}$ function of ϵ.

Finally, P_{tot} can be obtained from (5.44) and (5.49)-(5.50) as

$$-\frac{W}{\tau_E^{nom}} + P_{tot} = -K_E\tilde{W} + \frac{d\bar{W}}{dt} - \delta_W^{max}\frac{\tilde{W}}{|\tilde{W}|}, \quad \text{if } \delta_W^{max}|\tilde{W}| \geq \epsilon \tag{5.51}$$

$$-\frac{W}{\tau_E^{nom}} + P_{tot} = -K_E\tilde{W} + \frac{d\bar{W}}{dt} - (\delta_W^{max})^2\frac{\tilde{W}}{\epsilon}, \quad \text{if } \delta_W^{max}|\tilde{W}| < \epsilon. \tag{5.52}$$

5.3.6 Analysis of the Nominal q-subsystem for Feedback Linearization

In this Section, the nominal $\hat{\theta}$-subsystem in (5.30) ($\hat{\delta}_\theta = 0$) is studied in order to determine if a feedback-linearization control law for the interior nodes of the q profile can be found together with the I_p control law (5.42) for q_{edge} control and the P_{tot} control law (5.51)-(5.52) for W (or β_N) control. Through feedback linearization, a change of variables $z = T(\hat{\theta})$ and/or a control law $u = r(\hat{\theta}, v)$, where v is an auxiliary input-variable, are sought so that the $\hat{\theta}$ dynamics can be rewritten as a linear system [65],

$$\frac{dz}{dt} = Az + Bv. \tag{5.53}$$

First, the $\hat{\theta}$-subsystem in (5.30) is rewritten as explained next. Because I_p is determined by (5.42), P_{tot} is determined by (5.51)-(5.52), and $\bar{n}_e$ is non-controllable, it is found that u_η and u_{BS} in (5.31) and (5.34) are totally determined at each time step. Therefore, the only virtual inputs left for interior q-profile control are $u_{NBI,i}$ and u_{EC}, although they are not independent due to the constraint imposed by the P_{tot} control law, (5.51)-(5.52). Thus, it is convenient to rewrite the nominal $\hat{\theta}$-dynamics (5.30)-(5.38) as

$$G_{aux}[u_{NBI,1}, ..., u_{NBI,N_{NBI}}, u_{EC}]^T = \frac{d\hat{\theta}}{dt} - [G_\eta u_\eta + G_{BS} u_{BS}]. \tag{5.54}$$

Next, G_{aux} is analyzed. If an inverse G_{aux}^{-1} exists, then the nominal feedback linearization problem could be solved with $z = \tilde{\theta} \triangleq \hat{\theta} - \bar{\theta}$ (where $\bar{\theta}$ is the target θ profile, related to the target q profile, $\bar{q}$, by $\bar{\theta} = -\rho_b^2 B_{\phi,0} \hat{\rho}/\bar{q}$) just by setting

$$[u_{NBI,1}, ..., u_{NBI,N_{NBI}}, u_{EC}]^T = G_{aux}^{-1} \left[-(G_\eta u_\eta + G_{BS} u_{BS}) + A\tilde{\theta} + Bv + \frac{d\bar{\theta}}{dt} \right]. \tag{5.55}$$

However, an issue arises if a control law like (5.55) is employed. It must be noted that G_{aux} may not be square, so its inverse would not exist. One may be tempted to easily solve this inconvenience by doing the finite-differences discretization over $N - 1 = N_{aux}$ interior nodes. However, it has to be taken into account that only $N_{aux} - 1$ virtual inputs are independent due to the P_{tot} control law, which acts as an

extra constraint. This implies that (5.55) is in fact an over-constrained problem, so feedback linearization would only be achieved in an approximate fashion (as in [87]). The over-constrained nature of the problem just confirms that q_{edge}, W (or β_N), and q at N_{aux} interior nodes cannot all be controlled simultaneously with the available actuators[4]. To solve this issue, (5.55) is modified by embedding the P_{tot} control law within the feedback linearization scheme as

$$\begin{bmatrix} G^*_{aux} \\ 1...1 \end{bmatrix} \begin{bmatrix} P_{NBI,1} \\ \vdots \\ P_{NBI,N_{NBI}} \\ P_{EC} \end{bmatrix} = \begin{bmatrix} -(G_\eta u_\eta + G_{BS} u_{BS}) + A\tilde{\theta} + Bv + \frac{d\bar{\theta}}{dt} \\ P_{tot} \end{bmatrix}, \tag{5.56}$$

where $G^*_{aux}[P_{NBI,1}, ..., P_{NBI,N_{NBI}}, P_{EC}]^T = G_{aux}[u_{NBI,1}, ..., u_{NBI,N_{NBI}}, u_{EC}]^T$, with $G_{aux} \in \mathbb{R}^{(N_{aux}-1)\times(N_{aux}-1)}$ (i.e., discretizing over $N-1 = N_{aux}-1$ nodes instead of N_{aux} nodes), and P_{tot} is the value obtained from (5.51)-(5.52). This results in a square system with N_{aux} unknowns and equations from which values of $P_{NBI,i}$ and P_{EC} can be determined for simultaneous β_N + q-profile control over $N_{aux}-1$ nodes. Therefore, (5.56) defines the feedback-linearization control law once A, B, and the auxiliary input-variable v are specified (see Sections 5.3.7 and 5.3.8).

Still, for the control law (5.56) to make sense, the matrix

$$G^* = \begin{bmatrix} G^*_{aux} \\ 1...1 \end{bmatrix}, \tag{5.57}$$

must be full rank, i.e., the model deposition profiles associated with each NBI and EC, $j^{dep}_{aux,i}$ (see equation (2.32)), must produce a full rank G^* matrix. During the control design, it is necessary to make sure that the considered NBI and EC sources have different enough deposition profiles that produce linearly independent columns in G^* (this idea was first considered for DIII-D in [88], but using the original matrix G). If that is not the case, then the NBI and EC sources must be "grouped" so that their deposition profiles compose a linearly independent set of vectors and G^* is full

[4]This conclusion could have also been hinted by inspecting the number of controllable inputs available for inner q-profile control ($N_{aux}-1$) vs the to-be-controlled variables (N_{aux}).

rank. In the case in which all the auxiliary sources have the same deposition profile, then at least one group must exist. Such case would correspond to having just one controllable input (the total power, P_{tot}), thus it would not be possible to combine interior q-profile control with boundary (q_{edge}) and diffusivity (β_N) control. This would not be an issue of the control algorithm itself, but just a lack of actuation capability for q-profile control within a given tokamak or scenario.

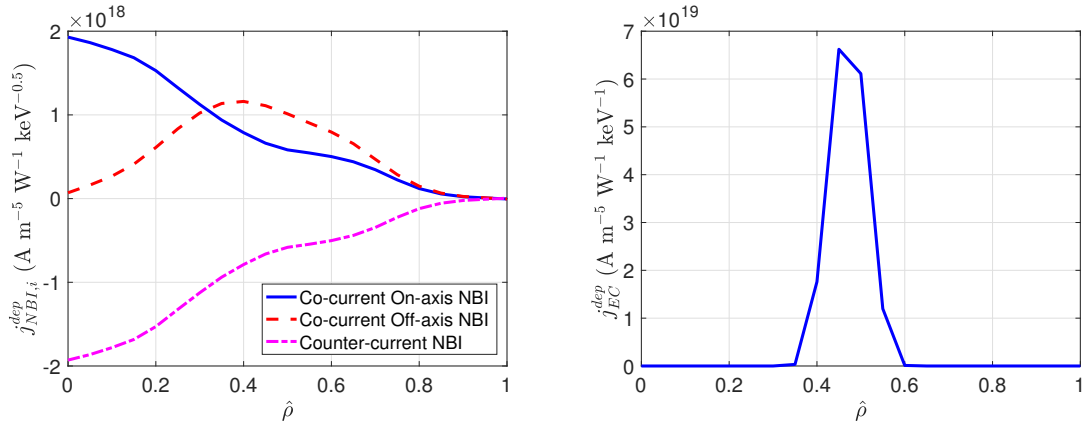

Figure 5.7: Deposition profiles for the auxiliary sources in DIII-D tailored to shot 147634.

An example of deposition profiles for NBI and EC is shown in Fig. 5.7 for DIII-D shot 147634. It can be seen that co-current on-axis NBI, co-current off-axis NBI, and EC have linearly independent deposition profiles. However, the counter-current NBIs have the same deposition profile as the co-current on-axis NBIs. Therefore, the counter-current NBIs and co-current on-axis NBIs are grouped together, and $N_{NBI} = 2$ ($N_{aux} = 3$) in this scenario.

5.3.7 Nominal q-profile Control by Means of Feedback Linearization

Assuming a careful control design with a full rank G^* matrix, the control law (5.56) reduces the nominal θ-subsystem ($\hat{\delta}_\theta = 0$) to equation (5.53) with $z = \tilde{\theta}$. A simple state-feedback control law,

$$v = -K\tilde{\theta}, \tag{5.58}$$

where $K \in \mathbb{R}^{1\times(N_{aux}-1)}$ is a design matrix, reduces (5.53) to

$$\dot{\tilde{\theta}} = (A - BK)\tilde{\theta}. \tag{5.59}$$

Without loss of generality, it is possible to set $A = 0$ and $B = I$ (0 and I are the zero and identity matrices, respectively, with the correct dimensions). The matrix K can be designed by means of any pole-placement technique to stabilize the $\tilde{\theta}$ evolution (note that this is a linear system, so it would be exponentially stable as well, see Appendices C.1.1 and C.1.2, and/or [65]). It must be taken into account that, although (5.56) always has a solution for $P_{NBI,i}$ ($i = 1$,..., N_{NBI}) and P_{EC}, it may not be within the feasible set due to physical actuation limits. A careful control design of the matrix K together with a reasonable choice of $\bar{\theta}$ must be carried out to avoid actuator saturation for too long periods of time, and the poor performance that it may imply.

As a summary, the solution of the system (5.56) with v given by (5.58) defines the nominal feedback-linearization control law.

5.3.8 Robust q-profile Control by Means of Lyapunov Redesign

In this section, the uncertainty in the θ-subsystem is not zero ($\hat{\delta}_\theta \neq 0$). The control law is modified by means of Lyapunov redesign techniques (see Appendices C.2.1 and C.2.2, and/or [65]) so that the θ-subsystem is stabilized even in the presence of this uncertainty. Using (5.56), equation (5.53) with $z = \tilde{\theta}$ and $\hat{\delta}_\theta \neq 0$ becomes

$$\dot{\tilde{\theta}} = A\tilde{\theta} + Bv + \hat{\delta}_\theta, \tag{5.60}$$

and taking $A = 0$, $B = I$ as for the nominal control law, it is found that

$$\dot{\tilde{\theta}} = v + \hat{\delta}_\theta. \tag{5.61}$$

If v is taken as

$$v = -\left(\frac{\hat{\delta}_\theta^{max}}{\|\tilde{\theta}\|_2} + K\right)\tilde{\theta}, \tag{5.62}$$

where $\hat{\delta}_\theta^{max} > 0$ is the maximum 2-norm attainable for $\hat{\delta}_\theta$, then using $V_\theta = \frac{1}{2}\|\tilde{\theta}\|_2^2$ yields

$$\dot{V}_\theta = \tilde{\theta}(v + \hat{\delta}_\theta) = -K\|\tilde{\theta}\|_2^2 - \hat{\delta}_\theta^{max}\frac{\|\tilde{\theta}\|_2^2}{\|\tilde{\theta}\|_2} + \hat{\delta}_\theta\tilde{\theta} \leq -K\|\tilde{\theta}\|_2^2, \tag{5.63}$$

thus the system remains exponentially stable despite $\hat{\delta}_\theta \neq 0$. The robust control law is slightly modified when $\|\tilde{\theta}\|_2 \to 0$ to avoid division by zero. Following similar arguments as in Appendix C.2.2 or [65], it can be shown that the control law

$$v = -\left(\frac{\delta_\theta^{max}}{\|\tilde{\theta}\|_2} + K\right)\tilde{\theta}, \quad \text{if } \delta_\theta^{max}\|\tilde{\theta}\|_2 \geq \epsilon^*, \tag{5.64}$$

$$v = -\left(\frac{(\delta_\theta^{max})^2}{\epsilon^*} + K\right)\tilde{\theta}, \quad \text{if } \delta_\theta^{max}\|\tilde{\theta}\|_2 < \epsilon^*, \tag{5.65}$$

where $\epsilon^* \to 0$ is a design parameter, ensures $\|\tilde{\theta}\|_2 < f^*(\epsilon^*)$, where f^* is a class $\mathcal{K}$ function of ϵ^*.

The solution of the system (5.56) with v given by (5.64)-(5.65) defines the robust feedback-linearization control law.

5.3.9 One-Dimensional Simulation Study

In this section, a simulation study is presented in which the controller is tested in COTSIM using full 1D simulations for both the MDE, Section 2.2.1, and EHTE, Section 2.2.2. The electron density n_e is estimated using a 0.5D model as shown in equation (2.34). The simulation scenario corresponds to DIII-D shot 147634. Three groups of auxiliary sources are considered, i.e., $N_{aux} = 3$. Those groups are on-axis NBI's (whose power is denoted by $P_{NBI,ON} = P_{30L/R} + P_{330L/R}$, as it comprises the 30L, 30R, 330L and 330R NBI's), off-axis NBI's (whose power is denoted by $P_{NBI,OFF} = P_{150L/R}$, as it comprises the 150L and 150R NBI's), and EC. The counter-current NBIs available in DIII-D (210L and 210R) are not used. This choice for the NBI groups ensures that G^* is always full rank, and that the feedback-linearization control law (5.56) is always defined, as described in Section 5.3.6. Thus, 2 interior nodes of the q profile are controllable. The controller

is configured to control q at the nodes $\hat{\rho} = 0.1$ and $\hat{\rho} = 0.4$, although any other two nodes could have been chosen instead.

For this simulation study, first an open-loop, feedforward-only (FF) simulation is run using the experimental inputs from shot 147634. The feedforward evolutions for q and β_N are denoted by q^{FF} and β_N^{FF}, respectively. Second, based on that feedforward simulation, targets for q and β_N are created (i.e., $\bar{q}$ and $\bar{\beta}_N$). Such targets are given by

$$\bar{q} = (1.09 - 0.03\hat{\rho})q^{FF}, \quad \bar{\beta}_N = 1.06\beta_N^{FF}, \tag{5.66}$$

i.e., it is desired that β_N has an increase of +6% when compared to shot 147634 while increasing q and modifying its shape. The q profile is increased by +9% at the center and +6% at the edge, and its shape is modified linearly in $\hat{\rho}$. Finally, a feedforward + feedback (FF + FB) simulation is run in which the controller tries to drive q and β_N to the desired targets.

Fig. 5.8 shows the q-profile evolution at fixed points in space, whereas Fig. 5.9 shows the q profile at given instants in time. Both the FF-only and FF+FB evolutions are shown together with the target $\bar{q}$. Fig. 5.10 shows the q_{edge} and I_p evolutions in FF-only and FF+FB, together with the target $\bar{q}_{edge}$. Fig. 5.11 shows the β_N and P_{tot} evolutions in FF-only and FF+FB, together with the target $\bar{\beta}_N$, whereas. Fig. 5.12 shows the NBI power ($P_{30L/R} \triangleq P_{30L} + P_{30R}$, $P_{330L/R} \triangleq P_{330L} + P_{330R}$, and $P_{150L/R} \triangleq P_{150L} + P_{150R}$) and P_{EC} evolutions in FF-only and FF+FB simulations.

Fig. 5.8 and Fig. 5.9 demonstrate the capability of the controller to modify the q-profile shape. As it can be seen in Fig. 5.12, $P_{NBI,ON} = P_{30L/R} + P_{330L/R}$ is initially decreased by the controller in the FF + FB case with respect to the FF-only case until around $t = 1$ s, while $P_{NBI,OFF} = P_{150L/R}$ and P_{EC} are increased, in order to increase q in the central region ($\hat{\rho} \lessapprox 0.5$, see also Fig. 5.8 at $t = 0.6$ s). At the same time, I_p is reduced to increase q_{edge}, as shown in Fig. 5.10. This increase in q_{edge} raises q in the region $\hat{\rho} \gtrapprox 0.75$, so the region $\hat{\rho} = (0.5, 0.75)$ is not initially driven to the target in FF + FB as fast as the other regions because of a lack of actuation capability (interior actuation focuses on $\hat{\rho} = 0.1$ and $\hat{\rho} = 0.4$ and boundary actuation focuses on $\hat{\rho} = 1$). As the discharge evolves in FF + FB, the change in q_{edge} caused

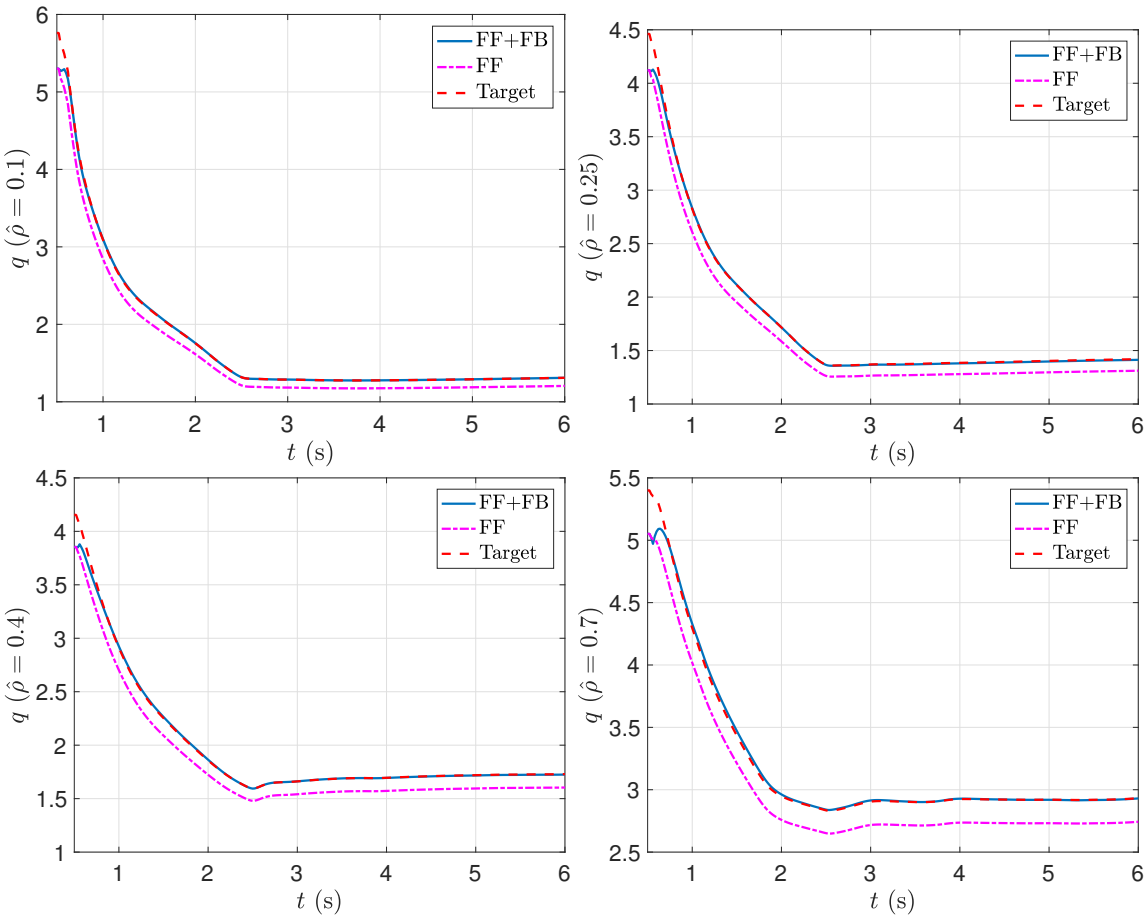

Figure 5.8: Time evolution for q at $\hat{\rho} = (0.10, 0.25, 0.40, 0.70)$ in FF-only (dashed-dotted magenta) and FF + FB (solid blue), together with the target $\bar{q}$ (dashed red).

by boundary control (see Fig. 5.10) diffuses further into the plasma core, raising the q-profile in $\hat{\rho} \in (0.5, 0.75)$ as well.

Fig. 5.11 shows that, initially, β_N is increased in the FF + FB case with respect to the FF-only case with a lower P_{tot}, mainly due to the I_p decrease, and also possibly because of a decrease in χ_e in the region $\hat{\rho} \lessapprox 0.4$ due to the increase in $dq/d\hat{\rho}$ (see Fig. 5.13 and Fig. 5.14). However, after $t = 1$ s, χ_e increases again due to the higher q and higher p_e (see Fig. 5.15), and P_{tot} must be increased in order to track β_N. From there and until the end of the shot, $P_{NBI,(\cdot)}$, P_{EC}, and I_p are regulated to achieve simultaneous β_N + q-profile tracking. The input P_{EC} is saturated from $t = 2.4$ s until the end of the shot, as in the FF-only shot. The input $P_{330L/R}$ is saturated

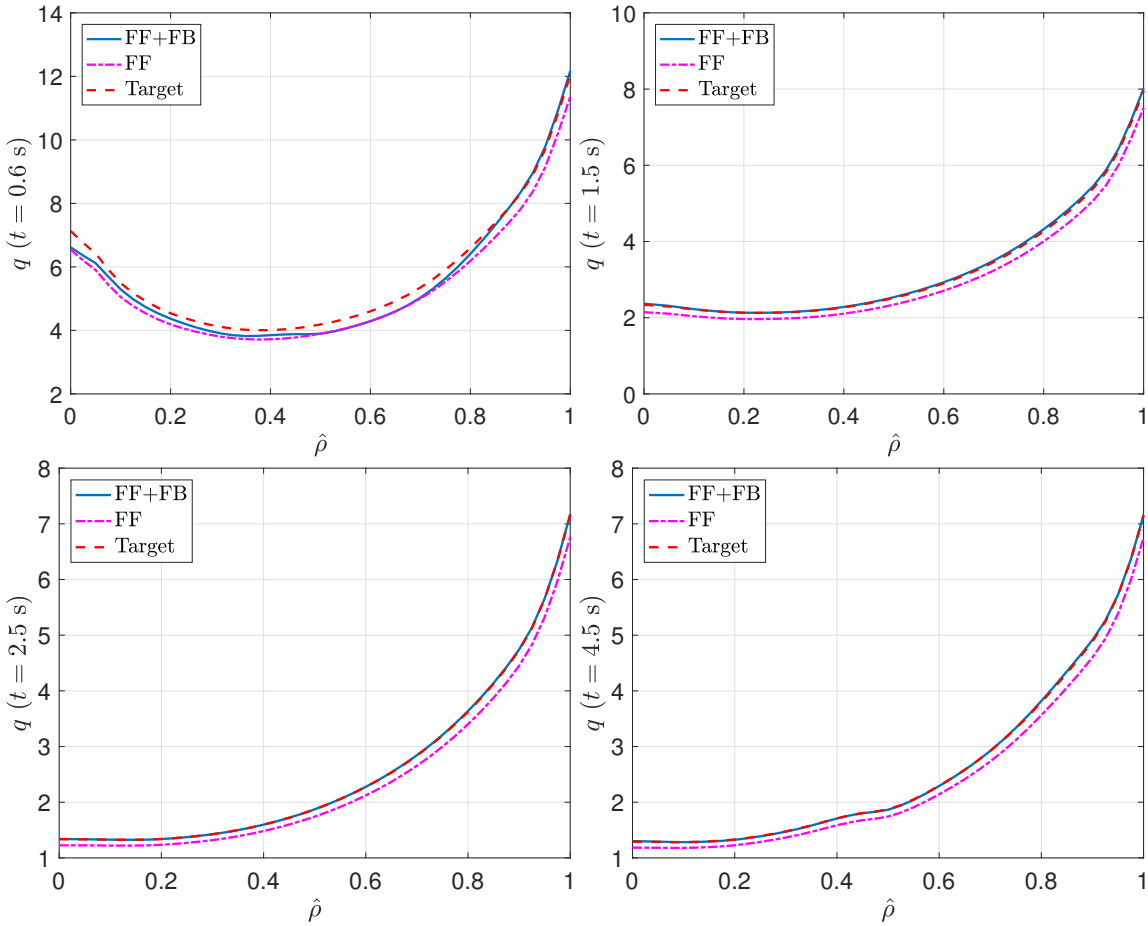

Figure 5.9: Comparison of q profiles at $t = (0.6, 1.5, 2.5, 4.5)$ s in FF-only (dashed-dotted magenta) and FF + FB (solid blue), together with the target $\bar{q}$ (dashed red).

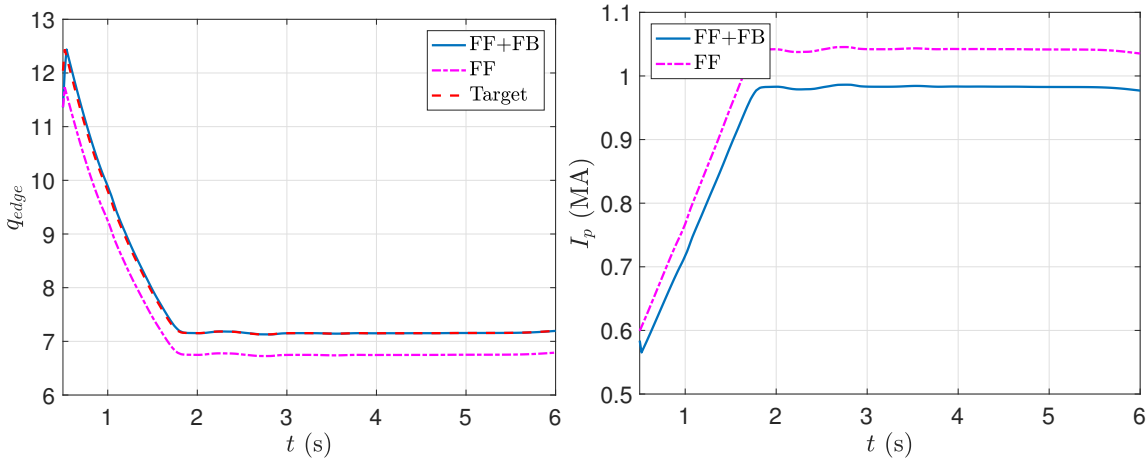

Figure 5.10: Time evolution for q_{edge} and I_p in FF-only (dashed-dotted magenta) and FF + FB (solid blue), together with $\bar{q}_{edge}$ (dashed red).

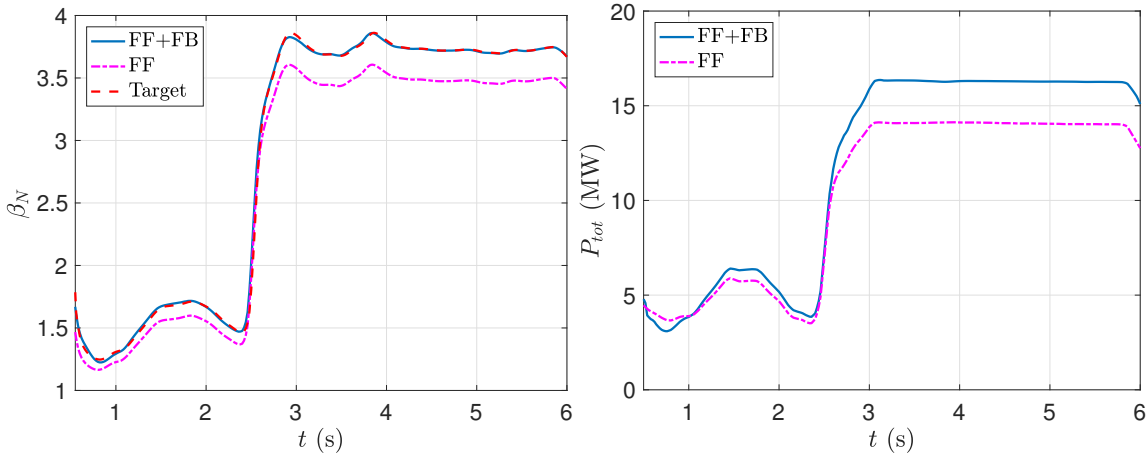

Figure 5.11: Time evolution for β_N and P_{tot} in FF-only (dashed-dotted magenta) and FF + FB (solid blue), together with the target $\bar{\beta}_N$ (dashed red).

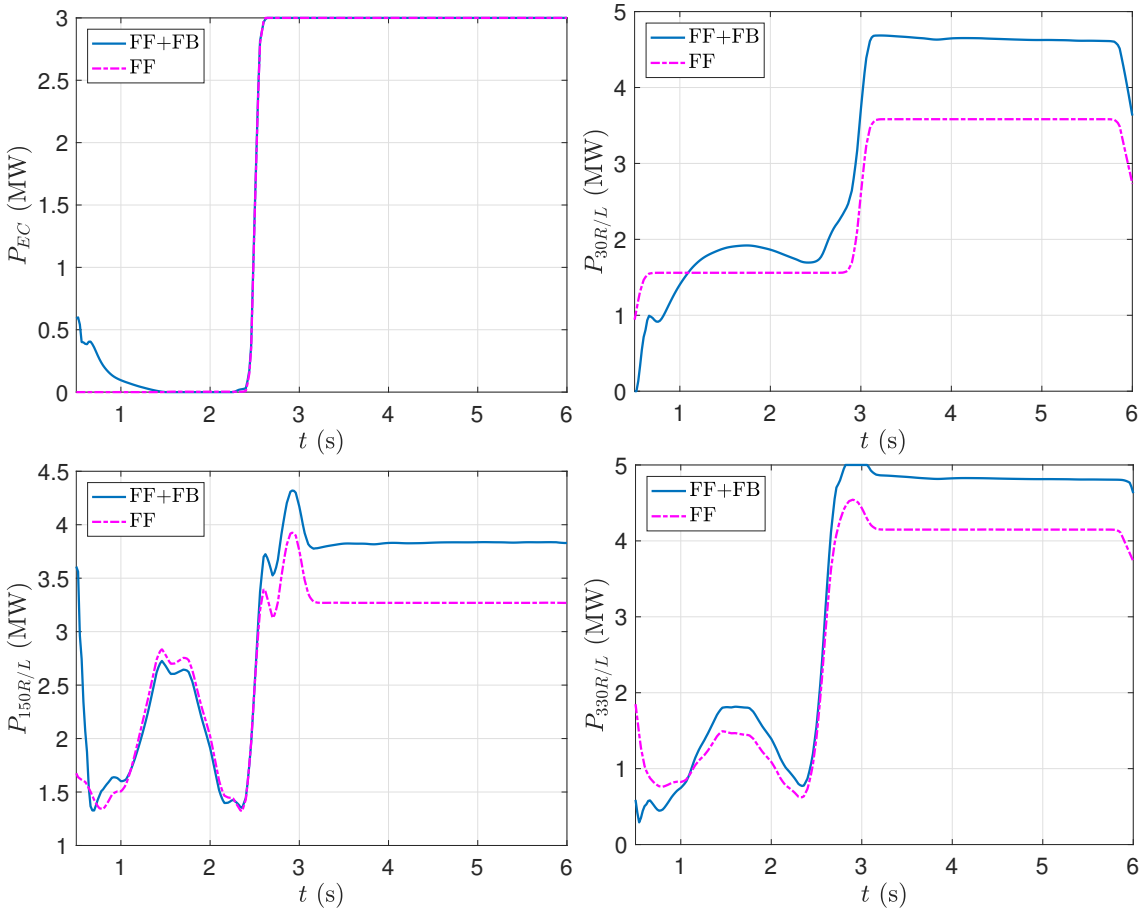

Figure 5.12: Time evolution for P_{EC} and $P_{NBI,(\cdot)}$ in FF-only (dashed-dotted magenta) and FF + FB (solid blue).

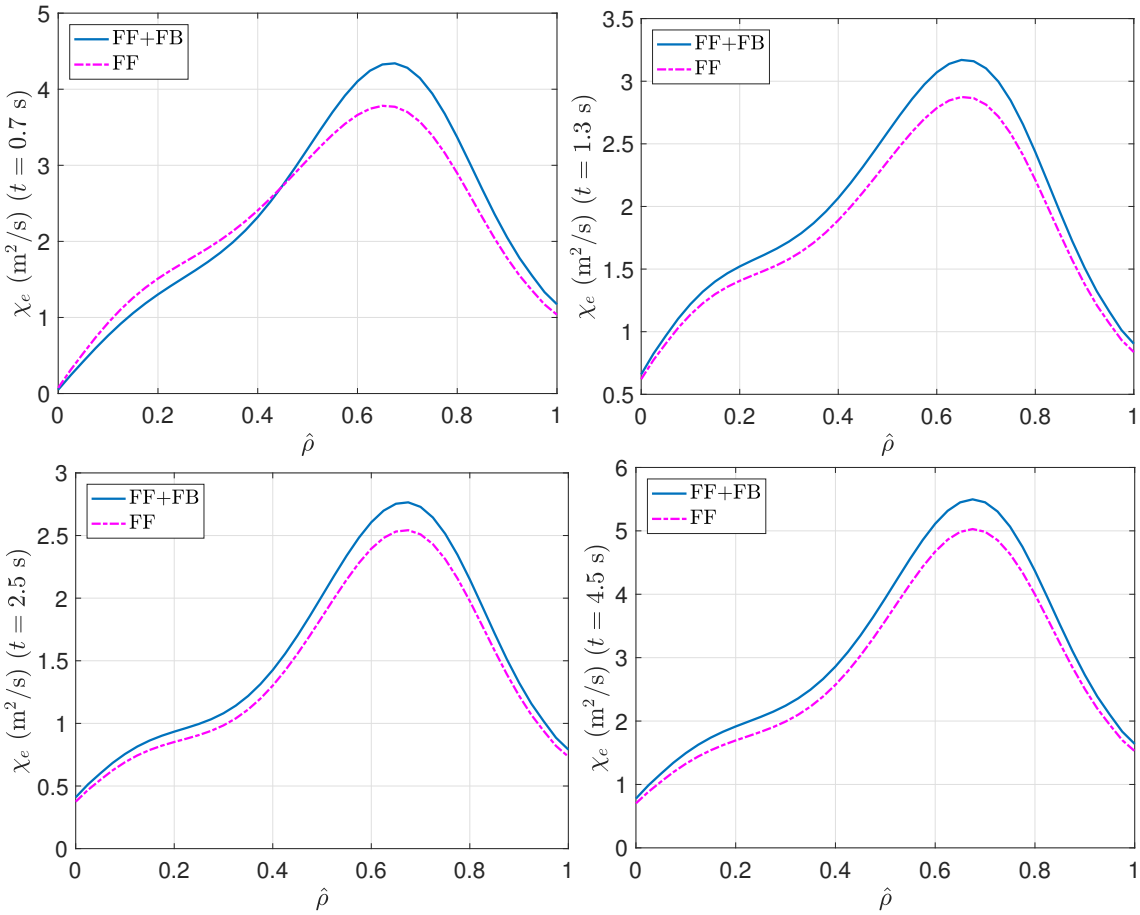

Figure 5.13: Comparison of χ_e profiles at $t = (0.7, 1.3, 2.5, 4.5)$ s in FF-only (dashed-dotted magenta) and FF + FB (solid blue).

too for a short period of time around $t \approx 3$ s. The other inputs do not saturate during the simulation. In any case, higher $P_{NBI,(\cdot)}$ and P_{EC} (and therefore, higher P_{tot}) are required to track $\bar{\beta}_N$ and $\bar{q}$. A decrease in $dq/d\hat{\rho}$ is achieved, as shown in Fig. 5.14, demonstrating again the controller's capability to change the q-profile shape. This should also enhance the plasma confinement by means of χ_e. However, the improvement caused by $dq/d\hat{\rho}$ does not seem to be enough to compensate for the decrease in χ_e caused by the higher q and p_e. Despite this, the control objective is fulfilled and good performance is achieved.

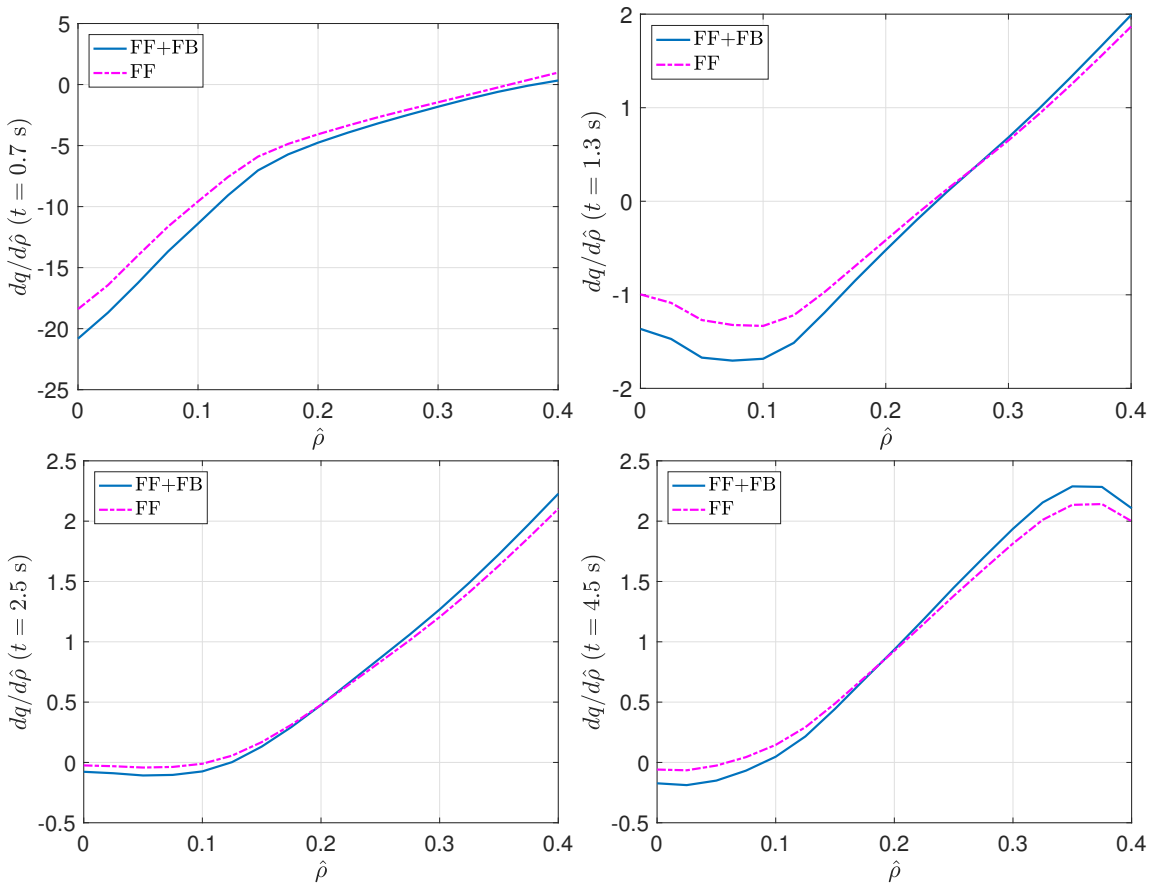

Figure 5.14: Comparison of $dq/d\hat{\rho}$ at $t = (0.7, 1.3, 2.5, 4.5)$ s in FF-only (dashed-dotted magenta) and FF + FB (solid blue) for $\hat{\rho} \leq 0.4$.

5.3.10 Conclusions

Regarding the feedback-linearization analysis, a few interesting conclusions can be drawn. The first, most evident conclusion is that the number of controllable nodes for q-profile control + β_N control is not only limited by the number of available auxiliary sources whose power can be controlled individually, but also by the shape of the deposition profiles of such sources. If $W + q_{edge}$ are controlled by I_p and P_{tot} but the auxiliary sources do not have different deposition profiles, then it is not possible to directly control the q profile at any inner node. This happens because, according to the model employed for control design, both I_p and P_{tot} would univocally determine the current diffusion rate by means of the plasma resistivity

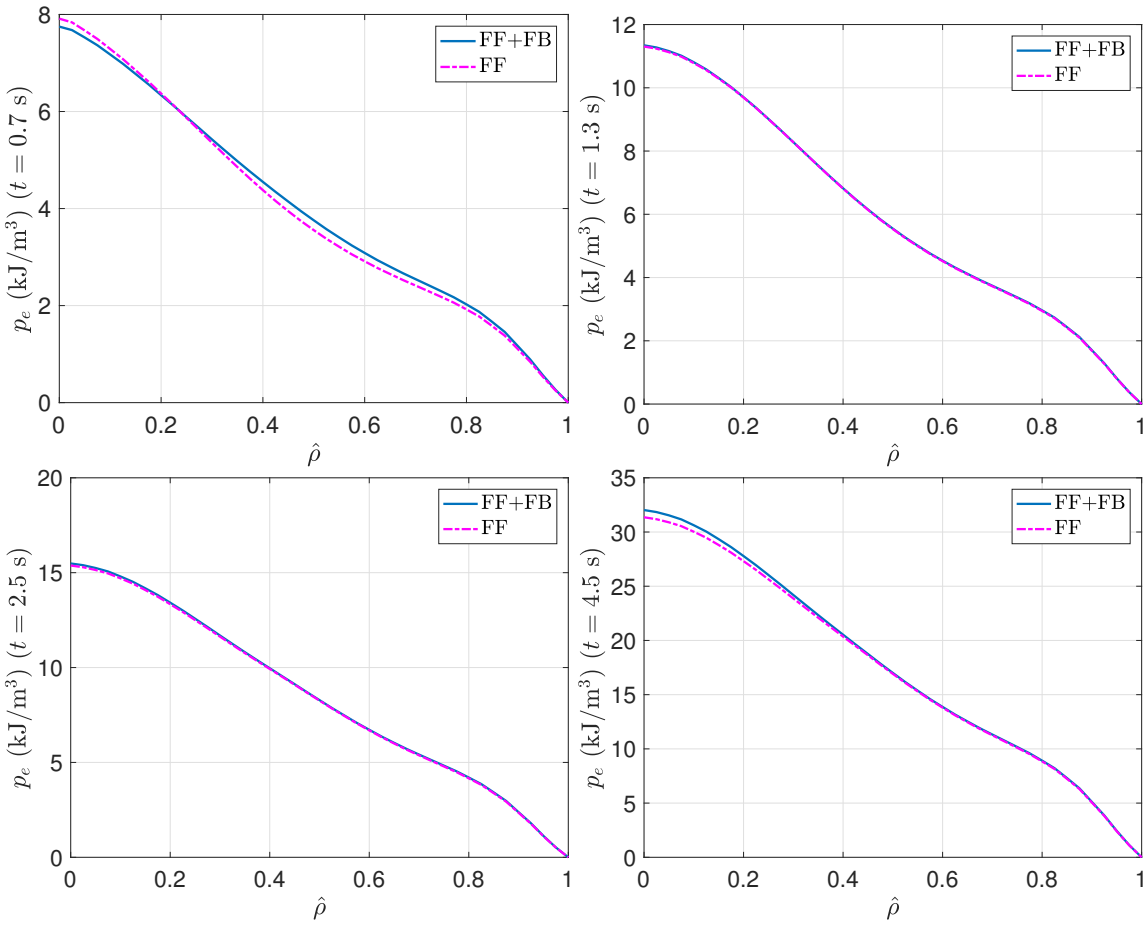

Figure 5.15: Comparison of p_e profiles at $t = (0.7, 1.3, 2.5, 4.5)$ s in FF-only (dashed-dotted magenta) and FF + FB (solid blue).

η, as well as the non-inductive current contribution, j_{ni}, and therefore $\beta_N + q_{edge}$ control and interior q-profile control could not be carried out independently. Even if q_{edge} is not directly controlled and I_p is used for interior q-profile control instead, the effect of I_p on the interior q profile would be limited by diffusion. As introduced before, I_p modulation may be limited by technological constraints (such as the current through the poloidal coils) and physical constraints (MHD instabilities), so it is normally desired that I_p is approximately constant during the flat-top phase, and it may not be the best way to control the q profile at the plasma core.

A second conclusion is that G^* is a tensor relating the $P_{(\cdot)}$ subspace ($(\cdot) =$

NBI, i or $(\cdot) = EC$) and the $\dot{\hat{\theta}}$ subspace. This is an interesting interpretation, as studying G^* in terms of its singular values indicates the input directions in which q-profile control can be carried out most efficiently, the output directions in which the q profile is more easily controllable, and the maximum (or minimum) achievable time-derivative for $\hat{\theta}$. Also, the image of the linear transformation $G^* : P_{(\cdot)} \rightarrow \dot{\hat{\theta}}$ subject to physical actuator constraints determines the reachable set of θ profiles (and therefore, q profiles) for given q_{edge} and β_N values. Such tool may be of great interest for tokamak-scenario planning and development.

Chapter 6

Integrated Magnetic and Kinetic Control: Individual Scalars Control

6.1 Introduction and Previous Work

As introduced earlier during this dissertation, some *plasma profiles* that are of interest in nuclear fusion research are the ion and electron thermal energy-density profiles, denoted by E_i and E_e respectively (see equations (2.21)), the ion toroidal angular-velocity profile, ω_ϕ (see equation (2.52)), and the safety factor profile, q (see equation (2.12)). Because E_i and E_e are directly proportional to $n_i T_i$ and $n_e T_e$, respectively, it is desired that E_i and E_e are as high as possible for long periods of time so that the triple product of density, temperature and τ_E is within the necessary required values to allow for fusion conditions (see Lawson's criteria, equation (1.11)). Moreover, both the ω_ϕ and q profiles have a close relationship with the confinement characteristics, MHD stability, and steady-state operation of tokamak plasmas. For example, it has already been introduced that some particular q-profile shapes (with low or negative spatial gradient, which is characterized by the magnetic shear, s) and ω_ϕ profiles are associated with the development of ITBs in some scenarios, which improve the plasma confinement. However, the physical mechanisms behind the ITB formation and their relationship with s and ω_ϕ are not completely understood

so far. In addition, the most common MHD instabilities found in tokamaks are also related to E_i, E_e, ω_ϕ and q (see Fig. 1.8), such as NTMs, RWMs, and ELMs.

As a result, active control of the E_i, E_e, ω_ϕ and/or q profiles are problems of significant interest in nuclear fusion research. Nonetheless, simultaneous control of these profiles is a big challenge due to the limited actuation capability existing in a tokamak. Instead, regulating a particular set of *scalar magnitudes* (such as global magnitudes related to the aforementioned profiles, or values of those profiles at particular spatial points) may be a more attainable control problem. In this Section, such individual-scalar control problem is tackled. The individual scalars considered are the stored thermal energy, W (related to E_i and E_e, see equation (2.22)), the central and edge safety factors, q_0 and q_{edge} (i.e., the value of q at the magnetic axis and plasma edge, respectively, see equations (2.93) and (2.118)), and the average ion toroidal-rotation frequency, Ω_ϕ (related to ω_ϕ, see equation (2.126)).

To the author's knowledge, there is no previous work on integrated control of individual scalars related to all energy, rotation, and safety factor simultaneously. Previous work on simultaneous rotation (either ω_ϕ or Ω_ϕ) and W control can be found in [91–93], whereas work on simultaneous control of some scalar or profile related to the plasma energy (either W, β_N, or T_e) and the q profile can be found in [81, 83, 84, 94].

In this Chapter, the work in [95–97] is reported. The 0D nonlinear, coupled models of the q_0, q_{edge}, W and Ω_ϕ dynamics (see Chapter 2, Section 2.3) are employed to synthesize controllers for the regulation of the individual scalars. A nonlinear, robust design that makes use of Lyapunov redesign techniques is employed to handle the model uncertainties. The actuators considered in the individual-scalars control problem are NBI, EC, and I_p. As it has already been introduced thoroughly during this dissertation, the coupled nature of the plasma dynamics brings up the issue of the integration of controllers that are initially designed for different and specific control objectives. It is proposed that the controllers are integrated by means of an actuator manager that takes the form of an optimization problem. Such actuator manager allows for a great flexibility to include additional constraints in the optimization problem, and permits the realization of the two actuator sharing strategies

envisioned for ITER: simultaneous multiple mission (SMM) sharing and repurposing (RP) sharing (see Section 1.3.5).

This Chapter mainly focuses on testing the SMM sharing capabilities of the actuator manager proposed, whereas Chapter 7 focuses on testing its RP sharing performance for simultaneous profile control (alternatively, individual-scalar control) and NTM suppression.

6.2 Modeling of the Individual Scalars Dynamics

The model employed is introduced in Chapter 2, Sections 2.3.1 (for W), 2.3.4 (for q_0), 2.3.5 (for q_{edge}), and 2.3.6 (for Ω_ϕ). The controllable inputs considered are $P_{NBI,i}$, P_{EC}, and I_p, i.e., the in-vessel and/or NRMF coils are not employed, and $I_{coil} = 0$ and $I_{NRMF} = 0$ is set always.

The state-space model for the system is given by

$$\dot{x} = \begin{bmatrix} f_{q_0}(x,u,t,\delta) \\ f_{q_{edge}}(x,u,\delta) \\ f_W(x,u,t,\delta) \\ f_{\Omega_\phi}(x,u,t,\delta) \end{bmatrix}, \tag{6.1}$$

where $x = [q_0, q_{edge}, W, \Omega_\phi]^T$ is the state vector, $u = [I_p, P_{NBI,1}, ..., P_{NBI,N_{NBI}}, P_{EC}]^T \in \mathbb{R}^{(N_{NBI}+2)\times 1}$ is the controllable-input vector, $\delta = [\delta_{q_0}, \delta_{k_{I_p}}, \delta_W, \delta_{\Omega_\phi}]^T$ is the uncertainty vector, and f_{q_0}, $f_{q_{edge}}$, f_W, and f_{Ω_ϕ} are given by (2.116), (2.119), (2.70), and (2.138), respectively. The explicit dependence with t is due to $\bar{n}_e$, which is assumed to be a non-controllable input in this individual-scalar control problem.

6.2.1 0D Models Validation for DIII-D Shot 147634

The prediction of the 0D models for individual scalars is compared to TRANSP data for the DIII-D H-mode discharge 147634. The parameters employed for the 0D models are $R_0 = 1.80$ m, $B_{\phi,0} = 1.65$ T, $H_H^{nom} = 1.4$, $V_p = 18$ m^3, $k_\Omega = 1$, $k_{int} = 3$, and $k_{NBI,i} = 2$ (kN·m)/MW for on-axis co-current NBI's (30 and 330 beamlines

in DIII-D), $k_{NBI,i} = 1.4$ (kN·m)/MW for off-axis co-current NBI's (150 beamline in DIII-D), and $k_{NBI,i} = -2$ (kN·m)/MW for on-axis counter-current NBI's (210 beamline in DIII-D). The inputs u and $\bar{n}_e$, and the parameter $\theta(2\Delta\hat{\rho})/\theta(\Delta\hat{\rho})|_{nom}$ correspond to the experimental values from shot 147634. It can be noted that the value taken for R_0 (see Fig. 6.1) is slightly different from the one employed in previous modeling work ($R_0 = 1.69$ m, see [18, 90]), despite using the same shot 147634. The reason is that such value, which corresponds to the geometric major radius in DIII-D, is not close to the actual major radius from TRANSP data. Hence, the 0D models would not produce the best fit to TRANSP data if this value was used, particularly for the q_{edge} model.

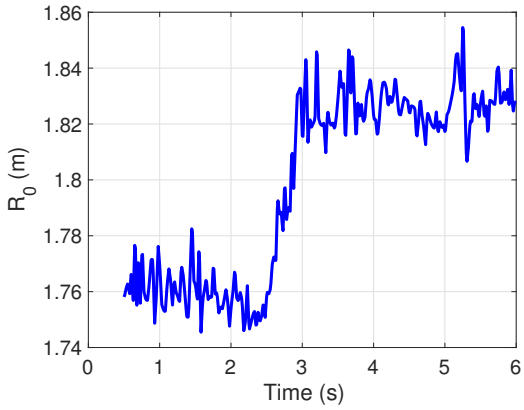

Figure 6.1: Evolution for R_0 from TRANSP corresponding to shot 147634.

Fig. 6.2 shows the time evolution for q_0, q_{edge}, W, and Ω_ϕ obtained from the 0D models, compared to TRANSP data. It can be noted that the 0D control-oriented models approximately replicates the TRANSP data. The main differences are found in the ramp-up phase for W, q_0, and Ω_ϕ, although the qualitative evolution obtained from the 0D models is in agreement with TRANSP. In any case, the ultimate objective of these control-oriented models is not to reproduce very accurately the experimental data or the prediction of more sophisticated codes, but to capture the main plasma dynamics in response to different actuators in order to serve as a tool for control synthesis.

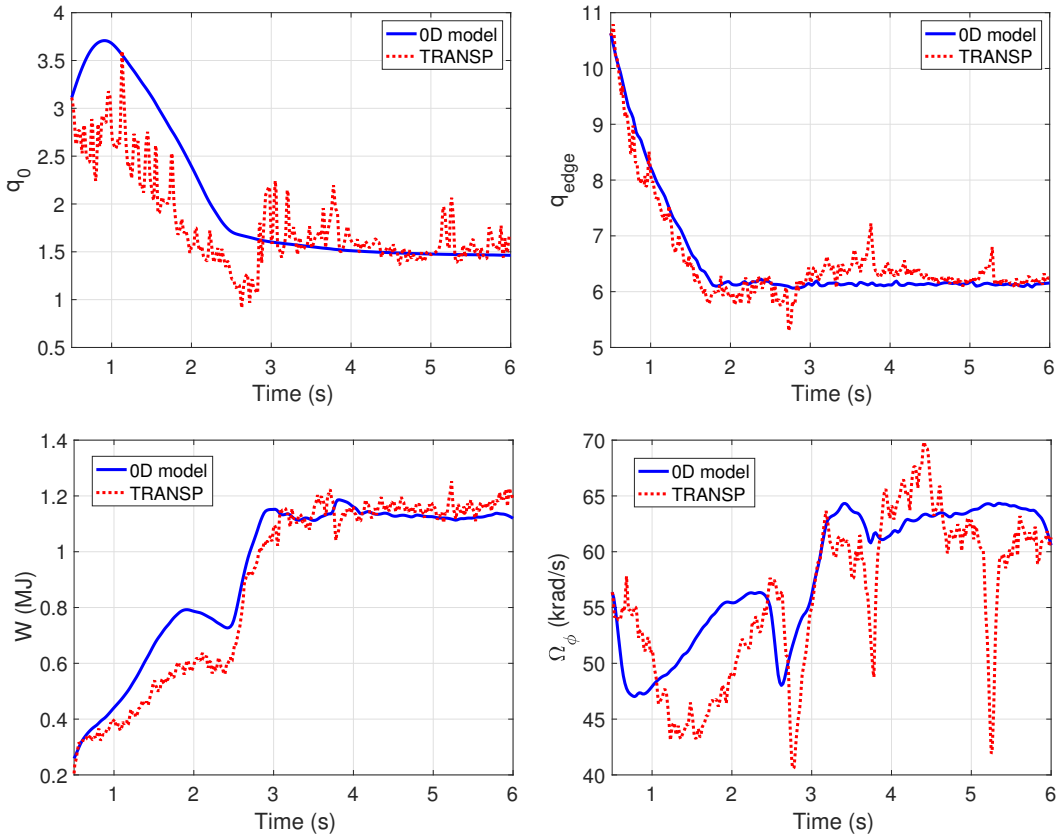

Figure 6.2: Model validation for q_0, q_{edge}, W, and Ω_ϕ dynamics: comparison between the 0D models and TRANSP evolutions for shot 147634.

6.3 Control Design via Lyapunov Redesign Techniques

In this Section, the control laws for the individual scalars are derived. Lyapunov redesign techniques are employed for the design of the nominal and robust control laws, respectively, for each individual scalar (see Appendices C.1.2 and C.2.2, and/or [65]). Specific actuators are chosen to control each individual scalar, attending to physical and practical reasons, as follows:

- $q_{edge} \implies$ **controlled by means of** I_p. From equation (2.119), it can be seen that other potential actuators for q_{edge} control are the vacuum toroidal magnetic field, $B_{\phi,0}$, the plasma position (by means of R_0, which enters the definition of k_{I_p}, see Section 2.3.5), and the magnetic configuration (by means

of $\hat{G}$ and/or $\hat{H}$, which enter the definition of k_{I_p}, or by means of ρ_b). However, employing these actuators to regulate q_{edge} may not be the most convenient approach. First of all, it may be desired that $B_{\phi,0}$, R_0, and the magnetic configuration are kept as constant as possible during operation, as all these characteristics are closely related among themselves and normally specified for a given plasma scenario in order to achieve a desired plasma performance. Second, there is a limited capability to vary to current driven through the toroidal coils during a shot, and therefore, there are significant limitations to modify $B_{\phi,0}$ as well. Also, it may not possible to modify R_0 and/or the magnetic configuration in a practical way, or even at all, as the shape and position controllers existing in current tokamaks are normally designed to maintain a specific position and shape defined by plasma-performance requirements and vertical instability avoidance[1]. Therefore, in this control design, I_p is chosen as the actuator for q_{edge} control.

- $W \implies$ **controlled by means of** P_{tot}. From equation (2.70), it can be seen that I_p, $B_{\phi,0}$, the plasma shape and position (R_0, ϵ, κ, etc.) and/or $\bar{n}_e$ also affect W and could be used as actuators. However, I_p has been chosen as the actuator for q_{edge} control, and for the same reasons as in the previous paragraph, $B_{\phi,0}$ and the plasma shape/position parameters are not considered as practical actuators to regulate W. Although $\bar{n}_e$ could be considered as an actuator for W control, it has already been mentioned that accurate density control is a challenge due to the highly nonlinear dynamics of such a problem, together with the lack of physical understanding of the particle transport. Therefore, for the purpose of the individual-scalar control design, $\bar{n}_e$ is considered as a non-controllable input (although it might be separately controlled, for example, by using a burn controller as the one introduced in Section 4 for burning plasmas, or simply a density controller for non-burning plasmas). The total power P_{tot} is chosen as the actuator for W control.

[1] In fact, the design of the ITER plasma shape and position control system is not well defined yet, and its capability to change R_0 and/or the magnetic configuration is unclear as of now.

- $\Omega_\phi \implies$ **controlled by means of** T_{NBI}. From equation (2.138), it can be seen that variables such as I_p, T_{NRMF}, T_{int}, m_p (related to $\bar{n}_e$ by means of (2.130)) and/or the parameters involved in the τ_E scaling (P_{tot}, $B_{\phi,0}$, R_0, ϵ, κ, etc.) could be considered as actuators for Ω_ϕ control. As I_p is taken for q_{edge} control, P_{tot} is taken for W control, and the reasons previously given to discard the τ_E-scaling parameters and $\bar{n}_e$, three actuators are left: T_{NBI}, T_{NRMF}, and T_{int}. First, because the NRMFs may be required for other control purposes, such as ELM suppression, they are not chosen as the primary actuator for Ω_ϕ control in this control design. Second, it has to be taken into account that T_{int} depends on I_p (used for q_{edge}) and W (controlled separately by means of P_{tot}), so Ω_ϕ control by means of T_{int} could only be carried out by driving q_{edge} and W towards particular target values. In order to avoid such coupling in the control objectives, T_{int} is not considered as an actuator for Ω_ϕ control, and T_{NBI} is chosen instead.

- $q_0 \implies$ **controlled by means of** $P_{NBI,i}$ **and** P_{EC}. From equation (2.116), it can be seen that three mechanisms can employed to regulate q_0: diffusion (i.e., $\lambda_{diff,(\cdot)}$ terms), auxiliary-driven current (i.e., $\lambda_{aux,i}$ terms), and bootstrap current (i.e., $\lambda_{BS,(\cdot)}$ terms). The 0D model employed for q_0 indicates that the inputs to both the diffusion and bootstrap current contributions are I_p, P_{tot}, and $\bar{n}_e$ (see u_η and u_{BS} definitions in (2.104) and (2.106)). As I_p and P_{tot} are employed for q_{edge} and W control, respectively, and $\bar{n}_e$ is not considered due to the aforementioned reasons, the diffusion and bootstrap mechanisms are not considered for q_0 control in this Section. Instead, both the diffusion and bootstrap contributions are considered as given for a particular scenario with a required I_p (or q_{edge}) and P_{tot} (or W) evolutions. The auxiliary-driven current contribution is a function of $P_{NBI,i}$ and P_{EC}, and it is chosen as the actuator employed for q_0 control.

It must be noted that controlling q_{edge} and W is equivalent to controlling β_N (see equations (2.25) and (2.26)), so the individual-scalar controllers allow for controlling β_N as well.

6.3.1 q_{edge} Control by means of I_p

A controller for q_{edge} is designed by employing I_p as the controllable input. The control objective is to drive q_{edge} to a reference value $\bar{q}_{edge}$, or alternatively, the error variable $\tilde{q}_{edge} \triangleq q_{edge} - \bar{q}_{edge}$ to zero. Instead of q_{edge}, it is convenient to employ θ at the edge, $\theta_N = -B_{\phi,0}\rho_b^2/q_{edge}$, for control design (because its dependence with I_p and k_{I_p} is linear, see the first equation in (5.41)). Also, because dI_p/dt is present in (2.119), the discretization $dI_p/dt \approx (I_p(t) - I_p^0)/\Delta t$ is employed in the synthesis of the controller, where $I_p^0 = I_p(t - \Delta t)$ is the value of I_p in the previous controller sampling-time, and Δt is the controller sampling-time.

First, the nominal system ($\delta_{k_{I_p}} = 0$) is considered. A control law $I_p = I_p^{nom}$ is sought. As $k_{I_p}^{nom}$ is a constant, (2.119) can be rewritten in terms of $\tilde{\theta}_N \triangleq \theta_N - \bar{\theta}_N$ with $\delta_{k_{I_p}} = 0$ as

$$\frac{d\tilde{\theta}_N}{dt} = -\frac{d\bar{\theta}_N}{dt} - k_{I_p}^{nom}\frac{I_p^{nom}(t) - I_p^0}{\Delta t} \triangleq f_{\theta_N}(I_p^{nom}), \tag{6.2}$$

where $\bar{\theta}_N$ is the reference for θ_N, which is related to $\bar{q}_{edge}$ as $\bar{\theta}_N = -B_{\phi,0}\rho_b^2/\bar{q}_{edge}$. By setting (6.2) as

$$f_{\theta_N}(I_p^{nom}) = -K_{P,\theta_N}\tilde{\theta}_N - K_{I,\theta_N}\int_{t_0}^{t}\tilde{\theta}_N dt, \tag{6.3}$$

where $K_{P,\theta_N} > 0$, $K_{I,\theta_N} > 0$ are design parameters, the θ_N-dynamics in (6.2) becomes

$$\frac{d\tilde{\theta}_N}{dt} = -\left(K_{P,\theta_N}\tilde{\theta}_N + K_{I,\theta_N}\int_{t_0}^{t}\tilde{\theta}_N dt\right), \tag{6.4}$$

which is a globally exponentially-stable system (see Appendix C.1.2). The global exponential stability of the system is in fact true for any values $K_{P,\theta_N} > 0$, $K_{I,\theta_N} > 0$, as it is demonstrated in Appendix F.1 by using a Lyapunov function given by

$$V_{\theta_N} = \frac{1}{2}\tilde{\theta}_N^2 + \frac{1}{2}\left(K_{I,\theta_N} + \frac{K_{P,\theta_N}^2}{1 + K_{I,\theta_N}}\right)\left(\int_{t_0}^{t}\tilde{\theta}_N dt\right)^2 + \frac{K_{P,\theta_N}}{1 + K_{I,\theta_N}}\tilde{\theta}_N\int_{t_0}^{t}\tilde{\theta}_N dt, \tag{6.5}$$

which yields

$$\dot{V}_{\theta_N} = -\frac{K_{P,\theta_N}K_{I,\theta_N}}{1 + K_{I,\theta_N}}\left(\tilde{\theta}_N^2 + \left(\int_{t_0}^{t}\tilde{\theta}_N dt\right)^2\right). \tag{6.6}$$

Thus, the nominal θ_N-subsystem is reduced to (6.4) as long as $I_p = I_p^{nom}$ is set as defined by (6.2)-(6.3). It is possible to solve for I_p^{nom} in (6.2)-(6.3) to obtain the nominal control law for I_p,

$$I_p^{nom} = I_p^0 + \frac{\Delta t}{k_{I_p}^{nom}} \left(K_{P,\theta_N} \tilde{\theta}_N + K_{I,\theta_N} \int_{t_0}^{t} \tilde{\theta}_N dt - \frac{d\bar{\theta}_N}{dt} \right). \tag{6.7}$$

Second, a robust control law for the uncertain system ($\delta_{k_{I_p}} \neq 0$) is sought. Equation (6.2) can be rewritten in the uncertain case as

$$\frac{d\tilde{\theta}_N}{dt} = -\frac{d\bar{\theta}_N}{dt} + \frac{k_{I_p}^{nom}}{\Delta t} I_p^0 - \frac{k_{I_p}^{nom}}{\Delta t} (I_p + \delta_{\theta_N}), \tag{6.8}$$

where

$$\delta_{\theta_N} = (I_p - I_p^0) \frac{\delta_{k_{I_p}}}{k_{I_p}^{nom}} + \frac{d\delta_{k_{I_p}}}{dt} \frac{I_p \Delta t}{k_{I_p}^{nom}} \tag{6.9}$$

is a term that bundles all the uncertain terms of the θ_N-subsystem. To ensure robustness under $\delta_{\theta_N} \neq 0$, a term I_p^{rob} is added to I_p^{nom}, so that the final control law is $I_p = I_p^{nom} + I_p^{rob}$. Using V_{θ_N} and (6.8), it is possible to write

$$\dot{V}_{\theta_N} = -\frac{K_{P,\theta_N} K_{I,\theta_N}}{1 + K_{I,\theta_N}} \left(\tilde{\theta}_N^2 + \left(\int_{t_0}^{t} \tilde{\theta}_N dt \right)^2 \right) - \tilde{\theta}_N \frac{k_{I_p}^{nom}}{\Delta t} (I_p^{rob} + \delta_{\theta_N}). \tag{6.10}$$

Taking $I_p^{rob} = \eta_{\theta_N} \tilde{\theta}_N$, for some positive function $\eta_{\theta_N} > 0$, the second term on the right hand side of (6.10) can be bounded from below as

$$\tilde{\theta}_N \frac{k_{I_p}^{nom}}{\Delta t} (I_p^{rob} + \delta_{\theta_N}) \geq \frac{k_{I_p}^{nom}}{\Delta t} \left(\eta_{\theta_N} \tilde{\theta}_N^2 - |\delta_{\theta_N}||\tilde{\theta}_N| \right), \tag{6.11}$$

and taking $\eta_{\theta_N} \geq |\delta_{\theta_N}|/|\tilde{\theta}_N|$,

$$\frac{k_{I_p}^{nom}}{\Delta t} \left(\eta_{\theta_N} \tilde{\theta}_N^2 - |\delta_{\theta_N}||\tilde{\theta}_N| \right) \geq \frac{k_{I_p}^{nom}}{\Delta t} \left(|\delta_{\theta_N}| - |\delta_{\theta_N}| \right) |\tilde{\theta}_N| = 0. \tag{6.12}$$

Therefore, (6.10) becomes

$$\dot{V}_{\theta_N} \leq -\frac{K_{P,\theta_N} K_{I,\theta_N}}{1 + K_{I,\theta_N}} \left(\tilde{\theta}_N^2 + \left(\int_{t_0}^{t} \tilde{\theta}_N dt \right)^2 \right), \tag{6.13}$$

showing that (6.8) remains globally exponentially stable if $I_p^{rob} \geq |\delta_{\theta_N}| \frac{\tilde{\theta}_N}{|\tilde{\theta}_N|}$ (see Appendix C.2.2). If an upper bound to δ_{θ_N} is known, denoted by $\delta_{\theta_N}^{max}$, then the control law

$$I_p^{rob} = \delta_{\theta_N}^{max} \frac{\tilde{\theta}_N}{|\tilde{\theta}_N|} \tag{6.14}$$

ensures the global exponential stability of the uncertain system (6.8). However, the control law (6.14) is discontinuous at $\tilde{\theta}_N = 0$. In order to make it continuous, it is modified as

$$I_p^{rob} = \delta_{\theta_N}^{max} \frac{\tilde{\theta}_N}{|\tilde{\theta}_N|}, \quad \text{if } \delta_{\theta_N}^{max} |\tilde{\theta}_N| \geq \epsilon_{\theta_N}, \tag{6.15}$$

$$I_p^{rob} = \left(\delta_{\theta_N}^{max}\right)^2 \frac{\tilde{\theta}_N}{\epsilon_{\theta_N}}, \quad \text{if } \delta_{\theta_N}^{max} |\tilde{\theta}_N| < \epsilon_{\theta_N}, \tag{6.16}$$

where $\epsilon_{\theta_N} \to 0$ is a design parameter. The control law (6.15)-(6.16) does not ensure global exponential stability, but it does ensure that $\tilde{\theta}_N$ is bounded by a class $\mathcal{K}$ function of ϵ_{θ_N}. More details can be found in Appendix C.2.2.

6.3.2 W Control by means of P_{tot}

A controller for $W$is designed by using P_{tot} as the controllable input. For the purpose of this control law, it is assumed that I_p is fixed[2]. The control objective is to drive W to a reference value $\bar{W}$, or alternatively, the error variable $\tilde{W} \triangleq W - \bar{W}$ to zero. The control design in this Section is essentially the same one as in Section 5.3.5, but adding an integral term in the nominal control law to improve its performance.

First, the nominal system ($\delta_W = 0$) is considered. A control law $P_{tot} = P_{tot}^{nom}$ is sought. Equation (2.70) can be rewritten in terms of $\tilde{W}$ as

$$\frac{d\tilde{W}}{dt} = -\frac{d\bar{W}}{dt} - \frac{\bar{W} + \tilde{W}}{H_H^{nom} k I_p^{0.93} P_{tot}^{nom-0.69}} + P_{tot}^{nom} = f_W(x, u^{nom}, t, 0). \tag{6.17}$$

[2]The reason for using this assumption at this point can be hinted from the actuator choice explained at the beginning of in Section 6.3. However, this assumption can be relaxed, as explained in Section 6.3.5.

By setting (6.17) as

$$f_W(x, u^{nom}, t, 0) = -K_{P,W}\tilde{W} - K_{I,W}\int_{t_0}^{t} \tilde{W} dt, \tag{6.18}$$

where $K_{P,W} > 0$, $K_{I,W} > 0$ are design parameters, the W-dynamics in (6.17) becomes

$$\frac{d\tilde{W}}{dt} = -\left(K_{P,W}\tilde{W} + K_{I,W}\int_{t_0}^{t} \tilde{W} dt\right), \tag{6.19}$$

which is a globally exponentially-stable system (see Appendix C.1.2). The global exponential stability of the system is in fact true for any values $K_{P,W} > 0$, $K_{I,W} > 0$, as it is demonstrated in Appendix F.1 by using a Lyapunov function given by

$$V_W = \frac{1}{2}\tilde{W}^2 + \frac{1}{2}\left(K_{I,W} + \frac{K_{P,W}^2}{1 + K_{I,W}}\right)\left(\int_{t_0}^{t} \tilde{W} dt\right)^2 + \frac{K_{P,W}}{1 + K_{I,W}}\tilde{W}\int_{t_0}^{t} \tilde{W} dt, \tag{6.20}$$

which yields

$$\dot{V}_W = -\frac{K_{P,W}K_{I,W}}{1 + K_{I,W}}\left(\tilde{W}^2 + \left(\int_{t_0}^{t} \tilde{W} dt\right)^2\right). \tag{6.21}$$

Thus, the nominal W-subsystem is reduced to (6.19) as long as $P_{tot} = P_{tot}^{nom}$ is set as defined by (6.17)-(6.18). It is not possible to solve explicitly for P_{tot}^{nom} in (6.17)-(6.18) due to the nonlinear dependence found, so its value has to be found using nonlinear solving methods.

Second, a robust control law for the uncertain system ($\delta_W \neq 0$) is sought. Equation (6.17) can be rewritten in the uncertain case as

$$\frac{d\tilde{W}}{dt} = -\frac{d\bar{W}}{dt} + (u_P + \delta_W), \tag{6.22}$$

where

$$u_P \triangleq P_{tot} - \frac{\bar{W} + \tilde{W}}{H_H^{nom} k I_p^{0.93} {P_{tot}}^{-0.69}} \tag{6.23}$$

is a virtual input defined just for the purpose of this robust law derivation. For the nominal case, it is found that

$$u_P = u_P^{nom} = P_{tot}^{nom} - \frac{\bar{W} + \tilde{W}}{H_H^{nom} k I_p^{0.93} {P_{tot}^{nom}}^{-0.69}}. \tag{6.24}$$

To ensure robustness under $\delta_W \neq 0$, a term u_P^{rob} is added to u_P^{nom}, so that $u_P = u_P^{nom} + u_P^{rob}$. Using V_W and (6.22), it is possible to write

$$\dot{V}_W = -\frac{K_{P,W}K_{I,W}}{1+K_{I,W}}\left(\tilde{W}^2 + \left(\int_{t_0}^{t}\tilde{W}dt\right)^2\right) + \tilde{W}(u_P^{rob} + \delta_W). \tag{6.25}$$

Taking $u_P^{rob} = -\eta_W\tilde{W}$, for some positive function $\eta_W > 0$, the second term on the right hand side of (6.25) can be bounded from above as

$$\tilde{W}(u_P^{rob} + \delta_W) \leq -\eta_W\tilde{W}^2 + |\delta_W||\tilde{W}|, \tag{6.26}$$

and taking $\eta_W \geq |\delta_W|/|\tilde{W}|$, then

$$-\eta_W\tilde{W}^2 + |\delta_W||\tilde{W}| \leq |\tilde{W}|(|\delta_W| - |\delta_W|) = 0. \tag{6.27}$$

Therefore, (6.25) becomes

$$\dot{V}_W \leq -\frac{K_{P,W}K_{I,W}}{1+K_{I,W}}\left(\tilde{W}^2 + \left(\int_{t_0}^{t}\tilde{W}dt\right)^2\right), \tag{6.28}$$

showing that (6.22) remains globally exponentially stable (see Appendix C.2.2). If an upper bound to δ_W is known, denoted by δ_W^{max}, then the control law

$$u_P^{rob} = -\delta_W^{max}\frac{\tilde{W}}{|\tilde{W}|} \tag{6.29}$$

ensures the global exponential stability of (6.22). However, the control law (6.29) is discontinuous at $\tilde{W} = 0$. In order to make it continuous, it is modified as

$$u_P^{rob} = -\delta_W^{max}\frac{\tilde{W}}{|\tilde{W}|}, \quad \text{if } \delta_W^{max}|\tilde{W}| \geq \epsilon_W, \tag{6.30}$$

$$u_P^{rob} = -\left(\delta_W^{max}\right)^2\frac{\tilde{W}}{\epsilon_W}, \quad \text{if } \delta_W^{max}|\tilde{W}| < \epsilon_W, \tag{6.31}$$

where $\epsilon_W \to 0$ is a design parameter. The control law (6.30)-(6.31) does not ensure global exponential stability, but it does ensure that $\tilde{W}$ is bounded by a class $\mathcal{K}$ function of ϵ_W. More details can be found in Appendix C.2.2.

Finally, P_{tot}^{rob} can be obtained from (6.24) and (6.30)-(6.31) as

$$P_{tot}^{rob} - \frac{\bar{W}+\tilde{W}}{H_H^{nom} k I_p^{0.93} (P_{tot}^{nom} + P_{tot}^{rob})^{-0.69}} = -\frac{\bar{W}+\tilde{W}}{H_H^{nom} k I_p^{0.93} P_{tot}^{nom\,-0.69}} - \delta_W^{max} \frac{\tilde{W}}{|\tilde{W}|}, \quad (6.32)$$

if $\delta_W^{max}|\tilde{W}| \geq \epsilon_W$, and

$$P_{tot}^{rob} - \frac{\bar{W}+\tilde{W}}{H_H^{nom} k I_p^{0.93} (P_{tot}^{nom} + P_{tot}^{rob})^{-0.69}} = -\frac{\bar{W}+\tilde{W}}{H_H^{nom} k I_p^{0.93} P_{tot}^{nom\,-0.69}} - (\delta_W^{max})^2 \frac{\tilde{W}}{\epsilon_W}, \quad (6.33)$$

if $\delta_W^{max}|\tilde{W}| < \epsilon_W$.

6.3.3 Ω_ϕ Control by means of $\sum_i T_{NBI,i}$

The average ion toroidal-rotation frequency, Ω_ϕ, is controlled by means of $\sum_i T_{NBI,i} \triangleq T_{NBI}$. For the purpose of this control law, it is assumed that I_p and P_{tot} are fixed[3]. The control objective is to drive Ω_ϕ to a reference value $\bar{\Omega}_\phi$, or alternatively, the error variable $\tilde{\Omega}_\phi \triangleq \Omega_\phi - \bar{\Omega}_\phi$ to zero.

First, the nominal system ($\delta_{\Omega_\phi} = 0$) is considered. A control law $T_{NBI} = T_{NBI}^{nom}$ is sought. Equation (2.138) can be rewritten in terms of $\tilde{\Omega}_\phi$ as

$$\frac{d\tilde{\Omega}_\phi}{dt} = -\frac{d\bar{\Omega}_\phi}{dt} - \frac{\bar{\Omega}_\phi + \tilde{\Omega}_\phi}{k_\Omega H_H^{nom} k P_{tot}^{-0.69}} + \frac{T_{NBI}^{nom}}{m_p R_0^2} + k_{int} \frac{\bar{W}+\tilde{W}}{I_p m_p R_0^2} = f_\Omega(x, u^{nom}, t, 0). \quad (6.34)$$

By setting (6.34) as

$$f_\Omega(x, u^{nom}, t, 0) = -K_{P,\Omega}\tilde{\Omega}_\phi - K_{I,\Omega}\int_{t_0}^{t} \tilde{\Omega}_\phi dt, \quad (6.35)$$

where $K_{P,\Omega} > 0$, $K_{I,\Omega} > 0$ are design parameters, the Ω_ϕ-dynamics in (6.34) becomes

$$\frac{d\tilde{\Omega}_\phi}{dt} = -\left(K_{P,\Omega}\tilde{\Omega}_\phi + K_{I,\Omega}\int_{t_0}^{t} \tilde{\Omega}_\phi dt\right), \quad (6.36)$$

[3] As in the W case, the reason for using this assumption at this point can be hinted from the actuator choice explained at the beginning of Section 6.3. However, this assumption can be relaxed, as explained in Section 6.3.5.

which is a globally exponentially-stable system (see Appendix C.1.2). The global exponential stability of the system is in fact true for any values $K_{P,\Omega} > 0$, $K_{I,\Omega} > 0$, as it is demonstrated in Appendix F.1 by using the following Lyapunov function,

$$V_{\Omega_\phi} = \frac{1}{2}\tilde{\Omega}_\phi^2 + \frac{1}{2}\left(K_{I,\Omega} + \frac{K_{P,\Omega}^2}{1+K_{I,\Omega}}\right)\left(\int_{t_0}^{t}\tilde{\Omega}_\phi dt\right)^2 + \frac{K_{P,\Omega}}{1+K_{I,\Omega}}\tilde{\Omega}_\phi\int_{t_0}^{t}\tilde{\Omega}_\phi dt, \quad (6.37)$$

which yields

$$\dot{V}_{\Omega_\phi} = -\frac{K_{P,\Omega}K_{I,\Omega}}{1+K_{I,\Omega}}\left(\tilde{\Omega}_\phi^2 + \left(\int_{t_0}^{t}\tilde{\Omega}_\phi dt\right)^2\right). \quad (6.38)$$

Thus, the nominal Ω_ϕ-subsystem is reduced to (6.36) as long as $T_{NBI} = T_{NBI}^{nom}$ is set as defined by (6.34)-(6.35). It is possible to solve for T_{NBI}^{nom} in (6.34)-(6.35) to obtain the nominal control law for T_{NBI},

$$T_{NBI}^{nom} = m_p R_0^2\left(\frac{\bar{\Omega}_\phi + \tilde{\Omega}_\phi}{k_\Omega H_H^{nom} k P_{tot}^{-0.69}} - K_{P,\Omega}\tilde{\Omega}_\phi - K_{I,\Omega}\int_{t_0}^{t}\tilde{\Omega}_\phi dt + \frac{d\bar{\Omega}_\phi}{dt}\right) - k_{int}\frac{\bar{W}+\tilde{W}}{I_p}. \quad (6.39)$$

Second, a robust control law for the uncertain system ($\delta_{\Omega_\phi} \neq 0$) is sought. Equation (6.34) can be rewritten in the uncertain case as

$$\frac{d\tilde{\Omega}_\phi}{dt} = -\frac{d\bar{\Omega}_\phi}{dt} - \frac{\bar{\Omega}_\phi + \tilde{\Omega}_\phi}{k_\Omega H_H^{nom} k P_{tot}^{-0.69}} + \frac{1}{m_p R_0^2}T_{int} + \frac{1}{m_p R_0^2}(T_{NBI} + \delta_{\Omega_\phi}). \quad (6.40)$$

To ensure robustness under $\delta_{\Omega_\phi} \neq 0$, a term T_{NBI}^{rob} is added to T_{NBI}^{nom}, so that $T_{NBI} = T_{NBI}^{nom} + T_{NBI}^{rob}$. Using V_{Ω_ϕ} and (6.40), it is possible to write

$$\dot{V}_{\Omega_\phi} = -\frac{K_{P,\Omega}K_{I,\Omega}}{1+K_{I,\Omega}}\left(\tilde{\Omega}_\phi^2 + \left(\int_{t_0}^{t}\tilde{\Omega}_\phi dt\right)^2\right) + \tilde{\Omega}_\phi\frac{1}{m_p R_0^2}(T_{NBI}^{rob} + \delta_{\Omega_\phi}). \quad (6.41)$$

Taking $T_{NBI}^{rob} = -\eta_\Omega\tilde{\Omega}_\phi$, for some positive function $\eta_\Omega > 0$, the second term on the right hand side of (6.41) can be bounded from above as

$$\frac{1}{m_p R_0^2}\tilde{\Omega}_\phi(T_{NBI}^{rob} + \delta_{\Omega_\phi}) \leq \frac{1}{m_p R_0^2}\left(-\eta_\Omega\tilde{\Omega}_\phi^2 + |\delta_\Omega||\tilde{\Omega}_\phi|\right), \quad (6.42)$$

and taking $\eta_\Omega \geq |\delta_{\Omega_\phi}|/|\tilde{\Omega}_\phi|$, then

$$-\eta_\Omega\tilde{\Omega}_\phi^2 + |\delta_{\Omega_\phi}||\tilde{\Omega}_\phi| \leq |\tilde{\Omega}_\phi|(|\delta_{\Omega_\phi}| - |\delta_{\Omega_\phi}|) = 0. \quad (6.43)$$

Therefore, (6.41) becomes

$$\dot{V}_{\Omega_\phi} \leq -\frac{K_{P,\Omega}K_{I,\Omega}}{1+K_{I,\Omega}}\left(\tilde{\Omega}_\phi^2 + \left(\int_{t_0}^{t}\tilde{\Omega}_\phi dt\right)^2\right), \tag{6.44}$$

showing that (6.40) remains globally exponentially stable (see Appendix C.2.2). If an upper bound to δ_{Ω_ϕ} is known, denoted by $\delta_{\Omega_\phi}^{max}$, then the control law

$$T_{NBI}^{rob} = -\delta_{\Omega_\phi}^{max}\frac{\tilde{\Omega}_\phi}{|\tilde{\Omega}_\phi|} \tag{6.45}$$

ensures the global exponential stability of the uncertain system (6.40). However, the control law (6.45) is discontinuous at $\tilde{\Omega}_\phi = 0$. In order to make it continuous, it is modified as

$$T_{NBI}^{rob} = -\delta_{\Omega_\phi}^{max}\frac{\tilde{\Omega}_\phi}{|\tilde{\Omega}_\phi|}, \quad \text{if } \delta_{\Omega_\phi}^{max}|\tilde{\Omega}_\phi| \geq \epsilon_{\Omega_\phi}, \tag{6.46}$$

$$T_{NBI}^{rob} = -\left(\delta_{\Omega_\phi}^{max}\right)^2\frac{\tilde{\Omega}_\phi}{\epsilon_{\Omega_\phi}}, \quad \text{if } \delta_{\Omega}^{max}|\tilde{\Omega}_\phi| < \epsilon_{\Omega_\phi}, \tag{6.47}$$

where $\epsilon_{\Omega_\phi} \to 0$ is a design parameter. The control law (6.46)-(6.47) does not ensure global exponential stability, but it does ensure that $\tilde{\Omega}_\phi$ is bounded by a class $\mathcal{K}$ function of ϵ_{Ω_ϕ}. More details can be found in Appendix C.2.2.

6.3.4 q_0 Control by means of $P_{NBI,i}$ and P_{EC}

The central safety factor, q_0, is controlled by means of $P_{NBI,i}$ and P_{EC}, which determine the auxiliary current-drive term in the q_0 model. For the purpose of this control law, and just like for the design of the Ω_ϕ controller in Section 6.3.3, it is assumed that I_p and P_{tot} are fixed[4]. The control objective is to drive q_0 to a reference value $\bar{q}_0$, or alternatively, the error variable $\tilde{q}_0 \triangleq q_0 - \bar{q}_0$ to zero.

First, the nominal system ($\delta_{q_0} = 0$) is considered. Equation (2.116) can be rewritten in terms of $\tilde{q}_0$ as

[4]As before, the reason for using this assumption at this point can be hinted from the actuator choice explained at the beginning of Section 6.3. However, this assumption can be relaxed, as explained in Section 6.3.5.

$$\frac{d\tilde{q}_0}{dt} = -\frac{d\bar{q}_0}{dt} - q_0 \left(\lambda_{diff,1} + \lambda_{diff,2} \left. \frac{\theta_2}{\theta_1} \right|_{nom} \right) u_\eta + q_0^2 FP \\ - q_0^3 \left(\lambda_{BS,1} + \lambda_{BS,2} \left. \frac{\theta_2}{\theta_1} \right|_{nom} \right) u_{BS} = f_{q_0}(x, u^{nom}, t, 0). \quad (6.48)$$

where $P = [P_{NBI,1}, ..., P_{NBI,N_{NBI}}, P_{EC}]^T$ is a vector with the NBI and EC powers that is defined for the purpose of this control law derivation, and $F \in \mathbb{R}^{1 \times N_{NBI}+1}$ is a vector whose i-th component, F_i, is given by

$$F_i \triangleq F_{NBI,i} = \lambda_{NBI,i} (I_p^\gamma P_{tot}^\epsilon \bar{n}_e^\zeta)^{(-3/2+\delta_{NBI})} \bar{n}_e^{-1}, \quad i = 1, ..., N_{NBI}, \quad (6.49)$$

except for the last one, which is given by

$$F_{N_{NBI}+1} \triangleq F_{EC} = \lambda_{EC} (I_p^\gamma P_{tot}^\epsilon \bar{n}_e^\zeta)^{(-3/2+\delta_{EC})} \bar{n}_e^{-1}. \quad (6.50)$$

In order to have a single-input single-output (SISO) system for q_0 control design, the scalar magnitude $P^* \triangleq FP$ is employed as the controllable input instead of the vector P. A nominal control law $P^* = P^{*,nom}$ is sought. By setting (6.48) as

$$f_{q_0}(x, u^{nom}, t, 0) = -K_{P,q_0} \tilde{q}_0 - K_{I,q_0} \int_{t_0}^{t} \tilde{q}_0 dt, \quad (6.51)$$

where $K_{P,q_0} > 0$, $K_{I,q_0} > 0$ are design parameters, the q_0-dynamics in (6.48) becomes

$$\frac{d\tilde{q}_0}{dt} = -\left(K_{P,q_0} \tilde{q}_0 + K_{I,q_0} \int_{t_0}^{t} \tilde{q}_0 dt \right), \quad (6.52)$$

which is a globally exponentially-stable system (see Appendix C.1.2). The global exponential stability of the system is in fact true for any values $K_{P,q_0} > 0$, $K_{I,q_0} > 0$, as it is demonstrated in Appendix F.1 by using a Lyapunov function given by

$$V_{q_0} = \frac{1}{2}\tilde{q}_0^2 + \frac{1}{2} \left(K_{I,q_0} + \frac{K_{P,q_0}^2}{1 + K_{I,q_0}} \right) \left(\int_{t_0}^{t} \tilde{q}_0 dt \right)^2 + \frac{K_{P,q_0}}{1 + K_{I,q_0}} \tilde{q}_0 \int_{t_0}^{t} \tilde{q}_0 dt, \quad (6.53)$$

which yields

$$\dot{V}_{q_0} = -\frac{K_{P,q_0} K_{I,q_0}}{1 + K_{I,q_0}} \left(\tilde{q}_0^2 + \left(\int_{t_0}^{t} \tilde{q}_0 dt \right)^2 \right). \quad (6.54)$$

Thus, the nominal q_0-subsystem is reduced to (6.52) as long as $P^* = P^{*,nom}$ is set as defined by (6.48) and (6.51). The nominal control law for P^* is obtained from (6.48) and (6.51) as

$$P^{*,nom} = \frac{1}{q_0^2}\left[-K_{P,q_0}\tilde{q}_0 - K_{I,q_0}\int_{t_0}^{t}\tilde{q}_0 dt + \frac{d\bar{q}_0}{dt} + q_0\left(\lambda_{diff,1} + \lambda_{diff,2}\left.\frac{\theta_2}{\theta_1}\right|_{nom}\right)u_\eta \right. \\ \left. + q_0^3\left(\lambda_{BS,1} + \lambda_{BS,2}\left.\frac{\theta_2}{\theta_1}\right|_{nom}\right)u_{BS}\right]. \quad (6.55)$$

Second, a robust control law for the uncertain system ($\delta_{q_0} \neq 0$) is sought. Equation (6.48) can be rewritten for the uncertain case as

$$\frac{d\tilde{q}_0}{dt} = -\frac{d\bar{q}_0}{dt} - q_0\left(\lambda_{diff,1} + \lambda_{diff,2}\left.\frac{\theta_2}{\theta_1}\right|_{nom}\right)u_\eta \\ - q_0^3\left(\lambda_{BS,1} + \lambda_{BS,2}\left.\frac{\theta_2}{\theta_1}\right|_{nom}\right)u_{BS} + q_0^2(P^* + \delta_{q_0}^*), \quad (6.56)$$

where the $\delta_{q_0}^* \triangleq \delta_{q_0}/q_0^2$ is a "virtual" uncertainty vector defined for the purpose of this control-law derivation. To ensure robustness under $\delta_{q_0}^* \neq 0$, a term $P^{*,rob}$ is added to $P^{*,nom}$, so that $P^* = P^{*,nom} + P^{*,rob}$. Using V_{q_0} and (6.56), it is possible to write

$$\dot{V}_{q_0} = -\frac{K_{P,q_0}K_{I,q_0}}{1+K_{I,q_0}}\left(\tilde{q}_0^2 + \left(\int_{t_0}^{t}\tilde{q}_0 dt\right)^2\right) + q_0^2\tilde{q}_0(P^{*,rob} + \delta_{q_0}^*). \quad (6.57)$$

Taking $P^{*,rob} = -\eta_{q_0}\tilde{q}_0$, for some positive function $\eta_{q_0} > 0$, the second term on the right hand side of (6.57) can be bounded from above as

$$q_0^2\tilde{q}_0(P^{*,rob} + \delta_{q_0}^*) \leq q_0^2\left(-\eta_{q_0}\tilde{q}_0^2 + \|\delta_{q_0}^*\||\tilde{q}_0|\right), \quad (6.58)$$

and taking $\eta_{q_0} \geq \|\delta_{q_0}^*\|/|\tilde{q}_0|$, it is found that

$$-\eta_{q_0}\tilde{q}_0^2 + \|\delta_{q_0}^*\||\tilde{q}_0| \leq |\tilde{q}_0|(\|\delta_{q_0}^*\| - \|\delta_{q_0}^*\|) = 0. \quad (6.59)$$

Therefore, (6.57) becomes

$$\dot{V}_{q_0} \leq -\frac{K_{P,q_0}K_{I,q_0}}{1+K_{I,q_0}}\left(\tilde{q}_0^2 + \left(\int_{t_0}^{t}\tilde{q}_0 dt\right)^2\right), \quad (6.60)$$

showing that the uncertain system (6.56) remains globally exponentially stable (see Appendix C.2.2). If an upper bound to $\|\delta_{q_0}^*\|$ is known, denoted by $\delta_{q_0}^{max}$, then the control law

$$P^{*,rob} = -\delta_{q_0}^{max} \frac{\tilde{q}_0}{|\tilde{q}_0|} \tag{6.61}$$

ensures the global exponential stability of (6.56). However, the control law (6.61) is discontinuous at $\tilde{q}_0 = 0$. In order to make it continuous, it is modified as

$$P^{*,rob} = -\delta_{q_0}^{max} \frac{\tilde{q}_0}{|\tilde{q}_0|}, \quad \text{if } \delta_{q_0}^{max}|\tilde{q}_0| \geq \epsilon_{q_0}, \tag{6.62}$$

$$P^{*,rob} = -\left(\delta_{q_0}^{max}\right)^2 \frac{\tilde{q}_0}{\epsilon_{q_0}}, \quad \text{if } \delta_{q_0}^{max}|\tilde{q}_0| < \epsilon_{q_0}, \tag{6.63}$$

where $\epsilon_{q_0} \to 0$ is a design parameter. The control law (6.62)-(6.63) does not ensure global exponential stability, but it does ensure that $\tilde{q}_0$ is bounded by a class $\mathcal{K}$ function of ϵ_{q_0}. More details can be found in Appendix C.2.2.

6.3.5 Integration of the Individual-scalar Control Laws

The individual controllers designed in Sections 6.3.1 through 6.3.4 are in principle decoupled from each other in the sense that, when one controller is carrying out its own computation, it does not need information about the computation carried out by the others. However, it can be seen that the controllers in Sections 6.3.2, 6.3.3, and 6.3.4 employ the same actuators, $P_{NBI,i}$ and P_{EC}, and need a value of I_p to have a fully defined control law. In addition, P_{tot} is assumed to be fixed in Sections 6.3.3 and 6.3.4, but those control laws do not ensure that their control requests ($T_{NBI}^{nom} + T_{NBI}^{rob}$ and $P^{*,nom} + P^{*,rob}$, respectively) actually fulfill $\sum_i P_{NBI,i} + P_{EC} = P_{tot}$. Therefore, there is in fact a high degree of actuator sharing between these control laws. In order to employ more than one controller at the same time while ensuring coherence between the control requests produced by each controller, an integrated scheme must be designed.

It is proposed that the individual-scalar controllers are interconnected as depicted in Fig. 6.3. Each controller can have three statuses: deactivated, activated in feedforward-only, or activated in feedforward+feedback. The control request that

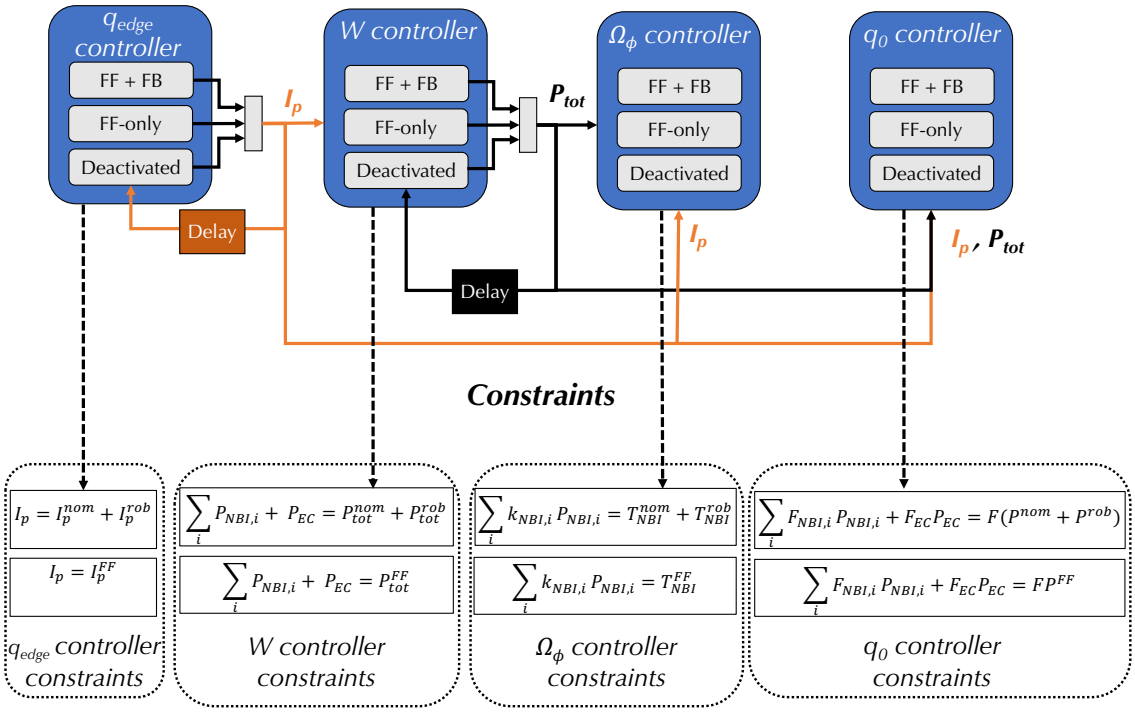

Figure 6.3: Integration of the individual-scalars controllers.

each controller creates changes according to such status. First, if the q_{edge} controller is activated in feedforward + feedback, it produces a signal for I_p which is determined from the control laws (6.7) and (6.15)-(6.16), and a constraint is generated so that $I_p = I_p^{nom} + I_p^{rob}$. If the q_{edge} controller is activated in feedforward-only, then a constraint is generated so that $I_p = I_p^{FF}$, where I_p^{FF} is a feedforward value for I_p. If the q_{edge} controller is deactivated, then I_p is set as its value at the previous controller sampling time. The applicable I_p value is then sent to the W controller. If the W controller is activated in feedforward + feedback, it produces a P_{tot} signal from the control laws (6.17)-(6.18) and (6.30)-(6.31), and a constraint is generated so that $\sum_i P_{NBI,i} + P_{EC} = P_{tot}$. If the W controller is activated in feedforward-only, a constraint is generated so that $P_{tot} = P_{tot}^{FF}$, where P_{tot}^{FF} is a feedforward value for P_{tot}. If the W controller is deactivated, then P_{tot} is set as its value at the previous controller sampling time, just like for the q_{edge} controller. Both the I_p and P_{tot} commands are sent to the Ω_ϕ and q_0 controllers. If the Ω_ϕ controller is activated in feedforward +

feedback, a constraint is generated from the control laws (6.39) and (6.46)-(6.47), whereas a constraint $T_{NBI} = T_{NBI}^{FF}$ is set if it is activated in feedforward-only. If it is deactivated, no constraint is generated. For the q_0 controller, a constraint is generated from the control laws (6.55) and (6.62)-(6.63) if the controller is activated in feedforward + feedback. If activated in feedforward-only, $P^{*,nom} + P^{*,rob} = P^{*,FF}$ (or its equivalent, $FP^{nom} + FP^{rob} = FP^{FF}$) is used as a constraint, whereas no constraint is generated if deactivated.

Therefore, the integrated scheme with the four individual-scalar controllers shown in Fig. 6.3 can control any combination of the four individual scalars by generating a maximum of 4 constraints (3 constraints for $P_{NBI,i}/P_{EC}$ together with 1 constraint for I_p). The shape and number of these constraints depends on the activation/deactivation statuses of the individual-scalar controllers. For example, when all the controllers are activated in feedforward + feedback, the control algorithm can be summarized as

$$I_p = I_p^{nom} + I_p^{rob}, \tag{6.64}$$

$$\sum_{i=1}^{N_{NBI}} P_{NBI,i} + P_{EC} = P_{tot}^{nom} + P_{tot}^{rob}, \tag{6.65}$$

$$\sum_{i=1}^{N_{NBI}} k_{NBI,i} P_{NBI,i} = T_{NBI}^{nom} + T_{NBI}^{rob}, \tag{6.66}$$

$$\sum_{i=1}^{N_{NBI}} F_{NBI,i} P_{NBI,i} + F_{EC} P_{EC} = F(P^{nom} + P^{rob}), \tag{6.67}$$

where I_p^{nom}, I_p^{rob}, P_{tot}^{nom}, P_{tot}^{rob}, T_{NBI}^{nom}, T_{NBI}^{rob}, P^{nom} and P^{rob} are determined from (6.7), (6.15)-(6.16), (6.17)-(6.18), (6.30)-(6.31), (6.39), (6.46)-(6.47), (6.55) and (6.62)-(6.63), respectively. If any controller is activated in feedforward-only instead, the applicable constraint is substituted by its equivalent feedforward constraint, whereas if any controller is deactivated, then the applicable constraint is removed.

It can be seen that, by employing fixed values for I_p and P_{tot} within the constraints generated by the Ω_ϕ and q_0 controllers (see Sections 6.3.3 and 6.3.4), the problem becomes linear with respect to $P_{NBI,i}$ and P_{EC}. This reduces the theoretical and computational complexity associated with nonlinear problems. In general,

the assumption of fixing I_p or P_{tot} could be relaxed, making (6.64)-(6.67) a nonlinear system. However, such case is not considered in this work, and for the remaining of this dissertation, it is assumed that (6.64)-(6.67) is a linear system.

The system (6.64)-(6.67) has 4 equations with $n \triangleq N_{NBI} + 2$ unknowns. The unknowns are $P_{NBI,i}$ for $i = 1, ..., N_{NBI}$, P_{EC}, and I_p, i.e., the components of the controllable input u. The system (6.64)-(6.67) is rewritten in matrix notation as

$$Au = b, \tag{6.68}$$

where u is defined in Section 6.2, and $A \in \mathbb{R}^{4\times(N_{NBI}+2)}$ and $b \in \mathbb{R}^{4\times 1}$ are given by

$$A = \begin{bmatrix} 1 & 0 & 0 & ... & 0 & 0 \\ 0 & 1 & 1 & ... & 1 & 1 \\ 0 & k_{NBI,1} & k_{NBI,2} & ... & k_{NBI,N_{NBI}} & 0 \\ 0 & F_{NBI,1} & F_{NBI,2} & ... & F_{NBI,N_{NBI}} & F_{EC} \end{bmatrix}, \quad b = \begin{bmatrix} I_p^{nom} + I_p^{rob} \\ P_{tot}^{nom} + P_{tot}^{rob} \\ T_{NBI}^{nom} + T_{NBI}^{rob} \\ F(P^{nom} + P^{rob}) \end{bmatrix}. \tag{6.69}$$

The solution of (6.68) defines u in the case when all controllers are activated in feedforward + feedback. A similar system would be obtained if feedforward-only control laws were employed, as the number of equations and unknowns remains the same. If any controller is deactivated, then the number of equations decreases. The number of deactivated controllers is denoted by N_{deac}, and the total number of equations becomes $m \triangleq 4 - N_{deac}$. In order to generalize (6.68) for the case in which some controllers may be deactivated, the following notation is employed,

$$A^\star u = b^\star, \tag{6.70}$$

where $A^\star \in \mathbb{R}^{(4-N_{deac})\times(N_{NBI}+2)}$ and $b^\star \in \mathbb{R}^{(4-N_{deac})\times 1}$ are composed of the rows of A and b in (6.69) which correspond to the activated controllers.

The existence/unicity of the solution of (6.70) depends, as in any other linear system, on three properties: the rank of $A^\star$, the number of unknowns, and the number of equations. First, the rank of $A^\star$ is analyzed. By simple inspection of the rows of A in (6.69), it can be noticed that $rank(A^\star) = m$ if $N_{deac} \geq 2$, making A^* a full rank matrix. This would correspond to the case in which only 1 or 2 individual scalars are regulated. However, if more scalars are regulated ($N_{deac} < 2$),

only $rank(A^{\star}) \geq 2$ is guaranteed and, in general, it cannot be assured that A^{*} is full rank. It is desired that A^{*} is full rank in order to prevent of the theoretical and numerical inconveniences associated with solving ill-conditioned problems. Following similar ideas as in the feedback linearization problem (Section 5.3), the auxiliary sources of the model can grouped so that they add rank in A, ensuring $rank(A^{*}) = m$. As for the feedback linearization case, there is a physical meaning for this requirement: auxiliary sources that produce torque or current in a similar or identical way should not be considered as separate actuators in the control problem. If the auxiliary sources are grouped so that $m > n = N_{NBI} + 2$, the system becomes overconstrained. This indicates that there is not enough controllability within the tokamak to simultaneously regulate all the requested individual scalars.

The second parameter that defines the existence/unicity of the solution of (6.70) is the number of unknowns, specified in this case by the number of available actuators ($N_{NBI} + 2$ at the most). If I_p is assumed to be available, a maximum to such parameter is determined by the total number of available auxiliary sources, $N_{NBI}+1$, that can be controlled independently within a given tokamak. In addition, $N_{NBI}+1$ is defined by the requirements introduced to ensure that A is full rank, i.e., the available auxiliary sources must be grouped according to the torque and current deposition that they produce. For example, in the DIII-D tokamak, 8 NBIs can be controlled independently (see Section 5.2.4) in conjunction with EC. All the NBIs and EC have the same effect on W, but they have different effects on q_0 and Ω_ϕ. The 4 co-current on-axis NBIs have a very similar effect on both q_0 and Ω_ϕ, thus they must be grouped together. The 2 co-current off-axis NBIs form a different group because their effect on q_0 is totally different from the co-current on-axis NBIs (generally speaking, off-axis injection raises q_0 whereas on-axis injection decreases it), whereas their influence on Ω_ϕ is smaller (off-axis injection produces less torque than on-axis injection). The 2 counter-current NBIs form another different group because they produce torque in the opposite direction that the co-current NBIs. Finally, EC does not affect Ω_ϕ. Therefore, $N_{NBI} = 3$ in this case, making a total of 4 auxiliary sources, and a total of 5 unknowns if I_p is added.

The third parameter that defines the existence/unicity of the solution of (6.70) is

the number of equations, defined by N_{deac}. Assuming that A^* is a full rank matrix, the following cases are found:

- If $2+N_{NBI} > 4-N_{deac}$ $(m < n)$, then (6.68) is an underconstrained system, and additional constraints must be added to univocally determine u. This indicates that there are more controllable inputs than to-be-regulated individual scalars.

- If $2+N_{NBI} = 4-N_{deac}$ $(m = n)$, then there are the same number of equations as unknowns. As the system (6.68) is linear, in principle one could use any method for linear systems to obtain a unique solution for u.

- If $2 + N_{NBI} < 4 - N_{deac}$ $(m > n)$, the system (6.68) is overconstrained and, in general, there is no solution. This indicates that there are not enough controllable inputs to regulate the individual scalars.

6.4 Actuator Management via Optimization

A possible way to solve (6.70) when underconstrained (i.e., $2 + N_{NBI} > 4 - N_{deac}$) is to rewrite it as an optimization problem. At every controller sampling time, a cost function of the inputs, J, is minimized while satisfying the activated time-varying constraints (6.64)-(6.67) imposed by the individual-scalar controllers. Additional constraints, such as physical saturation limits and/or control laws for other scalars/profiles, can be added to the scheme. The optimization problem is modified in every time step due to the activation/deactivation of the control laws. It is assumed that this modification is carried out as required by a supervisory system, which may override and/or remove some of the control laws and/or add additional constraints. Because of the possibility of modifying the constraints within the optimization problem, this actuator management scheme is very flexible in terms of its configuration and allows for performing both SMM and RP actuator sharing (see Chapter 1, Section 1.3.5). However, modifying the constraints has an evident impact on the feasibility of the optimization problem and, therefore, on the actuator manager performance. The constraints addition/removal must be made in a suitable

and organized manner that ensures the computational integrity of the scheme while fulfilling the required control objectives.

Mathematically, the optimization problem is written as,

$$\min_{u} J \tag{6.71}$$

$$I_p = I_p^{nom} + I_p^{rob}, \qquad \text{(if the } q_{edge} \text{ controller is activated)} \tag{6.72}$$

$$\sum_i P_{NBI,i} + P_{EC} = P_{tot}^{nom} + P_{tot}^{rob}, \qquad \text{(if the } W \text{ controller is activated)} \tag{6.73}$$

$$\sum_i k_{NBI,i} P_{NBI,i} = T_{NBI}^{nom} + T_{NBI}^{rob}, \qquad \text{(if the } \Omega_\phi \text{ controller is activated)} \tag{6.74}$$

$$F \begin{bmatrix} P_{NBI,1} \\ \vdots \\ P_{NBI,N_{NBI}} \\ P_{EC} \end{bmatrix} = F(P^{nom} + P^{rob}), \qquad \text{(if the } q_0 \text{ controller is activated)} \tag{6.75}$$

$$u \in \mathcal{U} \quad + \quad \text{Additional constraints from supervisory system} \tag{6.76}$$

where $\mathcal{U}$ is the set of feasible inputs.

An example of possible additional constraints and problem modification is as follows. Assume that the supervisory system detects a plasma state where NTMs are close to be triggered, and it is determined that the total power $\sum_i P_{NBI,i} + P_{EC}$ must be reduced to decrease β (which is directly proportional to W) and avoid the onset of the mode. Then, the supervisory system must override the W controller request by setting a different value of $P_{tot}^{nom} + P_{tot}^{rob}$, for example,

$$\sum_i P_{NBI,i} + P_{EC} = \left(P_{tot}^{nom} + P_{tot}^{rob}\right)^{NTM}, \tag{6.77}$$

where $\left(P_{tot}^{nom} + P_{tot}^{rob}\right)^{NTM}$ is the value required to decrease β below acceptable limits. If the NTM actually develops, the available P_{EC} for W control must be modified to allocate some P_{EC} for mode suppression, for example,

$$P_{EC} = P_{EC}^{NTM} + P_{EC}^{W}, \tag{6.78}$$

where P_{EC}^{NTM} is the minimum value required to suppress NTMs, and P_{EC}^{W} is the available power for W control. Other options, probably much less practical, would be

decreasing $I_p^{nom} + I_p^{rob}$ in (6.72) to increase the whole q profile, or setting $P_{NBI,i} \equiv 0$ for the i-th NBI to reduce the total available power.

6.4.1 Types of Optimization Problems: Linear and Quadratic Programming

The nature of the optimization problem is determined by the function J and the constraints imposed. As introduce above, all the controller constraints (6.72)-(6.75) are linear with respect to the controllable inputs. If the additional constraints from the supervisory system (6.76) are linear in I_p, $P_{NBI,i}$, and P_{EC} (as found, for instance, in the examples given above, (6.77) and (6.78)), and the cost function J is chosen linear or quadratic, then (6.71)-(6.76) becomes a linear or quadratic program, respectively. The theoretical and computational complexity of linear and quadratic programs is significantly lower than if nonlinear constraints or higher order cost functions were included, although feasibility is not ensured when arbitrary control requests and/or additional constraints are imposed.

Nowadays, tokamak experiments often require that the inputs are varied as little as possible with respect to those employed in a so-called *reference shot*[5]. Therefore, it is chosen that, if a linear cost function is employed, it is taken as

$$J = c^T \|\tilde{u}\|_1 = c_0|\tilde{I}_p| + c_1|\tilde{P}_{NBI,1}| + ... + c_{N_{NBI}}|\tilde{P}_{NBI,N_{NBI}}| + c_{N_{NBI}+1}|\tilde{P}_{EC}|, \quad (6.79)$$

where $c_T = [c_0, c_1, ..., c_{N_{NBI}+1}]$ is a design vector, $\tilde{I}_p \triangleq I_p - I_p^{ref}$, for a reference I_p trajectory, $\tilde{P}_{NBI,i} \triangleq P_{NBI,i} - P_{NBI,i}^{ref}$, for some reference trajectories of the NBI powers, $P_{NBI,i}^{ref}$, $\tilde{P}_{EC} \triangleq P_{EC} - P_{EC}^{ref}$, for a reference EC power trajectory P_{EC}^{ref}, and $\tilde{u}^T \triangleq [\tilde{I}_p, \tilde{P}_{NBI,1}, \tilde{P}_{NBI,2}, ..., \tilde{P}_{NBI,N_{NBI}}, \tilde{P}_{EC}]$. If the cost function is chosen quadratic, it is taken as

$$J = \tilde{u}^T Q \tilde{u}, \quad (6.80)$$

[5]Some experiments are carried out in a sort of trial-and-error fashion until a desired plasma evolution is obtained. Once the "trophy" shot is achieved, subsequent shots require that the inputs are varied as little as possible, in order to facilitate the interpretation of the experimental results.

where $Q \in \mathbb{R}^{(N_{NBI}+2)\times(N_{NBI}+1)}$ is a design matrix. Thus, if either (6.79) or (6.80) are employed, and I_p^{ref} and $P_{NBI,i/EC}^{ref}$ are taken as the inputs corresponding to a reference shot, then the actuator management fulfills the mission of reproducing the reference shot as closely as possible while keeping active feedback control.

6.4.2 Example: Actuator Management for $q_{edge} + W$ Control

In order to illustrate the characteristics of the actuator management scheme proposed, the problem of simultaneously controlling $q_{edge} + W$ by means of I_p, the total NBI power, $P_{NBI} \triangleq \sum_i P_{NBI}$, and total EC power, P_{EC}, is considered. In this case, $N_{NBI} = 1$ (all NBIs are considered as a single group) and $N_{deac} = 2$ (the equations for the Ω_ϕ and q_0 controllers are removed), so $2+N_{NBI} > 4-N_{deac}$ is fulfilled. A low number of variables and constraints is employed for the sake of easing the geometrical interpretation of the optimization problem, but the conclusions obtained can be directly extended to the case of a higher number of variables and constraints. Also, no additional constraints from supervisory systems are imposed, but the conclusions presented here can be easily extended to the case with such additional constraints.

The set of feasible inputs, $\mathcal{U}$, is defined by $I_p \in [I_p^{min}, I_p^{max}]$, $P_{NBI} \in [P_{NBI}^{min}, P_{NBI}^{max}]$, and $P_{EC} \in [P_{EC}^{min}, P_{EC}^{max}]$, where $(\cdot)^{min}$ and $(\cdot)^{max}$ are the minimum and maximum saturation values, respectively, for the corresponding input $(\cdot)$. The set $\mathcal{U}$ can be represented in the three-dimensional I_p-P_{NBI}-P_{EC} space as shown in Fig. 6.4. On the other hand, the constraints arising from the q_{edge} and W controller would be given by equations (6.72) and (6.73). In this case, the matrix A^* and vector b^* in (6.70) would be composed of only two rows, corresponding to the first two rows shown in (6.69). Clearly, A^* is a full rank matrix, and therefore, the solution of (6.70) is an $\mathbb{R}^3$ subset of dimension equal to $2+N_{NBI}-4+N_{deac} = 1$, i.e., a straight line (see Fig. 6.4).

Two characteristics of the optimization problem can be inferred. The first one is that, if the problem has an optimal solution, it must be bounded because the feasible set (if it exists) must be a bounded set. This is a natural result of imposing the physical saturation bounds. The second conclusion is that the problem may in

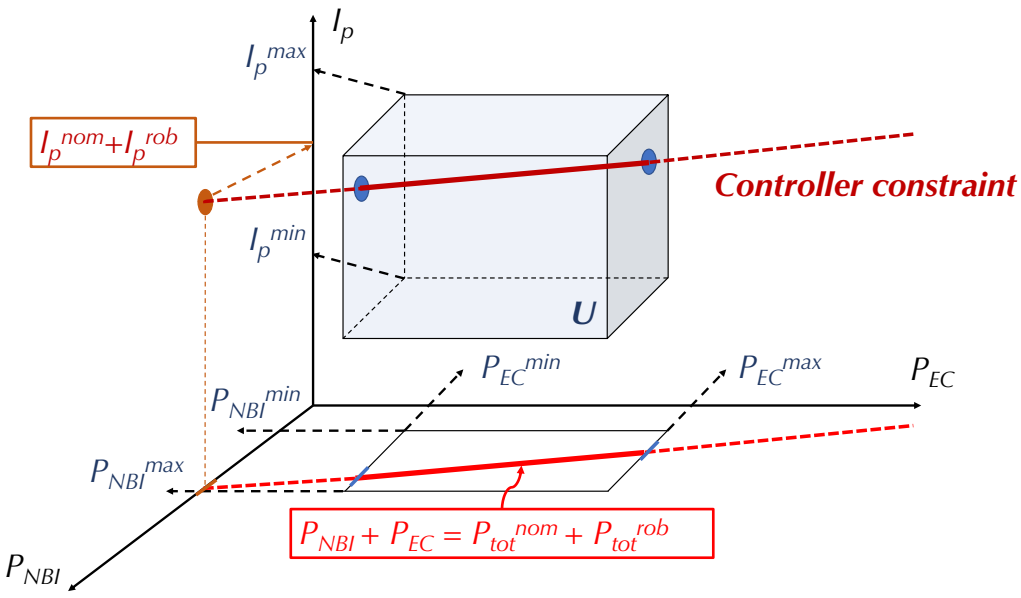

Figure 6.4: Geometrical interpretation of the actuator management problem for q_{edge} + W control. The problem is always bounded, and it is feasible if the controller constraint (brown, straight line) intersects the set of physically feasible inputs, $\mathcal{U}$ (blue prism). The projection of the controller constraint onto the I_p axis is the controller request, $I_p^{nom} + I_p^{rob}$, whereas its projection onto the P_{NBI}-P_{EC} is also a straight line (plotted in red).

fact be infeasible if the set defined by the controller constraints does not intersect the set defined by the physical saturation limits. Such infeasibility would be a result of the controller requesting values of u that exceed the achievable physical limits. This situation may correspond either to a case in which the controller has too high gains (i.e., the control design demands too aggressive control actions), or to a case in which the target is too far from the plasma state (i.e., the control objective is unrealistic for the existing actuation capability). Whereas the first case clearly requires a redesign of the applicable controllers, the second case is not a problem of the control scheme itself, but is just due to a lack of actuation capability to achieve a given target.

Assuming that a proper control design is carried out, the second case previously explained still poses the issue of having an actuator manager that does not provide an optimal solution due to the problem infeasibility. In order to ensure that the

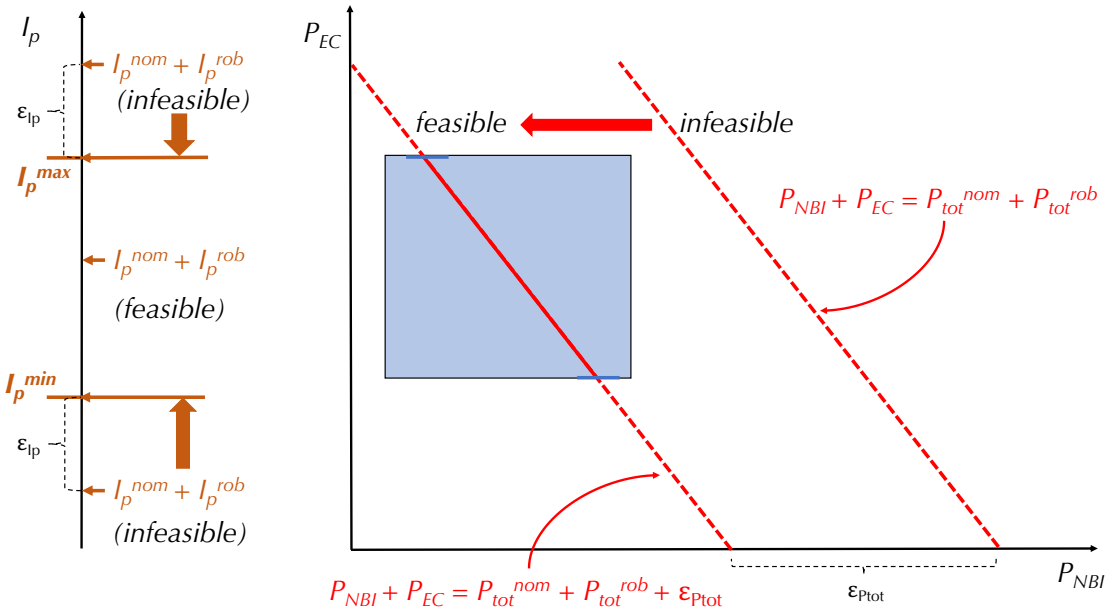

Figure 6.5: Geometrical interpretation of the addition of ϵ_{I_p} and $\epsilon_{P_{tot}}$ to the optimization problem, which makes it always feasible.

optimization algorithm always produces an optimal solution, the following method is proposed. The feasibility within the I_p-subspace can be studied separately from the feasibility within the P_{NBI}-P_{EC} subspace (the q_{edge} controller only uses I_p, whereas the W controller only uses P_{NBI} and P_{EC}). If $I_p^{min} \leq I_p^{nom} + I_p^{rob} \leq I_p^{max}$, then the problem is feasible in I_p. However, if $I_p^{nom} + I_p^{rob}$ violates any of the saturation limits, the problem becomes infeasible (see Fig. 6.5). It can be seen that "the best" that can be possibly done is to request $I_p = I_p^{max}$ if $I_p^{nom} + I_p^{rob} \geq I_p^{max}$, or request $I_p = I_p^{min}$ if $I_p^{nom} + I_p^{rob} \leq I_p^{min}$. Thus, by rewriting the constraint for I_p as $I_p = I_p^{nom} + I_p^{rob} + \epsilon_{I_p}$, where ϵ_{I_p} is a variable whose modulus has to be minimized, the problem is always feasible in I_p. Regarding the P_{NBI}-P_{EC} subspace, a similar situation is found. If the straight line $P_{NBI} + P_{EC} = P_{tot}^{nom} + P_{tot}^{rob}$ intersects the rectangle limited by $P_{NBI} \in [P_{NBI}^{min}, P_{NBI}^{max}]$, and $P_{EC} \in [P_{EC}^{min}, P_{EC}^{max}]$ (see Fig. 6.5), then the problem is feasible in P_{NBI}-P_{EC}. However, it may happen that these two subsets do not intersect at any point, indicating that it is impossible to satisfy both the controller request and the physical saturation limits. If the controller request is relaxed by

adding a fictitious variable $\epsilon_{P_{tot}}$,

$$P_{NBI} + P_{EC} = P_{tot}^{nom} + P_{tot}^{rob} + \epsilon_{P_{tot}}, \tag{6.81}$$

where $\epsilon_{P_{tot}}$ has to be minimized (just like ϵ_{I_p} in the I_p case), then the optimization problem is always feasible.

Assuming that the problem always has at least one optimal solution, the two cases introduced above are considered: a linear programming case (i.e., linear cost function) and a quadratic programming case (i.e., quadratic cost function). For I_p, because the q_{edge} controller requests a particular value to track $\bar{q}_{edge}$, the cost function choice does not affect its optimal solution, which is either $I_p^{nom} + I_p^{rob}$, or one of its saturation limits, I_p^{min} or I_p^{max}. Thus, the optimization problem can be reduced to the P_{NBI}-P_{EC} plane. The linear and quadratic cost functions are given by

$$J = c_1|\tilde{P}_{NBI}| + c_2|\tilde{P}_{EC}|, \;\; J = Q_{11}\tilde{P}_{NBI}^2 + Q_{22}\tilde{P}_{EC}^2 + Q_{12}\tilde{P}_{NBI}\tilde{P}_{EC}, \tag{6.82}$$

respectively, where Q_{ij} are the components of Q.

Fig. 6.6 shows an approximate schematic of the possible different solutions for the linear J case when $C \triangleq P_{tot}^{nom} + P_{tot}^{rob} - P_{tot}^{ref} > 0$, where $P_{tot}^{ref} = P_{NBI}^{ref} + P_{EC}^{ref}$, and P_{NBI}^{ref} and P_{EC}^{ref} are reference values in the optimization problem for P_{NBI} and P_{EC}, respectively. If $C \leq 0$, the reasoning would be analogous. The diagram is represented in the $\tilde{P}_{NBI}$-$\tilde{P}_{EC}$ plane. The blue box represents the set of feasible deviations, $\tilde{(\cdot)}$, with respect to P_{NBI}^{ref} and P_{EC}^{ref}. The controller constraint is rewritten as $\tilde{P}_{NBI}+\tilde{P}_{EC} = P_{tot}^{nom}+P_{tot}^{rob}-P_{tot}^{ref} \triangleq C$. The linear cost function J can be rewritten as

$$J = c_1|\tilde{P}_{NBI}| + c_2(C - |\tilde{P}_{NBI}|) = c_1(C - |\tilde{P}_{EC}|) + c_2|\tilde{P}_{EC}|, \tag{6.83}$$

or equivalently

$$J = (c_1 - c_2)|\tilde{P}_{NBI}| = (c_2 - c_1)|\tilde{P}_{EC}|. \tag{6.84}$$

It is well-known from the linear programming theory that (at least one of) the optimal solution always has to lie on one the vertices of the feasible set. It can be appreciated that, if $c_1 > c_2$, the optimal solution is $|\tilde{P}_{NBI}| = 0$. On the other

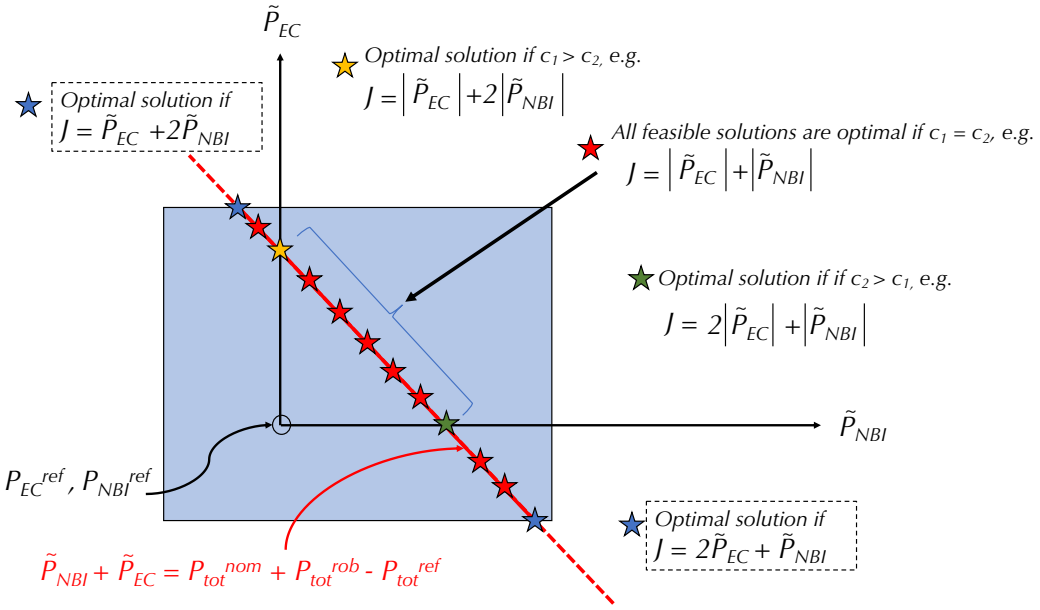

Figure 6.6: Geometrical interpretation of the linear J on the feasible set and optimal solution.

hand, if $c_2 > c_1$, the optimal solution is $|\tilde{P}_{EC}| = 0$. It can be noted that the feasible set is effectively reduced to the first quadrant when $c_1 \neq c_2$. This is due to the existence of the absolute values in J. If no absolute values were present in J, the optimal solutions would be found at the vertices of the feasible set. The last option is $c_1 = c_2$, in which all feasible solutions are optimal. This is a situation that should be avoided in the design of the actuator manager, as the control actions may "move" along the feasible set in a random way at every computation step. As a summary, it can be seen that by choosing c_i in a particular manner, the actuator manager can prioritize or penalize particular control actions, and therefore, allows for configuring the way in which the actuator manager uses the available actuators.

For the quadratic case, Fig. 6.7 shows an approximate schematic of the possible different solutions. For simplicity in the graphical representation, $Q_{12} = 0$ is assumed. For each particular value of the quadratic cost function $J = J^*$, an ellipse is defined whose shape is determined by the coefficients Q_{ij}. As J^* increases, the axes of the ellipses increase their length as well. The optimal solution is defined by the ellipse with the smallest J^* which is tangent to the controller constraint,

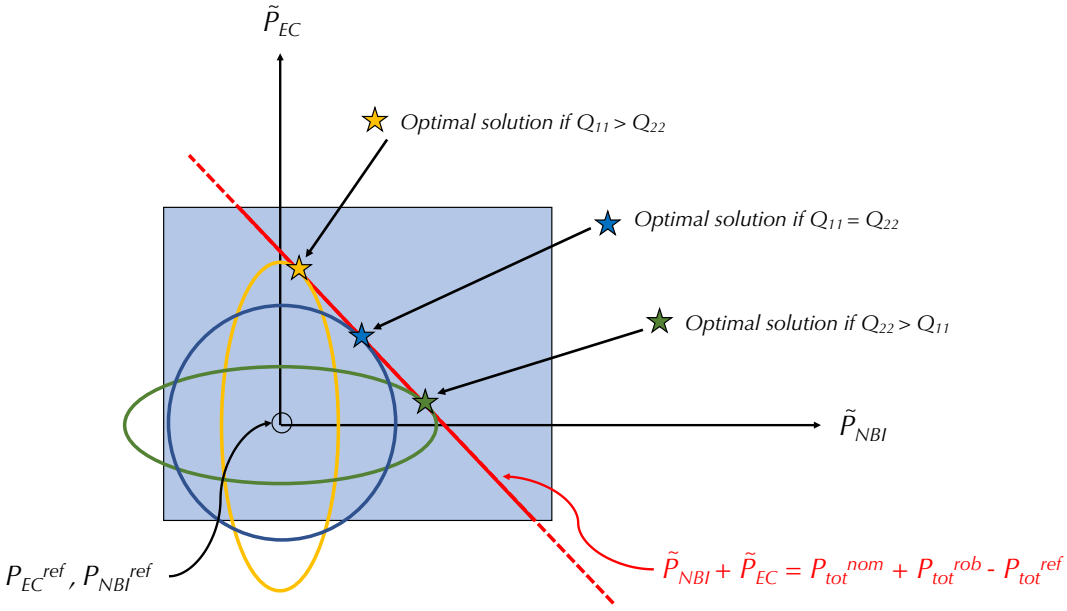

Figure 6.7: Geometrical interpretation of a quadratic J on the feasible set and optimal solution.

$\tilde{P}_{NBI} + \tilde{P}_{EC} = P_{tot}^{nom} + P_{tot}^{rob} - P_{tot}^{ref}$. If $Q_{11} > Q_{22}$, then the optimal solution will be closer to $\tilde{P}_{NBI} = 0$, whereas if $Q_{22} > Q_{11}$, the optimal solution will be closer to $\tilde{P}_{EC} = 0$. If $Q_{11} = Q_{22}$, the solution will actually be $\tilde{P}_{NBI} = \tilde{P}_{EC}$. As for the linear case, choosing Q_{ij} allows for configuring the way in which the actuator manager treats the different actuators.

6.5 Simulation Testing: $W + \Omega_\phi$ Control

In this Section, the problem of simultaneously controlling W and Ω_ϕ is studied. In order to make the control problem as challenging as possible, NBI is considered as the only actuator available for control (it can be noted that I_p is employed to regulate q_{edge}, and that P_{EC} only affects W). The control algorithm is tested both in 0D simulations (using the same model as the one employed for control design) and 1D simulations (using COTSIM with the models described in Sections 2.2.1, 2.2.2 and 2.2.3). First, 0D simulations are carried out to test the performance of the controllers and the actuator manager in a simpler model, and also to be able

to compare the performance of the nominal and robust control laws under different conditions, like for example, the existence of uncertainties. Then, 1D simulations are executed to test the capability of the 0D controller in a code which reproduces the more complex 1D plasma behavior with higher accuracy.

The simulation scenario is the one employed for both the 0D model validation (see Section 6.2.1) and 1D validation (see Chapter 3), i.e., DIII-D shot 147634. The 8 NBIs available in DIII-D are grouped in the aforementioned 3 sets ($N_{NBI} = 3$) as

- Group 1: consists of 4 Co-current on-axis NBIs. This group's total power, $P_{NBI,1}$, is denoted by P_{CO-ON}.
- Group 2: consists of 2 Co-current off-axis NBIs. This group's total power, $P_{NBI,2}$, is denoted by P_{CO-OFF}.
- Group 3: consists of 2 Counter-current NBIs. This group's total power, $P_{NBI,3}$, is denoted by $P_{COUNTER}$.

The optimization problem employed in this Section is slightly different from that in (6.71)-(6.76) because it only includes the W and Ω_ϕ control laws with the corresponding "extra" variables that ensure feasibility. Also, $\tilde{P}_{EC}$ is not a free variable and is set to zero.

The optimization problem is given by

$$\min_{P_{NBI,i},\epsilon_{(\cdot)}} J = [\tilde{P}_{NBI,1}, ..., \tilde{P}_{NBI,N_{NBI}}, \epsilon_{P_{tot}}, \epsilon_{T_{NBI}}] Q [\tilde{P}_{NBI,1}, ..., \tilde{P}_{NBI,N_{NBI}}, \epsilon_{P_{tot}}, \epsilon_{T_{NBI}}]^T \tag{6.85}$$

s.t.

$$\sum_i P_{NBI,i} + P_{EC} = P_{tot}^{nom} + P_{tot}^{rob} + \epsilon_{P_{tot}}, \tag{6.86}$$

$$\sum_i k_{NBI,i} P_{NBI,i} = T_{NBI}^{nom} + T_{NBI}^{rob} + \epsilon_{T_{NBI}}, \tag{6.87}$$

$$P_{NBI,i} \in \mathcal{U} \tag{6.88}$$

where $\tilde{P}_{NBI,i} \triangleq P_{NBI,i} - P_{NBI,i}^{ref}$, $P_{NBI,i}^{ref}$ is the reference trajectory of the i-th NBI power (corresponding to experimental values), Q is a positive definite matrix, $\epsilon_{P_{tot}}$

and $\epsilon_{T_{NBI}}$ are the variables introduced to make the optimization problem always feasible, $\mathcal{U}$ denotes the set of feasible NBI powers, and P_{tot}^{nom}, P_{tot}^{rob}, T_{NBI}^{nom}, and T_{NBI}^{rob} are computed from the nominal and robust control laws (6.17)-(6.18), (6.30)-(6.31), (6.39), and (6.46)-(6.47), respectively. Therefore, the objective of the optimization problem (6.85)-(6.88) is to minimize the deviations of the inputs $P_{NBI,i}$ with respect to $P_{NBI,i}^{ref}$. The saturation limits are $P_{NBI,i} \in [0, 2.5]$ MW.

6.5.1 0D Simulation: Nominal Control without Uncertainties

In this first part of the $W + \Omega$ control simulation study, only the nominal controller is tested using the 0D model. First, an open loop, feedforward-only 0D simulation is run with the experimental inputs corresponding to shot 147634. The individual-scalars evolution obtained in this open loop simulation are denoted by W^{exp} and Ω_ϕ^{exp} (it can be noted that they are the same as the evolutions shown in Fig. 6.2). Second, it is desired that, by means of feedback control, the individual-scalar evolutions are driven to given targets, $\bar{(\cdot)}$, which are different from the experimental values, $(\cdot)^{exp}$. The desired targets are chosen as

$$\bar{W} = W^{exp} + 0.08 \text{ MJ}, \tag{6.89}$$

$$\bar{\Omega}_\phi = \Omega_\phi^{exp} - \ 5 \text{ krad/s}. \tag{6.90}$$

Finally, a closed loop (feedforward + feedback) simulation is run to test the performance of the nominal controller.

Fig. 6.8 shows the state evolution in closed loop (solid blue) and open loop (dash-dotted magenta, corresponding to W^{exp} and Ω_ϕ^{exp}), together with the targets (i.e., $\bar{W}$ and $\bar{\Omega}_\phi$, dashed red). Fig. 6.9 shows the time evolution of P_{CO-ON}, P_{CO-OFF}, and $P_{COUNTER}$, both in open loop (i.e., P_{CO-ON}^{ref}, P_{CO-OFF}^{ref}, and $P_{COUNTER}^{ref}$) and in closed loop. Fig. 6.10 shows the constraint gaps for the optimization problem, $\epsilon_{(\cdot)}$, together with the quadratic cost function J. It can be seen that the controller successfully drives the system state to the target. In every step, a solution to the optimization problem is found, so P_{CO-ON}, P_{CO-OFF}, and $P_{COUNTER}$ are optimally determined to minimize the deviation with respect to the experimental inputs from

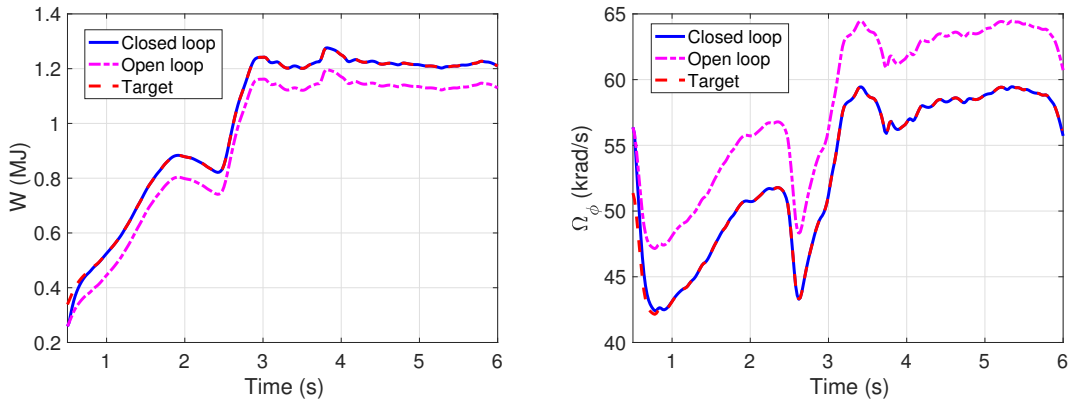

Figure 6.8: State evolution in 0D simulations for $W + \Omega_\phi$ control: open loop (dashed-dotted magenta), closed loop under the nominal law (solid blue), and target (dashed red).

shot 147634. All these powers are increased in order to regulate W and Ω_ϕ. It can also be appreciated that the variables $\epsilon_{P_{tot}}$ and $\epsilon_{T_{NBI}}$ are very small, so the controller's constraints are satisfied within an order of magnitude of 10^{-15} for the P_{tot} constraint and 10^{-16} for the T_{NBI} constraint. This indicates that, as long as the tolerance of the algorithm for solving the optimization problem is higher than $\epsilon_{P_{tot}}$, the problem is in fact feasible even if $\epsilon_{P_{tot}}$ and $\epsilon_{T_{NBI}}$ were not introduced in the formulation of the optimization problem. Finally, it can be seen that J increases substantially during the flat-top phase of the shot, indicating that a higher control effort is required to maintain the targets during that phase.

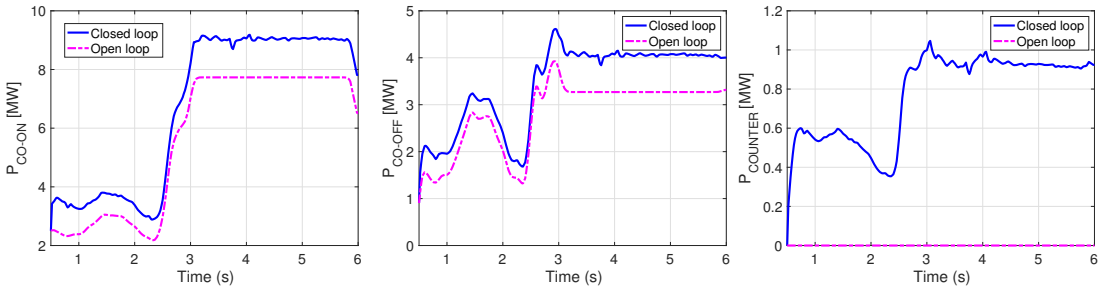

Figure 6.9: Controllable inputs evolution in 0D simulations for $W + \Omega_\phi$ control: open loop (dashed-dotted magenta) and closed loop under the nominal law (solid blue).

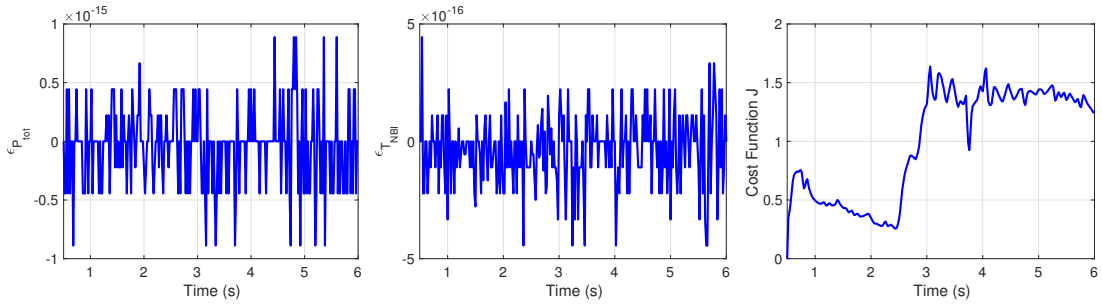

Figure 6.10: Optimization problem parameters in 0D simulations for $W + \Omega_\phi$ nominal control.

6.5.2 0D Simulation: Nominal Control with Uncertainties

In this second part of the $W + \Omega$ control simulation study, the nominal controller is tested again using the 0D model, but this time an uncertainty $\delta_{H_H} = -0.05$ is introduced. The control objective is the same as before, i.e., driving the individual-scalar evolutions to the targets defined in (6.89)-(6.90). First, an open loop, feedforward-only 0D simulation is run with the experimental inputs corresponding to shot 147634 and with $\delta_{H_H} = -0.05$. The individual-scalars evolution obtained in this open loop simulation are not the same as the evolutions shown in Fig. 6.2 as a result of introducing $\delta_{H_H} \neq 0$. Second, a closed loop (feedforward + feedback) simulation is run to test the performance of the nominal controller when $\delta_{H_H} = -0.05$.

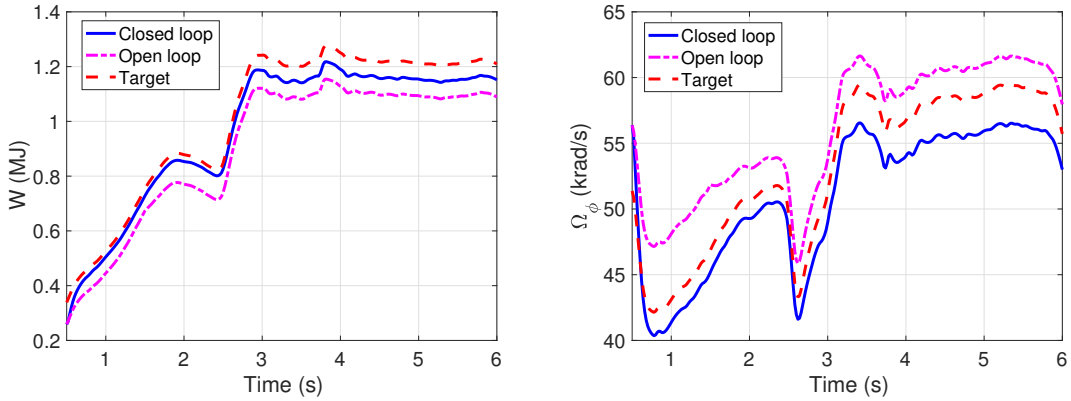

Figure 6.11: State evolution in 0D simulations with uncertainties ($\delta_{H_H} = -0.05$) for $W + \Omega_\phi$ control: open loop (dashed-dotted magenta), closed loop under the nominal law (solid blue), and target (dashed red).

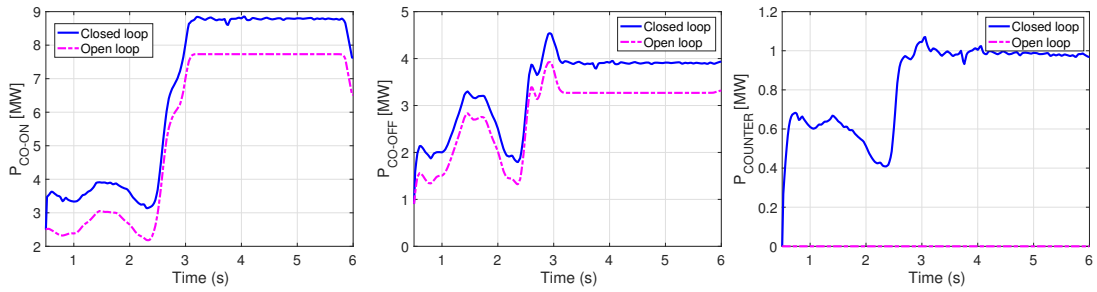

Figure 6.12: Controllable inputs evolution in 0D simulations with uncertainties for $W + \Omega_\phi$ control: open loop (dashed-dotted magenta) and closed loop under the nominal law (solid blue).

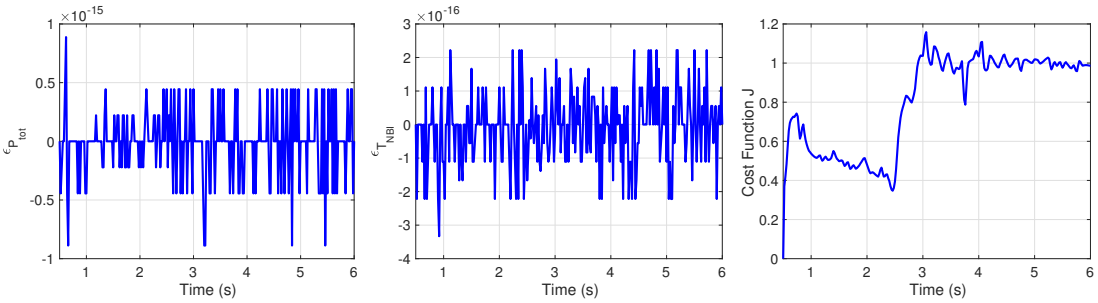

Figure 6.13: Optimization problem parameters in 0D simulations with uncertainties for $W + \Omega_\phi$ nominal control.

Fig. 6.11 shows the state evolution in closed loop (solid blue) and open loop (dash-dotted magenta), together with the targets (dashed red). Fig. 6.12 shows the time evolution of P_{CO-ON}, P_{CO-OFF}, and $P_{COUNTER}$, both in open loop and closed loop. Fig. 6.13 shows the constraint gaps for the optimization problem and the cost function value. It can be seen that the nominal controller is unable to drive the system state to the target. Instead, the value of W achieved remains below the target for the whole discharge. Regarding Ω_ϕ, it seems like the controller is capable of driving it close to $\bar{\Omega}_\phi$ initially, but it is unable to track it. The values of P_{CO-ON}, P_{CO-OFF}, and $P_{COUNTER}$ are very similar to those obtained in the previous simulation case with $\delta_{H_H} = 0$ (see Fig. 6.9), indicating that the nominal controller's requests do not compensate for the effects of the uncertainty $\delta_{H_H} = -0.05$. As before, the values of $\epsilon_{P_{tot}}$ and $\epsilon_{T_{NBI}}$ suggest that it is indeed not necessary to add them into the optimization scheme because feasible solutions could always be found. Also, as before, J is increased by the controller during the flat-top, despite not being able to achieve the targets.

6.5.3 0D Simulation: Robust Control with Uncertainties

In this third part of the $W + \Omega$ control simulation study, the robust controller is tested using the 0D model and $\delta_{H_H} = -0.05$. The control objective is the same as before, i.e., driving the individual-scalar evolutions to the targets defined in (6.89)-(6.90). A closed loop (feedforward + feedback) simulation is run to test the performance of the robust controller when $\delta_{H_H} = -0.05$.

Fig. 6.14 shows the state evolution in closed loop (solid blue) and open loop (dash-dotted magenta), together with the targets (dashed red). Fig. 6.15 shows the time evolution of P_{CO-ON}, P_{CO-OFF}, and $P_{COUNTER}$, both in open loop and closed loop. Fig. 6.16 shows the constraint gaps for the optimization problem and the cost function value. It can be seen that, unlike the nominal controller, the robust controller is in fact able to drive the system state substantially close to the target. The values of P_{CO-ON}, P_{CO-OFF}, and $P_{COUNTER}$ are much higher than in the previous simulation cases (see Fig. 6.9 and Fig. 6.12), indicating that the robust controller needs to be more aggressive in order to neutralize the effect of the uncertainty $\delta_{H_H} = -0.05$. However, it can be noted that P_{CO-ON} and P_{CO-OFF} are almost saturated during the flat-top phase, suggesting that this is possibly the reason why W and Ω_ϕ do not totally converge to their targets despite being significantly close. This would not be a problem of the control algorithm itself, but just an issue related with having too high $\bar{W}$ and $\bar{\Omega}_\phi$. Another reason why W and Ω_ϕ do not totally converge to their targets is also be the fact that the robust controller does not ensure exponential stability, but only boundedness by a function that can be made small (but not zero). As before, the values of $\epsilon_{P_{tot}}$ and $\epsilon_{T_{NBI}}$ suggest that it is indeed not necessary to add them into the optimization scheme. Also, as before, J is substantially higher than in previous simulations with the nominal controller (see Fig. 6.10 and Fig. 6.13), corroborating the fact that the robust controller is more aggressive.

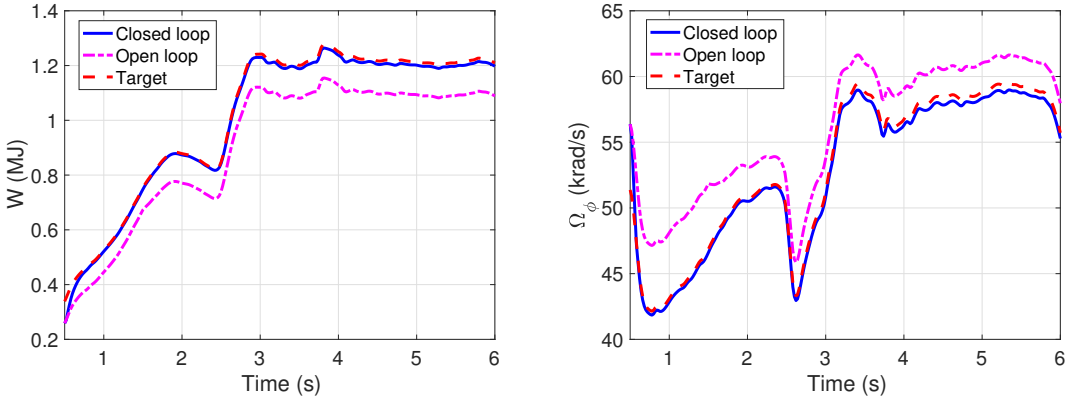

Figure 6.14: State evolution in 0D simulations with uncertainties ($\delta_{H_H} = -0.05$) for $W + \Omega_\phi$ control: open loop (dashed-dotted magenta), closed loop under the robust law (solid blue), and target (dashed red).

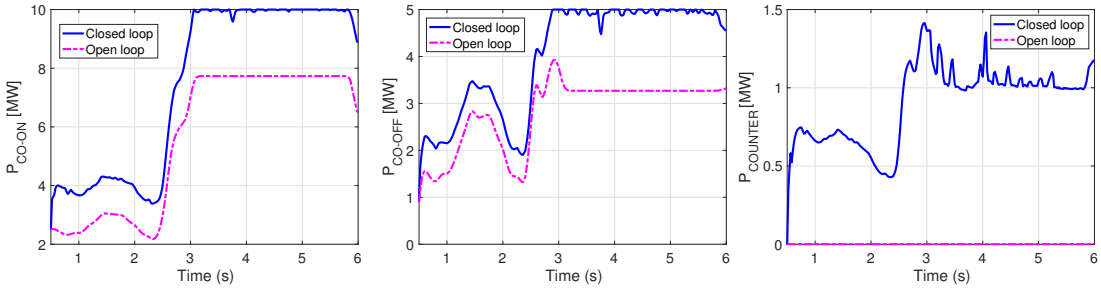

Figure 6.15: Controllable inputs evolution in 0D simulations with uncertainties for $W + \Omega_\phi$ control: open loop (dashed-dotted magenta) and closed loop under the

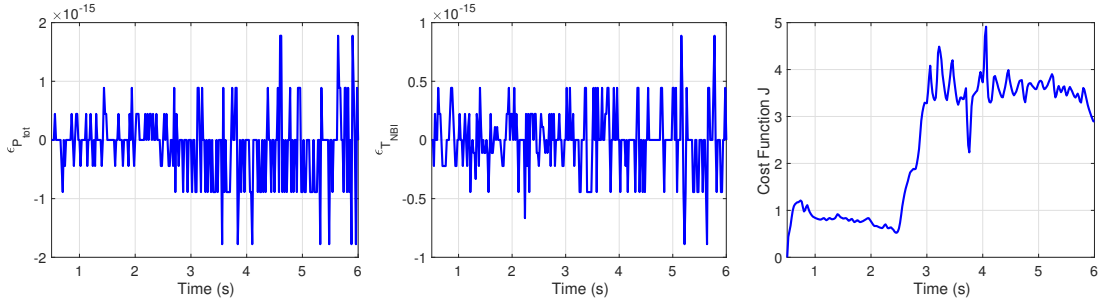

Figure 6.16: Optimization problem parameters in 0D simulations with uncertainties for $W + \Omega_\phi$ robust control.

6.5.4 1D Simulation

In this last part of the $W + \Omega$ control simulation study, both the nominal and the robust controllers are tested in 1D simulations using COTSIM. First, an open loop,

feedforward-only 1D simulation is run with the experimental inputs corresponding to shot 147634. The 0D variables in COTSIM are denoted by $W^{exp,1D}$ and $\Omega_\phi^{exp,1D}$, and are computed from the corresponding 1D variables (n_e, n_i, T_e, and T_i for W, and n_e and ω_ϕ for Ω_ϕ). The formulas employed for the computation of W and Ω_ϕ are (2.21)-(2.22) and (2.126), respectively. Then, targets are created based on the 1D open-loop evolution in the same way as for the 0D simulations, (6.89)-(6.90), so that $\bar{W} = W^{exp,1D} + 0.08$ MJ and $\bar{\Omega}_\phi = \Omega_\phi^{exp,1D} - 5$ krad/s. Finally, closed loop (feedforward + feedback) simulations are run to test the performance of the nominal and robust controllers when trying to achieve the targets $\bar{W}$ and $\bar{\Omega}_\phi$.

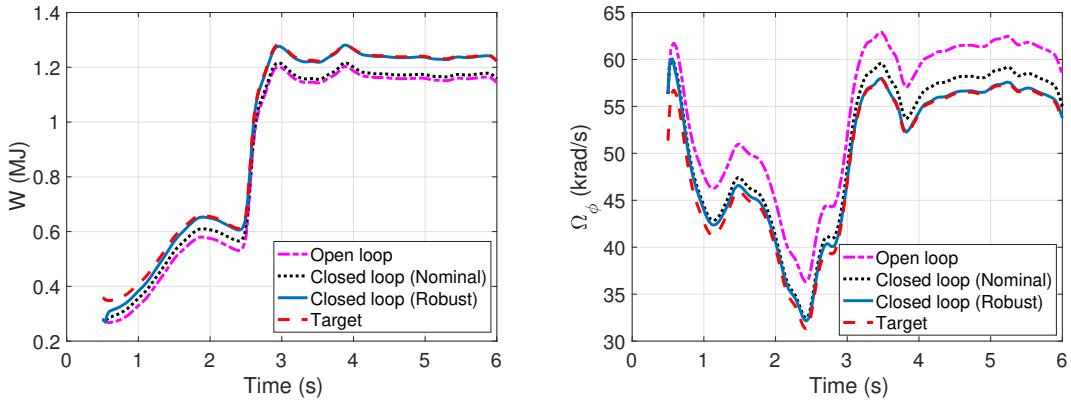

Figure 6.17: State evolution in 1D simulations for $W + \Omega_\phi$ control: open loop (dashed-dotted magenta), closed loop under the nominal law (dotted black), closed loop under the robust law (solid blue), and target (dashed red).

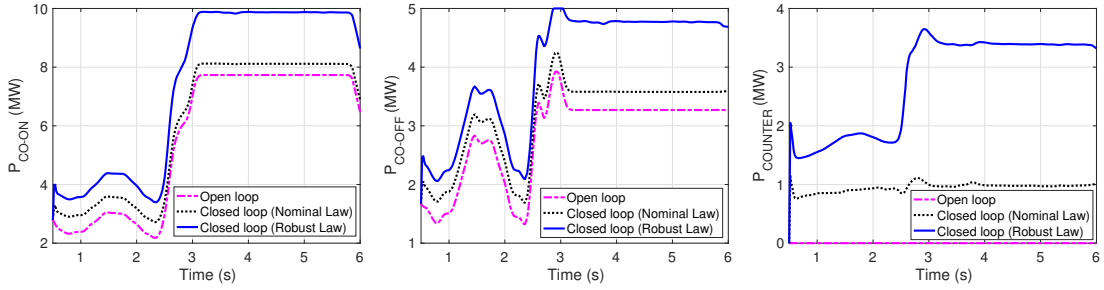

Figure 6.18: Controllable inputs evolution in 1D simulations for $W + \Omega_\phi$ control: open loop (dashed-dotted magenta), closed loop under the nominal law (dotted black), and closed loop under the robust law (solid blue).

Fig. 6.17 shows the state evolution in open loop (i.e., $W^{exp,1D}$ and $\Omega_\phi^{exp,1D}$) and closed loop under the nominal and robust control laws, together with the targets. Fig. 6.18 shows the time evolution of P_{CO-ON}, P_{CO-OFF}, and $P_{COUNTER}$. Fig. 6.19 shows the constraint gaps for the optimization problem and the cost function value when using the robust controller (the same qualitative evolutions are found for these variables when using the nominal controller). From Fig. 6.17, it can be seen that the nominal law drives W and Ω_ϕ closer to $\bar{W}$ and $\bar{\Omega}_\phi$, respectively, when compared to the open-loop evolution, but x does not converge to the target $\bar{x}$ within the simulation time. It can be seen that the robust controller drives x much closer to the target $\bar{x}$ than the nominal controller (with a small error associated with the parameters $\epsilon_{(\cdot)}$ in the control laws (6.17)-(6.18), (6.30)-(6.31), (6.39), and (6.46)-(6.47)). Fig. 6.18 shows how all the powers are increased by both the nominal and robust controllers to achieve the target $\bar{W} > W^{exp,1D}$. The robust controller requests a higher P_{tot} than the nominal controller (about 5 MW more), which seems to be the reason for its better performance. Also, as $\bar{\Omega}_\phi < \Omega_{exp}$, the NBI torque is decreased by both control laws (see that $P_{COUNTER}$ increases more than the sum of P_{CO-ON} and P_{CO-OFF}). As before, the robust controller is more aggressive and requests a lower NBI torque than the nominal controller. Fig. 6.18 shows that, when using the robust law, all $P_{NBI,i}$ are very close to saturation, and P_{CO-OFF} even saturates for a small period of time. This happens as a result of very demanding targets ($\bar{W}$, $\bar{\Omega}_\phi$), as it had already been hinted in the previous simulation. The comparison between the nominal and robust controllers suggests that the latter will have an improved performance in simulations using more complex codes than COTSIM, as well as in experiments. Finally, it can be appreciated from Fig. 6.19 that the optimization problem is always feasible, and that the cost function J is much higher than in any other simulation, specially during the flat-top phase. This increase in J is mostly due to the high $P_{COUNTER}$ employed.

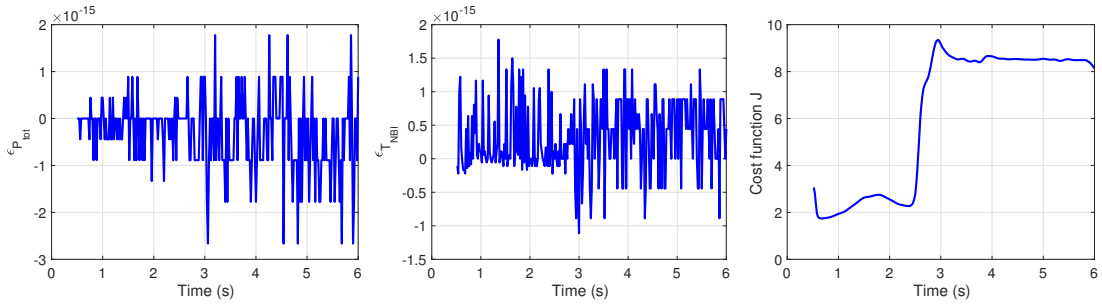

Figure 6.19: Optimization problem parameters in 1D simulations for $W + \Omega_\phi$ robust control.

6.6 Simulation Testing: $q_0 + q_{edge} + W + \Omega_\phi$ Control

The problem of simultaneously controlling all the individual scalars previously introduced (q_0, q_{edge}, W and Ω_ϕ) is studied in this Section. The actuators considered are I_p, NBI, and EC. The control algorithm is tested both in 0D and 1D simulations. The simulation scenario is the same as before, DIII-D shot 147634, and the NBIs are also grouped in the same 3 sets (co-current on-axis NBIs, $P_{NBI,1} = P_{CO-ON}$, co-current off-axis NBIs, $P_{NBI,2} = P_{CO-OFF}$, and counter-current NBIs, $P_{NBI,3} = P_{COUNTER}$).

The optimization problem employed in this Section is the one given by (6.71)-(6.76) but modified with the auxiliary variables that characterize the gap in each controller constraint: $\epsilon_{P_{tot}}$ for (6.73), $\epsilon_{T_{NBI}}$ for (6.74), and $\epsilon_{j_{aux}}$ for (6.75). As in the previous Section, the cost function is chosen to be quadratic, as given by equation (6.80). Additional constraints are added to (6.71)-(6.76) in Section 6.6.3. The saturation limits are $I_p \in [0, 2]$ MA, $P_{NBI,i} \in [0, 2.5]$ MW, and $P_{EC} \in [0, 3.5]$ MW.

6.6.1 0D Simulation: Nominal Control

In this first part of the $q_0 + q_{edge} + W + \Omega_\phi$ simulation study, the control algorithm and the actuator manager are tested in a 0D simulation using the same model as the one employed for control design. First, an open-loop, feedforward-only 0D simulation is run with the experimental inputs from shot 147634. The individual-scalar evolutions obtained in this 0D open-loop simulation are denoted by q_0^{exp}, q_{edge}^{exp}, W^{exp}, and Ω_ϕ^{exp} (it can be noted that they are the same as the evolutions shown in Fig. 6.2). It is desired that, by means of the nominal controller, the individual-scalar

evolutions are driven to given targets, $\bar{(\cdot)}$, which are different from the experimental values, $(\cdot)^{exp}$. The robust controller is not tested in this 0D simulation because no uncertainties are included, so the nominal controller must suffice to satisfy the control objective.

The targets are chosen to optimize the reference shot according to the following criteria. First, it is desired to increase the plasma resilience against MHD instabilities by increasing q (and therefore, increasing q_0 and q_{edge}). However, increasing q may have a negative impact in confinement (I_p decreases). Instead, it is desired that W is slightly increased with respect to the reference shot. Finally, it is also desired that Ω_ϕ is increased to improve the resilience against RWMs and locked modes, and increase the plasma performance in general. Thus, the targets are chosen as $\bar{q}_0 = q_0^{exp} + 0.1$, $\bar{q}_{edge} = q_{edge}^{exp} + 0.2$, $\bar{W} = W^{exp} + 0.03$ MJ, and $\bar{\Omega}_\phi = \Omega_\phi^{exp} + 1.5$ krad/s.

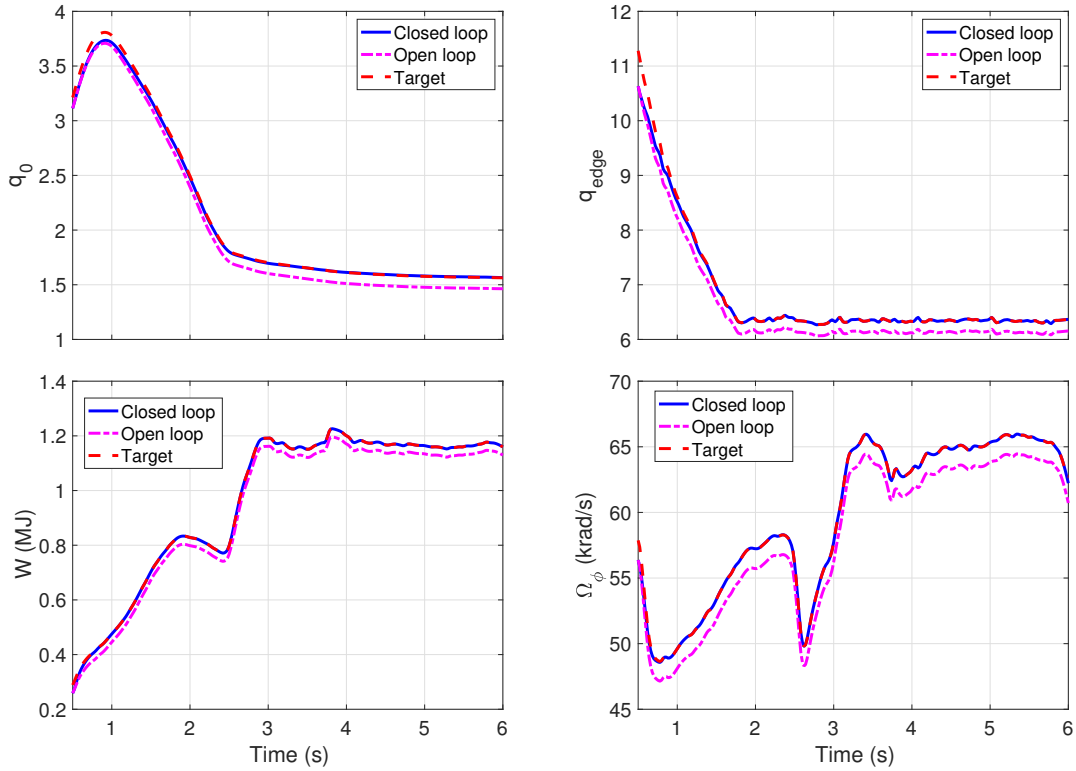

Figure 6.20: State evolution in 0D simulations for $q_0 + q_{edge} + W + \Omega_\phi$ control: open loop (dashed-dotted magenta), closed loop under the nominal law (solid blue), and target (dashed red).

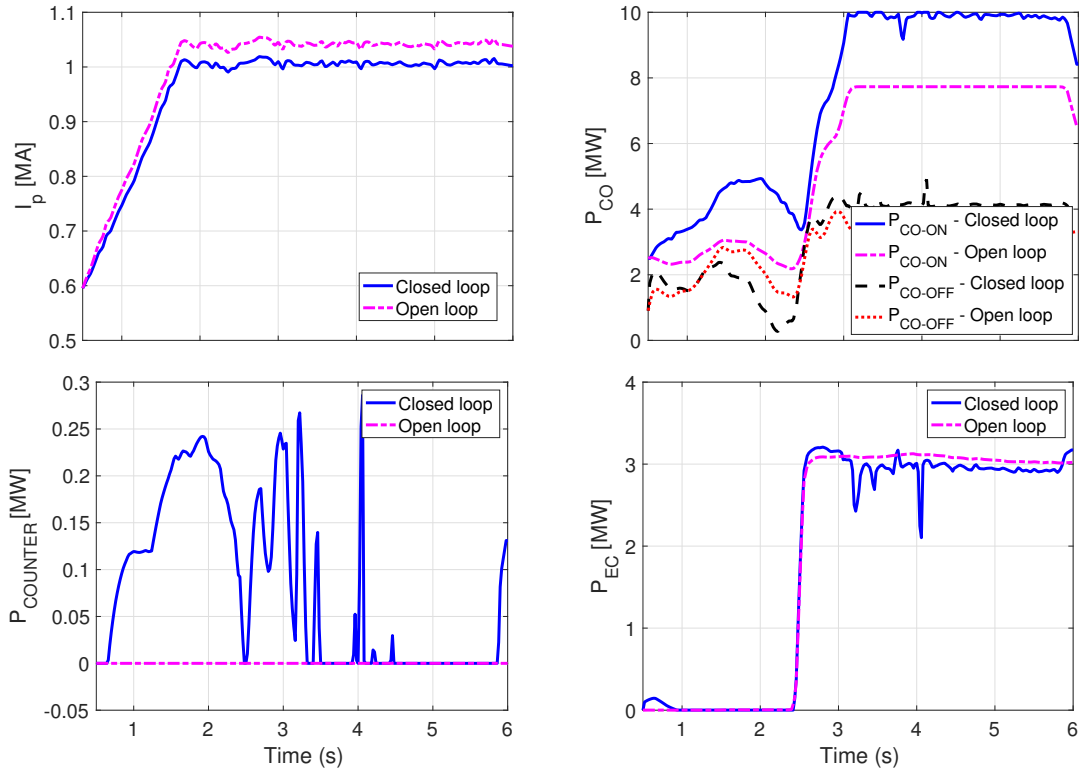

Figure 6.21: Controllable inputs evolution in 0D simulations for $q_0 + q_{edge} + W + \Omega_\phi$ control: open loop (dashed-dotted magenta) and closed loop under the nominal law (solid blue).

Fig. 6.20 shows the state evolution in closed loop (solid blue) and open loop (dash-dotted magenta), together with the targets (dashed red). Fig. 6.21 shows the I_p, P_{CO-ON}, P_{CO-OFF}, $P_{COUNTER}$ and P_{EC} evolutions. Fig. 6.22 shows $\epsilon_{(\cdot)}$ and J for the optimization problem. In every step, a solution to the optimization problem is found, so I_p, $P_{NBI,i}$ and P_{EC} are optimally determined to minimize the deviation with respect to the feedforward inputs from shot 147634 while driving the plasma to the desired state. The plasma current, I_p, is reduced with the goal of increasing q_{edge} to its target. It can be appreciated that the main variation in NBI power is found in the co-current on-axis power, P_{CO-ON}, which increases both W and Ω_ϕ, although its current drive should in principle reduce q_0. The reduction in q_0 is attenuated in part because of the higher W evolution found, which reduces η and, therefore, reduces the on-axis current (and increases q_0). The lower I_p value possibly contributes to the

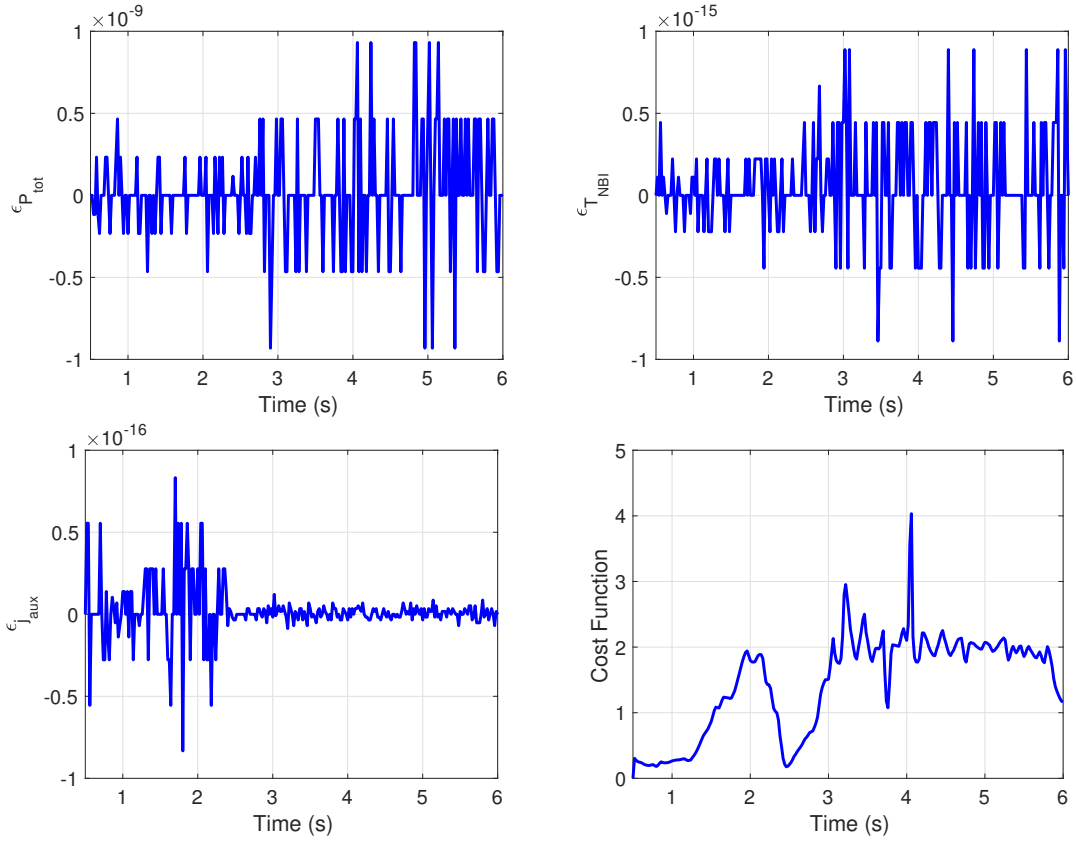

Figure 6.22: Optimization problem parameters in 0D simulations for $q_0 + q_{edge} + W + \Omega_\phi$ control.

increase of q_0 as well. Both P_{CO-OFF} and $P_{COUNTER}$ are also increased with respect to the references shot values, but proportionally less than P_{CO-ON}. This makes the co-current NBI torque increase more than the counter-current NBI torque, which in turn raises Ω_ϕ. The constraints are satisfied within an order of magnitude of 10^{-9} for the P_{tot} constraint, and 10^{-15} for the T_{NBI} constraint, and 10^{-16} for the q_0 constraint, indicating the feasibility of the optimization problem during the whole simulation.

6.6.2 1D Simulation: Nominal and Robust Control

In this part of the $q_0 + q_{edge} + W + \Omega_\phi$ simulation study, the controller is tested in 1D simulations using COTSIM. Like in the previous Section, the objective of this

simulation case is to show the controller's performance when driving the individual scalars towards targets that are different from the evolution during shot 147634. First, a 1D open-loop, feedforward-only simulation is executed with the experimental inputs corresponding to shot 147634. The individual scalar evolutions are obtained just like in previous Sections, and are denoted by $q_0^{exp,1D}$, $q_{edge}^{exp,1D}$, $W^{exp,1D}$, and $\Omega_\phi^{exp,1D}$, whereas the targets are also taken like in the previous Section. Then, two closed-loop simulations are carried out to compare the performance of the nominal and robust feedback controllers when trying to drive the state to the target.

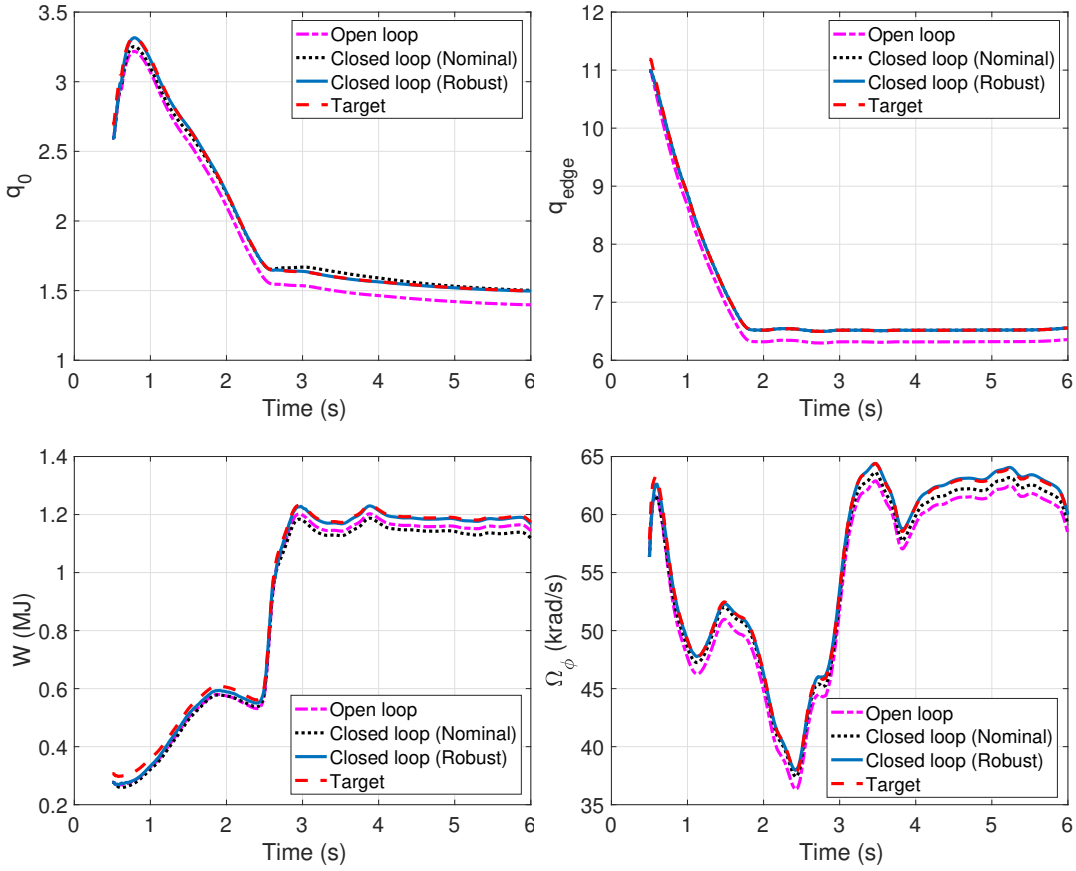

Figure 6.23: State evolution in 1D simulations for $q_0 + q_{edge} + W + \Omega_\phi$ control: open loop (dashed-dotted magenta), closed loop under the nominal law (solid blue), and target (dashed red).

Fig. 6.23 shows the time evolution of the different scalars in open loop (i.e., $q_0^{exp,1D}$, $q_{edge}^{exp,1D}$, $W^{exp,1D}$, and $\Omega_\phi^{exp,1D}$) and closed loop under the nominal and robust

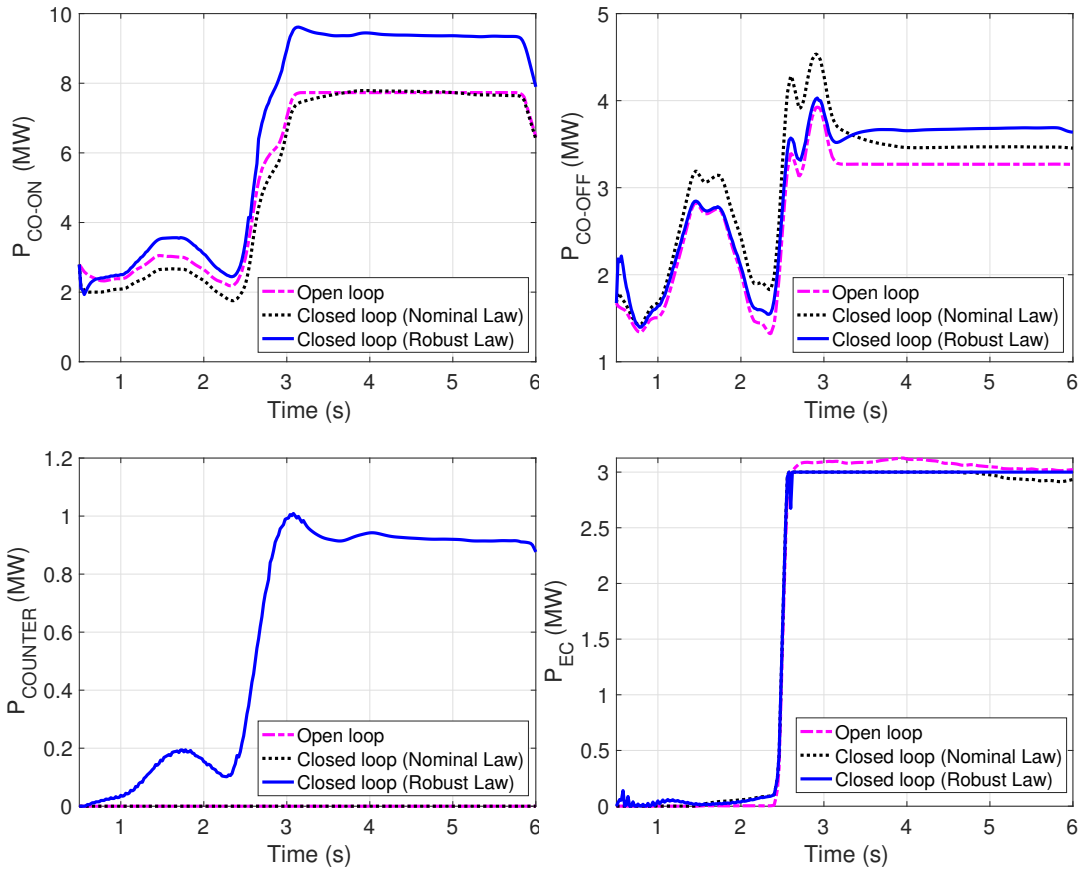

Figure 6.24: Controllable inputs evolution in 1D simulations for $q_0 + q_{edge} + W + \Omega_\phi$ control: open loop (dashed-dotted magenta), closed loop under the nominal law (dotted black), and closed loop under the robust law (solid blue).

control laws. Fig. 6.24 shows the time evolution of the different controllable powers (I_p is not included because it is the same as in Fig. 6.21). Fig. 6.25 shows the time evolution of $\epsilon_{(\cdot)}$ and J when using the robust controller. It can be seen that q_{edge} is driven to the target under both the nominal and robust control laws. Regarding q_0, the performance of the robust controller is better than the nominal controller, but the latter has an acceptable performance as well. The main differences in performance between control laws are found in the W and Ω_ϕ evolutions. It can be seen that the robust controller drives both W and Ω_ϕ significantly close to the target, whereas the nominal controller is unable to do so. For W, the nominal controller actually achieves values below the open-loop evolution, possibly due to

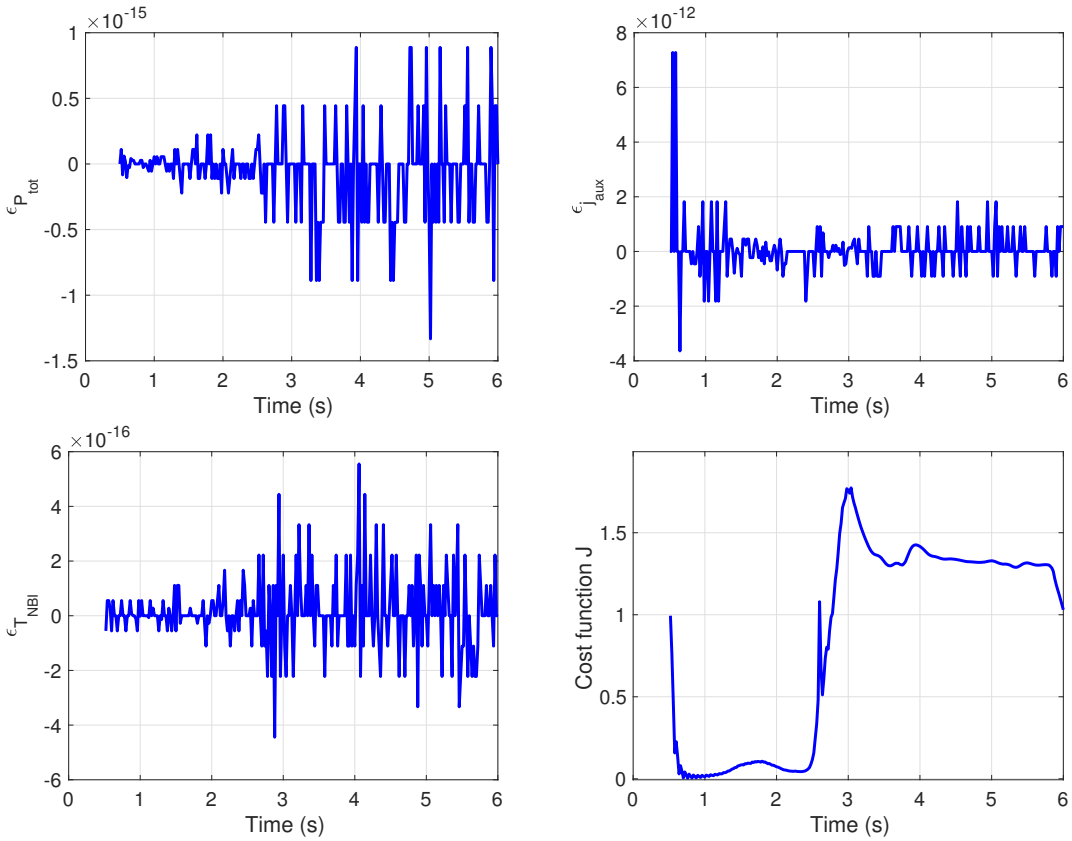

Figure 6.25: Optimization problem parameters in 1D simulations for $q_0 + q_{edge} + W + \Omega_\phi$ robust control.

the aforementioned increase in q. As in the 0D simulation, P_{CO-ON} is the power that is increased the most with respect to the reference shot by the robust controller, whereas the nominal controller employs P_{CO-ON} values very close to the reference shot. This is possibly the main reason for the difference in the W evolutions attained. Also, a higher $P_{COUNTER}$ is employed by the robust controller, whereas the nominal controller does not employ $P_{COUNTER}$. Finally, the values of $\epsilon_{P_{tot}}$, $\epsilon_{T_{NBI}}$ and $\epsilon_{j_{aux}}$ demonstrate the convergence of the actuator manager. The cost function J is smaller in the 1D simulation than in the 0D simulation, showing that the 1D model requires a higher control effort when compared to the 0D model in order to achieve the same control objectives.

6.6.3 1D Simulation: Nominal and Robust Control with Additional Constraints

This part of the $q_0 + q_{edge} + W + \Omega_\phi$ simulation study aims to demonstrate the actuator manager's capability to perform actuator management. The targets for q_0, W, and Ω_ϕ correspond to the experimental values from shot 147634, $(\cdot)^{exp,1D}$, whereas the target for q_{edge} is taken as $\bar{q}_{edge} = q_{edge}^{exp,1D} - 0.2$. In addition, the following constraints are imposed: the 2nd NBI is constrained for MSE measurements during the whole shot ($P_{NBI,30R} = 1$ MW), the 4th NBI is turned off ($P_{NBI,150R} = 0$) between $t = 1$ s and $t = 2$ s, and a gyrotron is assumed lost (i.e., $P_{EC}^{max} = 2.5$ MW) after $t = 5$ s. Only the robust controller is tested in this Section, as it normally has a better performance in 1D simulations.

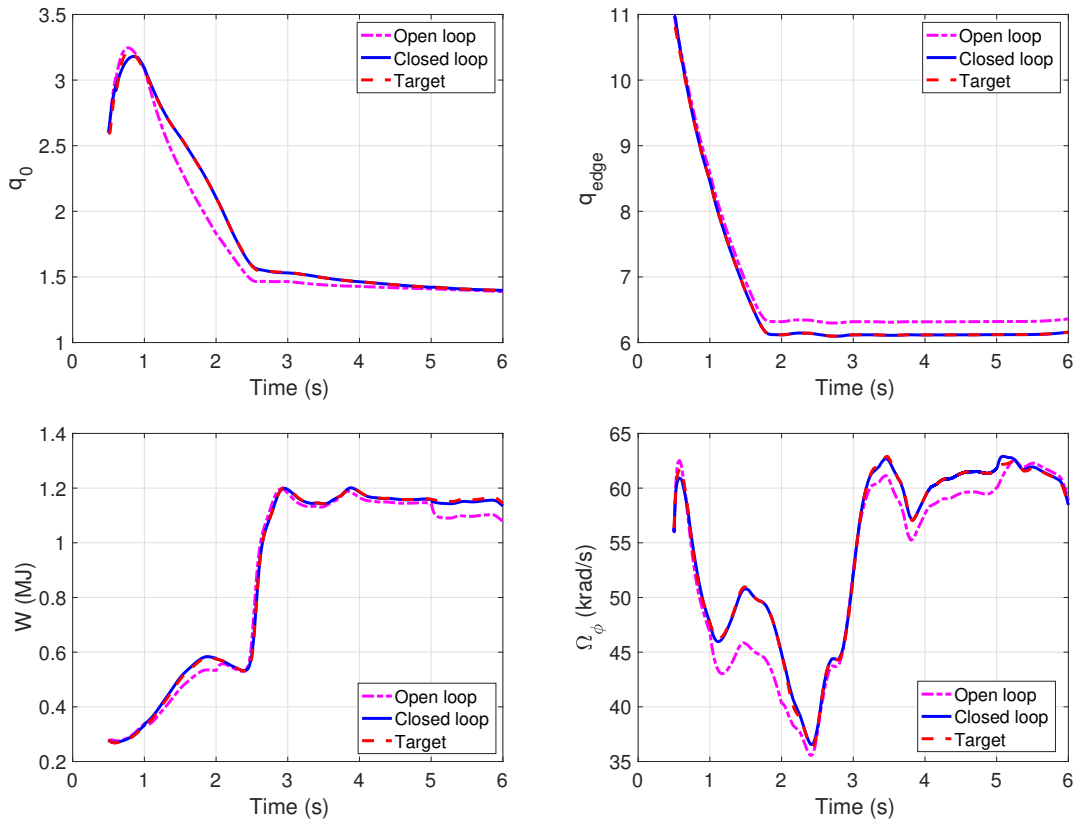

Figure 6.26: State evolution in 1D simulations for $q_0 + q_{edge} + W + \Omega_\phi$ control with additional constraints: open loop (dashed-dotted magenta), closed loop under the nominal law (solid blue), and target (dashed red).

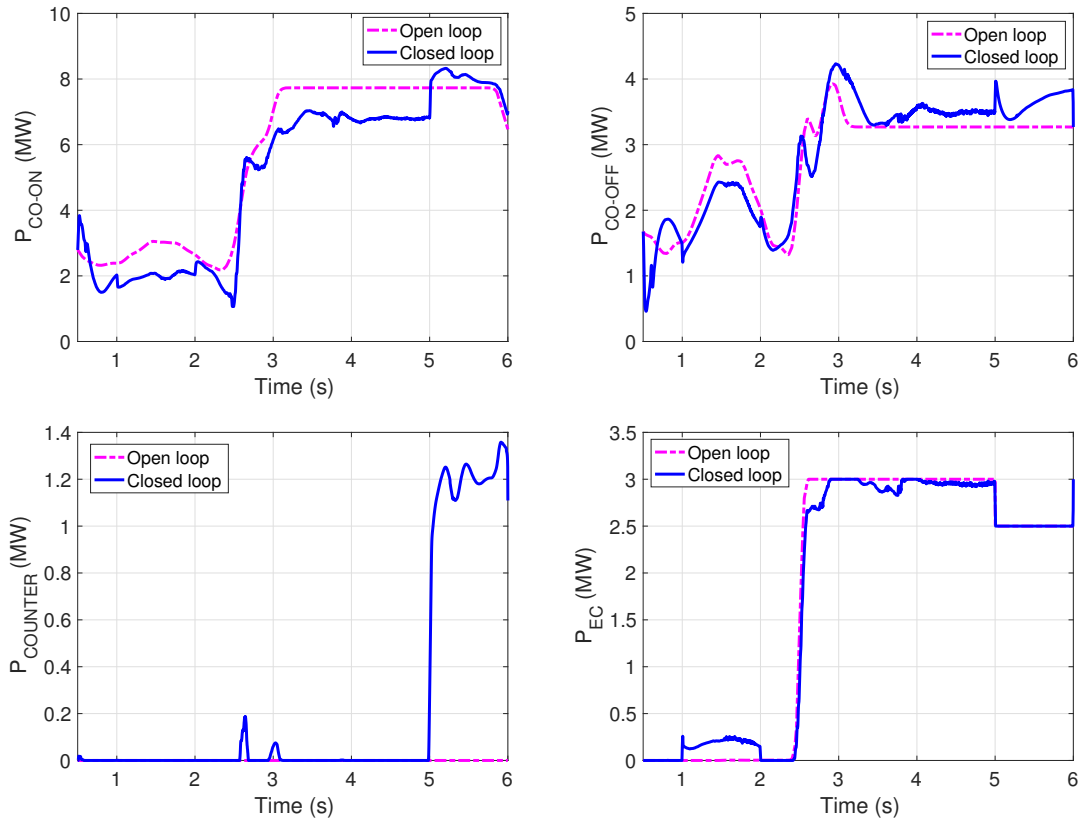

Figure 6.27: Controllable inputs evolution in 1D simulations for $q_0 + q_{edge} + W + \Omega_\phi$ control with additional constraints: open loop (dashed-dotted magenta) and closed loop under the nominal law (solid blue).

Fig. 6.26 shows the time evolution of the individual scalars, and Fig. 6.27 shows the controllable inputs evolution. The evolutions presented correspond to the open loop simulation (i.e., without feedback control and using the experimental inputs from shot 147634 constrained as explained in the previous paragraph) and closed loop simulation (i.e., feedback control activated), together with the targets. Fig. 6.28 shows the parameters of the optimization problem ($\epsilon_{(\cdot)}$ and J). It can be seen that, in open loop, the system evolves to values that are substantially different from the target, as expected from using the constrained inputs. In closed loop, the individual scalars are driven to their targets despite the aforementioned constraints. The controller increases P_{EC} between $t = 1$ s and $t = 2$ s (in order to compensate for $P_{NBI,150R} = 0$), and also increases all P_{CO-ON}, P_{CO-OFF} and $P_{COUNTER}$ after

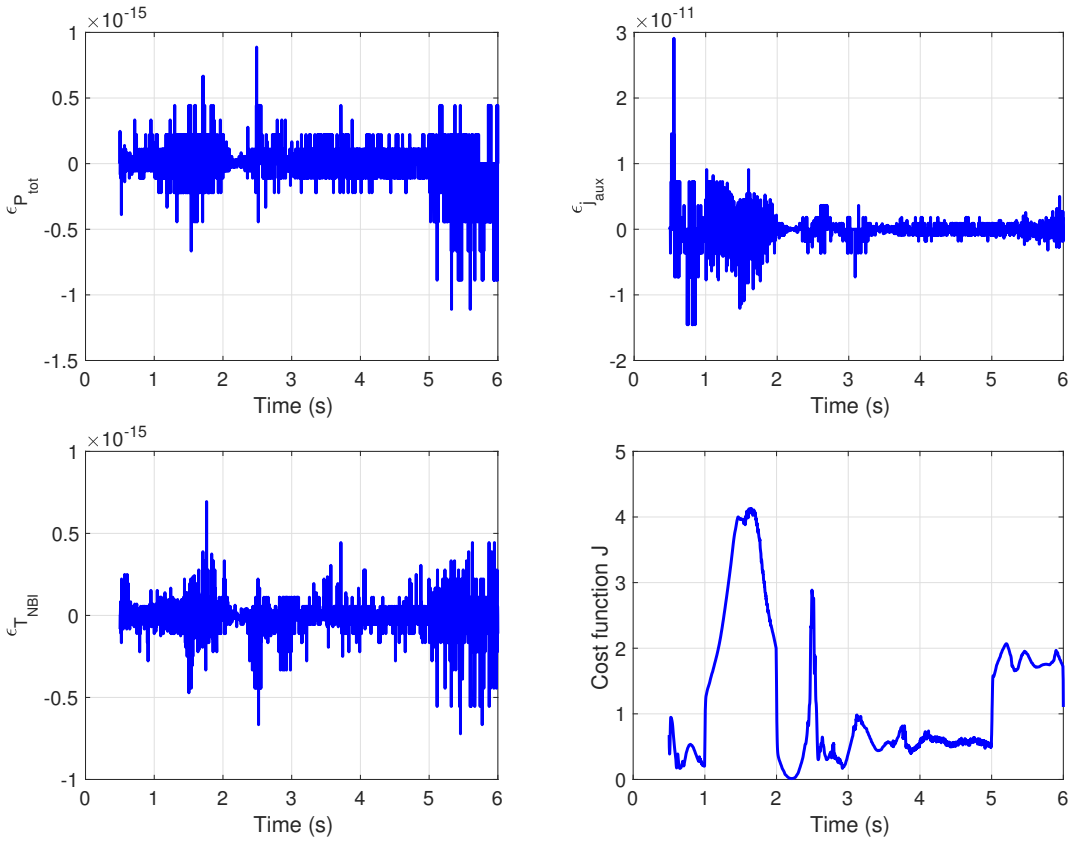

Figure 6.28: Optimization problem parameters in 1D simulations for $q_0 + q_{edge} + W + \Omega_\phi$ control with additional constraints.

$t = 5$ s (in order to compensate for $P_{EC} = 0$). Just like in the rest of the simulations presented in this Chapter, the values of the constraint gaps ($\epsilon_{P_{tot}}$, $\epsilon_{T_{NBI}}$ and $\epsilon_{j_{aux}}$) demonstrate the convergence of the actuator manager. The cost function J is never zero because there is always some controllable input that needs to be modified (due to the constraint $P_{30R} = 0$). It is also interesting to note how J is a figure of merit for the control effort, as it increases substantially when $t \in [1, 2]$ s and $t \in [5, 6]$ s, i.e., when there is some actuator failure taking place.

6.7 Conclusions

Individual controllers for the regulation of the central safety factor, edge safety factor, stored energy and bulk toroidal rotation in tokamaks have been designed in this Chapter. These are model-based controllers synthesized from 0D, nonlinear, control-oriented models of the dynamics of the individual scalars. Each controller is composed of a nominal control law and a robust control law designed using Lyapunov stability and redesign techniques, respectively.

The individual-scalar controllers are integrated by means of an actuator manager that is designed based on an optimization approach. This actuator manager is highly configurable, as it allows for a really easy integration of additional control commands either from other controllers or from supervisory systems, and is robust, as the optimization problem can always be converted into a feasible problem at the expense of relaxing the controllers' requests. When there is a suitable number of available actuators, the actuator manager always finds an optimal solution that lies within the set of feasible control commands while satisfying the constraints derived from the control laws.

This integrated control scheme has the capability of tracking targets and/or reproducing the experimental evolution of the individual scalars while handling input constraints in both 0D and 1D simulations. When the robust control laws are activated, the control scheme shows a better performance when compared to the nominal control laws working on their own. Moreover, the control scheme shows promising results in 1D simulations using the COTSIM code, although it has to be kept in mind that the controller design procedure is independent of the tokamak and/or scenario in question. This control tool can be implemented in integrated PCS designs like the one envisioned for ITER, and may be of interest in present and future tokamak-scenario planning and development. Future work may also include the implementation and experimental testing of the control algorithm in DIII-D, as well as the development of alternative optimization schemes with different cost functions and models that vary in real time according to the control needs.

Chapter 7

Integrated Kinetic, Magnetic and Instability Control: Profile and Scalars Control with NTM Suppression

7.1 Introduction and Previous Work

The neoclassical tearing modes (NTMs) are one of the MHD instabilities most commonly found in tokamak plasmas. NTMs are the resistive version of the kink stability [5]. At low β (i.e., low pressure), they are driven by the radial gradient of the toroidal current, whereas at high β, the pressure gradient also drives their triggering. As a result, NTMs are both current and pressure-driven instabilities. In tokamak plasmas, NTMs take the form of *magnetic islands*, isolated regions with their own separatrix that break the nesting of magnetic-flux surfaces around the magnetic axis predicted by the ideal MHD theory (see Fig. 2.9).

As a result, two regions are normally considered when studying NTMs:

- A thin *resistive layer* (i.e., the magnetic island) located at a given rational surface m/n of the mode (where m and n are the poloidal and toroidal mode

numbers, respectively). Inside the magnetic island, the plasma resistivity, η, cannot be neglected because it plays a significant role in the NTM island physics. Within a magnetic island, a local flattening of the temperature and pressure profiles is observed due to an increase in the particle and heat transport. It can be shown [5] that the contribution of $\vec{v} \times \vec{B}$ is very small in the MHD Ohm's law, (2.7), and $\eta\vec{j}$ is necessarily different from zero in order to compensate for $\vec{E}$. Also, the local flattening of the pressure profile comes with an associated decrease in the bootstrap current (see equation (2.33)) within the magnetic island. This lack of bootstrap current drives the island growth.

- The rest of the plasma domain, which is assumed to be in ideal MHD equilibrium (equation (2.8)) due to the slow NTM growth-rate normally found.

For an NTM to grow, a minimum island width is required, also known as *seed island* size. These seed islands are sometimes created by sawtooth instabilities or ELMs. Once the island starts to grow, it reaches a maximum island width, also known as *saturated island* width. A model for the dynamics of the NTM-island width that includes most of these effects has been introduced in Chapter 2, Section 2.3.7.

When an NTM develops, an overall decrease in the plasma performance is observed, limiting the achievable β (or p, therefore limiting the attainable triple product, see equation (1.12)). Due to this, NTMs are highly undesirable during a tokamak discharge, and their suppression is a topic of substantial interest within the fusion community (see Section 1.3). Significant work has been carried out to understand the NTM triggering mechanisms and develop control algorithms for their suppression. Successful NTM suppression has been achieved in experiments in different tokamaks [13, 32, 98–100]. The basic physical mechanism for NTM suppression that has been considered is "replacing" the loss of bootstrap current by means of auxiliary current deposition, mostly by means of radiofrequency (RF) waves (ECCD, ICCD, LHCD, etc). Work on modeling of RF effects on the NTM-island dynamics can be found in [101–104]. It is an experimental fact that current driven on or close to the O-point shrinks the magnetic island, whereas current driven near the X-point normally makes the island grow (see Chapter 2, Section 2.3.7). Other methods to

suppress NTMs have been considered, such as the application of nonresonant magnetic fields [13], although CD by means of RF will most likely be the main NTM suppression method in ITER.

The possible NTM impact on ITER has been a concerning issue for years [105–109], although these studies show that NTM suppression will most likely be successfully carried out in ITER. In this Chapter, repurposing (RP) actuator-sharing techniques are presented for simultaneous NTM suppression with q-profile control and/or scalar variables. This Chapter is divided in two main Sections. Section 7.2 reports experimental results on NTM suppression with q-profile + β_N control obtained in the DIII-D tokamak [110]. The control algorithms employed had already been developed and tested separately prior to this experimental demonstration for combined control (see [13] for NTM suppression, and [24, 83] for q-profile + β_N control via MPC). Section 7.3 reports 1D simulation results using COTSIM for simultaneous NTM suppression and individual-scalars control [111], using an adapted version of the actuator management scheme proposed in Chapter 6.

7.2 NTM Suppression and q-profile + β_N Control

7.2.1 The DIII-D Plasma Control System

The DIII-D PCS provides an excellent benchmark for testing and development of integrated-control strategies due to its parallel architecture [15]. It is composed of different categories which allocate algorithms with a specific purpose, such as Profile control, NBI control, Gyrotron control, etc. (see Fig. 7.1). Each category can work using multiple sequences (primary, secondary, and so on). These sequences are different pre-programmed configurations of that category which can be executed asynchronously within the same shot. Category-configuration changes that comprise each sequence may include, for example, the use of different control algorithms, saturation levels, control gains, and other control parameters. The active sequence of a particular category at a given instant is the sequence that is being utilized by such category. This PCS category-sequence structure allows for a flexible programming

environment, which is very useful for integrated control development.

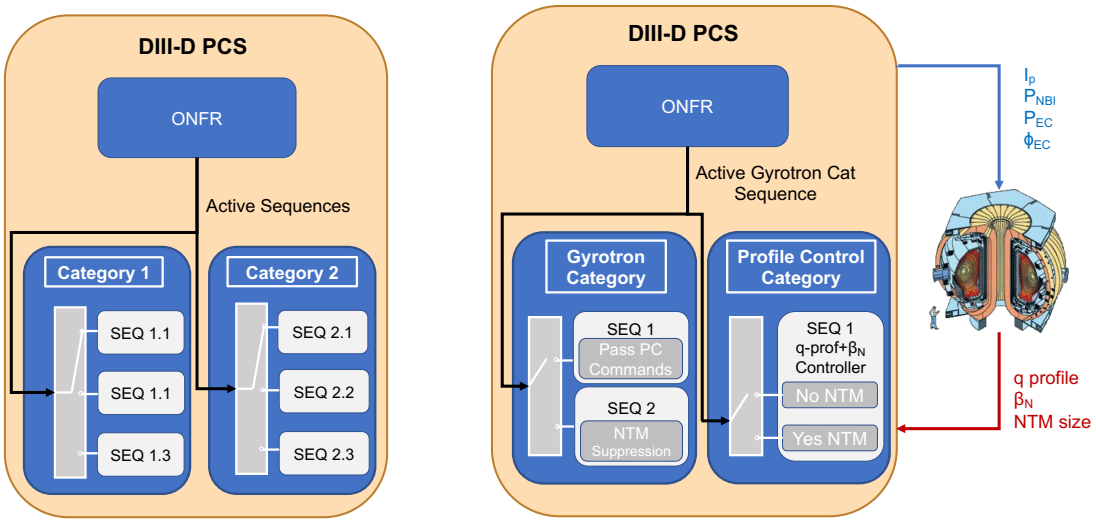

Figure 7.1: Schematics of the DIII-D PCS: on the left, general connection between ONFR and different categories and sequences; on the right, connection created for simultaneous NTM suppression and profile control.

In addition, the Off-Normal Fault-Response (ONFR) system [112], an algorithm based on finite-state logic that can work as a Supervisory and Exception Handling (S&EH) system, has been implemented and successfully tested in the DIII-D PCS. The ONFR system monitors the occurrence of some phenomena (such as NTMs, locked modes, and others) by means of relevant plasma-state data. With such information, ONFR can determine the active sequence for the different categories (see Fig. 7.1) according to the control requirements dictated by the plasma state.

7.2.2 Control Algorithms for NTM Suppression and q-profile + β_N Control

In this work, two DIII-D PCS categories are employed: the Profile Control category and the Gyrotron category (see Fig. 7.1). The Profile Control category works only with a single sequence that allocates a Model Predictive Controller [83] for q-profile control, in which a PID control law for β_N or energy regulation is embedded as a constraint. This MPC algorithm computes the required control signals for the

individual NBI powers, $P_{NBI,i}$ (i = 1,...,8, for the 8 NBIs present in DIII-D), total EC H&CD power, P_{EC}, EC poloidal mirror angles[1], ϕ_i (i = 1,...,6, for the 6 gyrotrons present in DIII-D), and I_p.

On the other hand, the Gyrotron category works with two sequences (primary and secondary). If in the primary sequence, the Gyrotron category just uses the P_{EC} and $\phi_{(\cdot)}$ requests computed by the Profile Control category. If in the secondary sequence, the Gyrotron category computes P_{EC} and ϕ_i as required for NTM suppression. In previous NTM suppression experiments [13, 114], it has been customary to employ the maximum available EC H&CD power, P_{EC}^{max}, and to aim the gyrotrons at the rational (m/n) surface that requires NTM suppression, either by modifying the plasma position or by modifying ϕ_i.

7.2.3 Integration of the NTM Suppression and q-profile + β_N Control Algorithms

The integrated-control architecture is summarized in Fig. 7.1, and described with more detail in Fig. 7.2. As a supervisor to the Profile Control and Gyrotron categories, the ONFR system monitors the plasma state for NTM occurrence, and computes a signal that indicates the need for NTM suppression. This signal is sent to both the Profile Control category and the Gyrotron category, and it is an integer that determines the active sequence of the Gyrotron category (1 for the primary sequence, and 2 for the secondary sequence).

If the ONFR system determines that there is no need for NTM suppression, the active sequence of the Gyrotron category is the primary sequence, and the Profile Control category is assigned control over EC H&CD. Although they are not modified, the P_{EC} and ϕ_i control requests computed by the Profile Control category must still pass through the Gyrotron category because the latter is the category allowed to send gyrotron-related commands in the current design of the DIII-D PCS.

[1]The gyrotron poloidal mirrors are in charge of the gyrotron steering towards different parts of the plasma domain, allowing for modifying the current-deposition location. More details can be found, for example, in [113].

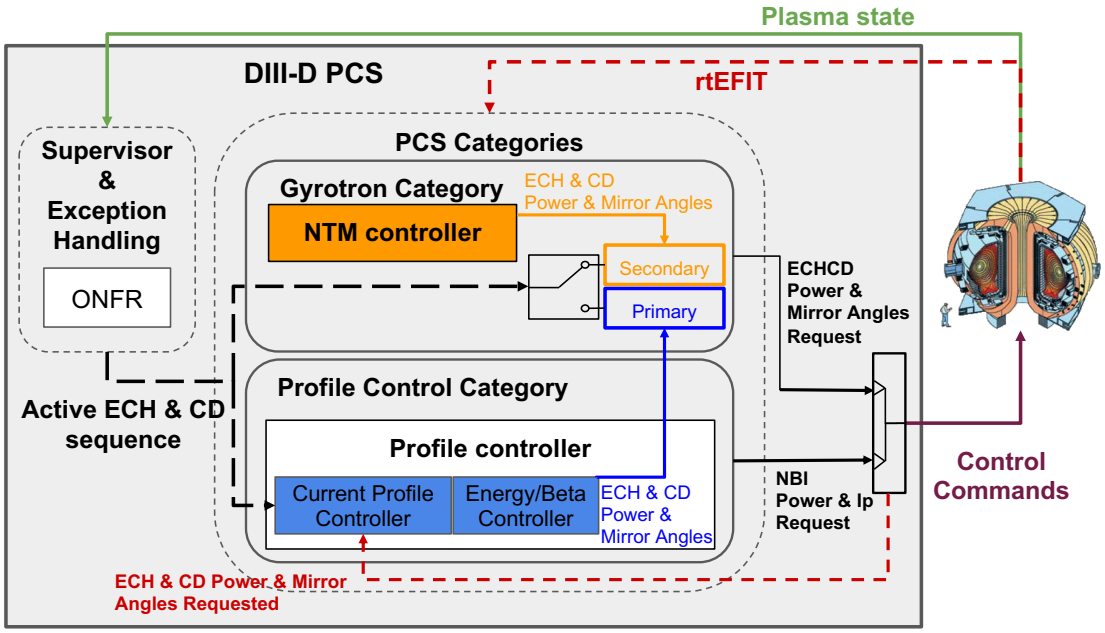

Figure 7.2: Integrated-control architecture developed for q-profile + β_N control and NTM suppression within the DIII-D PCS.

If the ONFR system determines that there is an NTM that needs suppression, then the secondary sequence is the active sequence of the Gyrotron category. In this case, the Gyrotron category takes control over EC H&CD as assigned by the ONFR system. The EC H&CD related control-requests, P_{EC} and ϕ_i, are fed-back into the Profile Control category, so that the MPC algorithm always has information about the P_{EC} and ϕ_i requests regardless of the active sequence of the Gyrotron category.

7.2.4 Experimental Results on Combined NTM Suppression and q-profile + β_N Control in DIII-D

In order to experimentally test the integrated-control scheme introduced, a hybrid scenario was chosen. In addition to being an H-mode scenario that may be of high interest for the development of ITER steady-state scenarios [10], such choice is also motivated by the fact that 3/2 NTMs normally arise, producing flux pumping, which in turn yields a high q profile that avoids 2/1 NTMs or sawtooth instabilities [114]. It has been experimentally demonstrated that 3/2 NTMs can be suppressed using

EC H&CD aimed at the $q = 3/2$ surface [114]. Although modeling of the q profile evolution in hybrid plasmas is still under research, this scenario seems suitable for a first preliminary test on combined q-profile + β_N control with NTM suppression.

The main purpose of the experiment is to assess the EC H&CD authority transfer between the Gyrotron category and the Profile Control category as requested by ONFR in the presence of a 3/2 NTM. In order to do so, a reference DIII-D shot, 162893, is reproduced with the goal of triggering a 3/2 NTM at the beginning of the flat-top phase. The β_N and q-profile evolutions from shot 162893 are used as targets for the MPC controller allocated in the Profile Control category. The reference plasma corresponds to a double-null shape in which the machine parameters are $B_T = 1.8$ T (normal direction in 162893, but reversed in this experiment), $R_0 = 1.78$ m, $a = 0.6$ m, $I_p = 1.2$ MA, and $\beta_N = 2.6$.

The configuration of the DIII-D PCS subsystems for the experiment is as follows. The ONFR system is set up to detect[2] 3/2 NTMs with an MHD amplitude similar to the one in the reference shot [114]. The NTM suppression algorithm is set up so that P_{EC}^{max} is employed when an NTM needs suppression. The EC toroidal mirror angles are fixed and set up so that the gyrotrons drive current in the same direction as I_p (i.e., co-ECCD is employed). Also, ϕ_i are regulated by the NTM suppression algorithm in order to track the $q = 3/2$ surface, whose location is estimated by means of the equilibrium reconstruction code rtEFIT constrained with MSE measurements [115]. Finally, the Profile Control category is configured to perform β_N + q-profile control in a feedforward + feedback scheme, so that it works in feedforward-only until 4.25 s, and in feedforward + feedback after 4.25 s. When working in feedback, rtEFIT is also needed to have an estimation of the q profile. The DIII-D PCS is configured to allow for a maximum of 4 s of ϕ_i control under the Profile Control category, so it is chosen that the time span during which ϕ_i are controlled by the Profile Control category is $t \in [1, 5]$ s. Also, for q-profile control, ECCD is aimed so that its peak is found at around $\hat{\rho} = 0.5$, or $\phi_i \approx 105$ degrees.

The experiment was carried out in March, 2018. Experimental results from shot

[2]The ONFR system computes the strength of an NTM based on its MHD n amplitude, and allows for setting a trip level above which a particular type of NTM is detected.

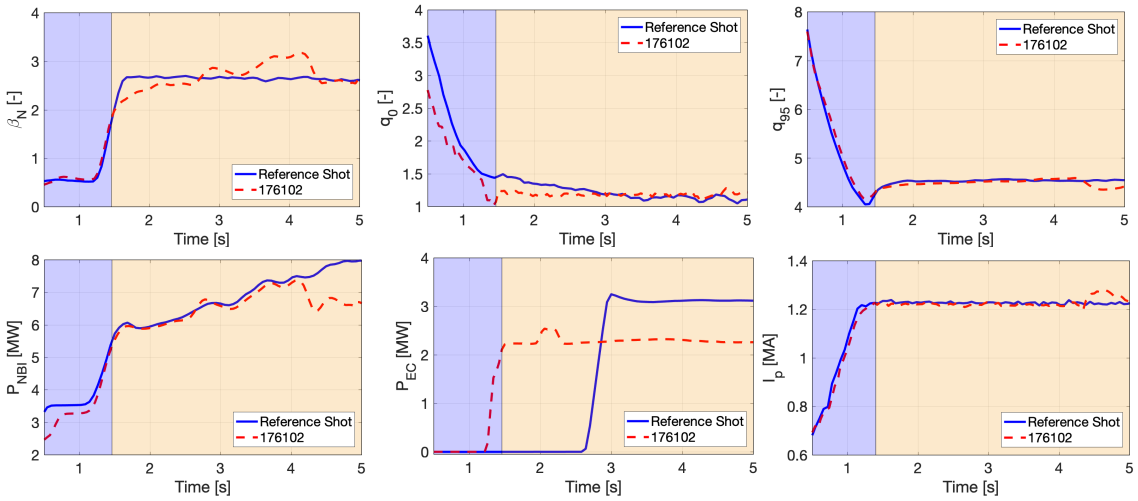

Figure 7.3: Time evolution for β_N, q_0, q_{95}, P_{NBI}, P_{EC}, and I_p for the reference shot (target) and shot 176102. The blue/(orange) shaded area indicates authority of the Profile Control Category/(NTM Control Category) over EC H&CD.

176102 are reported. Fig. 7.3 shows the time evolution for β_N, q_0, and q_{95}, together with $P_{NBI} = \sum_i P_{NBI,i}$, P_{EC}, and I_p. It can be seen that β_N in shot 176102 is not as constant in the flat-top phase as in the reference shot, despite using a very similar P_{NBI}: it is smaller in the early flat-top phase, higher later in the flat-top, and it is only similar to the reference shot when feedback is turned on at 4.25 s. Also, a lower q_0 is achieved in the ramp-up and early flat-top when compared to the reference shot, despite using EC H&CD earlier in the shot, which should in principle raise q_0 as it drives off-axis current. On the other hand, q_{95} evolves in a very similar way both in shot 176102 and the reference shot, as expected because I_p is also very similar. The only exception is at around 4.25 s, when I_p is increased by the feedback controller to track the β_N target at the expense of having a small deviation in q_{95}. The overall lower values of β_N and q_0 during the ramp-up and flat-top phases suggest a deteriorated confinement or a less optimal early-formation phase during shot 176102 when compared to the reference shot. The different B_T direction could also result in differences in the plasma behavior.

Fig. 7.4 shows the time evolution for P_{rad}, $\bar{n}_e$, the MHD $n = 2$ amplitude, the confinement H-factor, $H_{98(y,2)} = H_H$, P_{tot}, and the ONFR-related signals (which are the "NTM Strength" and its corresponding "NTM Trip Level") together with P_{EC}

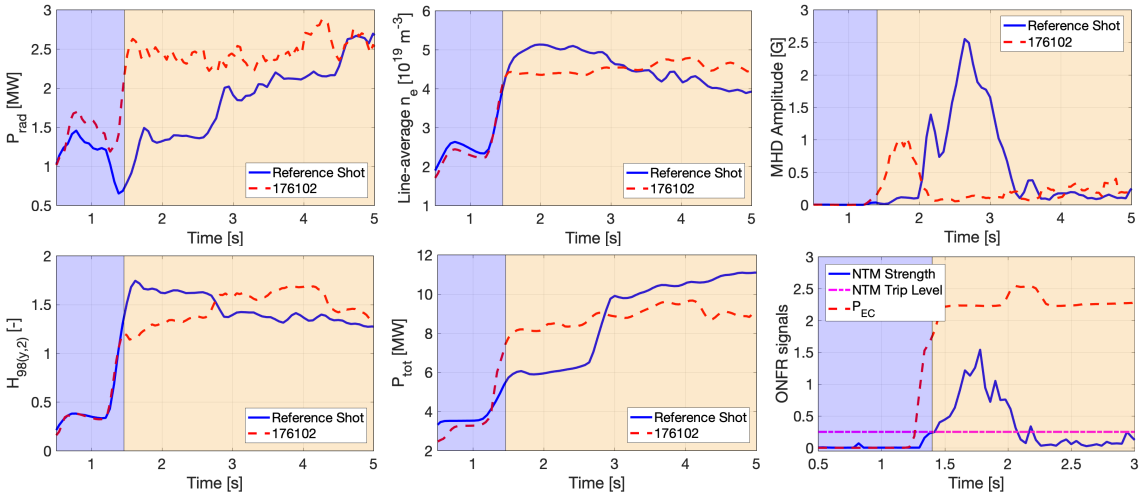

Figure 7.4: Time evolution for P_{rad}, $\bar{n}_e$, MHD $n = 2$ amplitude, $H_{98(y,2)}$, P_{tot}, and ONFR signals for the reference shot (target) and shot 176102. The blue/(orange) shaded area indicates authority of the Profile Controller/(NTM Controller) over EC H&CD.

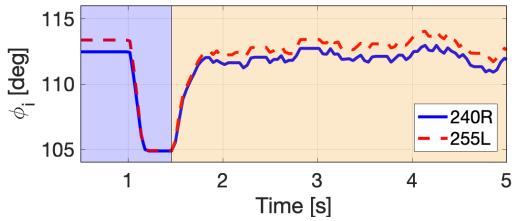

Figure 7.5: Time evolution for ϕ_{240R} and ϕ_{255L} for shot 176102.

from 0.5 to 3 s. The $\bar{n}_e$, P_{rad}, and $H_{H98(y,2)}$ evolutions confirm a lower confinement during the ramp-up and early flat-top than desired. Also, it can be noted that the MHD activity starts sooner in shot 176102, as reflected by the MHD $n = 2$ amplitude. Thus, EC H&CD is employed about a second earlier than in the reference shot, substantially increasing P_{tot} at approximately 1.4 s, when the NTM strength exceeds its trip level. This is when the EC H&CD authority is transferred from the Profile Control category to the Gyrotron category. In hybrid plasmas, q_0 may decrease when co-ECCD is employed to suppress 3/2 NTMs [116], as opposed to the intuition from previous q-profile control experiments [83]. These facts (poorer confinement, different early-formation phase, co-ECCD injection in a hybrid scenario)

may be the reason why β_N and q_0 are lower. After NTM suppression, both β_N and q_0 recover and get closer to their targets. Also, $\bar{n}_e$ and P_{rad} remain approximately flat until the end of the shot, whereas $H_{98(y,2)}$ increases. The MHD amplitude decreases due to the NTM suppression. The EC H&CD authority could have gone back to the Profile Control category once the NTM strength had become lower than its trip level (at $t \approx 2.1$ s), but the ONFR system was not configured to allow such transfer.

Finally, Fig. 7.5 shows the time evolution of $\phi_{(\cdot)}$ for two gyrotrons (the other $\phi_{(\cdot)}$ evolutions for the available gyrotrons are very similar). At $t = 1$ s, when the Profile Control category starts controlling ϕ_i, they are driven from their initial condition towards 105 deg for q-profile control. When EC H&CD is transferred to the Gyrotron category at 1.4 s, they are steered towards the $q = 3/2$ surface (whose position varies in time and is tracked until the end of the shot) for NTM suppression.

7.2.5 Conclusions

An integrated-control architecture for simultaneous q-profile + β_N control and NTM suppression has been developed in the DIII-D PCS. It integrates the Gyrotron and Profile Control Categories, while employing ONFR as a supervisor to perform RP actuator sharing of the gyrotrons between both Categories.

The control scheme has been experimentally tested for a hybrid-plasma scenario in DIII-D, with partially satisfactory results. Although 3/2 NTMs were suppressed while regulating q-profile + β_N, and the EC authority is transferred between Categories as requested by ONFR, further tuning of the parameters of the ONFR system and q-profile + β_N controller may improve this RP actuator sharing and overall performance. Future work will include experimental testing in different plasma scenarios and a refined ONFR set-up to allow for a second authority transfer (gyrotrons will return to Profile Control category after NTM stabilization). In addition, a refined and updated version of the MPC algorithm may be developed with a cost function that varies in real time (depending on the profile control and NTM suppression needs) and real-time-varying models that take into account the changes in the ECCD deposition location.

7.3 NTM Suppression + Individual-scalar Control

7.3.1 Actuator Management for Individual-Scalar Control and NTM Suppression

In this Section, the actuator management scheme proposed in Section 6.4 is modified to perform the RP actuator sharing required for simultaneous NTM suppression and individual-scalars control. The NTM suppression algorithm employed in this Section follows the same principles followed in previous experiments [13, 110]. When there is need for NTM suppression (as required by an external supervisory system), P_{EC} is not considered as a free variable in the optimization problem. Instead, it is fixed as $P_{EC} = P_{EC}^{max}$. When gyrotron-mirror steering is performed for NTM suppression, the term in F_{EC}, which is related to P_{EC}, varies due to the current-drive modification at the magnetic axis (see (6.50) and the constraint (6.75)), affecting the q_0 controller. However, in this work, it is assumed that the mirror steering effect on the current driven at the magnetic axis is negligible, and F is kept constant.

Mathematically, the optimization problem is written as

$$\min_{u,\epsilon_{(\cdot)}} J \tag{7.1}$$

$$I_p = I_p^{nom} + I_p^{rob}, \quad \text{(if the } q_{edge} \text{ controller is activated)} \tag{7.2}$$

$$\sum_i P_{NBI,i} + P_{EC} = P_{tot}^{nom} + P_{tot}^{rob} + \epsilon_{P_{tot}}, \quad \text{(if the } W \text{ controller is activated)} \tag{7.3}$$

$$\sum_i k_{NBI,i} P_{NBI,i} = T_{NBI}^{nom} + T_{NBI}^{rob} + \epsilon_{T_{NBI}}, \quad \text{(if the } \Omega_\phi \text{ controller is activated)} \tag{7.4}$$

$$F \begin{bmatrix} P_{NBI,1} \\ \vdots \\ P_{NBI,N_{NBI}} \\ P_{EC} \end{bmatrix} = F(P^{nom} + P^{rob}) + \epsilon_{j_{aux}}, \quad \text{(if the } q_0 \text{ controller is activated)} \tag{7.5}$$

$$P_{EC} = P_{EC}^{max}, \quad \text{(if NTM suppression is activated)} \tag{7.6}$$

$$u \in \mathcal{U}. \tag{7.7}$$

7.3.2 1D Simulation for Individual-Scalar Control and NTM Suppression

A simulation using COTSIM is carried out in this Section to test the capability of the actuator management scheme proposed in Section 7.3.1. The scenario employed corresponds to DIII-D shot 147634. The simulation is set up so that a $m/n = 2/1$ NTM develops as soon as the $q = m/n = 2$ magnetic-flux surface forms. This type of NTM is not found during shot 147634, but it is introduced in the simulation just for the purpose of this control test.

As stated in Chapter 3, the model described in Section 2.3.7 is employed in COTSIM to estimate the evolution of the island width. An initial NTM size of $w(0) = 1.1$ cm is taken (large enough to make the island grow), and a saturated island size $w_{sat} = 4$ cm is utilized. Although the values of the NTM parameters employed for this simulation are within the order of magnitude found in other DIII-D scenarios, such particular values are only chosen for the purpose of this control demonstration, rather than representing measured or real values that could be found in a plasma scenario corresponding to shot 147634.

First, an open-loop, feedforward-only simulation is run with the experimental inputs from shot 147634, adding the development of the 2/1 NTM introduced above. Second, a closed-loop simulation is run with NTM suppression only (i.e., $P_{EC} = P_{EC}^{max}$ with mirror steering, whereas the rest of the inputs are the same as in the open loop case). Third, a closed-loop simulation is run with NTM suppression + individual-scalar control. The NTM starts developing slightly after $t = 2$ s, but the NTM suppression algorithm is not activated until $t \geq 2.5$ s in both closed-loop simulations. By doing this, the simulation testing is more challenging, as the NTM is allowed to develop and spoil the plasma confinement before the controller is activated to try to recover the plasma state. Also, in each simulation, all the gyrotron poloidal-mirror angles are assumed to have the same value, and therefore, ρ_{ECCD} is the only variable needed to characterize the spatial ECCD deposition.

Fig. 7.6 shows the time evolution of the individual scalars together with the corresponding targets, whereas Fig. 7.7 shows the controllable inputs, in open loop,

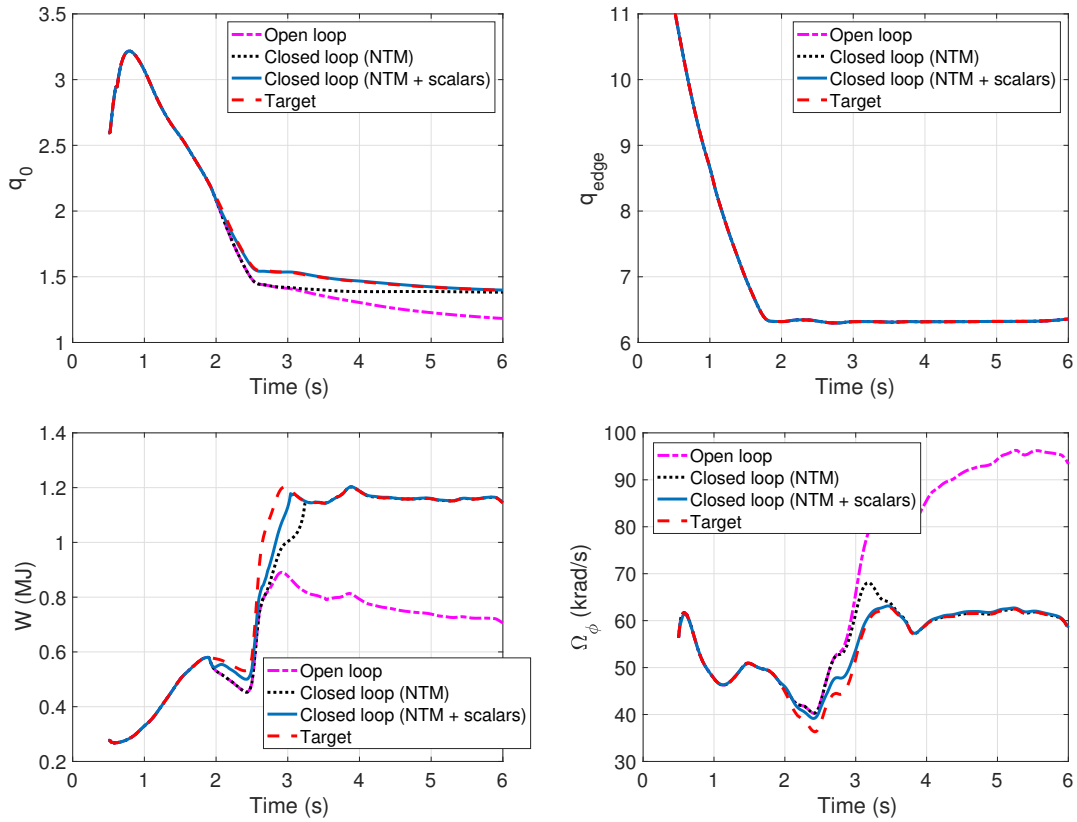

Figure 7.6: State evolution in 1D simulations for $q_0 + q_{edge} + W + \Omega_\phi$ control with NTM suppression: open loop (dashed-dotted magenta), closed loop under NTM suppression only (black dotted), closed loop under individual-scalar control and NTM suppression (solid blue), and target (dashed red).

closed loop with NTM suppression only, and closed loop with individual-scalar control and NTM suppression. Fig. 7.8 shows the w evolution in the same open-loop and closed-loop cases as before, together with the 2/1 NTM and ECCD deposition locations during the two closed-loop simulations. Fig. 7.9 shows the parameters of the optimization problem in closed loop with individual-scalar control and NTM suppression. It can be seen that the open-loop evolution drifts away from the target, specially W, which is substantially reduced. This is due to the development of the 2/1 NTM (see the w evolution in Fig. 7.8), which spoils the plasma confinement according to equation (3.1). In closed loop with NTM suppression only, it can be seen that w is decreased once the NTM suppression algorithm is activated at $t = 2.5$ s to

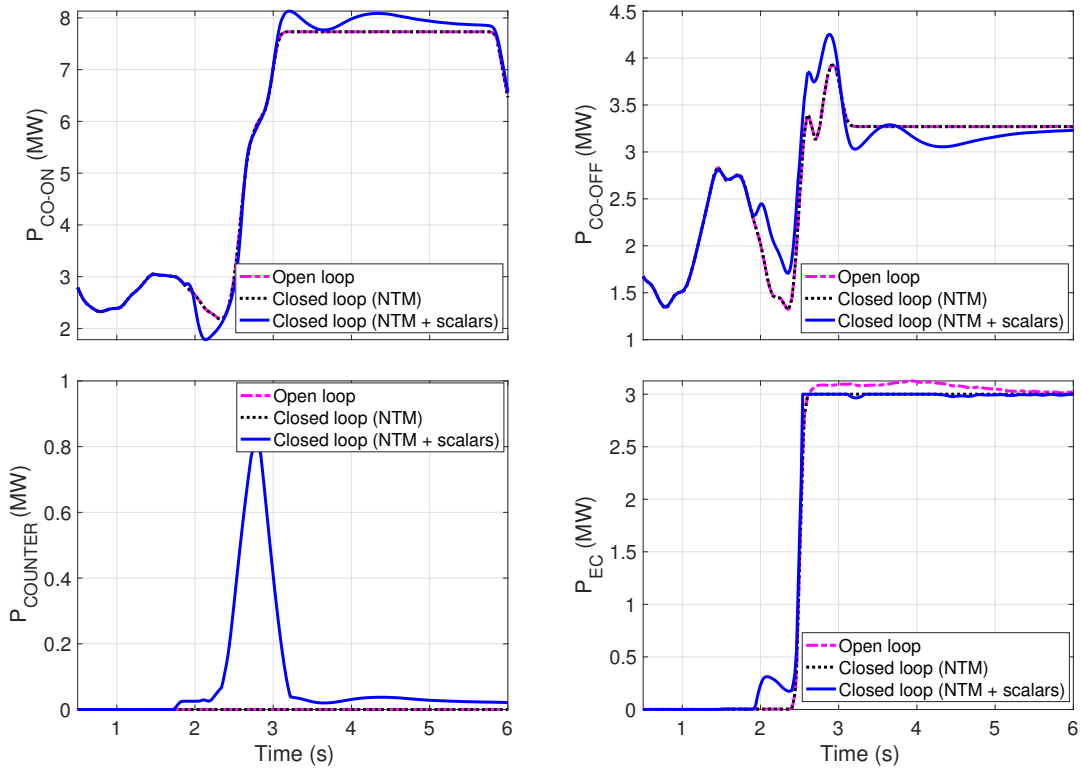

Figure 7.7: Controllable inputs evolution in 1D simulations for $q_0 + q_{edge} + W + \Omega_\phi$ control with NTM suppression: open loop (dashed-dotted magenta), closed loop under NTM suppression only (black dotted), closed loop under individual-scalar control and NTM suppression (solid blue).

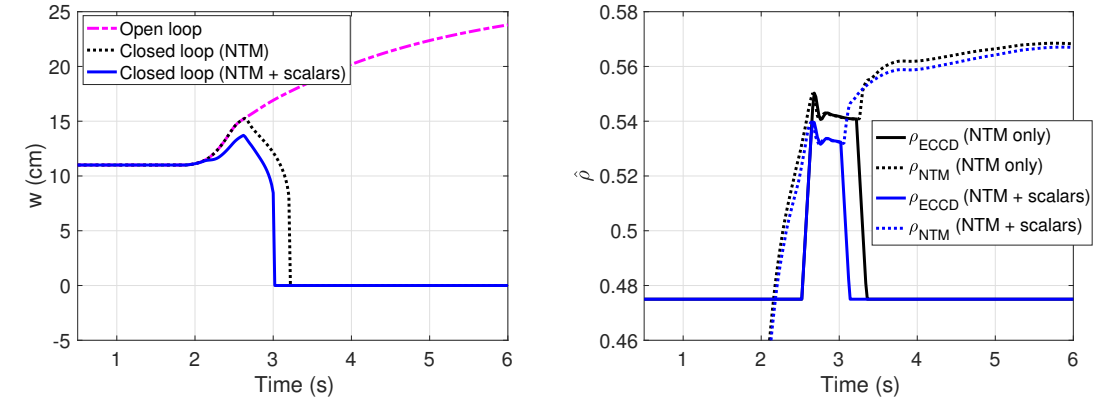

Figure 7.8: NTM island width and gyrotron/NTM spatial localizations in 1D simulations for $q_0 + q_{edge} + W + \Omega_\phi$ control with NTM suppression: closed loop under NTM suppression only (black), closed loop under individual-scalar control and NTM suppression (blue).

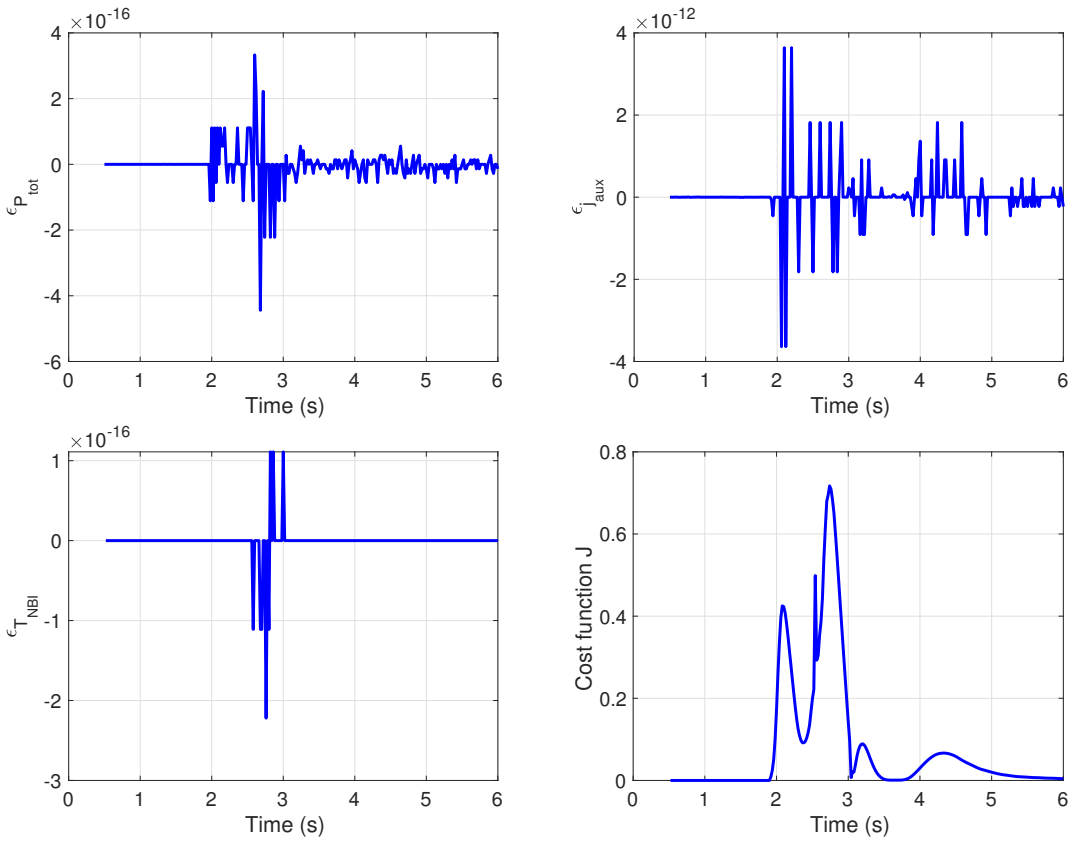

Figure 7.9: Optimization problem parameters in 1D simulations for q_0 + q_{edge} + W + Ω_ϕ control with NTM suppression.

make the gyrotrons track the 2/1 surface (see how ρ_{ECCD} tracks ρ_{NTM} in Fig. 7.8). The stored energy W recovers in approximately 0.5 s, i.e., the time needed for NTM suppression. Whereas q_{edge} is well controlled in this case, and Ω_ϕ also converges to its target after the NTM is suppressed, the q_0 evolution is much slower to reach its target, which is only achieved by the end of the simulation without any convergence guarantee. In closed loop with NTM suppression and individual-scalar control, it can be seen that w is also decreased when the NTM suppression algorithm is activated. In fact, the NTM suppression is carried out in a slightly smaller amount of time when the individual-scalar controllers are activated. This is due to the fact that their activation modifies the q profile, making the 2/1 surface (whose location is characterized by ρ_{NTM}) be closer to the gyrotron deposition location (ρ_{ECCD}). As

a result, and also possibly because of employing the W controller, the evolution of W shows higher values while the NTM is being suppressed than in the case of NTM suppression only. The other individual scalars are also driven to their targets in a more efficient way than in the case of NTM suppression only. From Fig. 7.7, it can be appreciated that the controller increases P_{tot} by increasing P_{CO-OFF}, P_{EC} and $P_{COUNTER}$ while slightly reducing P_{CO-ON}, with the objective of regulating W, Ω_ϕ, and q_0 around their targets. Finally, the values of the constraint gaps ($\epsilon_{P_{tot}}$, $\epsilon_{T_{NBI}}$ and $\epsilon_{j_{aux}}$) demonstrate the convergence of the actuator manager during the whole simulation. Also, a higher control effort is required during the part of the shot in which NTM suppression is needed, as it can be inferred from the higher J values found when $t \approx [2.5, 3]$ s.

7.3.3 Conclusions

The actuator manager based on optimization has been modified to integrate individual-scalars control and NTM suppression. Its performance has been tested in 1D simulations using COTSIM, showing its capability to perform RP actuator sharing. The performance of the integrated scheme to suppress NTM and control the individual scalars is improved when compared to the use of NTM suppression only. This suggests, as it was introduced before, that integrated schemes will have an edge over isolated controllers working separately. Future work in DIII-D may include further NTM + q-profile control experiments, and/or NTM + individual-scalar control experiments. In addition, further development is required in COTSIM to reproduce more accurately the effect that NTMs have on the plasma confinement through χ_e (i.e., the function $f_{NTM}(w)$ in equation (3.1)), as it has also been indicated in Chapter 3, Section 3.4.

Chapter 8

Conclusions and Future Work

The work presented in this dissertation focused on the development of integrated-control solutions for tokamak plasmas by exploiting nonlinear-robust control techniques and real-time optimization. These solutions can be employed in present physics studies, as well as in future reactor-grade tokamaks, in which integrated control strategies will be necessary. In this Chapter, a summary of contributions is presented, together with some key ideas concerning future work along the lines of this dissertation.

8.1 Contributions

1. Dynamical models have been developed for individual-scalar magnitudes (q_0, q_{edge}, W, Ω_ϕ, $\bar{n}_e$) of interest in tokamak plasma-control research. These models are nonlinear and zero-dimensional, and derived from first principles by using the MDE and its boundary conditions, and energy, momentum and particle transport equations. At some point during their derivation, some simplifying assumptions are employed in order to reduce their mathematical complexity. The main purpose of this modeling effort is to represent the main plasma dynamics by means of simple enough mathematical models that can be utilized for control synthesis.

2. The Control-Oriented Transport SIMulator (COTSIM) code has been further developed to evolve profiles related to magnetic, kinetic, and MHD instability control problems. The first version of COTSIM, developed before this dissertation work, included the 1D MDE equation to estimate the dynamics of ψ (from which q is computed) and a 0D energy-balance equation to evolve W. During this dissertation work, COTSIM was extended to include the 1D EHTE and TRE models for the dynamics of T_e and ω_ϕ, together with the 0D MRE model for the dynamics of the NTM magnetic-island width, w. The control-oriented models implemented for the diffusive and source terms (χ_e, χ_ϕ, Q_e, t_ω, etc.) also required some significant development before their implementation in COTSIM. In addition, the structure of COTSIM was revised and developed to couple all the aforementioned dynamical models, as well as to allow for the implementation of new models (like 0D, 0.5D, and 1D equations for n_e, T_i, and n_i). In summary, COTSIM has been evolved to make it a more sophisticated, comprehensive code that can serve as a testbed for integrated control-oriented testing by using coupled models of the plasma kinetics, magnetics, and MHD instabilities.

3. Several integrated-control schemes have been designed for kinetic, magnetic, and/or MHD instability control problems: an integrated burn-controller based on Lyapunov theory and Lyapunov redesign techniques, a $q_0 + \beta_N$ controller for zero NBI torque scenarios based on linear techniques, a q-profile + β_N controller based on feedback linearization, and controllers for individual-scalar variables based on Lyapunov theory and Lyapunov redesign techniques. Most of these controllers were synthesized by means of nonlinear and robust control techniques in order to handle the complex and uncertain plasma dynamics. The main purpose of these controllers is to serve as tools for the development of plasma experiments and scenarios, with the final goal of facilitating access to the conditions required for fusion.

4. An actuator manager based on optimization has been developed with the capability of integrating control laws, physical saturation limits, and other

externally-imposed constraints (for example, by a S&EH system). The first version of this actuator management algorithm integrates the control laws for individual scalars and NTM suppression together with physical saturation limits. The main purpose of this control tool is to enable the implementation of the two actuator management schemes foreseen for ITER: simultaneous multiple mission (SMM) and repurposing (RP) sharing.

8.2 Future Work

An important general feature of the models used in this dissertation work is their control-oriented nature, in which an intentional, moderate degree of simplification exists, together with a partial lack of physics understanding[1]. Although uncertainties have been included in the modeling process to deal with neglected and/or unknown dynamics, it is difficult to gauge if they will suffice to ensure a successful robust-control design for experiments. Although the control tools developed in this dissertation have been partially validated (using previous experimental data, simulation tests, and a few experimental tests), their full validation requires that more experiments are carried out. Experimental testing normally yields substantial insights into the suitability of the control approaches employed, and show the path towards how to improve the current control implementations.

Directions for future work within each topic of this dissertation have been introduced in each of the corresponding Chapters. Future work on COTSIM may include the implementation of different (possibly more accurate and/or sophisticated) models for particle and energy transport, including models based on neural networks, as well as further effort on coupling the kinetic, magnetic, and MHD instability dynamics. Regarding the design of model-based controllers for simultaneous regulation of a mix of plasma profiles and scalars, future work may include alternative approaches with higher level of actuation integration and more extensive 1D-simulation testing

[1]For example, it is known that the electron temperature does not follow a totally diffusive evolution, and that convective heat-transfer and other phenomena are present. Variables such as H_H or χ_e may significantly vary between shots in unexpected manners.

using COTSIM, as well as experimental testing in DIII-D. These experimental tests may use q-profile control to investigate the influence that the q-profile shape has on the plasma resilience against NTMs. Moreover, the real-time optimization algorithm for q-profile + β_N control with simultaneous NTM suppression (implemented in the DIII-D PCS) may be further developed to include real-time changes in the cost function and response model as determined by the control needs. Updates to the model in real time may also be included to characterize the current-deposition variations associated with ECCD mirror steering. Finally, regarding the integration of model-based controllers with actuator-management strategies, both alternative optimization schemes (possibly with different cost functions) and non-optimization schemes may be further considered.

Appendix A

Basic Plasma Physics

A.1 Particle trajectories and drifts

The equation of motion of a charged particle subject to electric and magnetic field forces is given by

$$m\frac{d\vec{v}}{dt} = q(\vec{E} + \vec{v} \times \vec{B}), \tag{A.1}$$

where m is the particle mass, $\vec{v}$ is the particle velocity, q is the particle electric charge, $\vec{E}$ and $\vec{B}$ are the electric and magnetic fields, respectively, and t is the time. When $\vec{B} = 0$, the electric field $\vec{E}$ accelerates the particle due to the electrical force, $q\vec{E}$. To see the effect of a unidirectional $\vec{B}$ on the particle motion, a coordinate frame x-y-z is chosen so that $\vec{B}$ is aligned with the ϕ axis, $\vec{B} = B\vec{\phi}$ (see Fig. 2.1). When $\vec{E} = 0$, the three components of equation (A.1) are given by

$$m\frac{dv_r}{dt} = qv_zB, \;\; m\frac{dv_z}{dt} = -qv_rB, \;\; m\frac{dv_\phi}{dt} = 0, \tag{A.2}$$

where v_r, v_z, and v_ϕ are the r, z, and ϕ components of $\vec{v}$, respectively. From the last equation in (A.2), it can be seen that v_ϕ is a constant. Taking time derivative in the r and z components of (A.2), and eliminating dv_z/dt and dv_r/dt, respectively, it is found that

$$\frac{d^2v_r}{dt^2} = -\left(\frac{q}{m}\right)^2 v_rB^2, \;\; \frac{d^2v_z}{dt^2} = -\left(\frac{q}{m}\right)^2 v_zB^2. \tag{A.3}$$

where it has been assumed that B is constant or varies very slowly when compared to $\vec{v}$. The solution of (A.3) is given by $v_r = v_{\perp,0}\cos(\omega_c t+\psi)$, $v_z = \mp v_{\perp,0}\sin(\omega_c t+\psi)$, where $\omega_c \triangleq |q|B/m$ is the so-called cyclotron frequency, $v_{\perp,0}$ and ψ are constants obtained from integrating (A.3) and applying the initial conditions, and the $\mp$ sign in v_z depends on the sign of q ($-$ if $q > 0$, and $+$ if $q < 0$). It can be inferred that $v_{\perp,0}$ is in fact the initial velocity of the particle in the r-z plane (which remains constant because the Lorentz force $q\vec{v} \times \vec{B}$ is always perpendicular to $\vec{v}$ and therefore does not exert any work). Further integration of v_r and v_z with respect to time yields the equations of motion,

$$r = r_0 + \frac{v_{\perp,0}}{\omega_c}\sin(\omega_c t + \psi), \quad z = z_0 \pm \frac{v_{\perp,0}}{\omega_c}\cos(\omega_c t + \psi), \tag{A.4}$$

where r_0 and z_0 are integration constants as well. The particles gyrate around the so-called guiding center, defined by (r_0, z_0), describing a circular motion of frequency ω_c and radius $r_L \triangleq v_{\perp,0}/\omega_c$, also known as Larmor radius.

It is of interest to analyze the particle motion when subject to a uniform $\vec{B}$ plus a uniform $\vec{E}$. It is straightforward to see that, along the ϕ direction, $\vec{B}$ does not vary the trajectory of the particle, whereas $\vec{E}$ produces a constant acceleration equal to qE_ϕ/m. Defining the velocity in the r-z plane, $\vec{v}_\perp \triangleq v_r\vec{r} + v_z\vec{z}$, and taking cross product with $\vec{B}$ in (A.1), it is found that

$$m\frac{d(\vec{v}\times\vec{B})}{dt} = q\left(\vec{E}\times\vec{B} + \left(\vec{v}\times\vec{B}\right)\times\vec{B}\right) = q\left(\vec{E}\times\vec{B} + \vec{B}\left(\vec{v}\cdot\vec{B}\right) - \vec{v}B^2\right), \tag{A.5}$$

which can be rewritten as

$$m\frac{d(\vec{v}_\perp\times\vec{B})}{dt} = q\left(\vec{E}\times\vec{B} + \vec{B}\left(\vec{v}_\phi\cdot\vec{B}\right) - \vec{v}B^2\right), \tag{A.6}$$

and taking into account that $\vec{v}_\perp$ and $\vec{B}$ are perpendicular to each other, (A.6) can be rewritten as

$$m\frac{d(\vec{v}_\perp\times\vec{B})}{dt} = q\left(\vec{E}\times\vec{B} - \vec{v}_\perp B^2\right). \tag{A.7}$$

The time-dependent solution of (A.7) is the Larmor gyration previously described, whereas the constant, particular solution of (A.7) is the so-called $\vec{E}\times\vec{B}$ drift, which

is given by

$$\vec{v}_E = \frac{\vec{E} \times \vec{B}}{B^2}. \tag{A.8}$$

It is also of interest to analyze the particle motion in a vacuum, curved magnetic field, as it is the situation found in tokamaks. A magnetic field $\vec{B}$ in a vacuum must fulfill Gauss' law of magnetism, $\nabla \cdot \vec{B} = 0$, and therefore the strength of the magnetic field must decrease in the radial direction. In addition to such ∇B, any particle with a gyrating motion experiences a centrifugal force, $F_c = \frac{mv_\phi^2}{r}\vec{r}$. Taking these two effects into account, the equation of motion (A.1) can be written as

$$m\frac{d\vec{v}}{dt} = q\vec{v} \times \left(\vec{B} + \nabla B \cdot d\vec{r}\right) + F_c. \tag{A.9}$$

The effect of F_c on the particle's motion is the same as the effect of the electrical force $q\vec{E}$, i.e., a drift of magnitude $\vec{F}_c \times \vec{B}/(qB^2)$. On the other hand, the effect of $\nabla\vec{B}$ is known as grad-B drift. Both drifts modify the Larmor gyration of the particles by adding a velocity component, $\vec{v}_c$, that is approximately given by [2]

$$\vec{v}_c = \frac{m}{q}\frac{\vec{r} \times \vec{B}}{rB^2}\left(v_\phi^2 + \frac{1}{2}(v_r^2 + v_z^2)\right), \tag{A.10}$$

where v_ϕ, v_r, and v_z are the ϕ-r-z velocity components.

A.2 Derivation of the MHD equations

The derivation of the MHD equations starts by describing the plasma as a fluid whose particles experience electrical and Lorentz forces, in addition to thermal, viscous and collision forces. This description follows the same principles of Continuum Mechanics employed to derive the ordinary fluid-mechanics equations.

The continuity equations for the plasma ions and electrons are given by

$$\frac{Dn_i}{Dt} = -n_i \nabla \cdot \vec{v}_i, \quad \frac{Dn_e}{Dt} = -n_e \nabla \cdot \vec{v}_e, \tag{A.11}$$

where $D/Dt \triangleq \partial/\partial t + v \cdot \nabla$ is the convective derivative, n_i is the ion density, n_e is the electron density, $\vec{v}_i$ is the ion velocity, and $\vec{v}_e$ is the electron velocity.

The momentum equations for ions and electrons are given by

$$m_i n_i \frac{D\vec{v}_i}{Dt} = -\nabla \cdot P_i + n_i q_i(\vec{E} + \vec{v}_i \times \vec{B}) + m_i n_i \vec{g} + m_i n_i(\vec{v}_i - \vec{v}_e)\nu_{i,e}, \tag{A.12}$$

$$m_e n_e \frac{D\vec{v}_e}{Dt} = -\nabla \cdot P_e + n_e q_e(\vec{E} + \vec{v}_e \times \vec{B}) + m_e n_e \vec{g} + m_e n_e(\vec{v}_e - \vec{v}_i)\nu_{e,i}, \tag{A.13}$$

where m_i and m_e are the ion and electron masses, respectively, q_i and q_e are the ion and electron electrical charges, respectively, P_i and P_e are general anisotropic pressure tensors for the ions and electrons, respectively, $\vec{g}$ is the gravity acceleration, and $\nu_{i,e}$ and $\nu_{e,i}$ are the collision frequencies between ions and electrons, which fulfill $m_i n_i \nu_{i,e} = -m_e n_e \nu_{e,i}$.

Also, the MHD theory states that Maxwell's equations for electromagnetism hold within the plasma domain,

$$\nabla \cdot \vec{E} = \frac{\sigma}{\epsilon_0}, \quad \nabla \times \vec{E} = -\frac{\partial \vec{B}}{\partial t}, \tag{A.14}$$

$$\nabla \cdot \vec{B} = 0, \quad \nabla \times \vec{B} = \mu_0 \left(\vec{j} + \epsilon_0 \frac{\partial \vec{E}}{\partial t} \right), \tag{A.15}$$

where ϵ_0 is the vacuum electric permittivity, μ_0 is the vacuum magnetic permeability, $\sigma = q_i n_i + q_e n_e$ is the charge density, and $\vec{j} = q_i n_i \vec{v}_i + q_e n_e \vec{v}_e$ is the current density.

In addition, the following assumptions are used:

- Quasi-neutral plasma with single-charged ions, i.e., $n_i \approx n_e \triangleq n$ and $q_i = -q_e$.
- Negligible viscous forces and isotropic pressure fields, so that $\nabla \cdot P_i = \nabla p_i$ and $\nabla \cdot P_e = \nabla p_e$, for isotropic ion and electron pressure fields, p_i and p_e, respectively.
- Negligible displacement current, $\epsilon_0 \frac{\partial \vec{E}}{\partial t} \approx 0$[1].

The MHD continuity equation is obtained by multiplying, in equation (A.11), the ion continuity equation by m_i and the electron continuity equation in by m_e,

[1]It can be demonstrated that if the characteristic plasma length, L, and the characteristic plasma time, T, fulfill $L/T << c$ (as is the case in tokamak plasmas), then $\mu_0 \epsilon_0 \partial \vec{E}/\partial t << 1$.

and adding both of them,

$$(m_i + m_e)\frac{Dn}{Dt} = -n\nabla \cdot (m_i\vec{v}_i + m_e\vec{v}_e), \tag{A.16}$$

which, defining "center of mass velocity", $\vec{v} \triangleq (m_i\vec{v}_i + m_e\vec{v}_e)/(m_i + m_e)$, becomes

$$\frac{Dn}{Dt} = -n\nabla \cdot \vec{v}. \tag{A.17}$$

Adding (A.12) and (A.13), the momentum equation is written as

$$n(m_i + m_e)\frac{D\vec{v}}{Dt} = -\nabla p + \vec{j} \times \vec{B}, \tag{A.18}$$

where $p = p_e + p_i$. Multiplying (A.13) by m_i, (A.12) by m_e, and subtracting (A.12) from (A.13), the so-called generalized Ohm's law can be derived [2],

$$\vec{E} + \vec{v} \times \vec{B} = \eta\vec{j} + \frac{1}{nq_i}(\vec{j} \times \vec{B} - \nabla p_e), \tag{A.19}$$

where $m_e << m_i$ and small cyclotron frequency effects have been assumed, and η is the so-called plasma resistivity, which is given by

$$\eta = \nu_{e,i}\frac{m_e}{nq_e^2}. \tag{A.20}$$

Finally, equation (A.18) can be particularized at equilibrium, which yields

$$\nabla p = \vec{j} \times \vec{B}. \tag{A.21}$$

A.3 Flux functions

First, it is convenient to define a potential vector $\vec{A}$ such that $\vec{B} = \nabla \times \vec{A}$. The magnetic field $\vec{B}$ can be expressed as

$$\vec{B} = \nabla \times \vec{A} = \left(\frac{1}{r}\cancelto{0}{\frac{\partial A_z}{\partial \phi}} - \frac{\partial A_\phi}{\partial z}\right)\vec{r} + B_\phi\vec{\phi} + \frac{1}{r}\left(\frac{\partial (rA_\phi)}{\partial r} - \cancelto{0}{\frac{\partial A_r}{\partial \phi}}\right)\vec{z}, \tag{A.22}$$

where $\vec{A} = A_r\vec{r} + A_\phi\vec{\phi} + A_z\vec{z}$, and $\vec{r}$, $\vec{\phi}$ and $\vec{z}$ are the unit vectors in the r, ϕ and z directions, respectively. Defining the poloidal-flux stream function, $\psi \triangleq rA_\phi$, equation (A.22) can be rewritten as

$$\vec{B} = -\frac{1}{r}\frac{\partial\psi}{\partial z}\vec{r} + B_\phi\vec{\phi} + \frac{1}{r}\frac{\partial\psi}{\partial r}\vec{z}. \tag{A.23}$$

It can be noted that $\vec{B}$ as given by (A.23) in fact fulfills Gauss' law for magnetism (first equation in (A.15)),

$$\nabla\cdot\vec{B} = \frac{1}{r}\frac{\partial(rB_r)}{\partial r} + \frac{1}{r}\frac{\cancelto{0}{\partial B_\phi}}{\partial\phi} + \frac{\partial B_z}{\partial z} = -\frac{1}{r}\frac{\partial^2\psi}{\partial r\partial z} + \frac{1}{r}\frac{\partial^2\psi}{\partial r\partial z} = 0. \tag{A.24}$$

The poloidal magnetic flux, Ψ, at a point P, is defined as

$$\Psi = \iint_S B_\theta dS, \tag{A.25}$$

where S is the surface that is perpendicular to the z-axis and whose boundary is defined by the ring passing through P (see Fig. 2.3). The relationship between Ψ and ψ is obtained from (A.25) and (A.23), and it is given by

$$\Psi = \int_0^{2\pi}\left[\int_0^r \frac{1}{\bar{r}}\frac{\partial\psi(\bar{r},z,t)}{\partial\bar{r}}\bar{r}d\bar{r}\right]d\phi = 2\pi\left(\psi(r,z,t) - \psi(0,z,t)\right), \tag{A.26}$$

where $\bar{r}$ is an auxiliary integration variable. If $\psi(0,z,t) = 0$ is taken, then $\Psi = 2\pi\psi$.

It can be shown that other variables are also constant as long as Ψ is constant. Such variables are referred to as flux functions. A possible flux function is the plasma pressure, p. From the MHD equilibrium equation (A.21), it can be seen that $\vec{B}\cdot\nabla p = 0$, which can be rewritten by using $\partial/\partial\phi = 0$ as

$$0 = (\vec{B}_\phi + \vec{B}_\theta)\cdot\left(\frac{\partial p}{\partial r}\vec{r} + \frac{\partial p}{\partial z}\vec{z}\right), \tag{A.27}$$

and using (A.23), it is found that

$$0 = \frac{1}{r}\left(-\frac{\partial\psi}{\partial z}\frac{\partial p}{\partial r} + \frac{\partial\psi}{\partial r}\frac{\partial p}{\partial z}\right) = (\nabla\psi\times\nabla p)\cdot\vec{\phi}, \tag{A.28}$$

thus $\nabla\psi$ is parallel to ∇p, which means that points with constant ψ also have constant p.

Another flux function considered is the toroidal magnetic flux, Φ, which is defined as

$$\Phi = \iint_{S_\phi} B_\phi dS_\phi, \tag{A.29}$$

where S_ϕ is the surface enclosed by enclosed by a magnetic-flux surface, and is perpendicular to the ϕ-axis as depicted in Fig. 2.3. In order to demonstrate that Φ is in fact a flux function, Ampere's law (second equation in (A.15)) is rewritten in terms of the components of $\vec{B}$ and ψ as

$$\mu_0 \vec{j} = \frac{1}{r}\left(\frac{\partial(rB_\phi)}{\partial r}\vec{z} - \frac{\partial(rB_\phi)}{\partial z}\vec{r}\right) + \left(\frac{\partial B_r}{\partial z} - \frac{1}{r}\frac{\partial(rB_z)}{\partial r}\right)\vec{\phi} = \\ = \frac{1}{r}\nabla(rB_\phi)\times\vec{\phi} - \frac{1}{r}\left(\frac{\partial^2\psi}{\partial r^2} + \frac{\partial^2\psi}{\partial z^2}\right)\vec{\phi}. \tag{A.30}$$

Multiplying (A.30) by ∇p, and taking into account that $\nabla p \cdot \vec{\phi} = 0$, it is found that

$$0 = \frac{1}{r}\left(\nabla(rB_\phi)\times\vec{\phi}\right)\cdot\nabla p, \tag{A.31}$$

which implies $\nabla(rB_\phi)$ and ∇p are parallel as well, i.e., $rB_\phi = F(\psi)$ is also a constant in a magnetic-flux surface and therefore a flux function. By means of the change of variables $R = \sqrt{(r-R_0)^2 + z^2}$, $\theta = \arctan\frac{z}{r-R_0}$ (see Fig. 2.4), it is found that $dS_\phi = R\,dR\,d\theta$, and therefore (A.29) can be written as

$$\Phi = \int_{S_\phi}\frac{F(\psi)}{r}drdz = \int_0^{2\pi}\left[\int_0^{\gamma(\theta,\psi)}\frac{F(\psi)}{R_0 + R\cos\theta}dR\,R\right]d\theta = \Phi(\psi), \tag{A.32}$$

so it can be concluded that Φ is also constant in a magnetic-flux surface.

A very commonly used flux function is the minor effective radius, ρ, which is defined from Φ as

$$\Phi = B_{\phi,0}\pi\rho^2, \tag{A.33}$$

where $B_{\phi,0}$ is a reference magnetic field (normally taken as the vacuum magnetic field at the magnetic axis). Therefore, ρ is a constant in the magnetic-flux surfaces by definition. It represents the radius of a circumference which is crossed by the same toroidal flux as the magnetic surface, Φ, but with a toroidal magnetic field equal to $B_{\phi,0}$ (see Fig. 2.4).

Finally, the safety factor, q, is a measure of the pitch of the magnetic field lines, and it is defined as

$$q \triangleq -\frac{d\Phi}{d\Psi}. \tag{A.34}$$

It can be seen that, by definition, q is also a flux function.

A.4 Physical meaning of β

If the MHD equilibrium equation, (A.21), is combined with Ampere's law (second equation in (A.15), using $\epsilon_0 \frac{\partial \vec{E}}{\partial t} \approx 0$), then it is possible to write

$$\nabla p = \frac{\nabla \times \vec{B}}{\mu_0} \times \vec{B} = \frac{1}{\mu_0} \left((\vec{B} \cdot \nabla)\vec{B} - \frac{1}{2} \nabla B^2 \right), \tag{A.35}$$

and re-arranging terms,

$$\nabla \left(p + \frac{B^2}{2\mu_0} \right) = \frac{1}{\mu_0} (\vec{B} \cdot \nabla)\vec{B}. \tag{A.36}$$

In some geometries and/or $\vec{B}$, it is found that $(\vec{B} \cdot \nabla)\vec{B} \approx 0$ (for example, in a straight cylinder). Then, $p + \frac{B^2}{2\mu_0}$ is a constant in the entire plasma domain. If this approximation is applied to a tokamak[2], then the pressure increase found in the plasma core implies that the magnetic field decreases there. Such effect is known as *plasma diamagnetism*: plasmas tend to reduce the externally created magnetic field to which they are subject.

The parameter $\beta = \frac{p}{B^2/(2\mu_0)}$ naturally arises in (A.36), and measures the relative importance of the kinetic pressure, p, and the "magnetic pressure", $B^2/(2\mu_0)$, in the plasma equilibrium. It can also be employed to characterize the intensity of the diamagnetic effects: high β implies strong diamagnetic effects.

[2]This is not a totally arbitrary assumption for a tokamak, as $\vec{B}_\theta$ is an order of magnitude smaller than $\vec{B}_\phi$, so $\vec{B}$ can be seen as "quasi-unidirectional".

Appendix B

Control-Oriented Modeling

B.1 Approximate computation of the bulk toroidal rotation

The magnetic-flux surfaces are approximated by circumferences with the same toroidal magnetic-flux as in the vacuum, whose radius is ρ by definition[1]. Under this assumption, $\xi_r \approx \rho\cos\theta$, $\xi_z \approx \rho\sin\theta$, where $\theta \in [0, 2\pi]$. Also, $d\Gamma \approx \rho d\theta$. Then, using (2.125) and employing average flux-surface values for $v_{\phi,i}$ and n, the integral (2.128) can be rewritten as

$$\Omega_\phi = 2\pi R_0 \frac{\int_{\rho=0}^{\rho=\rho_b} \rho\langle v_{\phi,i}\rangle\langle n\rangle \left[\int_{\theta=0}^{\theta=2\pi} \frac{d\theta}{R_0+\rho\cos\theta}\right] d\rho}{V_p}. \tag{B.1}$$

Integration with respect to θ can be done using the change of variables $z = e^{i\theta}$ and Cauchy's Residue Theorem,

$$\int_{\theta=0}^{\theta=2\pi} \frac{d\theta}{R_0+\rho\cos\theta} = \oint_{|z|=1} \frac{dz}{iz\left(R_0+\frac{\rho}{2}\left(z+\frac{1}{z}\right)\right)} = 2\pi Res\left(\frac{1}{z\left(R_0+\frac{\rho}{2}\left(z+\frac{1}{z}\right)\right)}, z^*\right), \tag{B.2}$$

[1]It is evident that is approach would not work very well for plasma shapes with very high κ, intense diamagnetic effects (high β), or high aspect ratio tokamaks (where B_ϕ varies substantially across the cross-section).

where z^* are the poles inside $|z| = 1$. Thus, to compute the residue, it is necessary to first find the poles of the following complex function

$$\frac{1}{z\left(R_0 + \frac{\rho}{2}\left(z + \frac{1}{z}\right)\right)} = \frac{1}{\rho z^2/2 + R_0 z + \rho/2}, \tag{B.3}$$

which are given by $z_1 = (R_0 + \sqrt{R_0^2 - \rho^2})/\rho$ and $z_2 = (R_0 - \sqrt{R_0^2 - \rho^2})/\rho$, i.e., two poles on the real axis (because $R_0 > \rho$). Whereas z_1 is not inside the circle $|z| = 1$ (again, because $R_0 > \rho$), z_2 is always inside, for any value $\rho \in [0, \rho_b]$. This can be shown by noting that, for $\rho = 0$,

$$\lim_{\rho\to 0} z_2 = \lim_{\rho\to 0} \frac{R_0 - \sqrt{R_0^2 - \rho^2}}{\rho} = \lim_{\rho\to 0} \frac{2\rho}{2\sqrt{R_0^2 - \rho^2}} = 0, \tag{B.4}$$

where L'Hopital's rule has been applied, whereas when $\rho \to R_0$

$$\lim_{\rho\to R_0} z_2 = 1, \tag{B.5}$$

thus all the other intermediate values, $\rho \in (0, R_0)$, yield $z_2 \in (0, 1)$. Therefore, $z^* = z_2$. The residue is found to be

$$Res\left(\frac{1}{z\left(R_0 + \frac{\rho}{2}\left(z + \frac{1}{z}\right)\right)}, z_2\right) = \frac{2}{\rho(z_2 - z_1)} = \frac{1}{\sqrt{R_0^2 - \rho^2}}, \tag{B.6}$$

and then,

$$\int_{\theta=0}^{\theta=2\pi} \frac{d\theta}{R_0 + \rho\cos\theta} = \frac{2\pi}{\sqrt{R_0^2 - \rho^2}}. \tag{B.7}$$

Finally, taking into account that $2\pi R_0 2\pi\rho = \partial V/\partial\rho$ (where V is the volume enclosed by the approximate, circular magnetic-flux surfaces) and using $\rho = \rho_b\hat{\rho}$, equation (B.1) can be rewritten as

$$\Omega_\phi = \frac{\int_{\hat{\rho}=0}^{\hat{\rho}=1} \langle v_{\phi,i}\rangle\langle n\rangle \frac{\partial V(\hat{\rho})}{\partial\hat{\rho}} \frac{1}{\sqrt{R_0^2 - \rho_b^2\hat{\rho}}}}{N_p}. \tag{B.8}$$

If $\rho_b^2 << R_0^2$ is fulfilled, which is true for very low aspect ratio tokamaks because $O(\rho_r/R_0) = O(a/R_0) << 1$, and a reasonable simplification for low aspect ratio tokamaks, then $\sqrt{R_0^2 - \rho_b^2\hat{\rho}} \approx R_0$, and (B.8) becomes

$$\Omega_\phi = \frac{\int_{\hat{\rho}=0}^{\hat{\rho}=1} \frac{\partial V(\hat{\rho})}{\partial\hat{\rho}} \frac{V_\phi(\hat{\rho},t)}{R_0} d\hat{\rho}}{V_p}. \tag{B.9}$$

Note that the previous expression (B.9) for Ω_ϕ is also obtained if $\rho_b + R_0 \approx R_0$, which implies $\xi_r + R_0 \approx R_0$. Equation (2.123) becomes

$$\omega_z(\hat{\rho}, t) = \frac{V_\phi(\hat{\rho}, t)}{R_0}, \tag{B.10}$$

and then, substituting (B.10) into (2.126), yields the same expression (B.9). However, $\rho_b^2 << R_0^2$ is a less restrictive condition than $R_0 + \xi_r << R_0$. In any case, both (B.8) and (B.9) give the same result for the relationship between $\vec{V}_\phi$ and $\vec{\Omega}$: for two magnetic-flux surfaces with the same $\vec{V}_\phi$, the outer magnetic-flux surface contributes more to the total plasma rotation $\vec{\Omega}$ than the inner magnetic-flux surface. Such result has an interesting physical meaning, as it suggests that accelerating the edge of the plasma could result in substantial improvements in the global plasma rotation. However, it is much more difficult to inject torque at or close to the plasma edge, mainly due to the low plasma density of that region. The main external torque sources (such as NBI and non-resonant magnetic fields) normally produce a much higher torque in the plasma core, where the plasma density is higher, hence resulting in a higher $\vec{V}_\phi$ velocity. Thus, in present-day tokamaks, the global plasma rotation dynamics is still dominated by the effects happening in the plasma core.

Appendix C

Lyapunov Theory Basics

C.1 Stability of Nonlinear Systems

C.1.1 Autonomous Systems

Consider a nonlinear, autonomous system

$$\dot{x} = g(x, u), \tag{C.1}$$

where $x \in \mathbb{R}^n$ is the state vector, $u \in \mathbb{R}^p$ is the input vector, and $g : \mathbb{R}^n \times \mathbb{R}^p \to \mathbb{R}^n$ is a nonlinear function. It is assumed that a control law $u = \psi_n(x)$ is known and set such that $g(x, \psi_n(x)) \triangleq \bar{f}(x)$, and also that the resulting function $\bar{f} : \mathbb{R}^n \to \mathbb{R}^n$ is locally Lipschitz in $\mathbb{R}^n$. It is said that $x = \bar{x}$ is an equilibrium of the system if

$$\bar{f}(\bar{x}) = 0. \tag{C.2}$$

Without loss of generality, it is possible to use the change of variables $\tilde{x} = x - \bar{x}$ so that (C.1) can be rewritten as

$$\dot{\tilde{x}} = \dot{x} - \dot{\bar{x}} = \bar{f}(\bar{x} + \tilde{x}) - \bar{f}(\bar{x}) = \bar{f}(\bar{x} + \tilde{x}) \triangleq f(\tilde{x}), \tag{C.3}$$

which is a system with an equilibrium at the origin ($\tilde{x} = 0$).

Next, stability, asymptotical stability, and global asymptotical stability of an equilibrium are defined. The equilibrium $\tilde{x} = 0$ of the system (C.3) is stable if, for

each $\epsilon > 0$, there exists $\delta = \delta(\epsilon) > 0$ such that

$$\|\tilde{x}(0)\| < \delta \Rightarrow \|\tilde{x}(t)\| < \epsilon, \forall t \geq 0. \tag{C.4}$$

Such equilibrium is asymptotically stable if it is stable and δ can be found such that

$$\|\tilde{x}(0)\| < \delta \Rightarrow \lim_{t\to\infty} \tilde{x}(t) = 0, \tag{C.5}$$

and it is globally asymptotically stable if $\|\tilde{x}(0)\|$ can be taken arbitrarily large. If a continuous function $V : \mathbb{R}^n \to \mathbb{R}^n$ can be found for the system (C.3) such that

$$V(0) = 0, \tag{C.6}$$

$$V(\tilde{x}) > 0, \ \forall \tilde{x} \neq 0, \tag{C.7}$$

$$\dot{V}(\tilde{x}) \leq 0, \forall x \neq 0, \tag{C.8}$$

then the equilibrium $\tilde{x} = 0$ is stable. If (C.6) and (C.7) are fulfilled, and condition (C.8) is strictly fulfilled, i.e., $\dot{V}(x) < 0$, $\forall x \neq 0$, then the equilibrium $\tilde{x} = 0$ is asymptotically stable. Finally, if the following condition holds

$$\|\tilde{x}\| \to \infty \Rightarrow V(\tilde{x}) \to \infty, \tag{C.9}$$

in conjunction with (C.6), (C.7), and the strict version of (C.8), then $\tilde{x} = 0$ is a globally asymptotically stable equilibrium.

In general, finding the function V, known as Lyapunov function, is a complicated problem. Typical candidates for Lyapunov functions are quadratic functions, $V = \tilde{x}^T P \tilde{x}$ $(P > 0)$, such that $\dot{V} = -\tilde{x}^T Q \tilde{x}$ with $Q > 0$. A more detailed introduction to Lyapunov stability theory for autonomous systems can be found in [65].

C.1.2 Non-Autonomous Systems

Consider a nonlinear, non-autonomous system

$$\dot{x} = g(x, u, t), \tag{C.10}$$

where $x \in \mathbb{R}^n$ is the state vector, $u \in \mathbb{R}^p$ is the input vector, and $g : \mathbb{R}^n \times \mathbb{R}^p \times [0, \infty) \to \mathbb{R}^n$ is a nonlinear function. It is assumed that a control law $u = \psi_n(x, t)$

is known and set such that $g(x, \psi_n(x), t) \triangleq \bar{f}(x, t)$, and also that the resulting function $\bar{f} : \mathbb{R}^n \times [0, \infty) \to \mathbb{R}^n$ is piecewise continuous in t and locally Lipschitz in x on $\mathbb{R}^n \times [0, \infty)$. A solution of the system, denoted by $\bar{x}(t)$, fulfills

$$\dot{\bar{x}}(t) = \bar{f}(\bar{x}(t), t). \tag{C.11}$$

Without loss of generality, it is possible to use the change of variables $\tilde{x} = x - \bar{x}$ so that (C.10) can be rewritten as

$$\dot{\tilde{x}} = \dot{x} - \dot{\bar{x}}(t) = \bar{f}(\bar{x}(t) + \tilde{x}, t) - \bar{f}(\bar{x}(t), t) \triangleq f(\tilde{x}, t), \tag{C.12}$$

which is a system with an equilibrium at the origin ($\tilde{x} = 0$).

The equilibrium $\tilde{x} = 0$ of the system (C.12) is exponentially stable if there exist positive c, k and λ such that

$$\|\tilde{x}\| \leq k \, \|x(t_0)\| \, e^{-\lambda(t-t_0)}, \;\; \forall \, \|x(t_0)\| \leq c. \tag{C.13}$$

If this condition holds for any $x(t_0)$, then the system is globally exponentially stable.

If a continuous function $V : \mathbb{R}^n \times [0, \infty) \to \mathbb{R}^n$ can be found for the system (C.10) such that

$$k_1 \|\tilde{x}\|^a \leq V(\tilde{x}, t) \leq k_2 \|\tilde{x}\|^a, \tag{C.14}$$

$$\dot{V}(\tilde{x}, t) \leq -k_3 \|\tilde{x}\|^a, \tag{C.15}$$

then the equilibrium $\tilde{x} = 0$ is exponentially stable.

As for the autonomous systems case, finding V can be a quite complicated problem. A more detailed introduction to Lyapunov stability theory for non-autonomous systems can be found in [65].

C.2 Lyapunov Redesign Basics

C.2.1 Autonomous Systems

Lyapunov redesign is the technique employed in this work to design a robust, nonlinear controller. Consider a nonlinear, autonomous, uncertain system with the

following shape

$$\dot{x} = f(x) + G(x)[u + \delta(x, u)], \tag{C.16}$$

where $x \in \mathbb{R}^n$ is the state vector, $u \in \mathbb{R}^p$ is the input vector, $\delta \in \mathbb{R}^p$ is the uncertainty vector, and $f : D \to \mathbb{R}^n$, $G : D \to \mathbb{R}^{n\times p}$ and $\delta : D \times \mathbb{R}^p \to \mathbb{R}^p$ are locally Lipschitz in x and u. It is assumed that a control law $u = \psi_n(x)$ and a Lyapunov function $V(x)$ have been found such that the origin of (C.16) is a globally asymptotically stable equilibrium in closed loop for the nominal system ($\delta = 0$). A control law $u = \psi_n + v$ is sought such that (C.16) is asymptotically stable when $\delta \neq 0$. The time derivative of V is given by

$$\dot{V} = \frac{\partial V}{\partial x}(f + G\psi_n) + \frac{\partial V}{\partial x}G\bigg(v + \delta\bigg), \tag{C.17}$$

where the dependence on x and u has been dropped to simplify notation. The term $\frac{\partial V}{\partial x}(f+G\psi_n)$ corresponds to the time derivative of V when the control law $u = \psi_n(x)$ is employed for the nominal system ($\delta \equiv 0$), which is negative by design. Therefore $\frac{\partial V}{\partial x}(f + G\psi_n) < -\alpha_c(\|x\|)$, where α_c is a class $\mathcal{K}$ function[1]. Then, it is found that

$$\dot{V} < -\alpha_c(\|x\|) + \frac{\partial V}{\partial x}G\bigg(v + \delta\bigg). \tag{C.18}$$

The term v must be designed such that $\dot{V} < 0$, regardless of the value of δ. Using the Cauchy-Schwarz inequality, (C.18) can be rewritten as

$$\dot{V} < -\alpha_c(\|x\|) + \frac{\partial V}{\partial x}Gv + \left\|\frac{\partial V}{\partial x}G\right\|_2 \|\delta\|_2 . \tag{C.19}$$

If there exists a bound with the shape

$$\|\delta(x, \psi_n(x) + v)\|_2 \leq \kappa_0(\|\rho_c(x)\|_2 + \|v\|_2), \tag{C.20}$$

where $\kappa_0 < 1$ and $\rho_c : D \to \mathbb{R}^p$ is non-negative, then

$$\dot{V} < -\alpha_c(\|x\|) + \frac{\partial V}{\partial x}Gv + \left\|\frac{\partial V}{\partial x}G\right\|_2 \kappa_0(\|\rho_c\|_2 + \|v\|_2), \tag{C.21}$$

and if v is taken as

$$v = -\frac{\kappa_0 \|\rho_c\|_2}{1 - \kappa_0}\frac{\left(\frac{\partial V}{\partial x}G\right)^T}{\left\|\frac{\partial V}{\partial x}G\right\|_2}, \tag{C.22}$$

[1] A function $f(x)$ belongs to class $\mathcal{K}$ iff (1) it is strictly increasing with x, and (2) $f(0) = 0$.

then

$$\frac{\partial V}{\partial x}Gv + \left\|\frac{\partial V}{\partial x}G\right\|_2 \kappa_0(\|\rho_c\|_2 + \|v\|_2) = 0, \tag{C.23}$$

and

$$\dot{V} < -\alpha_c(\|x\|). \tag{C.24}$$

Therefore, the origin of (C.16) is globally asymptotically stable under the control law $u = \psi_n + v$, with v given by (C.22), as long as a bound (C.20) can be found. However, a control law using (C.22) is undetermined at $\frac{\partial V}{\partial x}G = 0$. In order to avoid such problem, (C.22) is modified as

$$v = -\left(\frac{\kappa_0 \|\rho_c\|_2}{1-\kappa_0}\right)^2 \frac{\left(\frac{\partial V}{\partial x}G\right)^T}{\epsilon}, \tag{C.25}$$

whenever $\kappa_0 \|\rho_c\|_2 \left\|\frac{\partial V}{\partial x}G\right\|_2 < \epsilon$, for some design parameter ϵ. The control law (C.22)-(C.25) does not ensure global asymptotical stability, but it does ensures that x is bounded by a class $\mathcal{K}$ function[2] [65] of ϵ. Therefore, ϵ must be small in order to make the bound on x as small as possible, ensuring that x remains close to 0.

C.2.2 Non-Autonomous Systems

Consider a nonlinear, non-autonomous, uncertain system with the following shape

$$\dot{x} = f(x,t) + G(x,t)[u + \delta(x,u,t)], \tag{C.26}$$

where $x \in \mathbb{R}^n$ is the state vector, $u \in \mathbb{R}^p$ is the input vector, $\delta \in \mathbb{R}^p$ is the uncertainty vector, and $f : \mathbb{R}^n \times [0,\infty) \to \mathbb{R} \to \mathbb{R}^n$, $G : \mathbb{R}^n \times [0,\infty) \to \mathbb{R} \to \mathbb{R}^{n\times p}$ and $\delta : \mathbb{R}^n \times \mathbb{R}^p \times [0,\infty) \to \times\mathbb{R}^p \to \mathbb{R}^p$ are piecewise continuous in t and locally Lipschitz in x and u. It is assumed that a control law $u = \psi_n(x,t)$ and a Lyapunov function $V(x,t)$ have been found such that the origin of (C.26) is a globally exponentially stable equilibrium in closed loop for the nominal system ($\delta = 0$). A control law $u = \psi_n + v$ is sought such that (C.26) is asymptotically stable when $\delta \neq 0$. The time derivative of V is given by

$$\dot{V} = \frac{\partial V}{\partial t} + \frac{\partial V}{\partial x}(f + G\psi_n) + \frac{\partial V}{\partial x}G\Big(v + \delta\Big), \tag{C.27}$$

[2] A function $f(x)$ belongs to class $\mathcal{K}$ iff (1) it is strictly increasing with x, and (2) $f(0) = 0$.

where the dependence on x and u has been dropped to simplify notation. The term $\frac{\partial V}{\partial t} + \frac{\partial V}{\partial x}(f + G\psi_n)$ corresponds to the time derivative of V when the control law $u = \psi_n(x,t)$ is employed for the nominal system ($\delta \equiv 0$). Therefore $\frac{\partial V}{\partial t} + \frac{\partial V}{\partial x}(f + G\psi_n) \leq -k_3 \|x\|^a$, where a and k_3 are positive constants. Then, it is found that

$$\dot{V} \leq -k_3 \|x\|^a + \frac{\partial V}{\partial x} G\bigg(v + \delta\bigg). \tag{C.28}$$

The term v must be designed such that $\dot{V} < 0$, regardless of the value of δ. Using the Cauchy-Schwarz inequality, (C.28) can be rewritten as

$$\dot{V} \leq -k_3 \|x\|^a + \frac{\partial V}{\partial x} G v + \left\| \frac{\partial V}{\partial x} G \right\|_2 \|\delta\|_2 . \tag{C.29}$$

If there exists a bound with the shape

$$\|\delta(x, \psi_n(x) + v, t)\|_2 \leq \|\rho_c(x,t)\|_2 , \tag{C.30}$$

where $\rho_c : \mathbb{R}^n \times [0, \infty) \to \mathbb{R}^p$ is non-negative, then

$$\dot{V} \leq -k_3 \|x\|^a + \frac{\partial V}{\partial x} G v + \left\| \frac{\partial V}{\partial x} G \right\|_2 \|\rho_c\|_2 , \tag{C.31}$$

and if v is taken as

$$v = - \|\rho_c\|_2 \frac{\left(\frac{\partial V}{\partial x} G\right)^T}{\left\|\frac{\partial V}{\partial x} G\right\|_2}, \tag{C.32}$$

then

$$\frac{\partial V}{\partial x} G v + \left\| \frac{\partial V}{\partial x} G \right\|_2 \|\rho_c\|_2 = 0, \tag{C.33}$$

and

$$\dot{V} \leq -\alpha_c(\|x\|). \tag{C.34}$$

Therefore, the origin of (C.26) is globally exponentially stable under the control law $u = \psi_n + v$, with v given by (C.32), as long as a bound (C.30) can be found. However, a control law using (C.32) is undetermined at $\frac{\partial V}{\partial x} G = 0$. In order to avoid such problem, (C.32) is modified as

$$v = - \|\rho_c\|_2 \frac{\left(\frac{\partial V}{\partial x} G\right)^T}{\epsilon}, \tag{C.35}$$

whenever $\|\rho_c\|_2 \left\|\frac{\partial V}{\partial x}G\right\|_2 < \epsilon$, for some design parameter ϵ. The control law (C.32)-(C.35) does not ensure global exponential stability, but it does ensures that x is bounded by a class $\mathcal{K}$ function[3] of ϵ. Therefore, ϵ must be small in order to make the bound on x as small as possible, ensuring that x remains close to 0.

[3]A function $f(x)$ belongs to class $\mathcal{K}$ iff (1) it is strictly increasing with x, and (2) $f(0) = 0$.

Appendix D

Burn Control

D.1 Computation of κ_0

Using (4.54), (4.55), and (4.56), it is possible to write

$$||\delta(\psi_n + v)||_2 = \sqrt{2}\frac{||[\delta_{DT-line}, \delta_{D-line}]\psi_n + [\delta_{DT-line}, \delta_{D-line}]v||_2}{|\gamma^{nom}_{DT-line} - \gamma^{nom}_{D-line}|}, \tag{D.1}$$

which, by using the triangular inequality, can be rewritten as

$$||\delta(\psi_n + v)||_2 \leq \sqrt{2}\frac{||[\delta_{DT-line}, \delta_{D-line}]\psi_n||_2 + ||[\delta_{DT-line}, \delta_{D-line}]v||_2}{|\gamma^{nom}_{DT-line} - \gamma^{nom}_{D-line}|}, \tag{D.2}$$

and using the Cauchy-Schwarz inequality and the 2-norm properties, it is found that

$$||\delta(\psi_n + v)||_2 \leq \sqrt{2(\delta_{DT-line})^2 + (\delta_{D-line})^2}\frac{||\psi_n||_2 + ||v||_2}{|\gamma^{nom}_{DT-line} - \gamma^{nom}_{D-line}|}. \tag{D.3}$$

Finally, taking into account that $|\delta_{DT-line}| \leq \delta^{max}_{DT-line}$ and $|\delta_{D-line}| \leq \delta^{max}_{D-line}$, the following bound is found,

$$||\delta(\psi_n + v)||_2 \leq \sqrt{2(\delta^{max}_{DT-line})^2 + (\delta^{max}_{D-line})^2}\frac{||\psi_n||_2 + ||v||_2}{|\gamma^{nom}_{DT-line} - \gamma^{nom}_{D-line}|}, \tag{D.4}$$

and therefore,

$$\kappa_0 = \frac{\sqrt{2(\delta^{max}_{DT-line})^2 + (\delta^{max}_{D-line})^2}}{|\gamma^{nom}_{DT-line} - \gamma^{nom}_{D-line}|}. \tag{D.5}$$

D.2 Stability proof for Robust Control Law

The control law (4.57)-(4.58) assures that $|\tilde{n}_D|$ and $|\tilde{n}_T|$ are bounded by class $\mathcal{K}$ functions[1] of ϵ. It can be shown that, provided that $\tilde{E}$ is driven to zero, $|\tilde{n}_\alpha|$ and $|\tilde{n}_I|$ are also bounded by class $\mathcal{K}$ functions of ϵ. The definition of $n \triangleq n_i + n_e$, together with equations (2.75), (2.76), and (4.32) yield

$$\lim_{t\to\infty} n = \frac{3(\bar{n}_\alpha + \tilde{n}_\alpha) + 2(\bar{n}_D + \tilde{n}_D) + 2(\bar{n}_T + \tilde{n}_T)}{1 - f_I^{sp}(1 + Z_I)}. \tag{D.6}$$

It is known that $|\tilde{n}_D| < c(\epsilon)$ and $|\tilde{n}_T| < d(\epsilon)$, for some class $\mathcal{K}$ functions $c(\epsilon)$ and $d(\epsilon)$. This proof starts by assuming that initially, $|\tilde{n}_\alpha| > \frac{2}{3}(c(\epsilon) + d(\epsilon))$ (it can be seen below that this assumption does not imply a loss of generality in the proof). Then, an increase in $\tilde{n}_\alpha$ implies an increase in n, because the bound imposed through $c(\epsilon)$ implies that $\tilde{n}_D$ and $\tilde{n}_T$ can never compensate the variations in n produced by $\tilde{n}_\alpha$. This happens regardless of the dependence in $\tilde{n}_D$ and $\tilde{n}_T$ with $\tilde{n}_\alpha$. By the same token as in the proof for the nominal control law, an increase in n produces a decrease in T, and therefore a decrease in $\langle\sigma v\rangle_{DT}$, and vice versa, a decrease in n produces an increase in $\langle\sigma v\rangle_{DT}$. For S_α,

$$\begin{aligned} S_\alpha = (\bar{n}_D\bar{n}_T + \tilde{n}_D\bar{n}_T + \bar{n}_D\tilde{n}_T + \tilde{n}_D\tilde{n}_T)\langle\sigma v\rangle_{DT} \leq \\ (\bar{n}_D\bar{n}_T + |\tilde{n}_D|\bar{n}_T + \bar{n}_D|\tilde{n}_T| + |\tilde{n}_D\tilde{n}_T|)\langle\sigma v\rangle_{DT} = (\bar{n}_D\bar{n}_T + b(\epsilon))\langle\sigma v\rangle_{DT}, \end{aligned} \tag{D.7}$$

where $b(\epsilon) = \bar{n}_D d(\epsilon) + \bar{n}_T c(\epsilon) + c(\epsilon)d(\epsilon) > 0$ is a class $\mathcal{K}$ function of ϵ because $c(\epsilon)$ and $d(\epsilon)$ are class $\mathcal{K}$ functions, and $\bar{n}_D > 0$, $\bar{n}_T > 0$. The first term in (4.16) behaves with n_α in the same way as in the nominal control law proofs. By defining $-b'(\epsilon)\tilde{n}_\alpha = b(\epsilon)\langle\sigma v\rangle_{DT} > 0$, it is possible to write

$$\frac{d\tilde{n}_\alpha}{dt} \leq -\Big(f_\alpha + b'(\epsilon)\Big)\tilde{n}_\alpha. \tag{D.8}$$

It can be noted that $-b'(\epsilon)\tilde{n}_\alpha$ is a class $\mathcal{K}$ function, as $b(\epsilon)$ is a class $\mathcal{K}$ function and $\langle\sigma v\rangle_{DT} > 0$. Thus, it can be concluded that $\tilde{n}_\alpha$ tends to zero when $|\tilde{n}_\alpha| > \frac{2}{3}(c(\epsilon)+d(\epsilon))$, or what is the same, $|\tilde{n}_\alpha|$ decreases when $|\tilde{n}_\alpha| > \frac{2}{3}(c(\epsilon)+d(\epsilon))$. At some

[1] A function $f(x)$ belongs to class $\mathcal{K}$ iff (1) it is strictly increasing with x, and (2) $f(0) = 0$.

point, $|\tilde{n}_\alpha| = \frac{2}{3}(c(\epsilon) + d(\epsilon))$, and it cannot be assured that $|\tilde{n}_\alpha|$ decreases anymore. It may happen that $|\tilde{n}_\alpha|$ keeps on decreasing, that $|\tilde{n}_\alpha|$ stays at $\frac{2}{3}(c(\epsilon) + d(\epsilon))$, or that $|\tilde{n}_\alpha|$ grows above $\frac{2}{3}(c(\epsilon) + d(\epsilon))$ again. For any of those possibilities, it is always possible to find a class $\mathcal{K}$ function $h(\epsilon)$ such that $h(\epsilon) > \frac{2}{3}(c(\epsilon) + d(\epsilon))$, therefore bounding $|\tilde{n}_\alpha|$. From (D.6),

$$\lim_{t\to\infty} n = \bar{n} + \frac{3\tilde{n}_\alpha + 2\tilde{n}_D + 2\tilde{n}_T}{1 - f_I^{sp}(1 + Z_I)} \leq \bar{n} + \frac{3h(\epsilon) + 2c(\epsilon) + 2d(\epsilon)}{1 - f_I^{sp}(1 + Z_I)}, \tag{D.9}$$

and finally,

$$\begin{aligned} \lim_{t\to\infty} n_I = f_I^{sp} n &\leq f_I^{sp}\left(\bar{n} + \frac{3\tilde{n}_\alpha + 2\tilde{n}_D + 2\tilde{n}_T}{1 - f_I^{sp}(1 + Z_I)}\right) \\ &= \bar{n}_I + f_I^{sp}\left(\frac{3h(\epsilon) + 2c(\epsilon) + 2d(\epsilon)}{1 - f_I^{sp}(1 + Z_I)}\right), \end{aligned} \tag{D.10}$$

so $\tilde{n}_I$ is also bounded by a class $\mathcal{K}$ function of ϵ.

Appendix E

Feedback Linearization Control

E.1 Terms in MDE reduced model

The feedback-linearization model is obtained by discretizing the MDE over $m = 1, 2, ..., N-1$ nodes, where $\Delta\hat{\rho} = 1/N$ is the discretization step.

For the G_η subpart of G, equation (5.36), the terms α_m, β_m, and γ_m can be expressed as

$$\alpha_m = h^m_{diff,3} - \frac{2h^m_{diff,1}}{\Delta\hat{\rho}^2}, \;\; \beta_m = \frac{h^m_{diff,1}}{\Delta\hat{\rho}^2} + \frac{h^m_{diff,2}}{2\Delta\hat{\rho}}, \;\; \gamma_m = \frac{h^m_{diff,1}}{\Delta\hat{\rho}^2} - \frac{h^m_{diff,2}}{2\Delta\hat{\rho}}, \tag{E.1}$$

where $h_{diff,i}$ $(i = 1, ..., 3)$ are functions that are defined next, and $h^m_{diff,i}$ denotes the value of $h_{diff,i}$ at the m-th node. The $h_{(.)}$ functions in (E.1), together with those in the G_{aux} (see equation (5.37)) and G_{BS} (see equation (5.38)) subparts of G are given by

$$h_{diff,1} = f_\eta D_\psi, \;\; h_{diff,2} = f_\eta \left(\frac{D_\psi}{\hat{\rho}} + 2\frac{\partial D_\psi}{\partial \hat{\rho}} \right) + \frac{\partial f_\eta}{\partial \hat{\rho}} D_\psi, \tag{E.2}$$

$$h_{diff,3} = f_\eta \left(\frac{\partial^2 D_\psi}{\partial \hat{\rho}^2} + \frac{\hat{\rho}\frac{\partial D_\psi}{\partial \hat{\rho}} - D_\psi}{\hat{\rho}^2} \right) + \frac{\partial f_\eta}{\partial \hat{\rho}} \left(\frac{D_\psi}{\hat{\rho}} + D'_\psi \right), \tag{E.3}$$

$$h_{aux,i} = \frac{\partial f_{aux,i}}{\partial \hat{\rho}}, \;\; h_{BS,1} = \frac{\partial f'_{BS}}{\partial \hat{\rho}}, \;\; h_{BS,2} = f_{BS}, \tag{E.4}$$

where $D_\psi \triangleq \hat{F}\hat{G}\hat{H}$, and

$$f_\eta = \frac{Z_{eff} k_{sp}^{prof}}{\mu_0 \rho_b^2 \hat{F}^2 \left(T_e^{prof}\right)^{3/2} \left(n_e^{prof}\right)^{3/2\zeta}}, \tag{E.5}$$

$$f_{aux,i} = R_0 \hat{H} Z_{eff} k_{sp}^{prof} j_{aux,i}^{dep} \left(T_e^{prof}\right)^{\delta_{aux,i}-3/2} \left(n_e^{prof}\right)^{(\delta_{aux,i}-3/2)\zeta+1}, \tag{E.6}$$

$$f_{BS} = \frac{R_0^2 \hat{H} Z_{eff} k_{sp}^{prof}}{\hat{F} \left(T_e^{prof}\right)^{3/2} \left(n_e^{prof}\right)^{3/2\zeta}} \left(2\mathcal{L}_{31} T_e^{prof} (n_e^{prof})^{\zeta} \frac{\partial n_e^{prof}}{\partial \hat{\rho}} + \right.$$
$$\left. (2\mathcal{L}_{31} + \mathcal{L}_{32} + \alpha \mathcal{L}_{34}) n_e^{prof} \frac{\partial \left(T_e^{prof} (n_e^{prof})^{\zeta}\right)}{\partial \hat{\rho}} \right). \tag{E.7}$$

Appendix F

Individual Scalars Control

F.1 Asymptotical and Exponential Stability Proof

The stability properties of the first order system

$$\frac{d\tilde{x}}{dt} = -K_P\tilde{x} - K_I\int_{t_0}^{t}\tilde{x}dt, \tag{F.1}$$

are analyzed in this Section by using Lyapunov theory. It is assumed that $K_P > 0$ and $K_I > 0$. First, it is convenient to rewrite (F.1) as

$$\frac{d\tilde{x}_1}{dt} = -K_P\tilde{x}_1 - K_I\tilde{x}_2, \tag{F.2}$$

$$\frac{d\tilde{x}_2}{dt} = \tilde{x}_1, \tag{F.3}$$

where $\tilde{x}_1 = \tilde{x}$ and $\tilde{x}_2 = \int_{t_0}^{t}\tilde{x}dt$.

It can be noted that the dynamical system (F.1) (or alternatively, (F.2)-(F.3)) corresponds to a simple mass-spring-damper model. If the energy of the system, E, given by

$$E = \frac{1}{2}\tilde{x}_1^2 + \frac{1}{2}K_I\tilde{x}_2^2, \tag{F.4}$$

is employed as a Lyapunov function, $V = E$, then it is found that

$$\dot{V} = -K_P\tilde{x}_1^2 \leq 0, \tag{F.5}$$

for all $\tilde{x}_1 \neq 0$, $\tilde{x}_2 \neq 0$. Equation (F.5) demonstrates the stability of the system (F.2)-(F.3) (see also Appendix C.1.1, conditions (C.6)-(C.8)).

It can be appreciated that, in fact, $\dot{V} < 0$ for all $\tilde{x}_1, \tilde{x}_2 \neq 0$ with the only exception of the subset S such that $\tilde{x}_1 = 0$. It can also be seen that no solution to (F.2)-(F.3) can stay in S except for the trivial solution. This can be demonstrated by employing (F.2) with $\tilde{x}_1 \equiv 0$,

$$\frac{d\tilde{x}_1}{dt}^{0} = -\cancelto{0}{K_P\tilde{x}_1} - K_I\tilde{x}_2 \implies \tilde{x}_2 \equiv 0. \tag{F.6}$$

Therefore, using La Salle's invariance theorem, it can be concluded that (F.1) is in fact globally asymptotically stable.

With the goal of analyzing the global exponential stability of (F.2)-(F.3), V is modified as

$$V = \frac{1}{2}\tilde{x}_1^2 + \frac{1}{2}(K_I + a)\tilde{x}_2^2 + b\tilde{x}_1\tilde{x}_2, \tag{F.7}$$

for some constants a and b that need to be determined. Computing the time derivative of V yields

$$\dot{V} = (b - K_P)\tilde{x}_1^2 + (a - bK_P)\tilde{x}_1\tilde{x}_2 - K_I b\tilde{x}_2^2, \tag{F.8}$$

and by choosing

$$a - bK_P = 0, \quad b - K_P = -K_I b, \tag{F.9}$$

then $\dot{V} = (b - K_P)\left(\tilde{x}_1^2 + \tilde{x}_2^2\right)$. Solving for a and b in (F.9) yields

$$a = \frac{K_P^2}{1 + K_I}, \quad b = \frac{K_P}{1 + K_I}, \tag{F.10}$$

and therefore, (F.8) becomes

$$\dot{V} = -\frac{K_P K_I}{1 + K_I}\left(\tilde{x}_1^2 + \tilde{x}_2^2\right). \tag{F.11}$$

It can be seen that

$$\dot{V} \leq -K\left(\tilde{x}_1^2 + \tilde{x}_2^2\right), \tag{F.12}$$

for any constant K such that $K_P K_I/(1 + K_I) \geq K > 0$. In order to ensure $V > 0$ for all $\tilde{x}_1, \tilde{x}_2 \neq 0$, the following two conditions must be fulfilled

$$b < K_P, \tag{F.13}$$

$$K_I + a - b^2 > 0. \tag{F.14}$$

Employing (F.10), inequality (F.13) becomes

$$K_P > \frac{K_P}{1+K_I}, \tag{F.15}$$

which is fulfilled for any values $K_P > 0$ and $K_I > 0$. Inequality (F.14) can also be written, using (F.10), as

$$K_I \frac{K_P^2 + (1+K_I)^2}{(1+K_I)^2} > 0, \tag{F.16}$$

which is fulfilled for $K_I > 0$. Finally, it is convenient to rewrite V as

$$V = \frac{1}{2} \left[\tilde{x}_1, \tilde{x}_2\right] A \begin{bmatrix} \tilde{x}_1 \\ \tilde{x}_2 \end{bmatrix}, \tag{F.17}$$

where

$$A = \begin{bmatrix} 1 & \frac{K_P}{1+K_I} \\ \frac{K_P}{1+K_I} & K_I + \frac{K_P^2}{1+K_I} \end{bmatrix}. \tag{F.18}$$

Because $V > 0$, then all the eigenvalues of A, denoted by λ_i, are also > 0, and

$$\lambda_{min} \|[\tilde{x}_1, \tilde{x}_2]\|_2^2 \leq V \leq \lambda_{max} \|[\tilde{x}_1, \tilde{x}_2]\|_2^2. \tag{F.19}$$

Therefore, the system (F.2)-(F.3) fulfills all the conditions in (C.14)-(C.15) with a Lyapunov function V as given by (F.17), and its global exponential stability can be concluded.

Bibliography

[1] A. S. Eddington, "The Internal Constitution of the Stars," *The Scientific Monthly*, vol. 11, no. 4, pp. 297–303, Oct. 1920.

[2] F. F. Chen, *Introduction to Plasma Physics and Controlled Fusion.* New York: Springer, 1974.

[3] L. M. Hively, "Convenient Computational Forms For Maxwellian Reactivities," *Nuclear Fusion*, vol. 17, no. 4, pp. 873–876, 1977.

[4] A. Sonoc and J. Jeswiet, "A review of lithium supply and demand and a preliminary investigation of a room temperature method to recycle lithium ion batteries to recover lithium and other materials," *ScienceDirect, 21st CIRP Conference on Life Cycle Engineering*, vol. 15, pp. 289–293, 2014.

[5] J. Wesson, *Tokamaks.* Oxford, UK: Clarendon Press, 1984.

[6] I. H. Hutchinson, *Principles of Plasma Diagnostics.* New York: Cambridge University Press, 1987.

[7] The ASDEX Team, "The H-Mode of ASDEX," *Nuclear Fusion*, vol. 29, no. 11, pp. 1959–2040, 1989.

[8] K. H. Burrel *et al.*, "Quiescent H-mode Plasmas in the DIII-D Tokamak," *Plasma Physics and Controlled Fusion*, vol. 44, no. A253, 2002.

[9] P. B. Snyder *et al.*, "Super H-mode: Theoretical Prediction and Initial Observations of a New High Performance Regime for Tokamak Operation," *Nuclear Fusion*, vol. 55, no. 083026, 2015.

[10] E. Joffrin, "Advanced Tokamak Scenario Developments for the Next Step," *Plasma Physics and Controlled Fusion*, vol. 49, no. B629, 2007.

[11] D. A. Humphreys *et al.*, "Novel Aspects of Plasma Control in ITER," *Physics of Plasmas*, vol. 22, 021805, 26pp, 2015.

[12] M. Ariola and A. Pironti, "Plasma Shape Control for the JET Tokamak: an Optimal Output Regulation Approach," *IEEE Control Systems Magazine*, vol. 25, pp. 65–75, 2005.

[13] R. L. Haye *et al.*, "Control of Neoclassical Tearing Modes in DIII-D," *Physics of Plasmas*, vol. 9, no. 2051, pp. 2051–2060, 2002.

[14] T. E. Evans, "Suppression and Mitigation of Edge-Localized Modes in the DIII-D Tokamak with 3D Magnetic Perturbations," *Plasma and Fusion Research*, vol. 7, p. , 2012.

[15] D. A. Humphreys *et al.*, "Integrated Plasma Control in DIII-D," *Fusion Science and Technology*, vol. 48, no. 2, pp. 1249–1263, 2005.

[16] F. L. Hinton and R. D. Hazeltine, "Theory of Plasma Transport in Toroidal Confinement Systems," *Reviews of Modern Physics*, vol. 48, no. 2, pp. 239–308, 1976.

[17] Y. Ou, T. Luce, E. Schuster *et al.*, "Towards model-based current profile control at DIII-D," *Fusion Engineering and Design*, vol. 82, pp. 1153–1160, 2007.

[18] J. Barton, W. Shi *et al.*, "Physics-based Control-oriented Modeling of the Safety Factor Profile Dynamics in High Performance Tokamak Plasmas," *Proceeding of the 52nd IEEE International Conference on Decision and Control*, 2013.

[19] O. Sauter *et al.*, "Neoclassical Conductivity and Bootstrap Current Formulas for General Axisymmetric Equilibria and Arbitrary Collisionality Regime," *Physics of Plasmas*, vol. 6, no. 7, pp. 2834–2839, 1999.

[20] M. Erba *et al.*, "Validation of a New Mixed Bohm/gyro-Bohm model for Electron and Ion Heat Transport Against the ITER, Tore Supra and START Database Discharges," *Nuclear Fusion*, vol. 38, no. 7, pp. 1013–1028, 1998.

[21] F. Albajar *et al.*, "Importance of Electron Cyclotron Wave Energy Transport in ITER," *Nuclear Fusion*, vol. 45, no. 7, pp. 642–648, 2005.

[22] F. Felici and O. Sauter, "Non-linear Model-based Optimization of Actuator Trajectories for Tokamak Plasma Profile Control," *Plasma Physics and Controlled Fusion*, vol. 54, no. 2, p. 025002, 2012.

[23] J. R. Goldston, "Topics in Confinement Analysis of Tokamaks with Auxiliary Heating," *Proceeding Course Workshop (Varenna, 3-13 September)*, vol. 1, pp. 165–186, 1986.

[24] W. P. Wehner, "Strategies for Optimal Control of the Current and Rotation Profiles in the DIII-D Tokamak," Ph.D. dissertation, Lehigh University, Bethlehem, 2017. [Online]

[25] W. Solomon *et al.*, "Mechanisms for Generating Toroidal Rotation in Tokamaks without External Momentum Input," *Physics of Plasmas*, vol. 17, no. 5, 056108, 11 pp, 2010.

[26] A. Garofalo *et al.*, "Plasma Rotation Driven by Static Nonresonant Magnetic Fields," *Physics of Plasmas*, vol. 16, 056119, 2009.

[27] E. J. Doyle *et al.*, "ITER Physics Basis. Chapter 2: Plasma Confinement and Transport," *Nuclear Fusion*, vol. 47, no. 6, 2007.

[28] R. J. Hawryluk, N. W. Eidietis, B. A. Grierson, and A. W. Hyatt, "Control of Plasma Stored Energy for Burn Control using DIII-D In-vessel Coils," *Nuclear Fusion*, vol. 55, no. 5, 2015.

[29] M. D. Boyer and E. Schuster, "Nonlinear Burn Condition Control in Tokamaks using Isotopic Fuel Tailoring," *Nuclear Fusion*, vol. 55, no. 083021, 24pp, 2015.

[30] L. R. Baylor *et al.*, "Pellet Fuelling and Control of Burning Plasmas in ITER," *Nuclear Fusion*, vol. 47, pp. 443–448, 2007.

[31] R. A. Causey, "Hydrogen Isotope Retention and Recycling in Fusion Reactor Plasma-facing Components," *Journal of Nuclear Materials*, vol. 300, pp. 91–117, 2002.

[32] R. J. L. Haye *et al.*, "Higher Stable Beta by use of Pre-emptive Electron Cyclotron Current Drive on DIII-D," *Nuclear Fusion*, vol. 45, no. L37, 2005.

[33] F. Felici, "Real-Time Control of Tokamak Plasmas: from Control of Physics to Physics-Based Control," Ph.D. dissertation, Ecole Polytechnique Federale de Lausanne, Lausanne, Switzerland, 2011. [Online]

[34] TRANSP official website. [Online]

[35] ASTRA online manual. [Online]

[36] J. Martinell and J. Vitela, "Thermal Stability Studies of an Experimental Nuclear Fusion Reactor," *Journal of Physics: Conference Series*, vol. 511, no. 012043, 2014.

[37] E. Schuster and M. Krstic, "Burn Control in Fusion Reactors Via Nonlinear Stabilization Techniques," *Fusion Science and Technology*, vol. 43, 2003.

[38] L. Bromberg, J. L. Fisher, and D. R. Cohn, "Active Burn Control of Nearly Ignited Plasmas," *Nuclear Fusion*, vol. 20, p. 203, 1980. [Online]

[39] E. A. Chaniotakis, J. P. Freidberg, and D. R. Cohn, "CIT Burn Control using Auxiliary Power Modulation," in *Proc. 13th IEEE/NPSS Symp. Fusion Engineering*. Institute of Electrical and Electronics Engineers/Nuclear and Plasma Sciences Society, 1990, pp. 400–403. [Online]

[40] S. W. Haney and L. J. Perkins, "Operating Point Selection and Burn Stability Control for the International Thermonuclear Experimental Reactor," in *Proc. 13th IEEE/NPSS Symp. Fusion Engineering.* Institute of Electrical and Electronics Engineers/Nuclear and Plasma Sciences Society, 1990, pp. 396–399. [Online]

[41] D. Ashby and M. H. Hughes, "Dynamic Burn Control of a Tokamak Reactor by Fuel Injection," *Nuclear Fusion*, vol. 20, pp. 451–457, 1980.

[42] W. Hui and G. H. Miley, "Burn Control by Refueling," *Bull. Am. Phys. Soc*, vol. 37, no. 6, p. 1399, 1992. [Online]

[43] B. A. Bamieh, W. Hui, and G. H. Miley, "Robust Burn Control of a Fusion Reactor by Modulation of the Refueling Rate," *Fusion Technology*, vol. 25, no. 3, p. 318, 1994.

[44] W. Hui *et al.*, "Effectiveness and Constraints of using the Refueling System to Control Fusion Reactor Burn," in *15th IEEE/NPSS Symp. Fusion Engineering*, vol. 2. Institue of Electrical and Electronics Engineers/Nuclear and Plasma Sciences Society, 1994, pp. 562–564. [Online]

[45] D. A. Plummer, "Fusion Reactor Control," in *Proc. 16th IEEE/NPSS Symp. Fusion Engineering*, vol. 2. Institute of Electrical and Electronics Engineers/Nuclear and Plasma Sciences Society, 1995, pp. 1186–1189. [Online]

[46] M. Greenwald, "Density Limits in Toroidal Plasmas," *Plasma Physics and Controlled Fusion*, vol. 44, no. 8, 2002.

[47] O. Mitarai, A. Sagara, R. Sakamoto, N. Ohyabu, A. Komori, and O. Motojima, "High-Density, Low Temperature Ignited Operations in FFHR," *Plasma and Fusion Research*, vol. 5, pp. S1001–S1001, 2010. [Online]

[48] J. Mandrekas and W. M. Stacey, "Evaluation of Different Burn Control Methods for the International Thermonuclear Experimental Reactor," *Proceedings of the 13th IEEE Symposium on Fusion Engineering*, vol. 1, pp. 404–407, 1989.

[49] S. Haney, L. J. Perkins, J. Mandrekas, and W. M. Stacey, "Active Control of Burn Conditions for the International Thermonuclear Experimental Reactor," *Fusion Technology*, vol. 18, no. 4, pp. 606–17, 1990.

[50] S. McCool, A. J. Wootton, and M. Kotschenreuther, "Particle Transport Studies with Applied Resonant Fields on TEXT," *Nuclear Fusion*, vol. 30, no. 1, p. 167, 1990.

[51] A. Grosman, T. E. Evans *et al.*, "Ergodic Divertor Impact on Tore Supra Plasma Edge," *Journal of Nuclear Materials*, vol. 176-177, pp. 493–498, 1990.

[52] T. E. Evans, "Edge Stability and Transport Control with Resonant Magnetic Perturbations in Collisionless Tokamak Plasmas," *Nature Physics*, vol. 2, pp. 419–423, 2006.

[53] D. Anderson, T. Elevant, H. Hamen, M. Lisak, and H. Persson, "Studies of Fusion Burn Control," *Fusion Technology*, vol. 23, no. 1, pp. 5–41, 1993.

[54] A. Sestero, "Proposed Scenario for Burn Control in Tokamak Reactors," *Nucl. Technology/Fusion*, vol. 4, p. 437, 1983.

[55] G. Sager, G. Miley, and I. Maya, "Optimal Control Theory Applied to Fusion Plasma Thermal Stabilization," *Fusion Technology*, vol. 8, p. 1795, 1985.

[56] J. Vitela, "Burn Conditions Stabilization with Artificial Neural Networks of Subignited Thermonuclear Reactors with Scaling Law Uncertainties," *Plasma Physics and Controlled Fusion*, vol. 43, pp. 99–119, 2001. [Online]

[57] ——, "Stabilization of Burn Conditions in a Thermonuclear Reactor using Artificial Neural Networks," pp. 295–318, 1998.

[58] K. D. Zastrow *et al.*, "Tritium Transport Experiments on the JET tokamak," *Plasma Physics and Controlled Fusion*, vol. 46, no. 12B, pp. B255–B265, Dec. 2004. [Online]

[59] M. J. Gouge, W. A. Houlberg, S. E. Attenberger, and S. L. Milora, "Fuel Source Isotopic Tailoring and Its Impact on ITER Design, Operation and Safety," *Fusion Technology*, pp. 1–18, 1995.

[60] A. Pajares and E. Schuster, "Nonlinear Burn Control in Tokamaks Using In-Vessel Coils," in *Proc. 2016 IEEE Multi-Conference in Systems and Control*, Buenos Aires, Argentina, 2016.

[61] ——, "Nonlinear Burn Control Using In-Vessel Coils and Isotopic Fueling in ITER," *Fusion Engineering and Design*, vol. 123, pp. 607–611, 2017.

[62] ——, "Nonlinear Robust Burn Control in Tokamaks with Uncertainties in the Fueling Lines via Lyapunov Redesign," in *Proc. 2017 IEEE American Control Conference*, Seattle, Washington, 2017.

[63] ——, "Robust Nonlinear Burn Control in ITER to Handle Uncertainties in the Fuel-line Concentrations," *Nuclear Fusion*, submitted and accepted for publication.

[64] W. M. Stacey, *Fusion: An Introduction to the Physics and Technology of Magnetic Confinement Fusion*, 2nd ed. Weinheim: Wiley-VCH, 2010.

[65] H. Khalil, *Nonlinear Systems*, 3rd ed. Prentice Hall, 2001.

[66] T. Wijnands, D. Houtte, G. Martin, X. Litaudon, and P. Froissard, "Feedback Control of the Current Profile on Tore Supra," *Nuclear Fusion*, vol. 37, no. 6, p. 777, 1997.

[67] T. Suzuki, A. Isayama, S. Ide, T. Fujita, T. Oikawa, S. Sakata, M. Sueoka, H. Hosoyama, and M. Seki, "Recent RF Experiments and Application of RF Waves to Real-Time Control of Safety Factor Profile in JT-60U," *AIP Conference Proceedings*, vol. 787, no. 1, pp. 279–286, 2005. [Online]

[68] J. Ferron *et al.*, "Feedback Control of the Safety Factor Profile Evolution during Formation of an Advanced Tokamak Discharge," *Nuclear Fusion*, vol. 46, no. 10, p. L13, 2006.

[69] Y. Ou, C. Xu, and E. Schuster, "Robust Control Design for the Poloidal Magnetic Flux Profile Evolution in the Presence of Model Uncertainties," *IEEE Transactions on Plasma Science*, vol. 38, no. 3, pp. 375–382, 2010, http://ieeexplore.ieee.org/stamp/stamp.jsp?arnumber=05404914.

[70] F. Argomedo, E. Witrant, C. Prieur, D. Georges, and S. Bremond, "Model-based Control of the Magnetic Flux Profile in a Tokamak Plasma," in *Decision and Control (CDC), 2010 49th IEEE Conference on*, 2010, pp. 6926–6931.

[71] J. Barton, D. Boyer, W. Shi, E. Schuster *et al.*, "Toroidal Current Profile Control During Low Confinement Mode Plasma Discharges," *Nuclear Fusion*, vol. 52, no. 123018, 2012.

[72] M. Boyer, J. Barton, E. Schuster *et al.*, "First-Principles-Driven Model-Based Current Profile Control for the DIII-D Tokamak via LQI Optimal Control," *Plasma Physics and Controlled Fusion*, vol. 55, no. 105007, 2013.

[73] M. Boyer, J. Barton, E. Schuster, M. Walker, T. Luce, J. Ferron, B. Penaflor, R. Johnson, and D. Humphreys, "Backstepping Control of the Toroidal Plasma Current Profile in the DIII-D Tokamak," *Control Systems Technology, IEEE Transactions on*, vol. 22, no. 5, pp. 1725–1739, Sept 2014.

[74] Z. Ilhan, W. Wehner, J. Barton, E. Schuster, D. Gates, S. Gerhardt, and J. Menard, "First-Principles-Driven Model-Based Optimal Control of the Current Profile in NSTX-U," in *Proceedings of the 2015 IEEE Multi-conference on Systems and Control*, 2015.

[75] J. Barton, M. Boyer, E. Schuster *et al.*, "Physics-model-based Nonlinear Actuator Trajectory Optimization and Safety Factor Profile Feedback Control for Advanced Scenario Development in DIII-D," *Nucl. Fusion*, vol. 55, no. 093005, 2015.

[76] E. Schuster, J. Barton, W. Wehner, M. Boyer, T. Luce, J. Ferron, C. Holcomb, M. Walker, D. Humphreys, W. Solomon, B. Penaflor, and R. Johnson, "Enhanced Reproducibility of L-Mode Plasma Discharges via Physics-model-based q-profile Feedback Control in DIII-D," *Nuclear Fusion*, vol. 57, no. 116026, 2017.

[77] W. Wehner, J. Barton, E. Schuster, C. Holcomb, T. Luce, J. Ferron, M. Walker, D. Humphreys, B. Penaflor, and R. Johnson, "Optimal Current Profile Control for Enhanced Repeatability of L-mode and H-mode Discharges in DIII-D," *Fusion Engineering and Design*, vol. 123, pp. 513–517, 2017.

[78] D. Moreau *et al.*, "A Two-time-scale Dynamic Model Approach for Magnetic and Kinetic Profile Control in Advanced Tokamak Scenarios on JET," *Nuclear Fusion*, vol. 48, 2008.

[79] W. Shi, W. Wehner, J. Barton, M. Boyer, E. Schuster *et al.*, "A two-time-scale model-based combined magnetic and kinetic control system for advanced tokamak scenarios on DIII-D," in *Decision and Control (CDC), 2012 IEEE 51st Annual Conference on*, 2012, pp. 4347–4352.

[80] J. Barton, K. Besseghir, J. Lister, and E. Schuster, "Physics-based Control-oriented Modeling and Robust Feedback Control of the Plasma Safety Factor Profile and Stored Energy Dynamics in ITER," *Plasma Physics and Controlled Fusion*, vol. 57, no. 115003, 2015.

[81] J. Barton, W. Wehner, E. Schuster, F. Felici, and O. Sauter, "Simultaneous Closed-loop Control of the Current Profile and the Electron Temperature Profile in the TCV Tokamak," *2015 IEEE American Control Conference*, 2015.

[82] M. Boyer, R. Andre *et al.*, "Central Safety Factor and β_N Control on NSTX-U via Beam Power and Plasma Boundary Shape Modification," *Nuclear Fusion*, vol. 55, 2015.

[83] W. Wehner *et al.*, "Predictive Control of the Tokamak q Profile to Facilitate Reproducibility of High-$q_{\min}$ Steady-State Scenarios at DIII-D," in *2016 IEEE Conference on Control Applications (CCA)*, 2016, pp. 629–634.

[84] W. P. Wehner, A. Pajares, E. Schuster, J. R. Ferron, C. T. Holcomb, D. A. Humphreys, R. D. Johnson, B. Penaflor, K. Thome, B. S. Victor, and M. L. Walker, "Optimal Current Profile Control for Enhanced Repeatability of L-mode and H-mode Discharges in DIII-D," *Nuclear Fusion*, 2018.

[85] A. Pajares and E. Schuster, "Central Safety Factor Control in DIII-D using Neutral Beam Injection and Electron Cyclotron Launchers in Zero Input-Torque Scenarios," in *1st IEEE Conference on Control Technology and Applications*, 2017.

[86] A. Pajares *et al.*, "Central Safety Factor and Normalized Beta Control Under Near-Zero Input Torque Constraints in DIII-D," presented at the 59th Annual Meeting of the APS Division of Plasma Physics, 2017.

[87] A. Pajares and E. Schuster, "Safety Factor Profile Control in Tokamaks via Feedback Linearization," *55th IEEE Conference on Decision and Control*, 2016.

[88] ——, "Nonlinear Robust Safety Factor Profile Control in Tokamaks via Feedback Linearization and Nonlinear Damping Techniques," *2nd IEEE Conference on Control Technology and Applications*, 2018.

[89] ——, "Safety Factor Profile and Normalized Beta Control in Tokamaks via Feedback Linearization and Lyapunov Techniques," *Nuclear Fusion*, to be submitted.

[90] J. E. Barton, "Physics-model-based Optimization and Feedback Control of the Current Profile Dynamics in Fusion Tokamak Reactors," Ph.D. dissertation, Lehigh University, Bethlehem, 2015. [Online]

[91] J. T. Scoville *et al.*, "Simultaneous Feedback Control of Plasma Rotation and Stored Energy on the DIII-D Tokamak," *Fusion Engineering and Design*, vol. 82, no. 5-14, pp. 1045–1050, 2007.

[92] W. P. Wehner, J. Barton and E. Schuster, "Combined Rotation Profile and Plasma Stored Energy Control for the DIII-D Tokamak via MPC," in *2017 American Control Conference*, 2017.

[93] I. R. Goumiri *et al.*, "Simultaneous Feedback Control of Plasma Rotation and Stored Energy on NSTX-U using Neoclassical Toroidal Viscosity and Neutral Beam Injection," *Phys. Plasmas*, vol. 24, no. 056101, 2017.

[94] W. Shi, W. Wehner, J. Barton *et al.*, "System Identification and Robust Control of the Plasma Rotational Transform Profile and Normalized Beta Dynamics for Advanced Tokamak Scenarios in DIII-D," *Fusion Engineering and Design*, vol. 117, pp. 39–57, 2017.

[95] A. Pajares, E. Schuster, and the DIII-D Team, "Integrated Robust Control of the Global Toroidal Rotation and Total Plasma Energy in Tokamaks," *Transactions of Plasma Physics (SOFE special issue)*, 2019.

[96] ——, "Integrated Robust Control of Individual Scalar Variables in Tokamaks," *submitted to the proceedings of the 58th IEEE International Conference on Decision and Control*, 2019.

[97] ——, "Actuator Management via Real-time Optimization for Integrated Control in Tokamaks," *submitted to the proceedings of the 46th European Physical Society Conference on Plasma Physics*, 2019.

[98] G. Gantenbein *et al.*, "Complete Suppression of Neoclassical Tearing Modes with Current Drive at the Electron-Cyclotron-Resonance Frequency in ASDEX Upgrade Tokamak," *Phys. Rev. Lett.*, vol. 85, no. 1242, 2000.

[99] A. Isayama *et al.*, "Complete Stabilization of a Tearing Mode in Steady State High-β_p H-mode Discharges by the First Harmonic Electron Cyclotron Heating/Current Drive on JT-60U," *Plasma Physics and Controlled Fusion*, vol. 42, no. 12, pp. L–37 – L–45, 2000.

[100] D. A. Humphreys *et al.*, "Active Control for Stabilization of Neoclassical Tearing Modes," *Physics of Plasmas*, vol. 13, no. 056113, 2006.

[101] G. Giruzzi *et al.*, "Dynamical Modelling of Tearing Mode Stabilization by RF Current Drive," *Nuclear Fusion*, vol. 39, no. 107, 1999.

[102] X. D. Z. Q. Yu and S. Gunter, "Numerical Studies on the Stabilization of Neoclassical Tearing Modes by Radio Frequency Current Drive," *Physics of Plasmas*, vol. 11, no. 1960, 2004.

[103] J. Woodby *et al.*, "Model for Current Drive Stabilization of Neoclassical Tearing Modes," *Physics of Plasmas*, vol. 15, no. 092504, 2008.

[104] W. P. Wehner and E. Schuster, "Control-oriented Modelling for Neoclassical Tearing Mode Stabilization via Minimum-seeking Techniques," *Nuclear Fusion*, vol. 52, no. 074003, 2012.

[105] F. W. Perkins, R. W. Harvey, M. Makowski, and M. N. Rosenbluth, "Prospects for Electron Cyclotron Current Drive Stabilization of Neoclassical Tearing Modes in ITER," in *17th IEEE/NPSS Symposium Fusion Engineering*, vol. 2, 2017, pp. 749–751.

[106] R. J. Buttery *et al.*, "Neoclassical Tearing Modes," *Plasma Physics and Controlled Fusion*, vol. 42, no. B61, 2000.

[107] F. D. Halpern, G. Bateman, and A. H. Kritz, "Integrated Simulations of Saturated Neoclassical Tearing Modes in DIII-D, Joint European Torus, and ITER Plasmas," *Physics of Plasmas*, vol. 13, no. 062510, 2006.

[108] R. J. L. Haye *et al.*, "Cross-machine Benchmarking for ITER of Neoclassical Tearing Mode Stabilization by Electron Cyclotron Current Drive," *Nuclear Fusion*, vol. 46, no. 4, 2006.

[109] R. J. L. Haye, A. Isayama, and M. Maraschеck, "Prospects for Stabilization of Neoclassical Tearing Modes by Electron Cyclotron Current Drive in ITER," *Nuclear Fusion*, vol. 49, no. 045005, 2009.

[110] A. Pajares *et al.*, "Integrated Current Profile, Normalized Beta and NTM Control in DIII-D," *Fusion Engineering and Design*, 2018.

[111] A. Pajares, E. Schuster, and the DIII-D Team, "Progress Towards Integrated Profile Control and NTM Suppression in DIII-D," *to be presented the 61st Annual Meeting of the American Physical Society Division of Plasma Physics*, 2019.

[112] N. Eidietis *et al.*, "Implementing a Finite-State Off-Normal and Fault Response System for Disruption Avoidance in Tokamaks," *Nuclear Fusion*, vol. 58, no. 056023, p. , 2018.

[113] M. Cengher *et al.*, "DIII-D Electron Cyclotron Heating System Status and Upgrades," *IEEE Transactions on Plasma Science*, vol. 44, no. 12, p. , 2006.

[114] Z. Taylor *et al.*, "Magnetic Flux Conversion and the Role of Benign Tearing Modes in the DIII-D High-beta Hybrid Scenario," *58th Annual Meeting of the APS Division of Plasma Physics*, vol. 61, p. , 2016.

[115] OMFIT official website. [Online]

[116] M. R. Wade *et al.*, "Development, Physics Basis and Performance Projections for Hybrid Scenario Operation in ITER on DIII-D," *Nuclear Fusion*, vol. 45, no. 407, p. , 2005.

Vita

Mr. Andres Pajares Martinez was born on July 25, 1989 in Badajoz, Spain. He received a Masters of Science degree in Aerospace Engineering from the University of Seville in 2012. From 2012 until the end of 2014, he worked for Quest Global as a subcontractor for Airbus Military in the Final Assembly Line of the A400-M aircraft, in Seville. In 2015, he joined the Lehigh University Plasma-Control Group to pursue a Ph.D. in Mechanical Engineering, where he worked on developing a variety of plasma control solutions for tokamak plasmas and participated in several experiments in the DIII-D tokamak. In 2017, he moved to the DIII-D National Fusion Facility in San Diego, CA, to keep on with his Ph.D. as an on-site collaborator with General Atomics. Upon completion of his Ph.D. degree in 2019, he is getting a post-doctoral position with the Lehigh University Plasma-Control Group to further develop the existing control algorithms for DIII-D plasmas.